

# **The precipitation behaviour and the formation of deformation induced ferrite during a new type of thermomechanical processing**

**Peng Gong**



**Thesis submitted for the degree of Doctor of Philosophy**

**Department of Engineering Materials**

**The University of Sheffield**

**January 2016**

## Abstract

A new type of thermomechanical processing with rough rolling below the recrystallisation-stop temperature ( $T_{5\%}$ ), followed by a rapid reheat to 1200 °C for 10 s, and then finish rolling at the same temperature as the rough rolling, was investigated to better understand the kinetics of strain-induced precipitates (SIP). In addition, the deformation-induced ferrite transformation (DIFT) during the finishing passes was investigated as an efficient method to achieve the ultrafine ferrite grains. For comparative purposes, two experimental 0.06 wt% C steels were studied; one with 0.03 wt% Nb (Nb steel), and another one with both 0.03 wt% Nb and 0.02 wt% Ti (Nb-Ti steel).

To understand SIP behaviour and its effect on the recrystallisation, six different rough rolling temperatures were used in the range of 850-1100°C. The full recrystallisation temperature ( $T_1$ ) and recrystallisation stop temperature ( $T_s$ ) contributions of the precipitates start temperature were determined using the Dutta and Sellars's model approach on the basis of optical microscopy (OM) and transmission electron microscopy (TEM) characterization. It was found that there were mixed structures after rolling at 950 °C in Nb and Nb-Ti steels, which is consistent with the  $T_1$  (960 °C in Nb steel) and  $T_s$  (950 °C) by Dutta and Sellars's model. The number density and volume fraction of SIP increased as the rolling temperature was decreased, consistent with the prediction that the nose of the precipitates-time-temperature diagrams (PTT) is at 840 °C in both steels. The orientation relationship (OR) between precipitates and ferrite matrix has been identified by analysis of selection area electron diffraction patterns. While obeying OR, the nanoscale particles precipitated in the austenite region during deformation.

After the roughing schedule, with the final roughing pass taking place at 850 °C, the steels were rapidly reheated at a rate of 10 °C/sec to a temperature of 1200 °C, held at temperature for various times, and water quenched to room temperature. Then, both the precipitate dissolution kinetics, together with the austenite grain coarsening kinetics was established as a function of the holding time at 1200 °C. The importance to subsequent finish rolling was then used for the final part of the project.

Finally, processing these steels consisted of a simulated roughing rolling schedule with the final roughing pass taking place at 850 °C, followed by rapidly reheating at a rate of 10°C/sec to a temperature of 1200 °C, held at temperature for 10 s and 100 s, and then air cooled to the

final rolling temperature of 850 °C followed by deformation using different parameters. The effect of different rolling and reheating parameters on the microstructures and the SIP was fully analysed using various techniques. This thermomechanical process route resulted in DIFT, with ferrite nucleated primarily on the prior-austenite grain boundaries. The ferrite/martensite phase transformation temperature was increased by the heat treatment at 1200 °C. The volume fraction of SIP after finish rolling was influenced by the supersaturation of microalloyed elements in solution during heat treatment. The variation of micro-hardness correlated well with the change of volume fraction of SIP and DIFT, as well as the refinement of prior-austenite grain size.

# Contents

Abstract.....	I
Acknowledgements.....	VII
<b>CHAPTER 1: INTRODUCTION .....</b>	<b>1</b>
1.1. Micro-alloyed steels .....	1
1.2. Thermo-mechanical controlled processes .....	2
1.3. Objectives.....	3
<b>CHAPTER 2: LITERATURE REVIEW .....</b>	<b>6</b>
2.1. An introduction to microalloyed steels .....	6
2.2. Thermo-mechanical Controlled Processing (TMCP).....	7
2.2.1. The development of thermo-mechanical process (TMP).....	7
2.2.2. The wide use of microalloyed steels processed by TMCP .....	8
2.3. Deformation Microstructures .....	10
2.3.1. Deformation mechanism on the dislocation and deformation band .....	10
2.3.2. DIFT.....	11
2.4. Microstructural evolution.....	14
2.4.1. Recovery .....	14
2.4.2. Recrystallisation.....	16
2.4.3. Grain Growth .....	19
2.5. Precipitation and dissolution behaviours in microalloyed steels .....	19
2.5.1. Thermodynamic driving force for precipitation .....	19
2.5.2. Kinetics of SIP .....	21
2.5.3. Solubility of microalloyed elements in austenite and its effect on the austenite grain size during heat treatment .....	23
<b>CHAPTER 3: EXPERIMENTAL PROCEDURE AND TECHNIQUES .....</b>	<b>30</b>
3.1 Materials.....	30
3.2 Thermomechanical processes.....	31
3.2.1. Rough rolling .....	31
3.2.2. Reheat treatment .....	32
3.2.3. Finish rolling.....	33
3.3 Microscopy techniques.....	34
3.3.1. OM and scanning electron microscopy (SEM).....	35
3.3.2. Transmission electron microscopy (TEM) .....	36

3.3.3. Micro-hardness testing.....	38
<b>CHAPTER 4: THE EFFECT OF HOT ROLLING TEMPERATURES ON THE MICROSTRUCTURES AND PRECIPITATION BEHAVIOURS IN THE Nb AND Nb-Ti STEELS .....</b>	<b>39</b>
4.1. Introduction .....	39
4.2. Modelling the 5% recrystallization and PTT curves.....	39
4.3. Characteristic of the microstructure by OM.....	42
4.3.1. Morphology of prior austenite grains .....	42
4.3.2. Grain size measurements .....	43
4.4. TEM carbon extraction replicas .....	45
4.4.1. Morphology and chemistry of precipitate.....	45
4.4.2. The volume fraction and the content of microalloyed steels in precipitates.....	51
4.5. TEM thin foil analysis.....	54
4.5.1. Calculation of the orientation relationship between SIP and austenite, subsequently transformed to ferrite .....	54
4.5.2. The observation of strain-induced precipitation during rough rolling using TEM and HRTEM.....	56
4.6. Vickers micro-hardness.....	60
4.7. Summary .....	61
<b>CHAPTER 5: THE HEAT TREATMENT AT 1200 °C WITH DIFFERENT DURATION ON ROUGH ROLLING MICRO-ALLOYED STEELS .....</b>	<b>63</b>
5.1 Introduction .....	63
5.2 The morphology of prior-austenite grain size.....	64
5.2.1 Rough rolling microstructures .....	64
5.2.2 Reheating microstructures .....	65
5.3 Grain size measurements.....	66
5.4 TEM carbon extraction replicas .....	67
5.4.1. Rough rolling SIP .....	67
5.4.2. Reheating SIP.....	68
5.5 Precipitate morphology and chemistry.....	73
5.5.1. Nb steel .....	73
5.5.2. Nb-Ti steel .....	76
5.5 The solid solution of microalloyed elements during isothermal holding.....	79
5.5.1 The content of Nb in solid solution.....	79

5.5.2	Ti/(Ti+Nb) ratio from precipitation in the Nb-Ti steel .....	80
5.6	Vickers micro-hardness.....	82
5.7	Summary .....	82
CHAPTER 6: FINISH ROLLING IN STEELS MICROALLOYED WITH NIOBIUM .....		84
6.1	Introduction .....	84
6.2	Characterisation of the microstructures by OM and SEM .....	84
6.2.1.	Morphology of the prior-austenite grains and the DIFT .....	84
6.2.2.	Prior-austenite grain size and volume fraction of second phase ferrite measurements.....	91
6.3	TEM carbon extraction replicas .....	94
6.3.1	The size distribution of the SIP.....	94
6.3.2	The volume fraction of the SIP and the content of Nb in these precipitates ...	104
6.3.3	The chemical composition in SIP .....	105
6.4	Nano-scale cementite in the deform-induced ferrite .....	110
6.5	Vickers hardness .....	112
6.6	The ultrafine grains after a new TMCP rolling schedule .....	113
6.7	Summary .....	116
CHAPTER 7: DISCUSSION.....		118
7.1	Microstructures.....	118
7.1.1	Prior-austenite grain analysis .....	118
7.1.2	DIFT Analysis.....	127
7.2	SIP and the state of Nb in solution or in precipitates .....	130
7.2.1.	The state of Nb in precipitates after rough rolling .....	130
7.2.2.	The state of microalloyed elements in solution after reheating at 1200°C with different holding times.....	131
7.2.3	The state of Nb in precipitates after finish rolling .....	134
7.3	Vickers micro-hardness.....	136
7.3.1	The effect of rough rolling process on the Vickers micro-hardness.....	136
7.3.2	The effect of reheating on the Vickers micro-hardness .....	137
7.3.3	The effect of finish rolling on the Vickers micro-hardness .....	137
CHAPTER 8: CONCLUSIONS .....		141
8.1.	Rough rolling.....	141
8.2.	Reheating.....	142
8.3.	Finish Rolling.....	143

CHAPTER 9: FUTURE WORK .....	145
9.1 The deformation textures .....	145
9.2 Controlled cooling process.....	145
9.3 Chemical composition.....	145
CHAPTER 10: PUBLICATION AND CONFERENCE PRESENTATION .....	146
10.1 Publications .....	146
10.2 Conference presentation .....	146
References.....	147

## **Acknowledgements**

I am very grateful to Prof. Mark Rainforth and Dr. Eric Palmiere for their encouragement during my PhD in the Materials Science and Engineering Department, and for their patience, guidance and support during the course of the project. Without their selfless help and attention, my PhD project would not process successfully. I would also want to thank Prof. Brad Wynne for his helpful discussions on the textures analysis.

I would like to express my gratitude to the technical staff of the Materials Science and Engineering Department and the Sorby Centre of Electron Microscopy for their technical assistance, especially Mr Dean Haylock and Mr Michael Bell for support on the TMC machine, tensile and hardness testing machines, Dr Peter Korgul, Dr Peng Zeng, Dr Le Ma and Dr Cheryl Shaw for all the training and facilitating the Electron Microscopy Laboratory sessions.

Special thanks to my colleagues, especially in H6, for the friendly and enjoyable atmosphere, support me to finish my serious works.

Finally, I am truly grateful my parents for their unwavering support during my PhD study. I dedicate this work to them.

# CHAPTER 1: INTRODUCTION

## 1.1. Micro-alloyed steels

Microalloyed steels have become one of the most popularly researched steels, because of their combination of high strength, high toughness and excellent weldability as a result of reduction of carbon content and increase of the micro-alloying elements such as niobium, titanium and vanadium [1–4]. In recent years, microalloyed steels have widely been used in various fields due to the improvement in the final microstructure and mechanical properties, e.g. construction of hulls for naval warships, submarines and other large engineering machines [5–7].

Microalloy additions play an equally important role with the thermo-mechanical controlled processes (TMCP) on the evolution of the final microstructure and associated mechanical properties. Micro-alloying elements in steels, such as Ti and Nb, can facilitate grain refinement through their precipitation in austenite, and contribute to dispersion hardening through the precipitation in ferrite during or after phase transformation [8–10]. It is well known that Nb carbides or carbonitrides can inhibit the static recrystallisation of austenite and help to achieve fine final microstructures, because it has a significant effect on the microstructure and the mechanical properties of low-carbon microalloyed steels [11,12]. Furthermore, titanium has frequently been added to microalloyed steels to enhance the control of the austenite and the transformed ferrite grain size during deformation and heat treatment process [13].

Numerous studies of the precipitation kinetics on microalloyed steels focus on the isothermal heat treatment in austenite with the retardation of the recrystallization by precipitation, like Dutta and Sellars [11] or isothermal austenite to ferrite transformation in the intercritical region, like Sakuma and Honeycombe [14]. However, there was no systematic study that examined the solid solution behaviour of microalloyed elements during high temperature holding, where the isothermal temperature is extreme higher than the equilibrium temperature of Nb. Moreover, the supersaturation of microalloyed elements in the austenite region influence on the grain size coarsening during high temperature holding, and the precipitation behaviour followed by deformation has not been examined by other reserchers.

## 1.2. Thermo-mechanical controlled processes

Thermo-mechanical controlled processes (TMCP), consisting of controlled hot rolling followed by controlled cooling, are mainly used for microalloyed steels [1, 2]. The improvement of TMCP in mechanical properties is due to the ferrite grain refinement, which maximises the area of austenite grain boundaries and deformation bands density [15, 16]. For this reason, during TMCP, the final deformation temperature takes place below the recrystallisation-stop temperature ( $T_5\%$ ) to increase the nucleation sites by obtaining the ultra-fine ferrite grain size [17–19].

However, to produce superior quality microalloyed steels, some engineering problems need to be overcome for TMCP processing, such as the requirement of high load equipment, high energy consumption and the high demand for quantity from customers [20]. To improve the production efficiency and reduce its consumption, a new rolling process has been applied through the addition of a reheating process between rough and finish rolling as shown in Fig. 1.1. Therefore, the finish rolling temperature could be increased to higher temperature, which will increase the productivity and reduce the production cost. However, the effect of this reheating on the deformed austenite, and particularly the precipitate dissolution kinetics, has not yet been investigated. Much of the published work is concerned with precipitates of one type and their distribution in idealised solution treated and ageing experiments after deformation [2,21–26]. Moreover, the reheating process before final rolling will lead to the coarsening of the grain size, which will further influence the final structures by reducing the mechanical properties. To obtain a desired microstructure combined with excellent strength and impact toughness properties in microalloyed steels due to the new thermo-mechanical process [17,18], deformation induced ferrite transformation (DIFT) has been proposed as an effective method to achieve ultrafine ferrite grains in microalloyed low carbon steels. The  $\gamma \rightarrow \alpha$  phase transformation temperature can be influenced by the prior-austenite grain size, the microalloyed elements in solution and the deformation temperature, as well as the deformation strain and strain rate. Manipulating the  $\gamma \rightarrow \alpha$  phase transformation temperature has become a key subject for investigation to obtain ultrafine ferrite grains in recent years [27–33]. Few researches have been done on the effect of reheating process between roughing and finishing deformation on the DIFT.

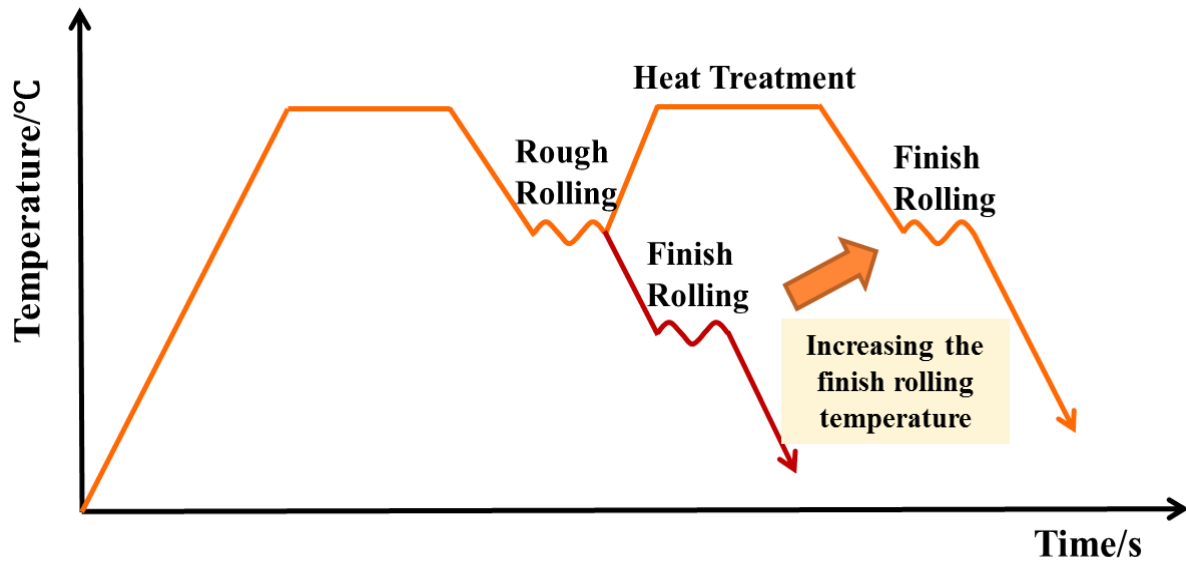


Fig. 1.1 Rolling schedule

### 1.3. Objectives

In this project, there are few questions need to be solved for the new type of TMCP, which are listed below:

- 1) Rough Rolling: Investigate the rough rolling temperature on the microstructures and precipitation behaviour, and select a final rough rolling temperature to obtain the highest volume fraction of precipitates.
- 2) Heat Treatment: To establish the precipitate dissolution kinetics together with the austenite grain coarsening kinetics during isothermal holding with different times and clarify the effect of Ti on the Nb precipitates and dissolution kinetics.
- 3) Finish Rolling: To refine the final grain size using the DIFT through the new TMCP rolling process.

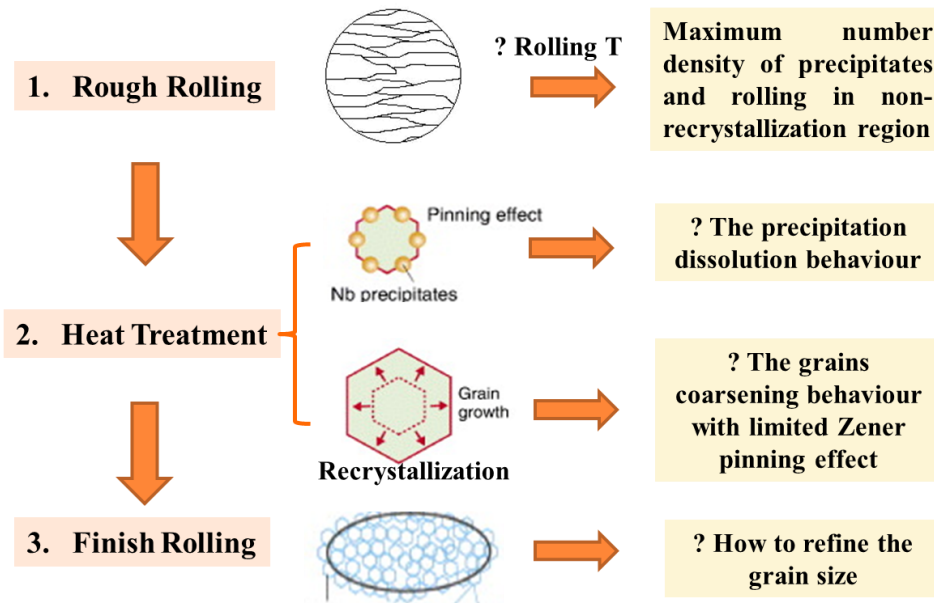


Fig. 1.2 Relevant research questions for this new TMCP.

With these objectives, the thesis has been structured in the following way:

Chapter 2 gives the necessary background in this project, which includes an introduction of microalloyed steels, TMCP process, and microstructures and precipitation during deformation and heat treatment.

Chapter 3 gives the experimental techniques and equipment used in this project, such as OM for microstructure analysis, transmission electron microscopy for precipitation and structure analysis and electron back scatter diffraction for texture analysis. Moreover, in this research, two types of Nb and Nb-Ti steels have been selected for comparative reasons.

Chapter 4 describes the determination of the effect of deformation temperatures on precipitation behaviour and on recrystallization microstructures. Furthermore, the orientation relationship between precipitates and austenite transformed to ferrite has been analysed, which suggest that those particles are SIP. The results of this chapter provide a final rough rolling temperature for obtaining non-recrystallisation structures with highest volume fraction of SIP.

Chapter 5 investigates the effect of reheating on the steels after rough rolling. The two steels were rough rolled at 850°C, followed by immediate reheating to 1200°C. At this isothermal reheating temperature, the state of Nb (Nb in solution or Nb(CN) as precipitates) over a range of holding times was analysed, so that the precipitate dissolution kinetics could be established,

together with the austenite grain coarsening kinetics. Through a comparison of the two steels, the effect of Ti on the Nb precipitates and dissolution kinetics can be clarified.

Chapter 6 examines a method to improve the production efficiency and reduce the energy consumption by increasing the final rolling temperature. A new type of TMCP rolling process has been applied through adding a reheating process between rough and finish rolling. The reheating process before finish rolling would lead to the coarsening of grain size combined with higher supersaturation of microalloyed and carbon elements, which is discussed in chapter 5. However, there is little research on the effect of a reheating process between deformation on the microstructure refinement, and the dissolution and precipitation behaviours of microalloyed elements. Therefore, the effect of dissolution and precipitation kinetics on refinement of the final grain size was investigated by various methods. Simultaneously, the DIFT has been observed on and within the prior austenite grains after finish rolling. To understand the effect of the undercooling, coarsening austenite grain size and supersaturation of elements on the DIFT behaviour, two isothermal holding times at the designed reheating temperature were investigated. The kinetic theories and mechanisms of DIFT formation are discussed, considering about the supersaturation of elements and the prior austenite grain size before deformation.

Chapter 7 provides a discussion of the experimental data from chapter 4, 5 and 6, to further understand the combination of microstructures and precipitation on the mechanical properties using related theories and different modelling equations.

Chapter 8 summarises all the chapters and gives conclusions for this project.

Chapter 9 proves suggestions on this project on the future work that can offset the deficiencies depending on the experimental data and their discussion from chapter 4 to chapter 7.

## CHAPTER 2: LITERATURE REVIEW

### 2.1. An introduction to microalloyed steels

Microalloyed steels are one type of alloy steels that have been developed since the 1960s, where small amounts of alloying elements (0.05 to 0.15 %), such as Nb, Ti and V are added to the steel [34]. The differences between alloy, low alloy and microalloy steels are listed in Table 2.1 [35]. Microalloyed steels can be defined as typically containing 0.07 to 0.12 % carbon, up to 2 % manganese and a small amount of Nb, Ti and V (maximum 0.1 %) [36]. Microalloyed steels are widely used in many areas, such as oil and gas transportation, because they provide better mechanical properties, such as high strength and toughness, and greater fatigue life and resistance to corrosion combined with weldability compared to conventional carbon steels [5,7,37].

Table 2.1

The different of alloy steel, low alloy steel and micro-alloy steel [35]

<b>Alloyed Steels</b>	<b>Alloy Steel</b>	<b>Low Alloy Steel</b>	<b>Microalloy Steel</b>
<b>Definitions</b>	<b>For different requirement on mechanical properties, it contents as possible as alloying elements</b>	<b>The contents of alloying elements less than 3.5 %</b>	<b>The contents of alloying elements less than 0.15%</b>

To obtain the full strengthening from the microalloy additions microalloyed steels need to have a soaking temperature prior to forging in order to dissolve all the microalloy elements. The Nb plays a critical role in delaying recrystallization during finish rolling which results in an elongated austenite microstructure and therefore produces fine ferrite grains during transformation [38,39]. The high temperature stable Ti in microalloyed steels has been shown to enhance the toughness, because the Ti carbides can inhibit the coarsening of austenite grains [40]. It was also reported that the shape of the Nb carbide was changed by the Ti additions which led to the formation of cuboid particles that are very stable at high temperatures [13]. Moreover, the dissolution behaviour of NbC can be influenced by adding

Ti into microalloyed steels, as this is known to delay the solution of the carbides into the matrix during reheating [6,41,42].

## 2.2. Thermo-mechanical Controlled Processing (TMCP)

### 2.2.1. The development of thermo-mechanical process (TMP)

The concept of thermo-mechanical processing was first proposed by BISRA (British Iron and Steel Research Association) at the end of the 1950s [43]. Irani, Irvine and others [44,45], [46] studied the controlled rolling and controlled cooling after hot rolling, which was regarded as a new thermo-mechanical processing. Their research focused on the static and dynamic restoration processes of austenite, the equilibrium solubility of microalloyed elements and precipitation behaviour during deformation and transformation, as well as the mechanical properties. The excellent advantages brought about by the addition of microalloyed elements in microalloyed steels was fully exploited by TMP through grain refinement and precipitation strengthening mechanisms [47,48]. The development process of TMP is listed in Fig. 2.1 [49]. In 1974 the Sumitomo High Toughness (SHT) process was analysed with extremely low slab reheating temperature followed by reducing the rolling temperature below the austenitic recrystallization temperature or even lower than  $A_{r3}$  [50]. It achieved superior low temperature toughness by refinement of the ferrite grain size. The researchers continually improved the controlled rolling process and, in 1970s, a Japanese steel company was the first to present a new TMP with accelerated cooling equipment after hot rolling, which was called TMCP [49]. In 1980s, the TMCP was widely used in the majority of steel companies around the world. There are many advantages of TMCP on grain refinement and the transformed microstructures particularly leading to increased strength and toughness in various steels [50–55]. TMCP is widely practised in Japan and Europe industries, but the cooling process has been further improved by changing continuous cooling to interrupted accelerated cooling (IAC), because IAC has advantages in saving energy and enhancing hardenability [47,56–58]. Later, direct quenching (DQ)-tempering process was developed and correlated with TMCP to satisfy the increasing production requirement in steel markets and improve the mechanical properties in line pipe steel, microalloyed steels and austenitic stainless steels [59–63]. The TMCP and DQ processes can obtain mechanical properties mainly by grain refinement and precipitation strengthening [64–66]. The new TMCP+DQ rolling process increased the total manufacturing tonnage by about 85 % with the main applications found in shipbuilding, bridges and other areas.

year	1970	1980	1990	2000
TMP	Controlled Rolling	$\gamma + \alpha$ two-Phase Region Rolling		R & D for Ultra-Fine Grain Steel
		SHT	OLAC	
	Low Temp. Rolling	Low Reheat. Temp. Rolling	TMCP	
			Accelerated Cooling	
			Direct Quenching	
			Modeling Study for Hot Rolling Process	
Strengthening Mechanism	Grain Refinement Precipitation Hardening	Deformation Strengthening	Strengthening due to Martensite or Bainite Transformation Strengthening	Strengthening due to Ultra-fine Grain Refinement
Code and Standard			○ ASTM A841 (TMCP Steel)	○ JIS-SN (Building use)

Fig. 2.1 Historical development progress of TMP [49]

### 2.2.2. The wide use of microalloyed steels processed by TMCP

The microalloyed steels have been widely used for ship-building, construction and pipe-line as well as automotive applications due to the excellent mechanical properties combined with weldability, which is produced by TMCP. Microalloyed steels coupled with TMCP have various advantages, for example superior weldability by reducing the carbon content, increasing the low temperature toughness and decreasing the production cost [67]. Table 2.2 presents an example of the advantages of TMCP compared with conventional rolling, which affects the mechanical properties of microalloyed steels.

Table 2.2

The mechanical properties of tensile and V-Charpy in TMCP steels [37].

Use	Type	Plate thick (mm)	Chemical composition (%)										Tensile prop		
			C	Si	Mn	P	S	Cu	Ni	Nb	Caq	Pcm	YP MPa	TS MPa	
Hull structure	TMCP	25	0.16	0.19	1.02	0.022	0.011					0.33	0.22	372	515
	Conventional	25	0.17	0.43	1.36	0.020	0.006					0.40	0.25	347	514
Off shore	TMCP	65	0.08	0.15	1.36	0.005	0.002	0.12	0.39	0.01	0.34	0.17	422	518	

There are numerous advantages of TMCP on the production of microalloyed steels. With different material property requirements required from microalloyed steels depending on the conditions of use, the process of TMCP can be tailored to satisfy these different conditions.

When considering heavy microalloyed plates for example, TMCP is required to improve the value of the crack tip opening displacement at low temperature both on the matrix and heat affected zone (HAZ) by readjusting the material properties [68–71]. By using TMCP to increase the pass reduction and the volume fraction of ferrite in HAZ islands, the microalloyed steels with extremely low carbon can be produced with thickness approaching 65 mm with excellent properties for offshore and ship-building environments [72–74].

Microalloyed steels can also be used on oil vessels, which require high tensile strength. By adding microalloyed elements like Nb and B, the bainite range can be extended during continuous-cooling over a wide range of cooling rates [75]. With a bainite structure TMCP can produce heavy microalloyed steel plates with excellent low weld cracking parameter ( $P_{cm}$ ) without control of the cooling rate [74,76]. As the production equipment became more advanced, higher specification microalloyed steels could be made, for example in building constructions the thickness of the plate could be increased up to 100 mm without decreasing the strength below 590 MPa, the yield ratio was also reduced below 80% and at the same time the weldability was improved [77]. A later development for TMCP was to deform in the  $\gamma$  and  $\alpha$  region due to the hard and soft phases optimized without needing to reduce the rolling temperatures any lower than the transformation temperature. Ferrite produced above the  $A_{r3}$  is called strain-induced ferrite, which can also refine the final grain size through the Zener pinning mechanism leading to an improvement in both strength and toughness [33,78,79]. With target strength of 780 MPa, without reducing the plate thickness, TMCP followed by DQ and tempering is the most efficient processing method for microalloyed steels. Another approach is to add around 1 % Cu as the addition of Cu allows a reduction in the carbon content by enhancing the strength through precipitation hardening of  $\epsilon$ -Cu, giving a new type of microalloyed steel with a strength of 780 MPa and low  $P_{cm}$  value [80–82].

In summary, over the years there has been a continuous increase in the required properties of microalloyed steels with higher strength, toughness and weldability as well as the lower yield ratio. To achieve this, TMCP followed by DQ has become widely useful in modern steel production, for applications in shipbuilding or civil engineering. However, TMCP associated with microalloyed steels also has its own weakness. The high strength means that high mill loads are required during rolling, which significantly increases the production and weld cost. The TMCP still has the potential to manufacture microalloyed steels with high integrated mechanical properties.

## 2.3. Deformation Microstructures

### 2.3.1. Deformation mechanism on the dislocation and deformation band

The body centred cubic metals will primarily deform to create defects as this allows stored energy to be present within the microstructure and minimises thermodynamic instabilities. Dislocations may be present individually, but also often aggregate into cells and subgrains in order to minimise the strain energy. Ewing et al. [83] established the slip system including slip plane and slip direction. The slip plane has the highest density of atoms, and the slip direction is also the closest packed direction. Dislocations are located between slipped and unslipped common boundaries, which was first reported by Polanyi in 1934 [84,85]. The dislocation can be described by the Burgers vector  $b$ , which is constant for a given dislocation. The Burgers vector is determined by means of a magnitude and direction of the failure of the circuit. There are two types of dislocation, which are separated by the direction of vector  $b$ . When the dislocation line is perpendicular to the slip direction, it is called a pure edge dislocation. Then, when the direction is changed to parallel, it is called a pure screw dislocation. In real materials, there are always mixed dislocations.

When considering the dislocation motion, there are two basic types: slip and climb. Slip is defined as a shear movement of dislocations in the plane. The dislocation slip requires less energy to break an atomic bond consecutively than all at once. The other motion is regarded as cross-slip that the screw dislocation move from one type of  $\{111\}$  planes to another if it contains the direction of the Burgers vector. In Body Centre Cubic crystals, the screw dislocation with a Burgers vector  $\frac{1}{2}\langle 111 \rangle$  can glide on three  $\{110\}$  planes and three  $\{112\}$  planes, which leads to the wavy slip lines [83].

The slip planes correspond to the slip system has the different orientation from grain to grain. The slip is confined in its initiated grain, but the deformation is not always homogeneous. Therefore, the deformation band has normally been used to describe the different of orientation in the same grain. The deformation band has been analysed by different researchers [86–89], because it provided to be influenced on deformation texture and the subsequent recrystallisation.

### 2.3.2. DIFT

In microalloyed steels, the matrix strength is a function of the solid solution strengthening, the dislocation density and precipitation hardening, which gives a yield strength level of about 300MPa [90]. However, the maximum tensile strength that can be achieved in these steels is no more than 1000 MPa. To raise the tensile strength level up to 1500 MPa, a new technique of TMCP was analysed to obtain ultra-refinement grains. According to the Hall-Petch relationship [91], yield strength associated with the from grain size:

$$\sigma_y = \sigma_0 + Kd^{-1/2} \quad (2.1)$$

Where  $\sigma_y$  is the yield stress,  $d$  is the grain size, and  $\sigma_0$  and  $K$  are constant. Using Eq. (2.1), the relationship between grain size and the yield stress can be established and is shown in Fig. 2.2. There are also other factors which influence the yield strength, such as precipitation strengthening, dislocation strengthening and solid solution strengthening. Fig. 2.3 shows the relationship between grain size and yield strength of microalloyed pipeline steel depending on all these factors [92]. The results show that the yield strength can be doubled by refining the grain size.

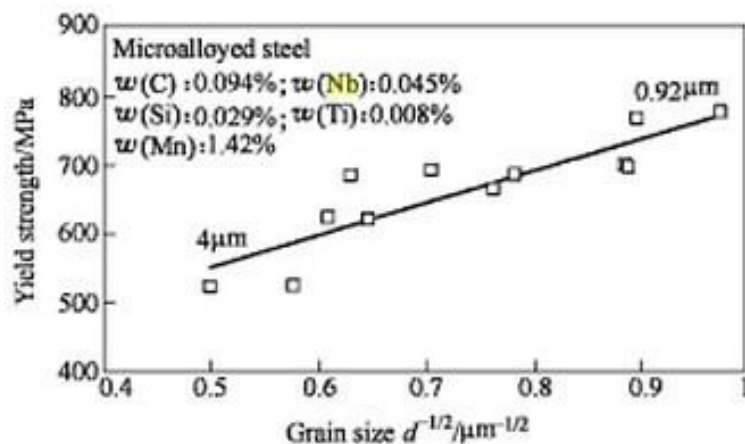


Fig. 2.2 Relationship of yield strength and grain size for a microalloyed steel [92].

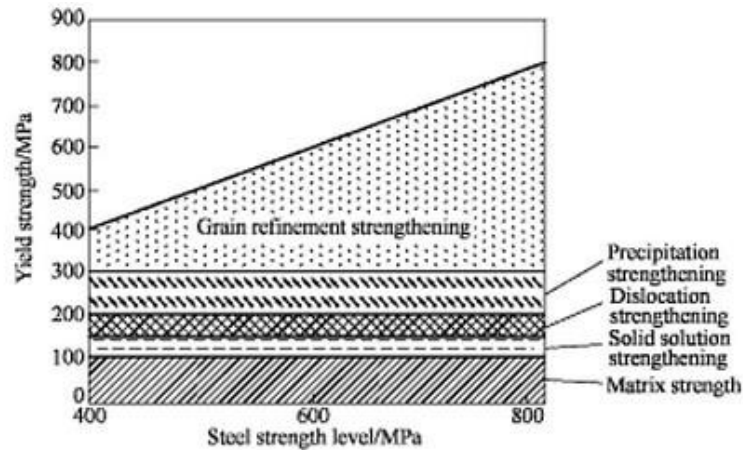


Fig. 2.3 Schematic of various strengthening effects [92].

In the last two decades, the fine grain size has been achieved by cold rolling and annealing, due to controlling the austenite to ferrite transformation. For example when combining controlled rolling and accelerated cooling, the ferrite grain size can be reduced to 5  $\mu\text{m}$ . However, the final ferrite grain size is about 5  $\mu\text{m}$  in conventional controlled rolled steels. If the final grain size can be refined to below 2  $\mu\text{m}$  (which is known as ultrafine grain size), depending on the Hall-Petch Eq. (2.1), the yield strength can increase to almost 350 MPa, and refining the grain size is also the only method that can increase both strength and toughness. There are several methods that can produce the ultrafine grain size, such as severe plastic deformation and advanced thermomechanical processing. When considering severe plastic deformation techniques, it produces ultrafine grain size steels through equal-channel angular pressing, accumulative roll bonding and high-pressure torsion [90,92]. However, the advanced thermomechanical methods which are utilized by phase transformation and controlled cooling are much more suitable industrial processes compared to the severe plastic deformation.

In 1980s, Tamura [93] and Priestner [94] found that the transformation temperature of  $\gamma$  to  $\alpha$  could be increased by deformation in low carbon steels. Then, a new advanced thermomechanical produced dynamically transformed ferrite was found to provide grain refined microstructures with the rolled temperatures being above  $A_{r3}$ , but below  $A_{e3}$  in the non-recrystallisation region, shown in Fig. 2.4. This kind of transformation was named as DIFT [92,95–98], which can result in a final grain size of around 1  $\mu\text{m}$ .

There are several factors that can enhance the formation of ultrafine ferrite grains during strain-induced transformation. First of all, there is a critical strain required for DIFT to occur depending on the deformation conditions and chemical compositions. Decreasing the

deformation temperature can decrease the critical strain, because the low temperature rolling can increase the transformation driving force [99]. Moreover, decreasing the deformation temperature can enhance the DIFT and reduce the final grain size of ferrite with the rolling temperature being higher than  $A_{r3}$ . On the other hand, the increase in the amount of carbon or niobium in solution can increase the critical strain and reduce the transformation driving force, which was proved by thermodynamics analysis [100]. Furthermore, with increasing strain, the mechanisms of DIFT nucleation can be changed from intergranular to intragranular nucleation. Eventually with various isothermal holding times after deformation, it is believed that the DIFT fraction increases at the beginning and then decreases with increased holding time, as shown in Fig. 2.5 [101]. This can be explained by the nucleation of precipitation which leads to the decreased amount of niobium in solution at the beginning. Then the stored energy becomes the main factor in influencing the volume fraction of DIFT. With increased holding time, the recrystallisation begins to appear at grain boundaries which releases the stored energy in austenite and decrease the fraction of DIFT [102, 103].

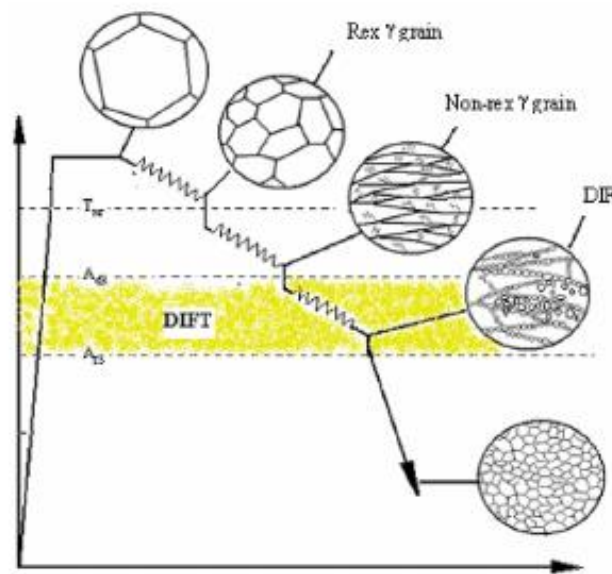


Fig. 2.4 The different microstructures that can be obtained by various TMCP rolling processes [99].

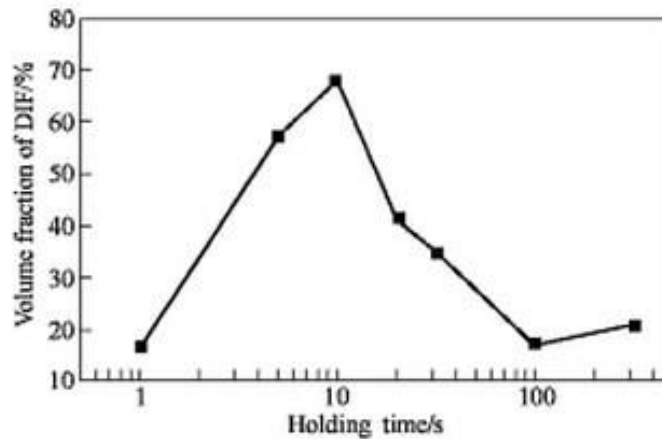


Fig. 2.5 Volume fraction of DIF as a function of the holding time [101].

## 2.4. Microstructural evolution

During deformation, the free energy stored in the structure is derived from point defects and dislocations. However, the deformed energy is thermodynamically unstable. Therefore, the deformed materials reduce the stored energy by two main methods: the first is recovery, in which only partial rearrangement of the dislocations occur and it does not usually affect the boundaries between the deformed grains; another restoration mechanism is called recrystallization, which can form new low dislocation density grains within the deformed or recovered structure. When the temperature is increased or the strain rate is decreased, dynamic recovery and dynamic recrystallisation can occur during deformation. The static recovery and static recrystallisation may occur during annealing after deformation. Furthermore, continual annealing will result in grain growth, which can reduce the energy at the grain boundaries. Grain growth mainly occurs after recrystallization. In certain conditions, uniform grain growth can be replaced by a smaller number of grains growing at a larger rate compared to other grains. This is known as abnormal grain growth or secondary recrystallization.

### 2.4.1. Recovery

Recovery which occurs prior to recrystallization results in changes in the dislocation arrangement, hardness and electrical conductivity [104,105]. There are various factors that can affect the occurrence of recovery, such as strain, deformation temperature and annealing temperature [106–108]. The recovery and the recrystallization processes are both derived from the stored energy of the deformed state. However, when recrystallisation takes place, recovery will no longer occur in the material. Because of the lower driving force needed for

recovery, this process is easier and quicker than recrystallisation [109,110]. Moreover, the prior recovery also influences the kinetics of recrystallisation. Therefore, recovery is very important in nucleating recrystallisation.

The measurement of recovery is difficult, because the microstructures does not show too much change when observed by using OM [111,112]. There are several indirect methods, such as electrical resistivity and mechanical tests that are used instead to detect the change of recovery [113]. Furthermore, there are several factors that can affect the extent of recovery. For example, the prerequisite for recovery in polycrystalline metals is that it is lightly deformed, especially for the highly strained materials [114]. Then, with the higher annealing temperatures, there is a much more complete recovery [115]. Moreover, the stacking fault energy of the material can also influence the recovery process. With low stacking fault energy, it is difficult to achieve glide, climb and cross-slip of dislocations and little recovery of the dislocation structure can occur before recrystallisation [116]. On the other hand, if dislocations with the opposite sign glide on the same slip plane, dynamic recovery can easily occur during deformation [117]. However, if dislocations with the opposite sign are on different glide planes, the glide and climb process can only occur at high homologous temperatures. The gliding and climbing of dislocations can lead to a three dimensional cell structure with complex tangles. As the dislocation density in these walls evolves, well defined sub-grains are formed with the decreasing number density of dislocations in the cell walls [118]. With the changing substructures from recovery, the yield stress is reduced and the work hardening is enhanced. The stored energy can be further lowered by the coarsening of sub-grains. Hu [119] suggested that the sub-grains grow by rotating the diffusion boundaries to similar orientations. In summary, recovery is a homogeneous process that is driven by stored energy and has no clear beginning or end. Fig. 2.6 shows the various stages of recovery in deformed materials

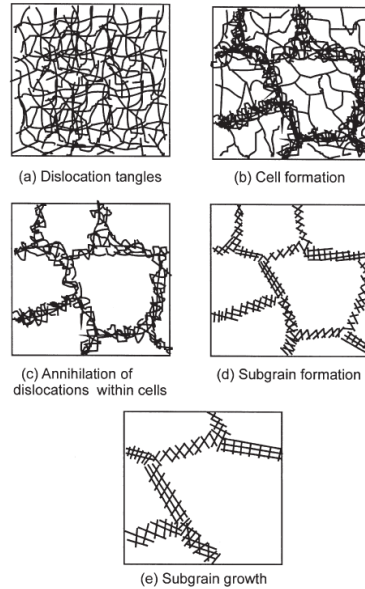


Fig. 2.6 Various stages in the recovery of a plastically deformed material [119].

#### 2.4.2. Recrystallisation

The recrystallisation process involves the formation of new strain-free grains in certain parts of the specimen and the subsequent growth of these grains to consume the deformed or recovered microstructure [120,121]. Depending on the composition of materials, the deformation parameters and the annealing temperature, the recrystallisation process can be divided into two types: one is called primary recrystallisation which occurs during deformation; the other is secondary recrystallization which can occur in fully recrystallized materials [122–124]. There are two stages of primary recrystallisation (Fig. 2.7), nucleation which is the initial formation of new grains in the microstructure and their growth which replaces the previous deformed structures [125,126]. To measure the quantitative recrystallization, the metallography and mechanical properties of the material can be used, because recrystallization will transform the entire microstructure [127]. The volume fraction of recrystallisation is a function of holding time and annealing temperature. The definition of the recrystallisation temperature depends on the stage where 50 % recrystallisation is achieved in the material with the time always being constant [128–130]. However, the fundamental measurements of recrystallisation is defined by nucleation and growth processes [131]. The measurement of nucleation are difficult, because the definition of the nuclei strongly depends on their observation and its variation with time and temperatures. When compared with the growth of recrystallisation, it becomes a more mature technique. The grain growth rate and the driving press for recrystallisation can be provided using various theories.

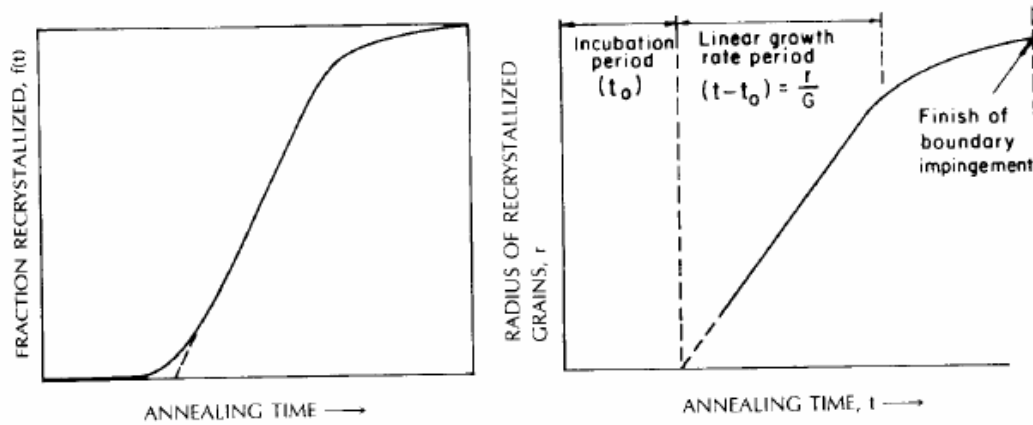


Fig. 2.7 The schematic illustration of recrystallisation kinetics [125].

The principles of recrystallization are found from the microstructure, deformation and annealing parameters along with recrystallisation temperature [132]. First of all, there is a minimum deformation to initiate recrystallisation, because there needs to be a sufficient driving force for the nucleation and growth for recrystallisation. The recrystallisation temperature as defined above decreases with increasing annealing time or deformed strain, as shown by the Arrhenius equation [133]. The recrystallised grain size is refined by increasing deformation strain due to higher nuclei per unit and stored energy. A larger starting grain size and higher deformation temperature leads to a higher recrystallisation temperature.

Recrystallisation influences the final grain size in terms of deformation and annealing parameters. For instance, a small final grain size can be obtained using high strain or a small initial grain size, as it leads to a larger fraction of nuclei or more rapid nucleation rate. However, the grain size is also not constant throughout the specimen, similar to the different texture components with the different recrystallisation rates [134–136].

There are two important modes of recrystallisation: dynamic and static recrystallisation [137]. In this section, the only focus is on static recrystallisation. When the pre-strain is above the critical value of static recrystallisation, but lower than that of dynamic recrystallisation, the classical recrystallisation mechanism occurs after deformation with high temperature annealing. Moreover, the high stacking fault energy in the material is beneficial for static recrystallisation, for the dislocation motion becomes easy for climb or glide to take place. In microalloyed steels, the volume fraction of recrystallisation,  $X_v$ , can be described using a Avrami equation [138]:

$$X_V = 1 - \exp\left[-\ln 2 \left(\frac{t}{t_{0.5}}\right)^n\right] \quad (2.2)$$

where  $t_{0.5}$  is the time when 50% of the volume of the material is recrystallised and  $n$  is the Avrami exponent.

However, the recrystallisation process can be retarded through SIP on the austenite grain boundaries or dislocations. Hansen et al [139] indicated that there are two kinds of driving forces: one is for recrystallisation  $F_R$ ; the other is the pinning force from precipitation,  $F_P$ . If the  $F_P$  is much larger than the  $F_R$ , the recrystallisation was fully retarded by precipitates. However, if the  $F_P$  is much less than the  $F_R$ , recrystallisation could occur and further reduce the dislocation density. Therefore, with a decreasing number of nucleation sites for precipitation, the precipitation process is retarded during recrystallisation. When considering the interaction between recrystallisation kinetics and precipitation kinetics, there is a diagram known as the recrystallisation-precipitation-time-temperature (RPTT) curve as shown in Fig. 2.8. This curve illustrates the relationship between recrystallisation and precipitation and how precipitation can retard recrystallisation.

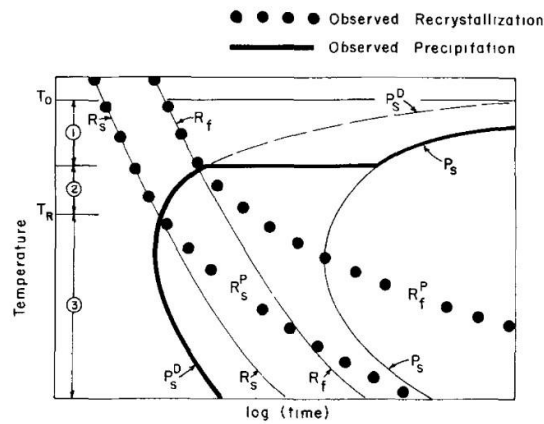


Fig. 2.8 Schematic illustration of recrystallisation-precipitation-time-temperature (RPTT) diagram proposed by [139].

In Fig. 2.8,  $T_0$  is the precipitates dissolution temperature,  $R_s$  and  $R_f$  are the recrystallisation start and finish curves and  $P_s^D$  and  $P_s$  are the precipitation start and stop curves. The recrystallisation stop temperature can be calculated by the intersection of  $P_s^D$  and  $R_s$  curves, regarded as  $T_R$ . The effect of microalloyed elements in solution on the recrystallisation temperature is shown in Fig. 2.9, which shows that  $T_R$  is increased when increasing the content of elements in solution [140].

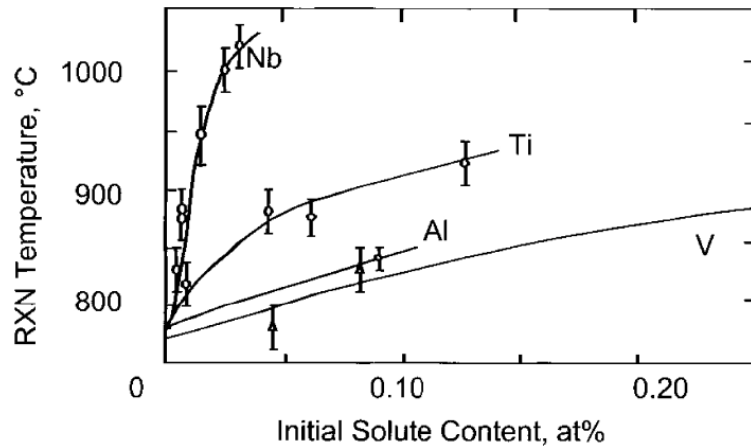


Fig. 2.9 Increase in recrystallisation temperature with the level of microalloy elements in solution [140].

### 2.4.3. Grain Growth

The previous section described how the local recovery processes is at the early stages of annealing and the recrystallization occurs during the later stages. After full recrystallisation, grain growth may occur in the microstructure in two different ways, known as continuous and discontinuous processes. With continuous annealing, the uniform coarsening of high or low angle boundaries may lead to the process of subgrain coarsening and normal grain growth [141–144]. There are several common characteristics of recrystallised grain growth microstructures. The grains are approximately equiaxed and free of dislocations and local misorientation.

Moreover, the inhomogeneous growth results in the discontinuous processes of abnormal grain growth. The microstructures of abnormal grain growth have the following characteristics [144,145]; An amount of abnormal grains is surrounded by normal equiaxed grains. The mechanism of abnormal grain growth is mainly influenced by second phase particles, texture and surface effects that have been investigated by Holm [146] and simulated through Monte Carlo techniques [147]. Boundary mobility was established as the most important effect in the simulation, because it permits a grain to grow at the expense of its neighbours.

## 2.5. Precipitation and dissolution behaviours in microalloyed steels

### 2.5.1. Thermodynamic driving force for precipitation

Generally, microalloy elements are in solution in the matrix at high temperatures and precipitate out at lower temperatures. The microstructure and the final properties of

microalloyed steels have been determined by solid state transformations [148,149]. Therefore, the analysis of the nucleation of a new phase during transformation and its driving force becomes valuable in understanding the mechanism.

The basic theory of phase nucleation indicates that there are two kinds of energy that contribute to the driving force of phase transformation. The first one is the interfacial energy, which comes from the interface between the new phase and parent phase. Here, the strain energy is raised because of the elastic misfit between two phases. The total free energy can be expressed by the Eq. (2.3) [150,151]:

$$\Delta G_{TOT} = A\sigma + V(\Delta G_S + \Delta G_V) \quad (2.3)$$

Where the  $\Delta G_{TOT}$  is the total increase of free energy;  $\Delta G_S$  is the elastic strain energy per unit volume of precipitate;  $\Delta G_V$  is the free energy per unit volume of precipitate;  $\sigma$  is the interfacial energy.

The interfacial energy can be replaced by  $\sum A_i \sigma_i$ , when considering about various interfaces between coherent and incoherent. Nabarro [152] indicated that the elastic strain energy can be expressed as:

$$\Delta G_S = \frac{2}{3}\mu\delta^2V_h f\left(\frac{c}{a}\right) \quad (2.4)$$

Where the  $\delta$  is the square of the volume misfit;  $V_h$  is the volume of the unconstrained hole in the matrix;  $\mu$  is the shear modulus of the matrix;  $f\left(\frac{c}{a}\right)$  is a factor of precipitate's shape.

Moreover, considering Henry's law, the driving force per unit volume of precipitation can be given by:

$$\Delta G_V = \frac{RT}{V} \ln\left(\frac{C_0}{C_e}\right) \quad (2.5)$$

Where  $C_0$  and  $C_e$  are the composition of the alloy in the initial solid and at the treatment temperature of  $T_e$ . Therefore, to obtain the maximum driving force for precipitation, it would seem from Eqs. (2.3)–(2.5) that the answer is to increase the undercooling and supersaturation.

All the equations above were only based on assuming a homogeneous structure. However, in real materials, there will be existing non-equilibrium defects, such as grain boundaries, deformation bands, dislocations and free surfaces. These act as further evidence that the

nucleation system is heterogeneous instead of homogeneous [153,154]. Therefore, the increase in critical free energy for heterogeneous nucleation [155] can be given by:

$$\Delta G_{het} = \Delta G_{hom} S(\theta) \quad (2.6)$$

Where  $S(\theta)$  is an orientation or shape factor given by:

$$S(\theta) = \frac{1}{2} (2 + \cos\theta)(1 - \cos\theta)^2 \quad (2.7)$$

For any given orientation, the free energy for heterogeneous nucleation is lower than homogeneous nucleation, as shown in Fig. 2.10, since the nucleation at grain boundaries is much easier than homogeneous nucleation in the grain interior [156,157]. Moreover, Cahn [158] noticed that nucleation on the grain edge or grain corner is even lower than on the grain boundaries. This discovery was further shown by Aaronson [159] using different modelling.

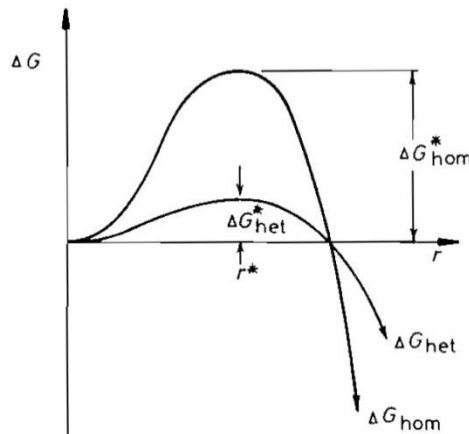


Fig. 2.10 The excess free energy of solid clusters for homogeneous and heterogeneous nucleation [157].

### 2.5.2. Kinetics of SIP

SIP is nucleated on the dislocations in austenite by diffusion controlled mechanisms [160]. Dutta et al. [11,161] first showed the concept of the kinetics of SIP and provide an equation to calculate the SIP start time (5% precipitation) shown by:

$$t_{0.05} = A[Nb]^{-1} \varepsilon^{-1} Z^{-0.5} \exp\left(\frac{Q_{ppt}}{R_g T}\right) \exp\left(\frac{B}{T^3 (\ln k_s)^2}\right) \quad (2.8)$$

where,  $t_{0.05}$  is the precipitation start time which defined at 5% of SIP; [Nb] is the weight percent of niobium in solution during reheating;  $\varepsilon$  is the true strain;  $Z$  is the Zener-Hollomon parameter;  $k_s$  is the solute supersaturation ratio expressed by:

$$k_s = \frac{\log[Nb][C + \frac{12}{14}N]}{2.26 - \frac{6770}{T}} \quad (2.9)$$

There are also some experimental methods that can measure the precipitation start and finish behaviours, such as electron microscopy using thin foils or extraction replicas, decreases in secondary hardening and electrical resistivity. However, those methods have weaknesses in detecting the very small precipitates at the early stage. Jonas et al. [162] developed a new method to detect the SIP using a stress relaxation test. When the SIP occurred during the relaxation test, the curve became flat, as shown in Fig. 2.11. Then, after precipitation is finished, the curve starts to decrease again. Therefore, the precipitation start and end time can be identified through the change in slope on the relaxation curve as shown in Fig. 2.11. This method has been further used in the niobium microalloyed steels by Sellars et al. [163].

However, Jonas' method is not direct measurement to calculate the start and end precipitation times, because the stress relaxation can be detected only after a certain amount of precipitates are present. Therefore, as with the other methods such as thin foil or electrical resistivity, the Jonas's method has a problem in giving the exact start and end time of precipitation.

Mathematical models have been developed to simulate the SIP behaviour during the deformation and ageing process. Dutta et al. [164] developed their own model to describe the precipitation kinetics. Initially some researchers believed that precipitates growth occurs prior to precipitate coarsening. However, depending on the solute depleted zones around the precipitates, the growth and coarsening can occur at the same time [161]. This theory explained that the nucleation and growth of precipitates can occur from the bulk diffusion of solute atoms in the matrix, and the coarsening behaviour of precipitates is caused by the diffusion of solute atoms from the dislocation cores. In the new model, the precipitation process was divided into two stages. Initially the nucleation and growth of precipitates occur and then, in the second stage, the precipitates grow and coarsen at the same time. The new model has also been used in HSLA steels [165] and a model of a microalloyed steel [166], which indicated that the precipitates were all sited on the dislocation network. This model also widely extends into other types of precipitates, such as aluminium or vanadium carbonitrides.

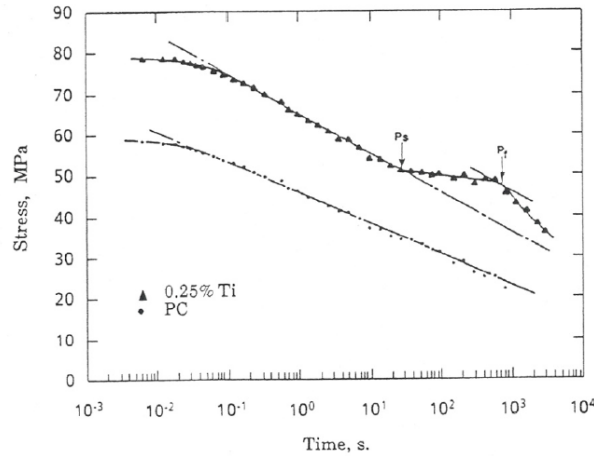
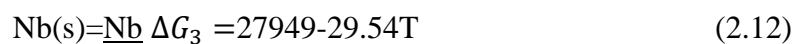
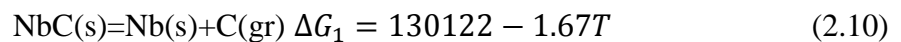


Fig. 2.11 Stress relaxation curve for SIP in a 0.25% Ti HSLA steel showing the precipitation start and finish times [162].

### 2.5.3. Solubility of microalloyed elements in austenite and its effect on the austenite grain size during heat treatment

#### 2.5.3.1. Thermodynamic solution behaviour of microalloyed elements and its solubility product

Generally, the solubility of microalloy elements in the solid metal increases with the temperature. There is a solubility limit for different elements at a given temperature. When the given temperature is reached, the solution is said to be saturated. Therefore the solubility equilibrium and equilibrium constant of microalloy elements in precipitates and the matrix during reheating is given by [167,168]:



Where  $\Delta G_1$ ,  $\Delta G_2$  and  $\Delta G_3$  are the positive change in free energy for the reaction. NbC (s), Nb (s) and C (gr) are the pure components at a given temperature. Therefore, when considering equations from (2.10) to (2.12), the corresponding change in free energy can be expressed by:

$$\Delta G = 137235 - 64.43T \quad (2.13)$$

Returning to the thermodynamic solubility of microalloy elements in precipitates, the relative amounts of products and reactants at a given temperature are determined by the tension between the tendency toward maximum entropy and the tendency toward minimum energy.

The free energy change,  $\Delta G$ , has a relationship with the equilibrium constant and is represented as:

$$\Delta G = -RT \ln K \quad (2.14)$$

Where the equilibrium constant is expressed as the solubility product constant and given the symbol of K;  $R=8.31\text{J/molK}$  and  $T$  is the temperature in Kelvin. Therefore, the free energy change at a certain temperature can also be determined from the value of K. The amount of NbC that dissolves is the same as the amount of Nb and C that enters the solid solution. Thus, the solubility of NbC can be rewritten to be in equilibrium as:

$$K=[\text{Nb}][\text{C}] \quad (2.15)$$

The content of Nb and C in solution has the stoichiometric relationship, which means that there is a single variable between  $[\text{Nb}]$  and  $[\text{C}]$ . However, it is difficult to measure the accurate values of K, because of the interaction occurring between elements in solution. Therefore, in Eq. (2.15), it is assumed that Nb and C are dilute in austenite and the effects of solute interaction in the equilibrium system are ignored. Hence, combining the equations of (2.13), (2.14) and (2.15), the solubility product under the theoretical treatment is found to be:

$$\log [\text{Nb}][\text{C}] = 3.36 - \frac{7167}{T} \quad (2.16)$$

When considering about the solution of nitrogen in niobium precipitates, the solubility product equation was modified by Irvine et al [45]:

$$\log [\text{Nb}][\text{C} + \frac{12}{14}\text{N}] = 2.26 - \frac{6770}{T} \quad (2.17)$$

Therefore, with this solubility equation, the equilibrium of those elements, such as Nb in solution can also be calculated at any given temperature. Using Eq. (2.17), the equilibrium of niobium in solution at a certain temperature can be rewritten as:

$$[\text{Nb}]^{\text{equilibrium}} = \frac{10^{(2.26 - \frac{6770}{T})}}{[\text{C} + \frac{12}{14}\text{N}]} \quad (2.18)$$

Fig. 2.12 shows solubility lines of different precipitation systems in steels [169]. It is clear to note from this image that Ti nitride has the highest equilibrium solution temperature, which is regarded as the highest temperature stable precipitate [170]. V carbide has the lowest equilibrium solution temperature when compared with other elements in Fig. 2.12.

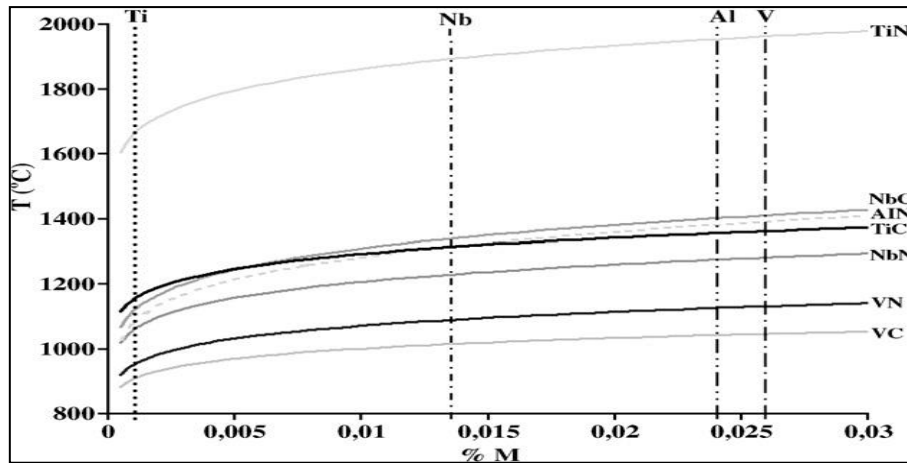


Fig. 2.12 Correlation between the micro-alloying content (M%) and the solubility temperatures for the precipitates present in the HSLA steel [169].

Furthermore, the increase in solid solution of microalloy elements increases the frictional stress, which means the driving force to move the boundaries has been increased by the solute atoms near the boundaries. In other words, there is a drag force that comes from the solute atoms with regards to the moving boundary, known as the solute drag effect [171,172]. Finally, increasing the content of microalloy elements in solution in austenite increases the hardness due to the solid solution strengthening [173].

#### 2.5.3.2. The prior austenite grain coarsening during heat treatment

Grain growth is driven by the stored energy of deformation. The driving force energy of grain growth is less than the primary recrystallisation [123]. However, the boundary movement velocities of grain growth is slower than that of primary recrystallisation, because of the effect of pinning force and the solute drag on grain migration is much higher compared to primary recrystallisation [173,174]. The understanding of the grain growth behaviour during reheating or ageing has become extremely important, because it further influence the final grain size after cold working. The grain size is important to determine the mechanical behaviour [175,176]. For example, a large grain size is beneficial for high temperature creep. Therefore, a good understanding of grain growth is required for control of the microstructure and properties of the metal. As discussed before, there are two types of grain growth; one is normal grain growth regarded as the continuous process, and the other is abnormal grain growth which is a discontinuous process. When abnormal grain growth occurs initially a few grains grow and a bimodal grain size distribution appears. Then with the continually

consumed smaller grains, the microstructure changes to having only large grains and normal grain growth begins to happen again (shown in Fig. 2.13) [177].

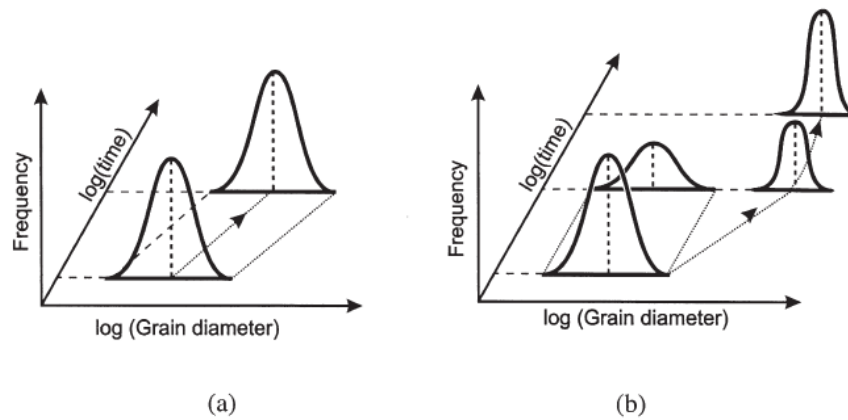


Fig. 2.13 Schematic representation of the change in grain size distribution during (a) normal grain growth and (b) abnormal grain growth [177].

There are several factors that can influence the grain growth, such as the heat treatment temperature, the solute drag effect and the pinning of the second phase particles. Moreover, the grain growth rate decreases with higher initial grain size. In the following section, the mechanism and kinetics of grain growth at high temperatures are discussed.

The higher the reheat temperature, the faster the boundary mobility and reduced energy requirement. Gleiter [178] also found that the high temperature regime needs a low activation energy for migration, whereas at lower temperatures the activation energy is closer to that for boundary diffusion.

The grain growth kinetics were analysed by Burke and Turnbull [143]. In their theory, it assumes that the driving pressure ( $P$ ) on a boundary only relates to the curvature of the boundary. The driving pressure can then be expressed by:

$$P = \gamma_b \left( \frac{1}{R_1 + R_2} \right) \quad (2.19)$$

Where  $\gamma_b$  is the energy;  $R_1$  and  $R_2$  are the radii of curvature of a boundary in different direction. If the boundary is a sphere with radius  $R$ , then  $R=R_1=R_2$ . The Eq. (2.19) can then be rewritten as:

$$P = \frac{2\gamma_b}{R} \quad (2.20)$$

Burke et al further assumed that  $\gamma_b$  is the same for all boundaries and the radius of curvature is proportional to the mean radius of an individual grain. Therefore the Eq. (2.20) is changed to:

$$P = \frac{\alpha\gamma_b}{R} \quad (2.21)$$

where  $\alpha$  is a small geometric constant. Meanwhile, the grain boundary moves with a velocity ( $v$ ) in response to the net pressure on the boundary and is expressed as:

$$v = \frac{d\bar{R}}{dt} = \frac{\alpha c_1 \gamma_b}{\bar{R}} \quad (2.22)$$

And then integrating the functions of Eq. (2.22) give the equation as:

$$\bar{R}^2 - \bar{R}_0^2 = 2\alpha c_1 \gamma_b t = c_2 t \quad (2.23)$$

where  $\bar{R}$  is the mean grain size at time  $t$ ,  $\bar{R}_0$  is the initial mean grain size and  $c_2$  is a constant.

This grain growth law can be written in a more general form:

$$\bar{R}^n - \bar{R}_0^n = c_2 t \quad (2.24)$$

$$\bar{R} = c_2 t^{1/n} \quad (2.25)$$

where  $n$  is the grain growth exponent and in this study is equal to 2. The exponent values of  $n$  is defined between 2 and 4, with an average of  $2.4 \pm 0.4$   $\mu\text{m}$ . Depending on multiple experimental tests, the values of  $n$  become lower with increasing reheating temperatures. The values of the exponent are determined by the boundary mobility variety and the limiting grain size.

Burke et al. only considered that the grains can influence the migration rate of one boundary and did not consider the interaction between grains. Smith et al. [179] initially indicated the interaction between the topological aspects of space-filling and surface tension equilibrium on grain growth. Fig. 2.14 shows the gradual shrinkage of the 5-sided grain, because the 7-sided one is the maintained structure. Then, with the grains becoming curved by maintaining the  $120^\circ$  angles at the vertices, the migration of the grain boundary has been activated.

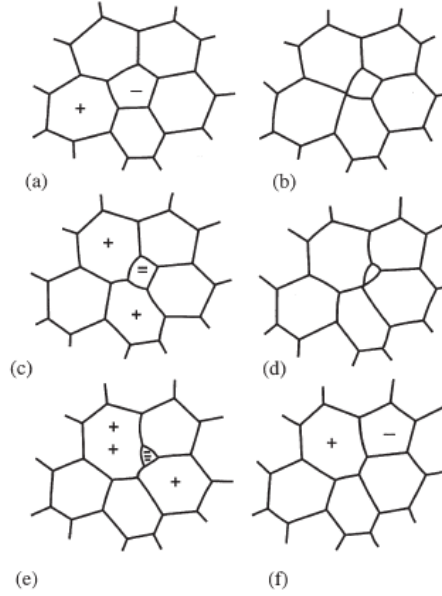


Fig. 2.14 Schematic diagram of growth of a 2-dimensional grain structure (a) a grain of less than or more than 6 sides introduces instability into the structure, (b)-(f) shrinking and disappearance of the 5-sided grain [180].

A complete grain growth theory should consider both the topological space-filling requirements and the boundary migration kinetics. Therefore, many researchers have attempted to improve the grain growth theory and one of the most famous theories are by Feltham [181] and Hillert [180]. Hillert's theory takes into account the Ostwald ripening of the second-phase particles and the relationship between the velocity of grain boundaries and the radius of curvature. The new grain growth model can be rewritten as:

$$\frac{dR}{dt} = cM\gamma_b \left( \frac{1}{R_{crit}} - \frac{1}{R} \right) \quad (2.26)$$

where  $c=0.5$  is for a 2-D dimensional grain and 1 for a 3-D dimensional.  $R_{crit}$  is the critical grain size that is expressed as:

$$\frac{dR_{crit}}{dt} = \frac{cM\gamma_b}{4R_{crit}} \quad (2.27)$$

When the  $R_{crit}$  is less than  $R$ , the grain will shrink and on the opposite side the grain will grow. Hillert indicated that the mean grain radius,  $\bar{R}$ , will be equal to  $R_{crit}$ , when considering the topographic aspects. Then, with equation (2.26) and (2.27), the model of grain growth equation can be further rewritten as:

$$\frac{dR^2}{dt} = c \ln \left( \frac{R}{\bar{R}} \right) \quad (2.28)$$

where  $c$  is constant. Hillert also provided a direct method to separate the normal and abnormal grain growth. He deduced that when the initial grain size distribution contained no

grains larger than  $1.8\bar{R}$ , normal grain growth would occur. On the other hand, if there are grains larger than  $1.8\bar{R}$ , then abnormal grain growth would be occurring in the system.

## CHAPTER 3: EXPERIMENTAL PROCEDURE AND TECHNIQUES

### 3.1 Materials

The materials used in this research are two microalloyed steels for comparative purposes of the different effect of microalloyed elements: one with 0.03%Nb (Nb steel) and another one with both 0.03% Nb and 0.01% Ti (Nb-Ti steel). The steels were made by vacuum induction melting and casting into to 220mm×65mm×28mm square ingots, at ArcelorMittal. The chemical composition of those steels analysed by Sheffield Testing Laboratories, are listed in Table 3.1.

Table 3.1  
Chemical composition of the experimental steels (wt%)

	C	Si	Mn	Cr	Ni	Nb	Ti	N	P
Nb Steel	0.067	0.11	0.77	0.01	0.02	0.03	<0.01	0.0058	0.016
Nb-Ti Steel	0.065	0.11	0.77	0.01	0.02	0.03	0.02	0.0062	0.016

The ingots were soaked at 1300°C for 2 h and hot-rolled into 12 mm thick plates in a 2-high experimental rolling mill. After hot-rolling, the plates were quenched in ice water, and then machined into thermomechanical compression (TMC) specimens with the dimensions of 60 mm×30 mm×10 mm shown in Fig. 3.1. The thermocouple hold was drilled into the centre of 60 mm×10 mm face, with 0.5mm in diameter and 15mm deep.

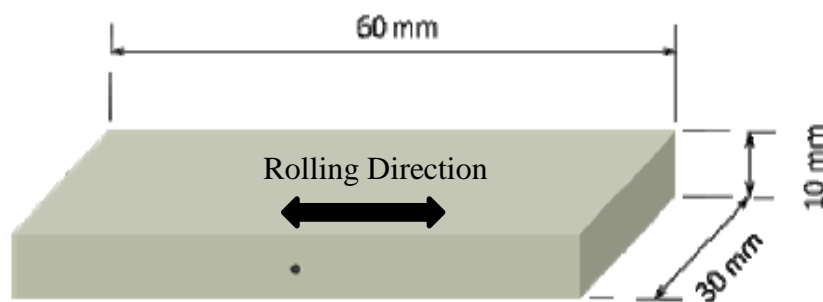


Fig. 3.1 Schematic diagram of the specimen geometry for plane strain compression testing.

## 3.2 Thermomechanical processes

The thermomechanical strain compression tests were processed by the thermomechanical compression simulator in the University of Sheffield [182]. It can simulate the hot rolling and monitor the temperatures which are controlled by computer, as shown in Fig.3.2. To understand the effect of each process on the microstructures and properties, in this project, the processing was separated into three major parts: 1) rough rolling; 2) a reheat treatment process; 3) finish rolling. In the following sections, the details of each rolling and heating parameters and schedules are presented.



Fig. 3.2 The photo of servotest thermomechanical compression simulator.

### 3.2.1. Rough rolling

In the first part of rough rolling process, prior to the deformation using a computer controlled the TMC, the samples were preheated to 1100 °C for 30 s, and then air cooled to deformation temperatures ranging from 850 °C to 1100 °C. Deformation tests were conducted at 850 °C, 900 °C, 950 °C, 1000 °C, and 1050 °C as well as 1100 °C with a strain of 0.3 and strain rate of 10 s<sup>-1</sup> followed by water quenching to room temperature. The thermal schedule for each experiment is shown schematically in Fig. 3.3.

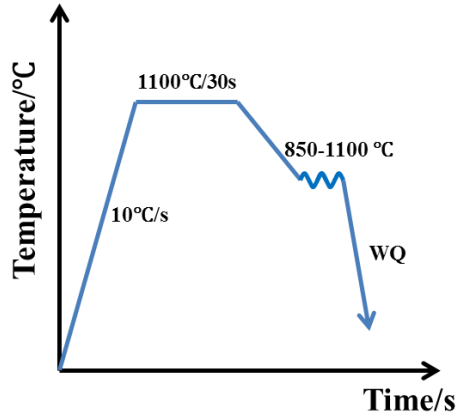


Fig. 3.3 Schematic illustration of the thermomechanical test schedule for plane strain compression test in the TMC machine.

### 3.2.2. Reheat treatment

In this section, the reheating process is described after rough rolling at 850 °C. The samples were preheated at 1100 °C for 30 s prior to deformation in the TMC and then air cooled to the deformation temperature at 850 °C. Deformation was undertaken to a strain of 0.3 with a true strain rate of 10 s<sup>-1</sup>. Then, the steels were rapidly reheated at a rate of 10 °C/s to a temperature of 1200 °C after deformation, and held for different times followed by water quenching to room temperature. The rolling and heat treatment schedule is shown in Fig. 3.4. The details of the reheating tests on these two Nb and Nb-Ti steels are listed in Table 3.2.

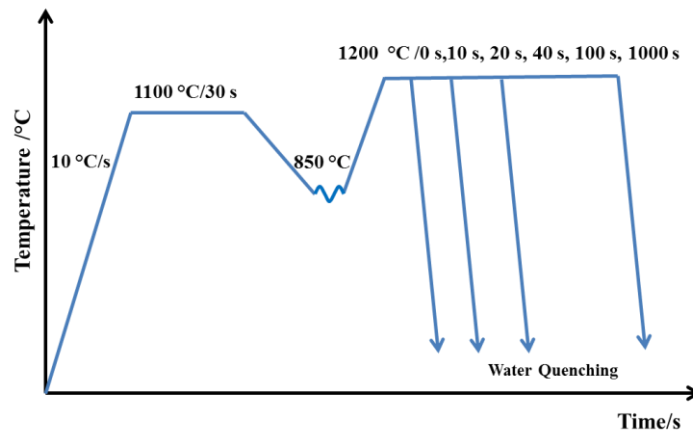


Fig. 3.4 Schematic illustration of the thermomechanical test and heat treatment schedule in the TMC machine.

Table 3.2

The series of plane strain compression and reheat treatment experimental tests conducted on Nb and Nb-Ti steels.

Materials	Deformation	Heat treatment	
		Temperature (°C)	Holding Time (s)
Nb Steel	850 °C with a strain of 0.3 and strain rate of 10 s <sup>-1</sup>	1200	0, 10, 20, 40, 100, 1000
Nb-Ti Steel	850 °C with a strain of 0.3 and strain rate of 10 s <sup>-1</sup>	1200	0, 10, 40, 100, 1000

### 3.2.3. Finish rolling

After the rough rolling and reheat treatment investigation, the experimental parameters had been decided. The steels were first deformed at 850 °C and rapidly reheated at a rate of 10 °C/s to a temperature of 1200 °C, and held for 10 s and 100 s respectively. Then, in the finish rolling, with air cooling to 850 °C at a rate of 10 °C/s, the deformation was done to a strain of 0.3 with a true strain rate of 10 s<sup>-1</sup> on the first pass, followed by water quenching immediately, regarded as A-10 and A-100. Then, by adding a holding time of 10 s after the first pass, the schedule was decided as B-10 and B-100. After the 10 s holding, the steels were then deformed by the second pass with the same rolling parameter as the first pass (C-10 and C-100). The final schedule was holding for 10 s after the second pass and then water quenching to room temperature (D-10 and D-100). The rolling and heat treatment schedule is shown in Table 3.3 and Fig. 3.5.

Table 3.3

The series of rolling schedules with respect to the reheat treatment condition.

Schedule	Reheated Process
A-10	1200 °C for 10 s
B-10	
C-10	
D-10	
A-100	1200 °C for 100 s
B-100	
C-100	
D-100	

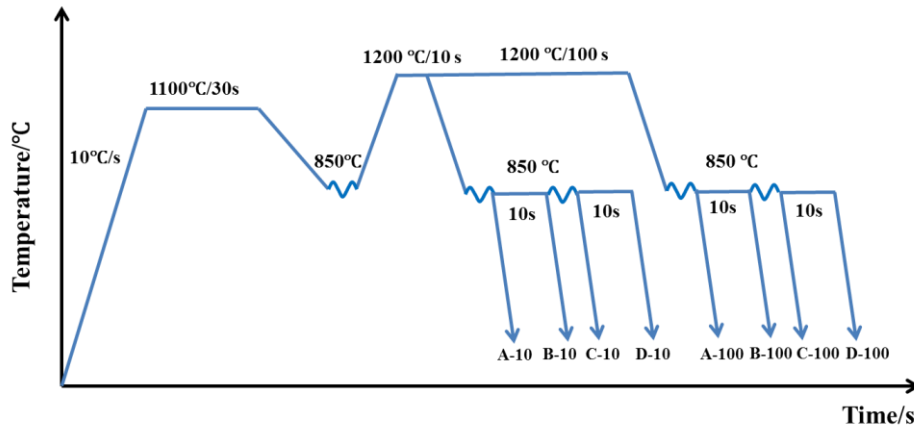


Fig. 3.5 Schematic illustration of the thermomechanical tests finish rolling in the TMC machine.

A typical specimen after the rolling or reheating process is shown in Fig. 3.6, with the orientations defined corresponding rolling direction.

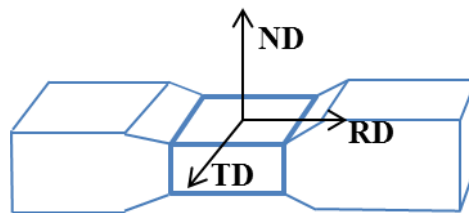


Fig. 3.6 Schematic illustration of a specimen after plane strain compression and the corresponding orientations with respect to industrial rolling practice.

### 3.3 Microscopy techniques

Optical microscopy (OM), scanning electron microscopy and transmission electron microscopy (TEM) as well as electron backscattered diffraction (EBSD) were used to investigate the microstructures, the morphology and composition of precipitates on the central areas of plane strain compression (PSC) specimens. The specimens were cut along the rolling direction and perpendicular to transverse direction as shown in Fig. 3.7.

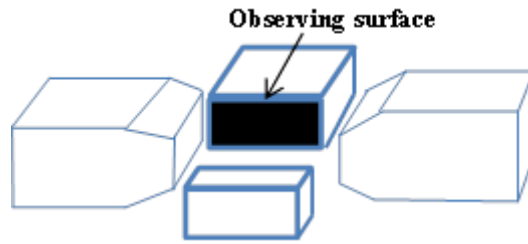


Fig. 3.7 Schematic illustration of a deformed specimen showing cut cross sectional area and the area of interest to observe which denoted by an arrow.

### 3.3.1. OM and scanning electron microscopy (SEM)

#### 3.3.1.1 Metallographic specimen preparation

After cutting samples from the PSC specimens, they were mounted in Bakelite for automatic grinding and polishing, with the sample surface exposed on one side of the disc. Therefore, the grinding and polishing was used to remove the deformed layer left from the coarsening to the fine stage.

At first, the samples after mounting were ground from 240 to 1200 grade silicon carbide papers with water to flush away the particles. One of the important cautions of grinding is to move the scratches that are left from the previous paper. So, in proceeding from one coarser paper to the next fine paper, the specimen was rotated by an angle of  $90^\circ$ . After grinding, the specimens were moved to the polishing stage from 6 microns to 1 micron on diamond cloths under diamond suspension lubricants. Finally, the specimens were polished using colloidal silica and then cleaned using water. After carefully grinding and polishing, a final scratch free surface was obtained, but without etching, it is impossible to observe the microstructures from microscopy. In the traditional method, 2 % nitric acid is useful to etch microstructures, like martensite, bainite or ferrite. However, to reveal the prior austenite grain boundaries, picric acid was the best suitable etching solution. After heating the picric acid to  $60^\circ\text{C}$ , the specimens were boiled in this solution for 30 to 60 seconds, and then cleaned using the distilled water. The etching time varied from specimen to specimen, because of the different microstructures after deformation and heat treatment.

#### 3.3.1.2 Grain size measurements

The linear intercept method (ASTM E-112) was used to measure the average prior austenite grain size. Depending on the linear intercept theory, the distance between each drawn line is larger than the largest grain size to avoid the double calculation of the same grain. The Nikon

ECLIPSE LV150 OM was used to observe the microstructures and take the standard images. Buehler Omnimet 9.5 software was used to measure the grain size from the OM images with 95% confidence limit.

### 3.3.1.3 Volume fraction of ferrite

The specimens which were etched by 2 % nitric acid have been used to separate the ferrite structures from the martensite matrix by SEM, and then the volume fraction of ferrite has been measured from the SEM images by a point counting method. The SEM images were used in this study which was performed on the JEOL JSM 6400 and FEI Inspect F with the voltage of 20 kV and at a magnification of 1500 x and 3000 x. The distance between two grids is larger than the largest grain of ferrite, which make sure that each grain is counted once.

### 3.3.2. Transmission electron microscopy (TEM)

TEM is one of the most useful techniques to observe and analyse the nanometer-sized precipitates and their composition by bright and dark-field images, Energy Dispersive X-ray Spectroscopy (EDX) and high resolution TEM (HRTEM), as well as energy loss spectroscopy (EELS). Because of the nature of the diffraction contrast between precipitates and the matrix and the dislocations, it is difficult to calculate the nanometer-sized precipitation using thin foil specimens. Therefore, to avoid the interference of contrast from the matrix, the carbon extraction replica specimens were used to calculate the volume fraction, composition and structures of precipitates as well as the size distribution. However, the carbon extraction replica specimen also has its limitation. For instance, the location and the orientation relationship of precipitates corresponding to the matrix can only be analysed by the thin foil samples. Therefore, both the carbon replica and thin foil specimens were used in this project. The negative film was used in this study to take image from carbon replica and thin foil specimens.

#### 3.3.2.1 TEM carbon extraction replicas

The composition and the volume fraction of precipitates in these two steels was analysed by the carbon extraction replicas specimens and there were roughly 200-400 particles examined depending on the rolling or heat treatment parameters. The specimens were mounted in Bakelite and ground and polished using the same procedure as used for OM or SEM sample preparation. Then, the specimens were slightly etched using 2 % nital solution followed by

isopropanol cleaning in an ultrasonic bath to remove the etchant from the surface. Then an evaporator operated in a high vacuum carbon coating device was used to deposit a carbon layer onto the surface. The carbon coated surfaces were then scratched to produce squares of around 2 mm × 2 mm in size. The replicas were placed in a 10 % nital solution until the surface colour of the specimens changed to dark grey. Then the samples were immersed in a methanol solution to let the carbon replicas lift off from the surface. The replicas were floated onto 400 mesh copper grids in the final step. The illustration of the carbon extraction replica process is shown in Fig. 3.8.

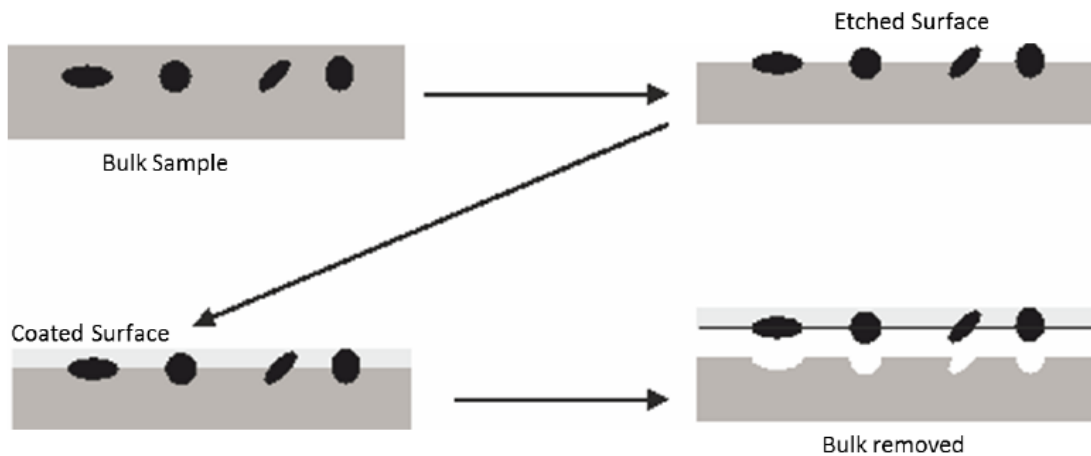


Fig. 3.8 Schematic diagram of the carbon extraction replica process [183].

### 3.3.2.2 TEM thin foils

The TEM thin foil specimens were cut off from longitudinal sections of the PSC specimens with a thickness about 300 to 500  $\mu\text{m}$ , using the Isomet 5000 cutting machine. Then this specimen was stuck on a flat metal by beeswax and ground from 240 to 1200 grade silicon carbide paper down to a thickness of 90-150  $\mu\text{m}$ . Slices were then punched to the 3 mm diameter disks and further ground to a thickness of 60 to 90  $\mu\text{m}$ . Finally, the discs were electropolished using the Metalthin twin jet electropolisher. The electrolyte solution contained 5 % perchloric acid, 35 % butoxyethanol and 60 % methanol for thinning the thin foil specimens by the electropolisher. The electropolishing conditions have been controlled at 30 to 50 mA with a jet sensitivity of 8 at a temperature of -40  $^{\circ}\text{C}$ .

FEI Tecnai T20 and JEOL 2010 TEMs, both operating at 200 kV, were used in this study to analyse the morphology and composition of nanometer sized precipitates. The chemical analysis for the precipitates was conducted using an Oxford instruments energy dispersive X-

ray spectroscopy (EDX) detector (Oxford Instruments, Oxford, UK) and electron energy loss spectroscopy (EELS) analysis. The structures of precipitates have been observed by HRTEM with a CCD camera integrated into a Gatan image filter.

### 3.3.2.3 Microscopy data analysis

To calculate the size distribution and volume fraction of precipitates, TEM bright-field images were used which were taken from carbon extraction replicas specimens on random areas. The Image J software was used to identify the diameter of precipitates, depending on their shape. Additionally, the measurement of the sample thickness was carried out using EELS in Gatan GIF. This was estimated from the low energy region of the spectrum, given by Equation (3.1) [184,185]:

$$t = \lambda \ln(I_t/I_0) \quad (3.1)$$

where  $t$  represents the thickness of material;  $\lambda$  is the mean free path of specimen;  $I_t$  is the total number of electrons in the EEL spectrum and  $I_0$  is the number of electrons having lost no energy.

The volume fraction of particles was calculated in this study as well with the expression by [186]:

$$f_v = \frac{\pi}{6} N_s (\bar{x}^2 + \sigma^2) \quad (3.2)$$

where  $\bar{x}$  and  $\sigma$  are the respective mean and standard deviation of particles.  $N_s$  is the number density of precipitates per unit area from replica specimens.

### 3.3.3. Micro-hardness testing

To further investigate the elements in solution, micro-hardness testing was conducted using a Durascan 70 micro-hardness tester on both Nb and Nb-Ti steels. A Vickers diamond indenter tip was used in this study with load of 1 N and a hold time of 15 s in the micro-hardness tests. The indentation size was automatically adjusted according to the material surface condition being tested. The micro-hardness tests were performed 0.5 mm apart with about forty test measurements on each sample. The sample preparation for micro-hardness is similar to the microstructure specimens with grinding and polishing until 1  $\mu\text{m}$  without etching

## CHAPTER 4: THE EFFECT OF HOT ROLLING TEMPERATURES ON THE MICROSTRUCTURES AND PRECIPITATION BEHAVIOURS IN THE Nb AND Nb-Ti STEELS

### 4.1. Introduction

In recent years, microalloyed steels have widely been used in various fields, e.g. construction of hulls for naval warships, submarines and other large engineering machines [5,7,187]. To produce a desired microstructure combined with excellent strength and impact toughness properties in microalloyed steels, the thermo-mechanical process has been investigated [17], [18]. The final deformation step of TMCP is chosen to be below the recrystallisation stop temperature to obtain a higher volume fraction of SIP. For this reason, in this chapter, the effect of the rough rolling temperatures on the recrystallisation and precipitation have been analysed using OM, TEM and micro-hardness, as well as thermo-mechanical modelling. The full recrystallisation temperature, recrystallisation stop temperature and the precipitation start time from the precipitation-time-temperature (PTT) curve have been calculated using different models and found to fit well with the experimental data. Moreover, the nanoscale precipitates in the Nb and Nb-Ti steels have been determined as SIP depending on the orientation relationship between these nanoscale sized particles and austenite transformed to ferrite.

### 4.2. Modelling the 5% recrystallization and PTT curves

In this study, the recrystallization behaviour for both Nb and Nb-Ti steels are important, because the extent of recrystallization determines the volume fraction of SIP and the final grain size, which are the main factors to be controlled to obtain good mechanical properties. It is well known that the recrystallization behaviour for Nb and Nb-Ti steels can be influenced by the microalloy elements, because the recrystallisation is inhibited when the precipitates pinning force ( $F_{pin}$ ) exceed the driving force ( $F_R$ ) for recrystallisation [166,188].

Therefore, the Dutta and Sellars's precipitation model [11] was used to predict the precipitation behaviour by calculating the precipitation start temperature-time diagrams (Eq. (4.1)).

$$t_{0.05} = 3 \times 10^{-6} [Nb]^{-1} \varepsilon^{-1} Z^{-0.5} \times \exp \frac{270000}{RT} \exp \frac{2.5 \times 10^{10}}{T^3 (\ln K_s)^2} \quad (4.1)$$

where  $t_{0.05}$  is time for 5% precipitation; [Nb] is the niobium in solution; Z is the Zener-Hollomon parameter; Ks is the supersaturation ratio which determines the driving force (see equation (2.9)). The [Nb] was calculated using carbon replica specimens after reheating to 1100 °C for 30 s followed by water quenching. With experimental data from Nb and Nb-Ti steels, the typical “C” shaped curves were obtained and shown in Fig. 4.1. The nose of the precipitation start temperature diagram for the SIP is located at 0.3 s and 840 °C in the Nb steel, and at 0.36 s and 840 °C in the Nb-Ti steel.

There are various definitions of the recrystallization start and complete temperatures. In this study, the recrystallization start temperature is defined as 5 % recrystallization, and the recrystallization complete temperature is at 95 % recrystallization [189]. Then, considering the effect of niobium in solid solution on the recrystallisation kinetics of austenite, Dutta and Sellars [11] provided another model to calculate the 5 % recrystallization curves for Nb and Nb-Ti steels using Eq. (4.2).

$$t_{0.05x} = 6.75 \times 10^{-20} d_0^2 \varepsilon^{-4} \times \exp \frac{300000}{RT} \exp \left\{ \left( \frac{2.75 \times 10^5}{T} - 185 \right) [Nb] \right\} \quad (4.2)$$

where  $t_{0.05x}$  is time for 5% recrystallization,  $d_0$  is original grain size in  $\mu\text{m}$ , and  $\varepsilon$  is strain. Finally, the full recrystallization time expressed as a function of the recrystallized volume fraction (X) has been calculated by Johnson et al. model [190,191] and is given by Eq. (4.3).

$$X = 1 - \exp \left( -\ln(0.95) \left( \frac{t}{t_{0.05x}} \right)^2 \right) \quad (4.3)$$

Full recrystallization is defined as the volume fraction of recrystallization at 95%. Then, with 95% substituted into Eq. (4.3), the recrystallization finish time ( $t_f$ ) can be estimated as:

$$t_f = 7.66 \times t_{0.05x} \quad (4.4)$$

Using Equations (4.1), (4.2) and (4.4), the interaction of precipitation and recrystallization with different rough rolling temperatures were carried out and shown in Fig. 4.1. Then, the full recrystallization ( $T_1$ ) and the recrystallization stop ( $T_s$ ) temperatures were calculated using the time for 5% and 95% recrystallisation equalling to the time for 5% SIP. For the Nb steel, the  $T_s$  is at 917°C and  $T_1$  is at 957°C. The  $T_s$  is at 907°C and  $T_1$  is at 951 °C for Nb-Ti steel.

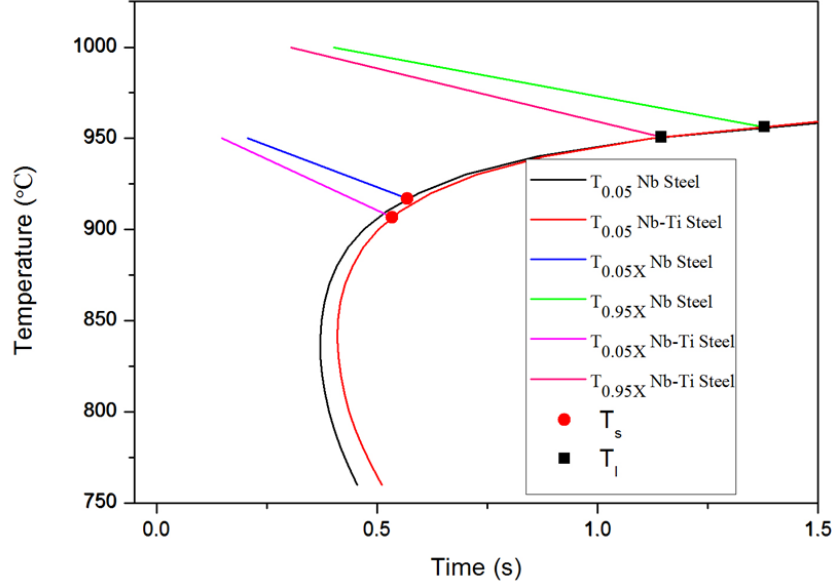


Fig. 4.1 Interaction of recrystallisation and start of SIP as function of niobium content in the Nb and Nb-Ti steels rolled by 30% reduction;  $T_l$  shows the lower temperature limit for ‘full’ (95%) recrystallisation and  $T_s$  shows upper temperature limit for complete stoppage of recrystallisation. A and B [11] are constant, and for micro-alloyed low carbon steels, they are  $1.6 \times 10^{-6}$  and  $1 \times 10^{-10}$ , respectively.

Furthermore, the non-recrystallization temperature can also be predicted for the Nb steel by Fletcher’s equation [19,192]:

$$T_s = 849 - 349C + 676\sqrt{Nb} \quad (4.5)$$

where C, Nb are the elements in wt pct. The predicted  $T_s$  value is 941°C. The value is slightly higher than the predicted value using the Dutta and Sellars' model. When considering the utilizing strain, Fletcher modified the Eq. (4.5) as given by:

$$T_s = 203 - 310C + 657\sqrt{Nb} + 683e^{-0.36\varepsilon} \quad (4.6)$$

where  $\varepsilon$  is the pass strain. The predicted  $T_s$  value in this study is 909°C, which is as close as the calculated data of 917°C by Dutta’s equation for Nb steel.

To summarise, the recrystallization stop temperature is approximately 900°C, and the full recrystallization temperature is above 950°C, for both Nb and Nb-Ti steels. A rolling temperature between 950°C and 900°C should therefore give mixed structures.

### 4.3. Characteristic of the microstructure by OM

#### 4.3.1. Morphology of prior austenite grains

Fig. 4.2 and 4.3 show representative optical images of prior austenite grains at six deformation temperatures viz. (a) 850 °C, (b) 900 °C, (c) 950 °C, (d) 1000 °C, (e) 1050 °C and (f) 1100 °C for Nb steel (Fig. 4.2) and Nb-Ti steel (Fig. 4.3). The equiaxed prior-austenite grain size was stable with the hot rolling temperatures in the range of 1000 °C and 1100 °C for Nb and Nb-Ti steels. With the hot rolling temperature being reduced to 950 °C, the prior austenite grains became slightly elongated in the rolling direction (RD). Decreasing the hot rolling temperature from 900 °C down to 850 °C, the prior austenite grains became fully elongated with size coarsening in RD.

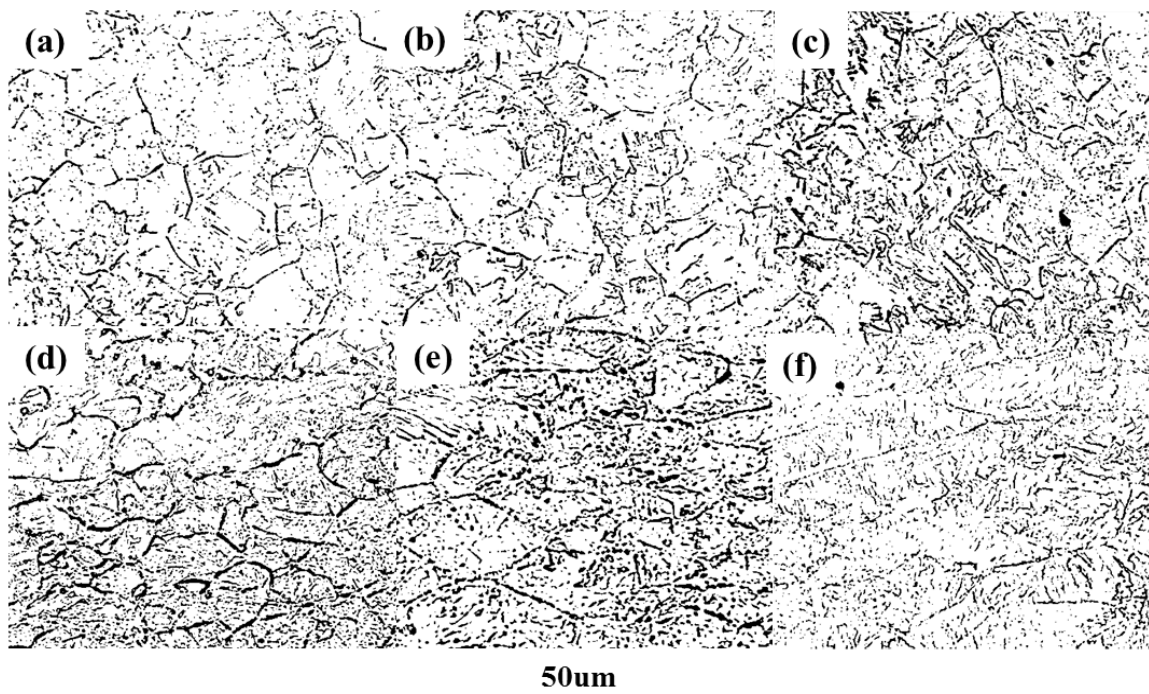


Fig. 4.2 Optical microstructural images of prior austenite grains etched by picric acid for different deformation temperatures with water quenching immediately in the Nb steel, deformation strain (0.3) and strain rate ( $10 \text{ s}^{-1}$ ): (a) 1100 °C; (b) 1050 °C; (c) 1000 °C; (d) 950 °C; (e) 900 °C; (f) 850 °C.

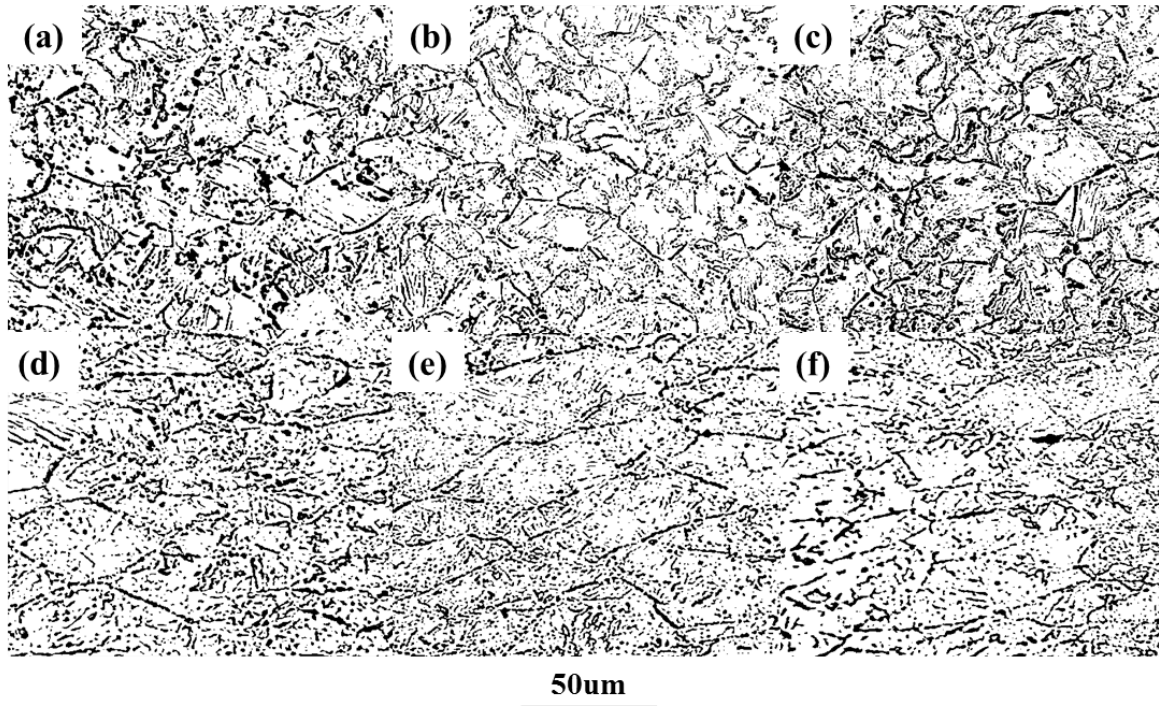


Fig. 4.3 Optical microstructural images of prior austenite grains for different deformation temperature with water quenching immediately in Nb-Ti steel, deformation strain (0.3) and strain rate ( $10 \text{ s}^{-1}$ ): (a) 1100 °C; (b) 1050 °C; (c) 1000 °C; (d) 950 °C; (e) 900 °C; (f) 850 °C.

The optical images in Figs. 4.2 and 4.3 indicate that the recrystallization stop temperature is higher than 900 °C. Partial recrystallization takes place at 950 °C, which is the temperature between the recrystallization limit temperature and recrystallization stop temperature. The prior austenite grains plateau at 1000-1100 °C, which further illustrates that full recrystallization occurs.

#### 4.3.2. Grain size measurements

The average prior austenite grain size was measured on the Nb and Nb-Ti steels at different rolling temperatures using the linear intercept method (ASTM E-112). To compute the dimensions of prior austenite grains in the RD, 8 images at each deformation temperature were calculated and the mean value of grain size was plotted as a function of temperature presented in Table 4.1 and Fig. 4.3.

Table 4.1

The average grain size in RD with different rolling temperatures

Materials	Rolling Temperature (°C)	RD ( $\mu\text{m}$ )
Nb Steel	1100	30.4±4.8
	1050	29.5±3.9
	1000	28.8±4.3
	950	31.2±4.9
	900	38.5±4.2
	850	59.8±3.1
Nb-Ti Steel	1100	23.9±5.8
	1050	23.2±3.2
	1000	23.7±3.1
	950	31.7±1.7
	900	44.1±5.5
	850	58.9±4.8

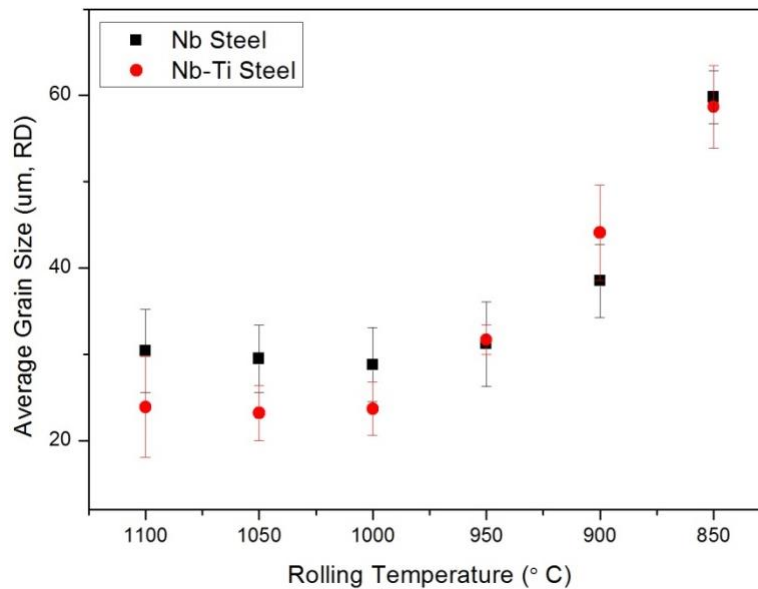


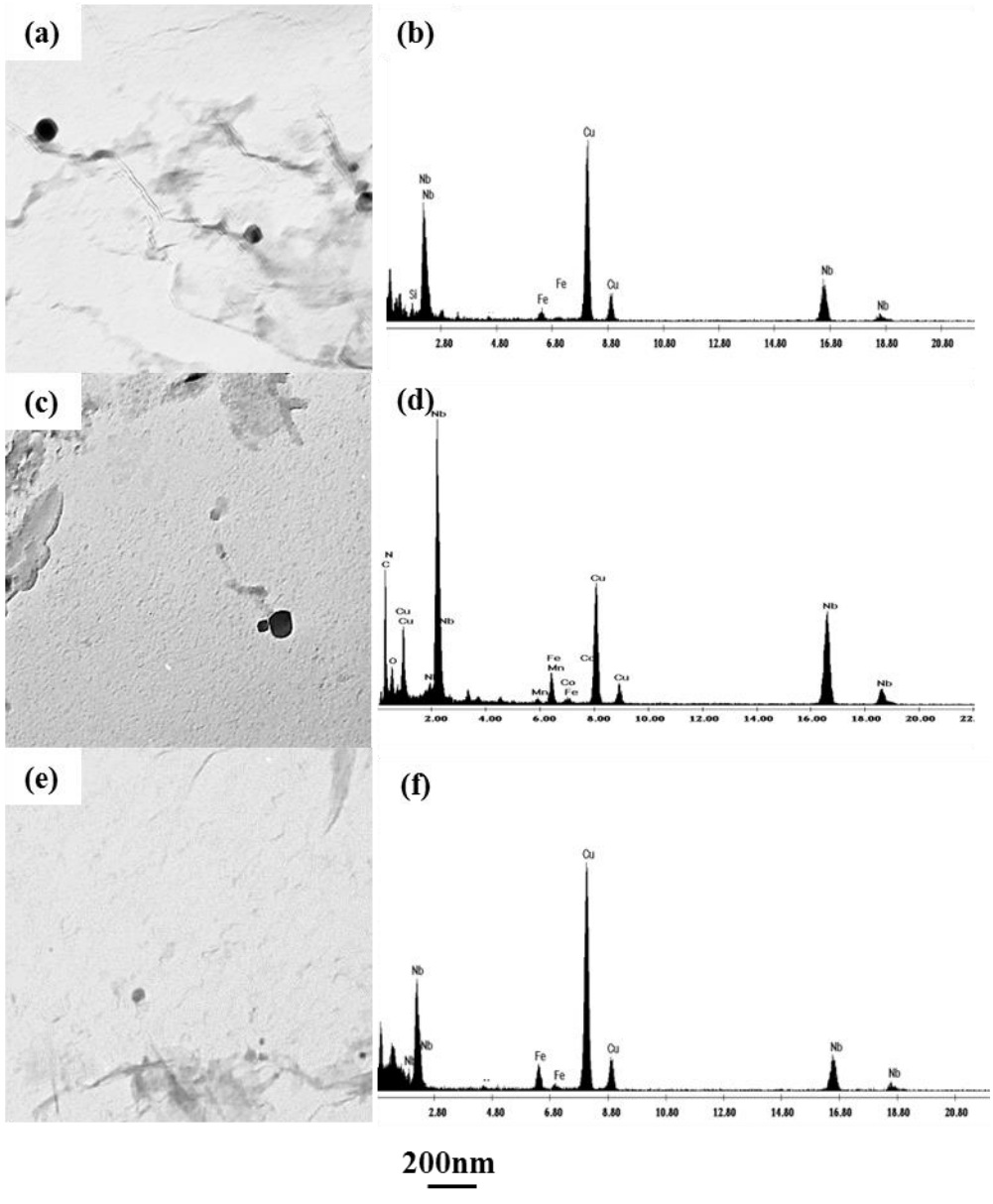
Fig. 4.4 Effect of rough rolling temperature on the prior-austenite grain size in RD

The average dimensions of the prior austenite grains in the RD does not change appreciably between 1100 °C and 1000 °C, and then gradually grows with the temperature decreasing until 850 °C. The long axis of the grain increased from 30.4  $\mu\text{m}$  at 1100 °C to 59.1  $\mu\text{m}$  at 850 °C in the Nb steel, and from 23.9  $\mu\text{m}$  at 1100 °C to 58.9  $\mu\text{m}$  at 850 °C in the Nb-Ti steel. The average prior-austenite grain size is slightly larger for the Nb steel with deformation temperatures in the range of 1100 °C to 1000 °C, and then becomes similar with respect to the Nb-Ti steel.

#### 4.4. TEM carbon extraction replicas

##### 4.4.1. Morphology and chemistry of precipitate

The morphology and composition of precipitates was investigated by TEM, TEM-EDX spectrum and HRTEM from the carbon replica specimens after rough rolling at different temperatures with water quenching immediately and the results are shown in Figs. 4.5, 4.6 and 4.7. The TEM observation revealed that the number density of precipitates increased as the rough rolling temperature decreased. As reported by several researchers, the size of SIP are normally less than 20 nm [193]. For the rolling temperatures from 1100 °C to 1000 °C, Figs. 4.5 (a-f) and 4.6 (a-f) show that most precipitates had a size larger than 20 nm, but only a few were smaller than 20 nm. In contrast, between 950 °C and 850 °C, there were large number of precipitates with a size less than 20 nm at the rolling temperatures, Figs. 4.5 (g-l) and 4.6 (g-l) for both steels. The composition of these particles show that the content of Nb in the precipitates depends on the size of precipitates for the Nb steel, with the larger the precipitate size, the higher content of Nb in the particles. When considering the effect of the rough rolling temperatures on the content of Nb and Ti in precipitation for Nb-Ti steel, the ratios of Ti/(Ti+Nb) has been estimated using the EDX spectrum shown in Fig. 4.7. The mean Ti/(Ti+Nb) value obtained from over 30 precipitates per specimen after rough rolling and separated into two different groups: the first type with the size less than 20 nm and the second type with the size larger than 20 nm. Fig. 4.7 showed that the ratio of Ti/(Ti+Nb) increased with a decreasing rolling temperature to 1000 °C, and then decreased with the rolling temperature continually decreasing to 850 °C for the first type of precipitates. **This is because** the lower rolling temperature between 950 °C and 850 °C is conducive to NbC in precipitation, with rapid increase in their number density (less than 20 nm). For the precipitates with a size larger than 20 nm, the ratio of Ti/(Ti+Nb) was much higher and more stable than for those with a size less than 20 nm, which shows that the different rolling temperatures have almost no effect on the composition of large precipitates for Nb-Ti steel. The results also showed that the lower rough rolling temperature increases the proportion of the niobium in the precipitates.



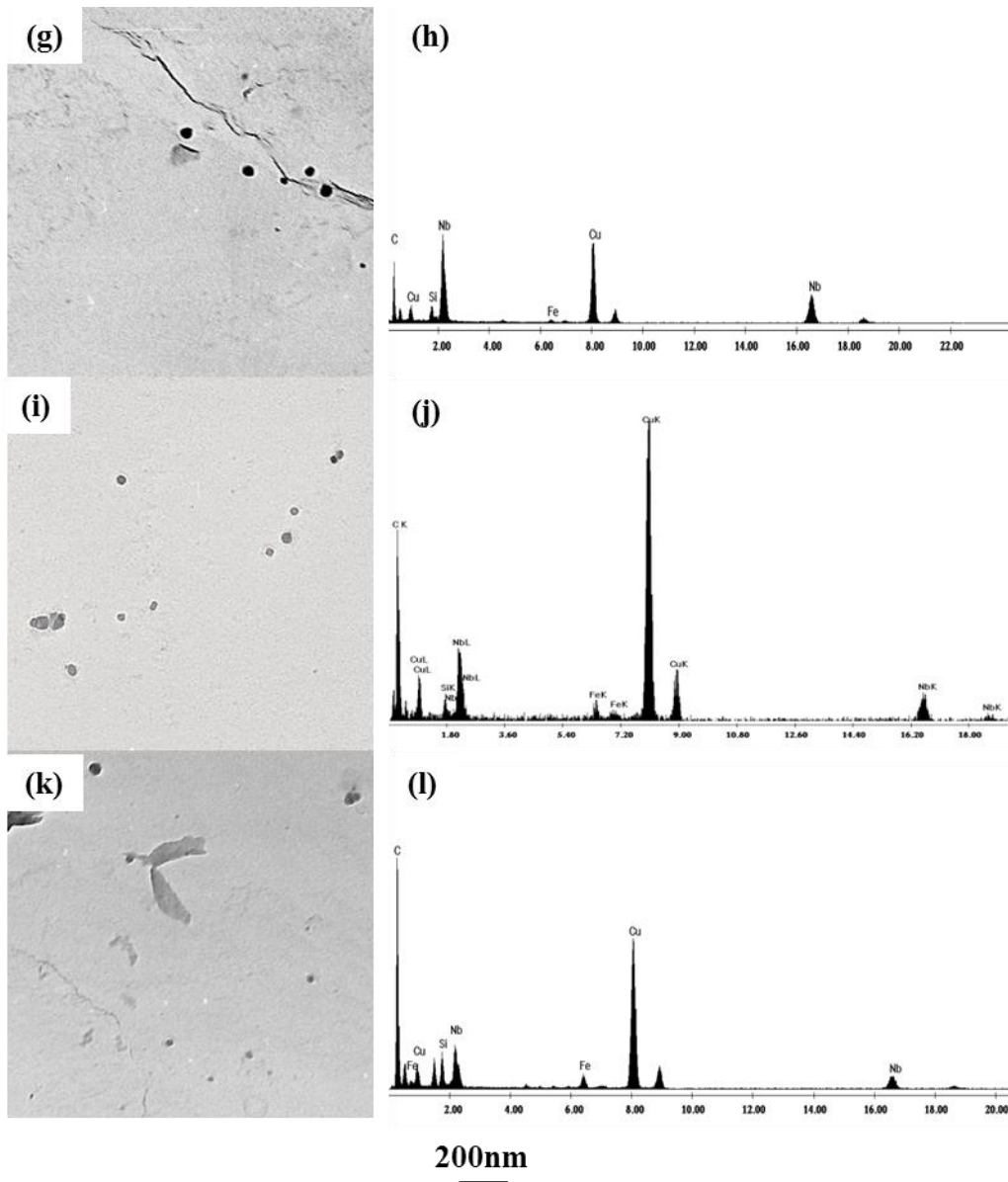
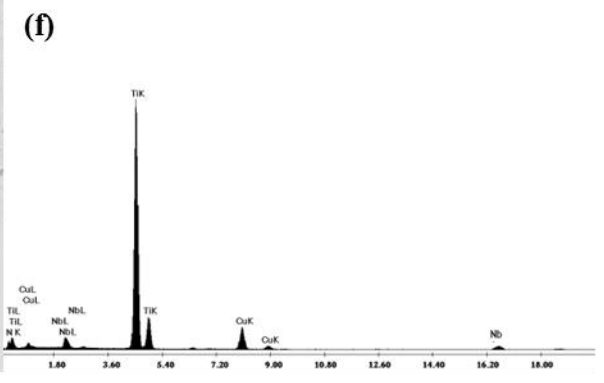
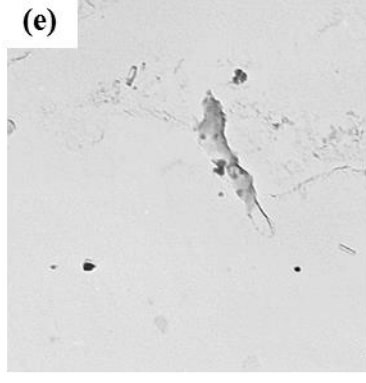
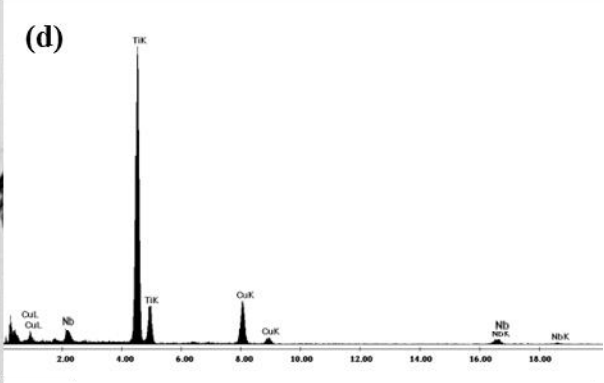
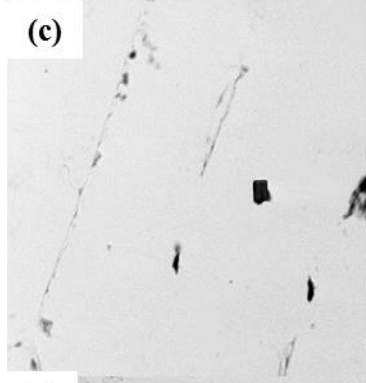
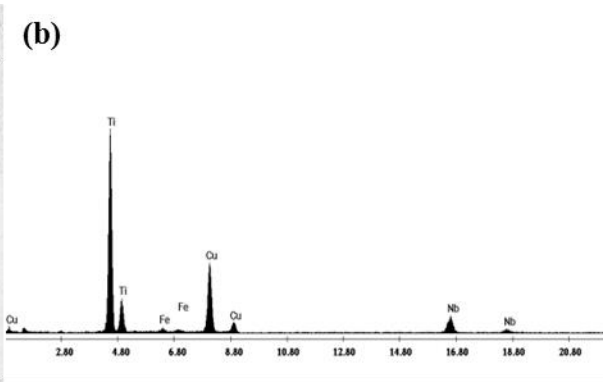
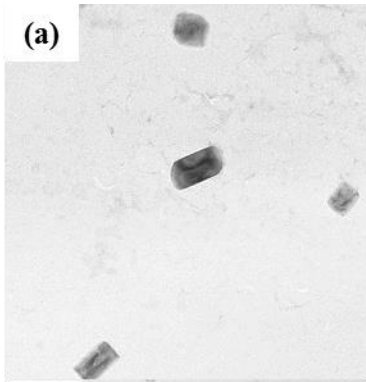


Fig. 4.5 TEM images of NbC precipitates and the corresponding EDS spectrum in the Nb steel deformed at (a) and (b) 1100 °C; (c) and (d) 1050 °C; (e) and (f) 1000 °C; (g) and (h) 950 °C; (i) and (j) 900 °C; (k) and (l) 850 °C.



**200nm**

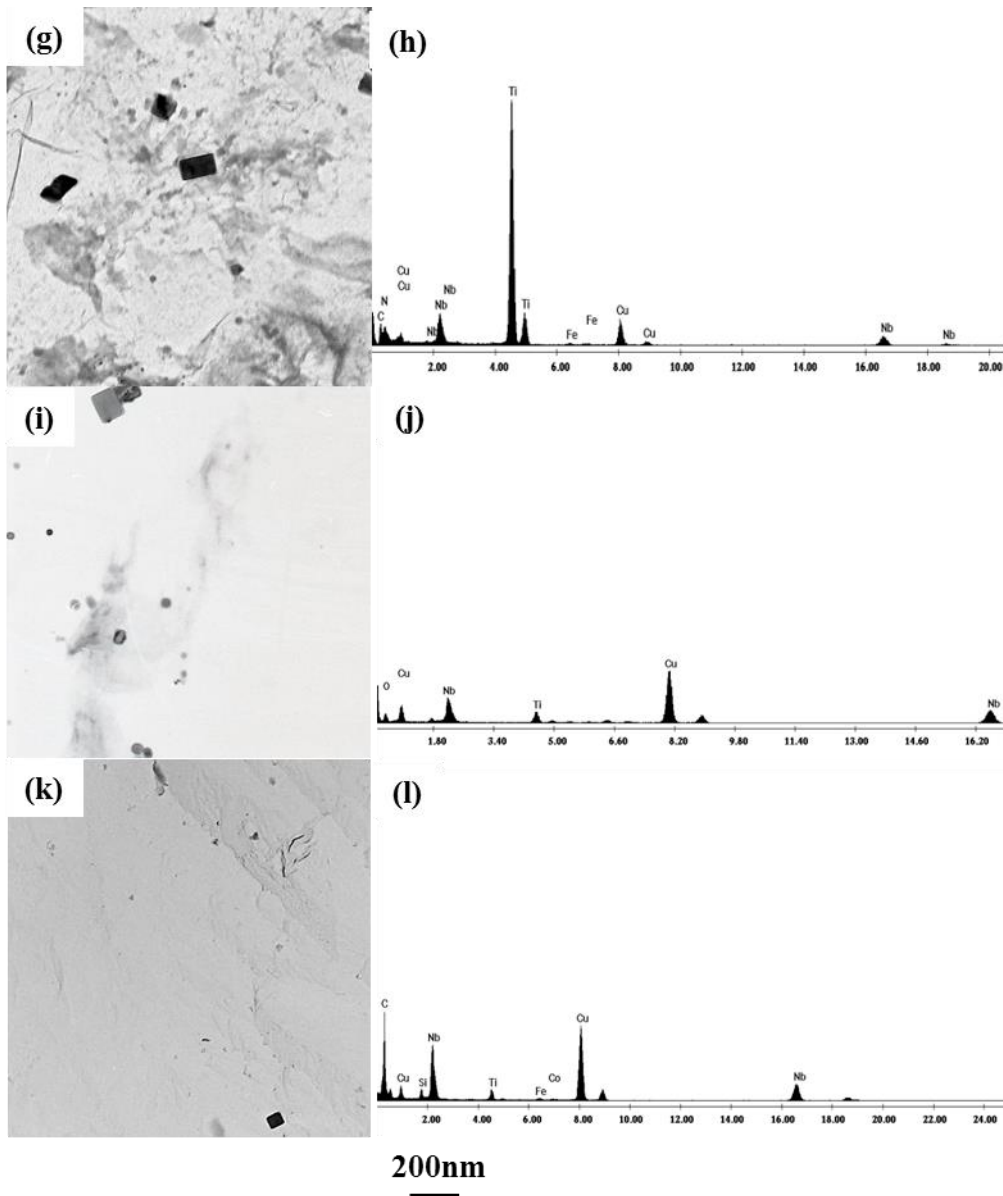


Fig. 4.6 TEM images of (Ti, Nb)C precipitates and the corresponding EDS spectrum in the Nb-Ti steel deformed at (a) and (b) 1100 °C; (c) and (d) 1050 °C; (e) and (f) 1000 °C; (g) and (h) 950 °C; (i) and (j) 900 °C; (k) and (l) 850 °C.

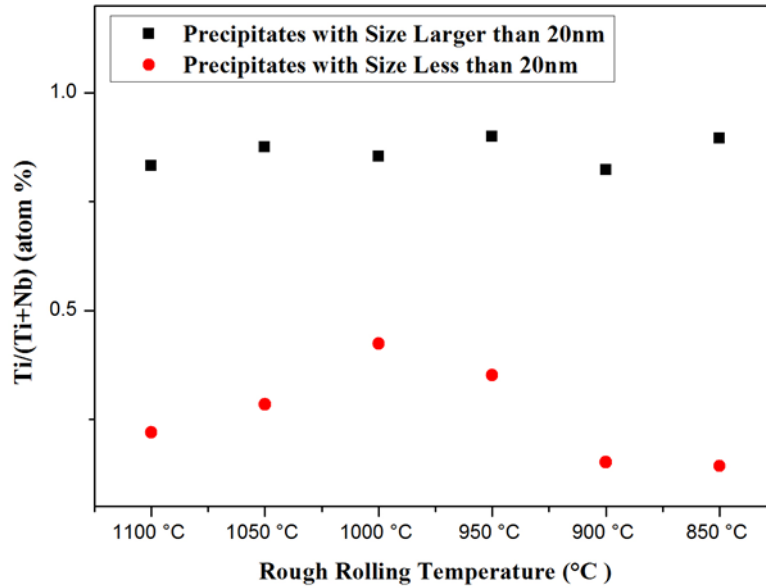


Fig. 4.7 The ratios of Ti/(Ti+Nb) as a function of different rough rolling temperatures.

HRTEM was used to analyse the crystal structure of precipitates with a dimension less than 20 nm produced after deformation at 850 °C followed by water quenching, for both Nb and Nb-Ti steels. The HRTEM observations revealed that the d spacing of the nano-sized particle in Fig. 4.8 (a) was 0.257 nm and the coherent precipitates had a d spacing of 0.218 nm in Fig. 4.8 (b). The EDX spectrum further demonstrated that the particle in Fig. 4.8 (a) contains Nb (Fig.4.8 (c)) and the coherent precipitates contain Nb and Ti (Fig. 4.8 (d)). The Nb carbide with a  $d_{(111)}$  equal to 0.258 nm and the Nb and Ti carbide with a  $d_{(002)}$  of 0.211 nm fit well with the measured data of d spacing from Fig. 4.8 (a) and (b). Therefore, combining the HRTEM and EDS spectrum, these two particles were shown to be NbC in Fig. 4.8 (a) and (Ti, Nb)C in Fig. 4.8 (b).

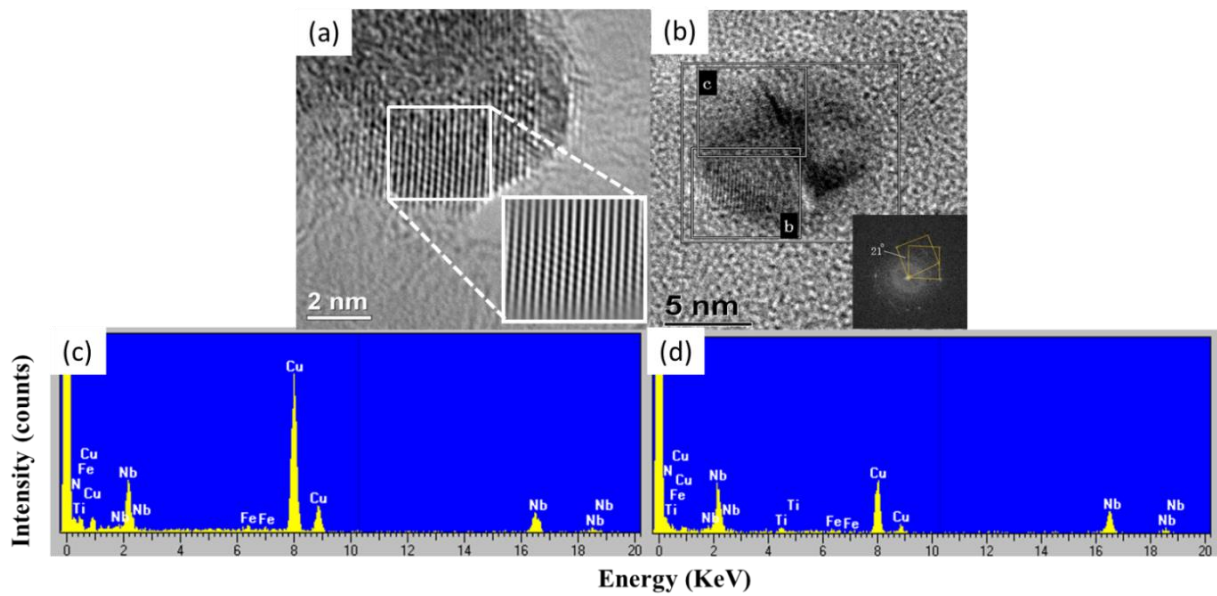


Fig. 4.8 TEM micrographs showing the typical morphology of the precipitates deformed at 850 °C, (a) a high-resolution TEM image from Nb carbide in Nb steel; (b) a high-resolution TEM image from (Ti,Nb)C in Nb-Ti steel; (c) EDS spectra of (a); (d) EDS spectra of (b).

#### 4.4.2. The volume fraction and the content of microalloyed steels in precipitates

The precipitates at each rolling temperature were separated into two groups by the precipitate size; one group had dimensions larger than 20 nm, believed to be the precipitates that had not dissolved on heating, while the other group was SIP with a size less than 20 nm. In order to identify the effect of the hot rolling temperatures on the precipitation behaviour, the volume fraction of precipitates were calculated using the TEM replica data shown in Figs. 4.5 and 4.6. Then, using the volume fraction of precipitates, the amounts of Nb or Nb and Ti in precipitates can be expressed using Eq. (4.7) [20,194,195] and the results are shown in Table 4.2.

$$f(t) = \left[ \frac{\rho_r}{\rho_{\text{precipitate}}} \times \left( \frac{Z+1}{Z} \right) / 100 \right] \times \{M\} \quad (4.7)$$

where  $f(t)$  is volume fraction of precipitates as a function of holding time;  $\rho_r$  and  $\rho_{\text{precipitate}}$  are the densities of austenite and precipitates, respectively;  $Z$  is the stoichiometric ratio of the precipitates;  $\{M\}$  is the Nb or Nb and Ti concentration in the precipitates. From Table 4.2, the volume fraction of precipitates as a function of rolling temperatures appears to be logical in these two steels. It can be seen that the volume fraction of precipitates, as well as the

content of Nb or Nb and Ti in precipitates increased as the roughing temperature decreased for Nb and Nb-Ti steels, respectively.

Table 4.2

The overview of the experimentally measured data on the precipitation state after deformation at different rolling temperatures. The number density, volume fraction was measured by TEM and the wt% of the precipitates calculated from Eq. 4.7.

Materials	Rolling Temperature (°C)	Category	Volume Fraction of Precipitates ( $10^{-3}$ )	Precipitated Nb (wt%) in Nb steel	Precipitated Nb (wt%), total
Nb Steel	1100	>20 nm	0.065	0.0057	0.0057
		<20 nm	0 (0%)	0	
	1050	>20 nm	0.119	0.0105	0.011
		<20 nm	0.006(4.8%)	0.00053	
	1000	>20 nm	0.187	0.0165	0.017
		<20 nm	0.0095(4.8%)	0.0008	
	950	>20 nm	0.209	0.0184	0.021
		<20 nm	0.033(13.8%)	0.0029	
	900	>20 nm	0.204	0.0179	0.021
		<20 nm	0.035(14.6%)	0.0031	
	850	>20 nm	0.243	0.0213	0.025
		<20 nm	0.042 (14.8%)	0.0037	
Materials	Rolling Temperature (°C)	Category	Volume Fraction of Precipitates ( $10^{-3}$ )	Precipitated Nb and Ti (wt%) in Nb-Ti steel	Precipitated Nb and Ti (wt%), total
Nb-Ti Steel	1100	>20 nm	0.47	0.0343	0.035
		<20 nm	0.0035 (0.7%)	0.0003	
	1050	>20 nm	0.504	0.0361	0.037
		<20 nm	0.0104 (2%)	0.0009	
	1000	>20 nm	0.54	0.0386	0.039
		<20 nm	0.0131 (2.4%)	0.0012	
	950	>20 nm	0.525	0.0376	0.040
		<20 nm	0.0299 (5.4%)	0.0026	
	900	>20 nm	0.534	0.0382	0.042
		<20 nm	0.0401(7%)	0.0035	
	850	>20 nm	0.542	0.0388	0.044
		<20 nm	0.0556 (9.3%)	0.0049	

No SIP (less than 20 nm) were observed at 1100 °C in the Nb steel, but some did exist in the Nb-Ti steel. At 1000 °C, the volume fraction of SIP was  $6 \times 10^{-6}$  (4.8 % for total precipitation) in the Nb steel and  $1.3 \times 10^{-5}$  (2.4 % for total precipitation) in the Nb-Ti steel, which are smaller amounts than would be expected to stop recrystallisation [193]. At 950 °C, more than half of the precipitates observed were smaller than 20 nm in the Nb steel and 48% of them in the Nb-Ti steel. Because the mixed microstructures were observed at 950 °C in both steels (Fig. 4.2 and 4.3), it is probable that recrystallization initially occurred, but was halted by the

rapid increase in number density of small precipitates. As the volume fraction and the rate of evolution of SIP (less than 20 nm) significantly increased due to the rolling temperature reduced to 850 °C, recrystallization was stopped at this temperature (Fig. 4.2 and 4.3). The highest volume fraction of SIP was at 850 °C for both steels. For precipitates with the size larger than 20 nm, the volume fraction continuously increased with the decreasing rolling temperature (Table 4.2). However, the rate of increase of the larger precipitates was lower than that for SIP with the deformation temperature lower than 950 °C. The average diameter of the SIP decreased with a decrease in the rough rolling temperature.

The content of Nb or Nb and Ti in the precipitates as a function of the rolling temperature was shown in Figs. 4.9 and 4.10 for the Nb and Nb-Ti steels, respectively. The Nb in the undissolved precipitates in the Nb steel increased as the rolling temperature decreased from 1100 °C to 950 °C, and was then approximately constant as the deformation temperature was decreased from 950 °C to 850 °C. However, in the Nb-Ti steel, the content of Nb and Ti in the undissolved precipitates hardly changed with the different rolling temperatures. For the SIP, the Nb content increased gradually with the decreasing deformation temperature for both Nb and Nb-Ti steels.

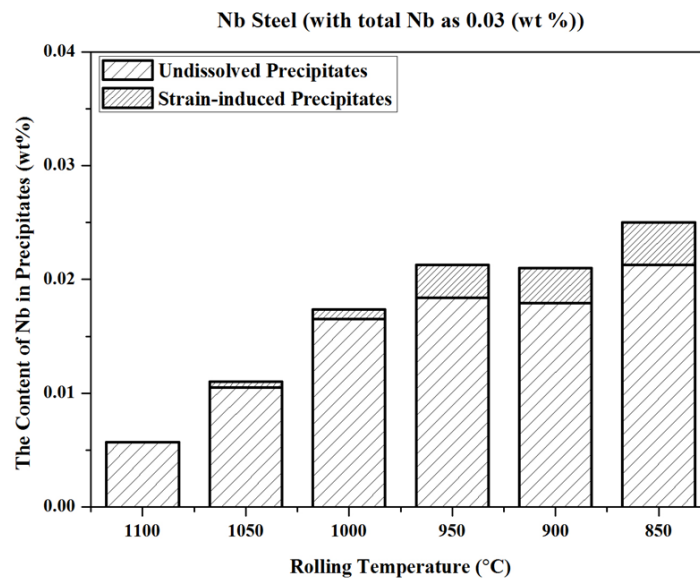


Fig. 4.9 The content of Nb in strain-induced and undissolved precipitates in Nb steel

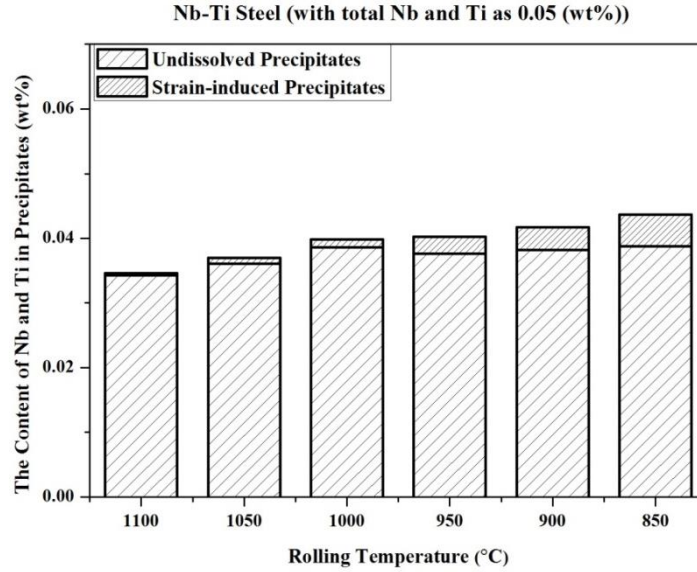


Fig. 4.10 The content of Nb and Ti in strain-induced and undissolved precipitates in Nb-Ti steel

#### 4.5. TEM thin foil analysis

##### 4.5.1. Calculation of the orientation relationship between SIP and austenite, subsequently transformed to ferrite

The SIP formed in austenite could be related to the ferrite by the orientation relationship of austenite when observed at room temperature. There would be no orientation relationship (OR) between the SIP, the austenite and the final ferrite matrix, if recrystallisation occurred in the austenite grains before phase transformation [196]. Therefore, to demonstrate that the particles extracted by carbon replicas (Figs. 4.4 and 4.5) from the ferritic matrix are SIP formed in the austenite region, the OR between precipitates and austenite transformed to the ferrite matrix have been calculated using the corresponding transformation matrix and Kurdjumov-Sachs (K-S) OR for Nb and Nb-Ti steels.

Davenport et al. [197] indicated that the SIP and austenite have a cube-cube relationship, i.e.:  $[010]_{\text{precipitate}} // [010]_{\text{austenite}}$ ,  $(100)_{\text{precipitate}} // (100)_{\text{austenite}}$ . From the above OR of SIP (suggested as NbC) and austenite, the corresponding coordinate transformation matrix,  $M_{\gamma}^p$  can be readily determined as

$$M_{\gamma}^p = \begin{bmatrix} 1.25 & 0 & 0 \\ 0 & 1.25 & 0 \\ 0 & 0 & 1.25 \end{bmatrix} \quad (4.8)$$

Then, an arbitrary pair of parallel directions,  $r_p$  and  $r_\gamma$ , will be related by

$$r_p = M_\gamma^p r_\gamma \quad (4.9)$$

With the OR matrix, the pair of conjugate planes and direction of NbC parallel with the pair of [110] and (111) of austenite can be deduced as

$$[110]_{\text{NbC}} // [110]_{\text{austenite}} \quad (4.10a)$$

$$(111)_{\text{NbC}} // (111)_{\text{austenite}} \quad (4.10b)$$

It is well known that the austenite transforms to ferrite and obeys the Kurdjumov-Sachs (K-S) OR [198]:  $[110]_{\text{austenite}} // [111]_{\text{ferrite}}$ ,  $(111)_{\text{austenite}} // (110)_{\text{ferrite}}$ . The OR between SIP of NbC and austenite transformation to ferrite can be further indicated as  $[110]_{\text{NbC}} // [110]_{\text{austenite}} // [111]_{\text{ferrite}}$ ,  $(111)_{\text{NbC}} // (111)_{\text{austenite}} // (110)_{\text{ferrite}}$ , depending on (4.10a), (4.10b) and K-S OR.

The coordinate transformation matrix of NbC and ferrite is shown in table 4.3, which indicates that the precipitates cannot have the same characteristics as the Bagaryatski OR (fcc/bcc system) [199][6].

Table 4.3  
Coordinate transformation matrix for  $[\bar{1}10]_{\text{NbC}} // [111]_{\text{ferrite}}$

$$M_f^{\text{NbC}} = \begin{bmatrix} 0.479 & -0.431 & -0.049 \\ 0.42 & -0.479 & -0.108 \\ 0.108 & 0.049 & 0.636 \end{bmatrix}$$

Face-centered cubic (fcc) precipitates in a body-centered cubic (bcc) ferrite can be indicated by  $\{111\}_{\text{fcc}} // \{110\}_{\text{bcc}}$  and  $\langle 110 \rangle_{\text{fcc}} // \langle 111 \rangle_{\text{bcc}}$ . On a given (011) bcc plane (two-fold rotation axis), there are two  $\langle 111 \rangle$  directions:  $[11\bar{1}]_{\text{bcc}}$  and  $[\bar{1}11]_{\text{bcc}}$ , which are perpendicular. As there are six two-fold rotation axes of  $\{110\}$  in bcc matrix, six variants of SIP and ferrite matrix OR can be derived, which are listed in Table 4.4.

In summary, the variants of SIP and ferrite matrix OR have been deduced via the corresponding transformation matrix. The results need to be further demonstrated through experimental test using TEM and HRTEM.

Table 4.4  
Six variants of NbC and Ferrite ORs in FCC/BCC system

Ferrite-NbC Variant	Plane BCC//FCC	Direction BCC//FCC
1a	$(011)_{\text{bcc}}//(\overline{111})_{\text{fcc}}$	$[\overline{111}]_{\text{bcc}}//[\overline{110}]_{\text{fcc}}$
1b		$[\overline{111}]_{\text{bcc}}//[\overline{110}]_{\text{fcc}}$
2a	$(101)_{\text{bcc}}//(\overline{111})_{\text{fcc}}$	$[\overline{111}]_{\text{bcc}}//[\overline{110}]_{\text{fcc}}$
2b		$[\overline{111}]_{\text{bcc}}//[\overline{110}]_{\text{fcc}}$
3a	$(110)_{\text{bcc}}//(\overline{111})_{\text{fcc}}$	$[\overline{111}]_{\text{bcc}}//[\overline{110}]_{\text{fcc}}$
3b		$[\overline{111}]_{\text{bcc}}//[\overline{110}]_{\text{fcc}}$
4a	$(\overline{110})_{\text{bcc}}//(\overline{111})_{\text{fcc}}$	$[\overline{111}]_{\text{bcc}}//[\overline{110}]_{\text{fcc}}$
4b		$[\overline{111}]_{\text{bcc}}//[\overline{110}]_{\text{fcc}}$
5a	$(\overline{101})_{\text{bcc}}//(\overline{111})_{\text{fcc}}$	$[\overline{111}]_{\text{bcc}}//[\overline{110}]_{\text{fcc}}$
5b		$[\overline{111}]_{\text{bcc}}//[\overline{110}]_{\text{fcc}}$
6a	$(0\overline{11})_{\text{bcc}}//(\overline{111})_{\text{fcc}}$	$[\overline{111}]_{\text{bcc}}//[\overline{110}]_{\text{fcc}}$
6b		$[\overline{111}]_{\text{bcc}}//[\overline{110}]_{\text{fcc}}$

#### 4.5.2. The observation of strain-induced precipitation during rough rolling using TEM and HRTEM

The morphology and the OR of precipitated carbides with respect to the ferrite matrix have been analysed for the deformation temperatures between 950 °C and 850 °C followed by water quenching. This was not possible at the higher temperature due to the limited SIP during deformation between 1000 °C and 1100 °C. The location of precipitation has been analysed using TEM bright- and dark-field from thin foil samples for Nb and Nb-Ti steels shown in Figs. 4.11 and 4.12. The selected area diffraction patterns have been used to analyse the orientation relationship between SIP and the ferrite matrix. Following deformation at 850 °C, the carbides in ferrite could be clearly identified by bright and dark-field imaging and the dark-field image taken from the  $(\overline{111})_{\text{NbC}}$  reflection, shown in Figs. 4.11 (a, b and c) and Fig. 4.12 (a, b and c). From the dark-field image in Figs. 4.11 (b) and 4.12 (b), these carbides sit on the dislocations and sub-grain boundaries. The selected area diffraction patterns (SADP) in Figs. 4.11 (c) and 4.12 (c) reveal that the carbides, which are NbC and (Ti,Nb)C for Nb and Nb-Ti steels respectively, obey the orientation relationship with ferrite as follows:

$$[\overline{110}]_{\text{NbC}}//[\overline{111}]_{\text{Ferrite}} \text{ and } (111)_{\text{NbC}}//(\overline{101})_{\text{Ferrite}} \quad (4.11)$$

$$[\overline{110}]_{(\text{Ti,Nb})\text{C}}//[\overline{111}]_{\text{Ferrite}} \text{ and } (111)_{(\text{Ti,Nb})\text{C}}//(\overline{011})_{\text{Ferrite}} \quad (4.12)$$

Increasing the deformation temperature to 900 °C still resulted in an unrecrystallised structure, but it would be expected that the dislocation density in the austenite was lower than that with the deformation temperature at 850 °C. The bright and dark-field images in Figs. 4.11 (d, e and f) and 4.12 (d, e and f) showed that carbides were often located on dislocations and sub-grain boundaries, with the same orientation relationship as observed at 850°C between SIP and ferrite matrix. The OR between precipitates and ferrite for the deformation temperature between 900 °C and 850 °C were the same as the deduced OR from the corresponding coordinate transformation matrix shown in Table 4.2. Therefore, the evidence indicates that the precipitation for Nb and Nb-Ti steels was SIP after rough rolling at 900 °C and 850 °C.

When the deformation temperature was increased to 950 °C, the bright- and dark-field images in Figs. 4.11 (g, h and i) and 4.12 (g, h and i) clearly show that carbides precipitated on grain boundaries and within grains. The dark-field images were taken from  $(\bar{2}02)_{\text{NbC}}$  for Nb steel and  $(\bar{2}02)_{(\text{Ti,Nb})\text{C}}$  for Nb-Ti steel. The SADP in Figs. 4.12 (i) and 4.13 (i) exhibited the orientation relationship for Nb and Nb-Ti steels as follows:

$$[111]_{\text{NbC}}//[110]_{\text{Ferrite}} \text{ and } (2\bar{2}0)_{\text{NbC}}//(002)_{\text{Ferrite}} \quad (4.13)$$

$$[111]_{(\text{Ti,Nb})\text{C}}//[110]_{\text{Ferrite}} \text{ and } (2\bar{2}0)_{(\text{Ti,Nb})\text{C}}//(002)_{\text{Ferrite}} \quad (4.14)$$

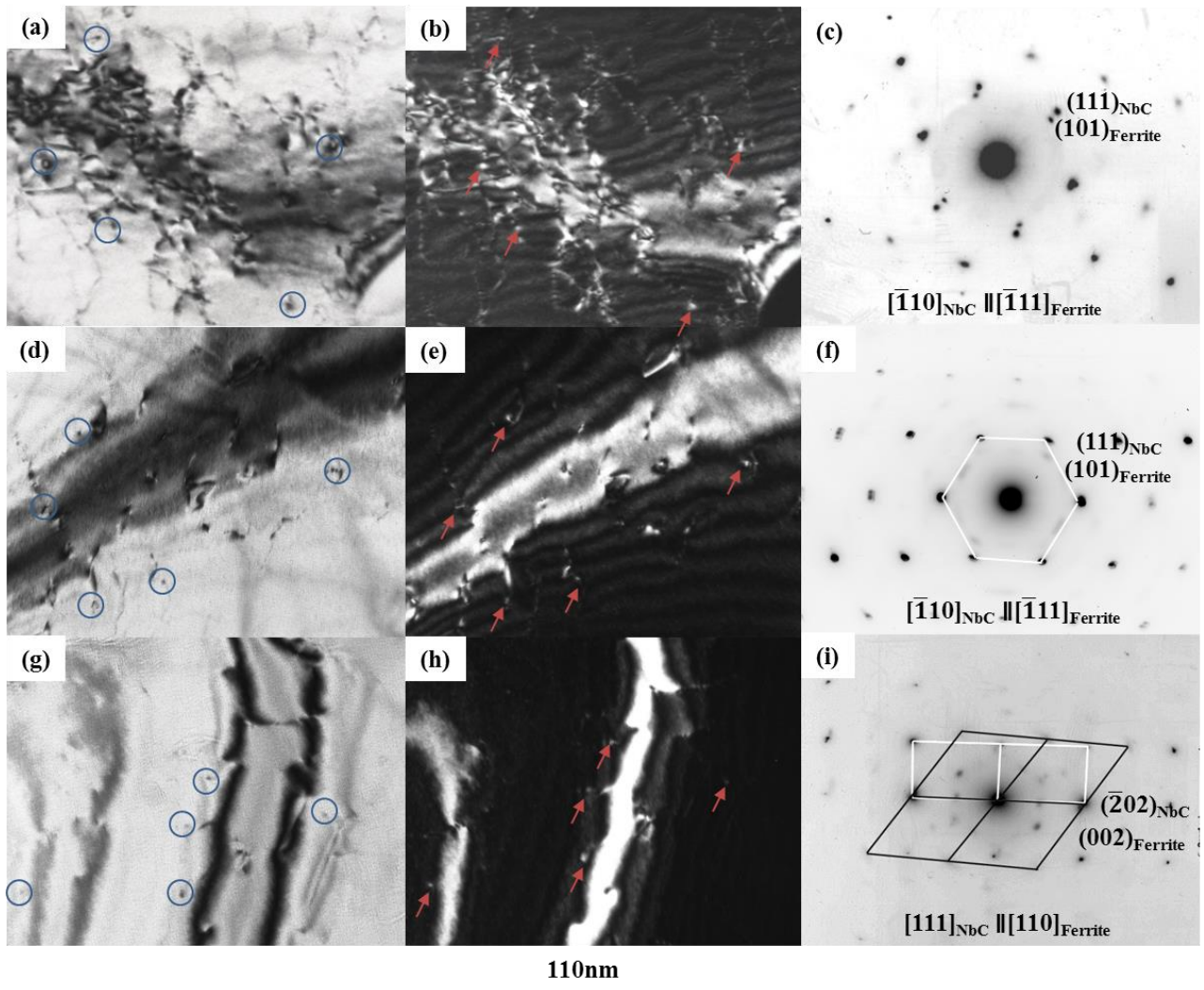


Fig. 4.11 TEM images of Nb steel deformed from 850°C to 950°C, (a) A bright-field image with the deformation temperature at 850°C; (b) Centered-dark-field image formed with  $(1\bar{1}1)_{\text{NbC}}$  from the same region of (a); (c) the corresponding SADP of SIP and ferrite matrix from (a); (d) A bright-field image with the deformation temperature at 900°C; (e) Centered-dark-field image formed with  $(\bar{1}11)_{\text{NbC}}$  from the same region of (d); (f) the corresponding SADP of SIP and ferrite matrix from (d); (g) A bright-field image with the deformation temperature at 950°C; (h) Centered-dark-field image formed with  $(\bar{2}02)_{\text{NbC}}$  from the same region of (g); (i) the corresponding SADP of SIP and ferrite matrix from (g).

The OR between precipitates and ferrite for the deformation temperature at 950 °C was different from the OR for the temperature between 850 °C and 900 °C (Figs. 4.11 and 4.12). The OR between SIP and ferrite after rough rolling at 950 °C has been lost through recrystallization of the austenite, as evidenced by the partial recrystallization structures that were observed using OM, shown in Figs. 4.2(d) and 4.3 (d).

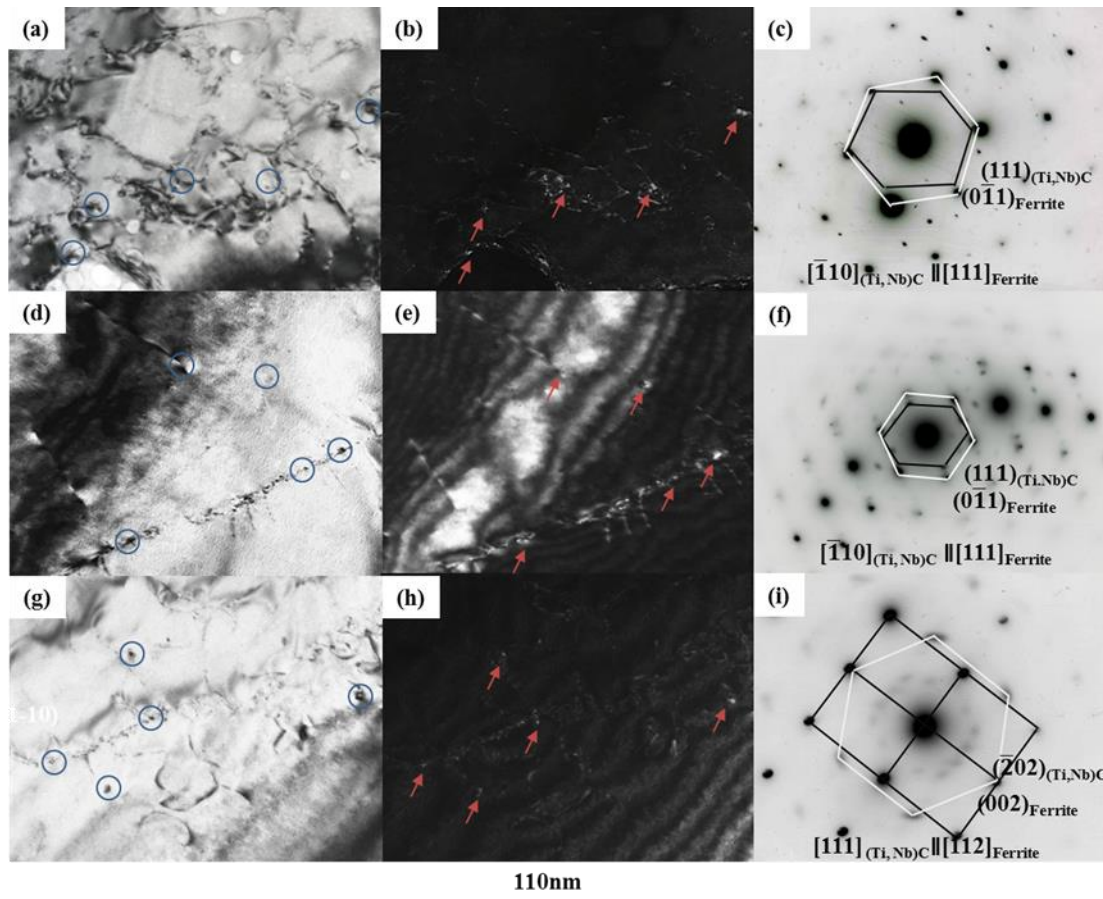


Fig. 4.12 TEM images of Nb-Ti steel deformed from 850°C to 950°C, (a) A bright-field image with the deformation temperature at 850°C; (b) Centered-dark-field image formed with  $(1\bar{1}1)_{(Ti,Nb)C}$  from the same region of (a); (c) The corresponding SADP of SIP and ferrite matrix from (a); (d) A bright-field image with the deformation temperature at 900°C; (e) Centered-dark-field image formed with  $(1\bar{1}1)_{(Ti,Nb)C}$  from the same region of (d); (f) The corresponding SADP of SIP and ferrite matrix from (d); (g) A bright-field image with the deformation temperature at 950°C; (h) Centered-dark-field image formed with  $(\bar{2}02)_{(Ti,Nb)C}$  from the same region of (g); (i) the corresponding SADP of SIP and ferrite matrix from (g).

As expected, the number density of precipitates was greater at 850°C than at 900 °C and 950 °C, Fig. 4.11 and 4.12, which is in agreement with the carbon replica data. SIP is widely believed to nucleate on dislocations and grain boundaries [166]. Therefore, with the highest dislocation density, deformation at 850 °C would be expected to lead to the highest volume fraction of the carbides, since they nucleated on dislocations and boundaries. However, relatively little SIP occurred within the grains for the rolling temperature of 950 °C, because the recovery and recrystallization substantially reduced the dislocation density.

High-resolution TEM (HRTEM) was used to investigate the nanometer-sized carbides in this program. A lattice image of the ferrite matrix containing carbides is shown in Fig. 4.13 which was taken from the Nb steel after deformation at 850 °C. The inverse fast Fourier

transformation (IFFT) was used for the carbide shown in Fig. 4.13 (b). The zone axis of the ferrite matrix and carbides was identified as  $[111]_{\text{ferrite}}$  direction in Fig. 4.13 (b) parallel with the  $[110]$  zone axis of carbides, i.e.:  $[110]_{\text{NbC}} // [111]_{\text{ferrite}}$ . Under this condition, the lattice image of the carbide has been identified with the  $d_{(111)}$  spacing equal to 0.251nm. There are two carbides, shown in Fig. 4.11(b), which have the cube-cube orientation relationship with two different growing along directions of  $g(1\bar{1}1)$  and  $g(\bar{1}11)$ . The dimensions of each carbide has been measured directly as 3 nm in thickness and 7.5 nm in length. The orientation relationship has been identified by the fast Fourier transformed (FFT) diffractogram shown in Fig. 4.13 (c). The NbC precipitates obey the orientation relationship with ferrite matrix as shown by:

$$[\bar{1}10]_{\text{NbC}} // [\bar{1}\bar{1}1]_{\text{Ferrite}} \text{ and } (111)_{\text{NbC}} // (\bar{1}01)_{\text{Ferrite}}.$$

The OR between the precipitates and the matrix shown Fig. 4.13 (c) are the same with the calculated OR from the corresponding transformation matrix shown in Table 4.3.

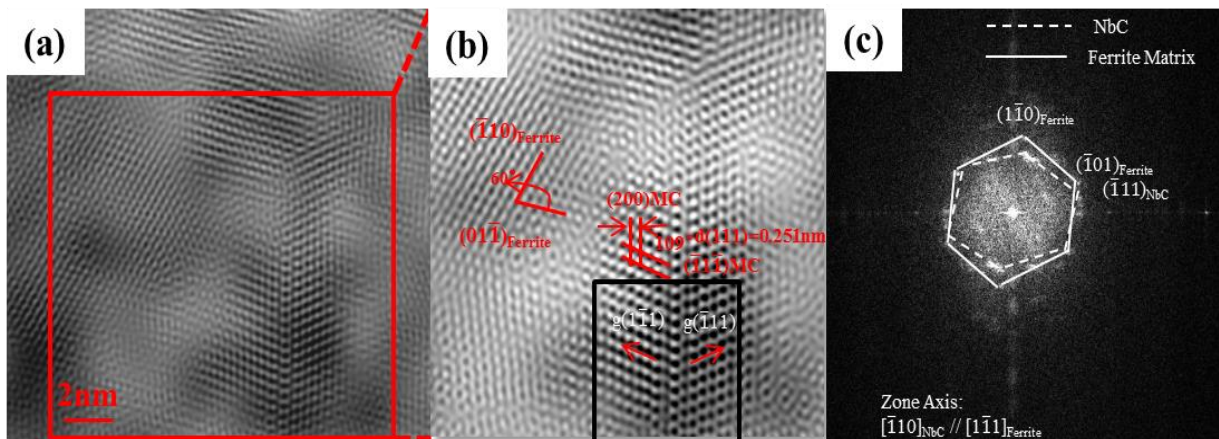


Fig. 4.13 HRTEM image and IFFT lattice image of the nano-meter sized carbide (a)HRTEM image of the nanometer-sized NbC obtained from the Nb steel after deformation at 850 °C with water quenching immediately; (b) IFFT lattice image in the range of red line of (a); (c) the corresponding fast Fourier transformed diffractogram from (b).

#### 4.6. Vickers micro-hardness

The specimens used for Vickers micro-hardness testing in this study were those that had been rough rolled at different temperatures, and then water quenched to room temperature with the deformation schedules shown in Fig. 3.3. The Vickers micro-hardness values were measured and listed in Fig. 4.14 for Nb and Nb-Ti steels. The Vickers micro-hardness slightly decreased with decreasing the deformation temperature from 1100 °C to 1000 °C, and then increased as the deformation temperature decreased to 850 °C for both Nb and Nb-Ti steels. The micro-hardness for Nb steel was much higher than that for Nb-Ti steel at the rough

rolling temperatures between 1100 °C and 1000 °C. Then the micro-hardness difference between the Nb and Nb-Ti steels became smaller as the deformation temperature decreased to 850 °C.

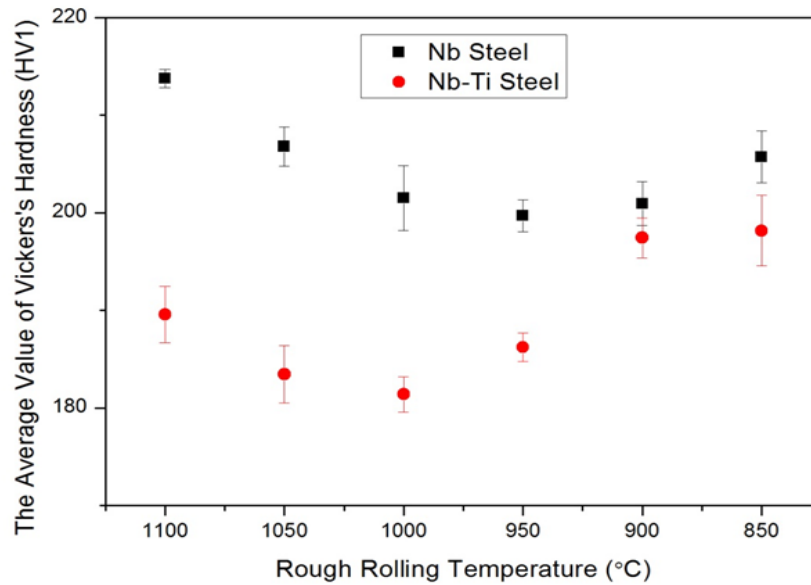


Fig. 4.14 The average Vicker's Hardness in the Nb and Nb-Ti steels

#### 4.7. Summary

The prior austenite grains obtained in the rough rolling process had recrystallized at the rolling temperatures ranging between 1100 °C and 1000 °C in the Nb and Nb-Ti steels (Figs. 4.2 (a-c) and 4.3 (a-c)). When considering the effect of SIP on the recrystallization, the Zener pinning force from SIP was too low at this temperature to halt the recrystallization, because of the small volume fraction of the precipitates with the rolling temperatures in the range of 1100 °C-1000 °C. When the rolling temperature was reduced to 950 °C (Figs. 4.2 (d) and 4.3 (d)), the microstructures become mixed with evidence of partial recrystallization. It is believed that recrystallization started at the beginning of deformation, but with the increase in SIP, the Zener pinning force became important to retard the recrystallizing driving force. Reducing the rolling temperatures from 900 °C to 850 °C, largely stopped recrystallization, resulting in elongated austenite structures between 900 °C and 850 °C (Figs. 4.2 (e, f) and 4.3 (e, f)). This is a consequence of the rapid precipitation of a large volume fraction of precipitates at the start of deformation that retards the recrystallization.

The SIP in the Nb and Nb-Ti steels has been examined via analyses of bright/dark field images, electron diffraction patterns, HRTEM and EDX (Fig. 4.8). The results strongly suggest that these carbides have the lattice parameters of 0.447 nm identified as NbC in the Nb steel and 0.437 nm as (Ti, Nb)C in the Nb-Ti steel.

The orientation relationship between SIP and the ferrite matrix has been investigated by SADP with rolling temperatures from 950 °C to 850 °C. The different orientation relationships shown in Figs. 4.11 and 4.12 further demonstrated that the recrystallization can eliminate the orientation relationship between SIP and austenite subsequently transformed to ferrite.

## **CHAPTER 5: THE HEAT TREATMENT AT 1200 °C WITH DIFFERENT DURATION ON ROUGH ROLLING MICRO-ALLOYED STEELS**

### 5.1 Introduction

Thermomechanical controlled processes (TMCP), consisting of controlled hot rolling followed by controlled cooling, have been developed to improve strength, toughness and weldability of microalloyed steels [1,2]. The improvement in mechanical properties from TMCP is due to the refinement of the austenite microstructure, maximising the austenite boundary area and deformation band density, subsequently increasing the number of nucleation sites prior to the development of the transformation microstructure. The enhanced mechanical properties of low-carbon microalloyed steels thereby arises from a combination of the refined ferrite grain size and the dispersion hardening through the precipitation in ferrite [3–9].

Microalloy additions play an equally important role with the thermo-mechanical processes on the evolution of the final microstructure and associated mechanical properties. Microalloyed elements in steels, such as Nb, facilitate grain refinement through precipitation of carbides/carbonitrides in austenite thereby inhibiting the static recrystallisation of austenite, resulting in a fine final microstructure. In addition, titanium has frequently been added to microalloyed steels to enhance the control of the austenite and transformed ferrite grain sizes during both the deformation and subsequent heat treatment process [10,11]. Therefore, during TMCP, these microalloying elements can precipitate as carbides or carbonitrides to increase the nucleation sites for obtaining a fine ferrite grain size [12,13].

The consequence of a low finishing temperature is high energy consumption through high mill loads [24]. To improve the production efficiency and reduce energy consumption, a new rolling process is explored in this work, which involves the addition of a reheating process between rough and finish rolling. The effect of this reheating on the deformed austenite, and particularly the precipitate dissolution kinetics, is the focus of this study.

Much of the existing published work is concerned with the type and distribution of precipitates based on single microalloy additions with idealised solution treatment and ageing experiments after deformation [8,21,22,24,25,169]. Less work has been directed towards the effects of multiple microalloy additions during the thermomechanical processing. Therefore,

in this work, two types of Nb and Nb-Ti steels were selected for comparative reasons. These two steels were rough rolled at 850 °C, followed by immediate reheating to 1200 °C. This low roughing temperature of 850 °C was below the recrystallisation-stop temperature ( $T_{5\%}$ ) for each steel. The state of Nb (Nb in solution or Nb(CN) as a precipitate) was analysed as a function of holding time at this isothermal reheat temperature of 1200 °C, to establish the precipitate dissolution and austenite grain coarsening kinetics. Through a comparison of the two steels, the effect of Ti on the NbC precipitates and dissolution kinetics has been clarified.

## 5.2 The morphology of prior-austenite grain size

Specimens were examined following rough rolling at 850 °C and reheating at 1200 °C for various holding times. Optical micrographs, Figs. 5.1-5.3, reveal different prior-austenite grain morphologies as a function of process conditions and composition in the Nb and Nb-Ti steels.

### 5.2.1 Rough rolling microstructures

The average prior austenite grain size was first examined after rough rolling at 850 °C with the measurement in normal direction (ND) as  $18.7 \pm 1.6 \mu\text{m}$  in the Nb steel and  $16.9 \pm 0.7 \mu\text{m}$  in the Nb-Ti steel, shown in Fig. 5.1.

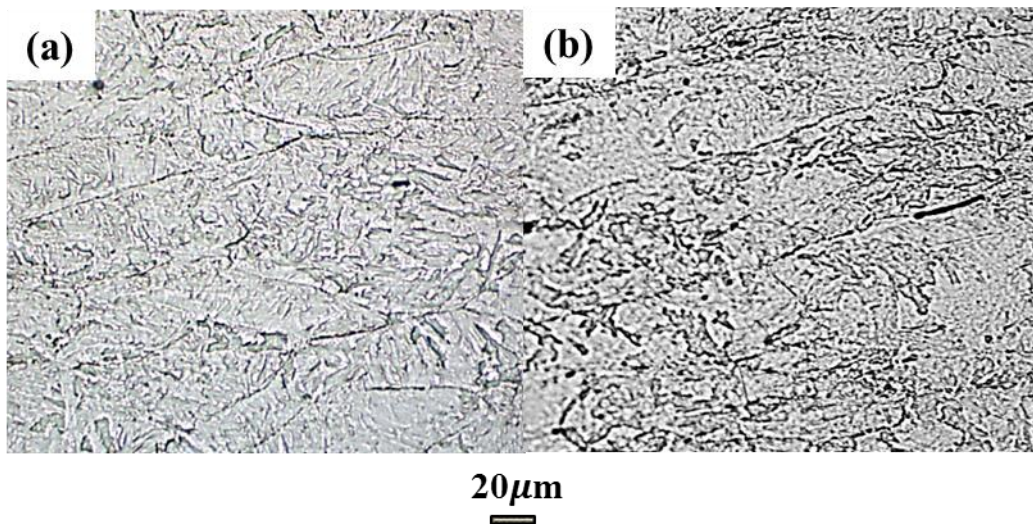


Fig. 5.1 Light micrographs illustrating the rough rolling prior-austenite grains: (a) Nb steel; (b) Nb-Ti steel.  
(Etched by picric acid)

## 5.2.2 Reheating microstructures

The deformed and reheated optical microstructures are presented in Figs. 5.2 and 5.3 for both the Nb and Nb-Ti steels, respectively.

### 5.2.2.1 Nb steel

Fig. 5.2 shows the samples reheated to 1200 °C with various isothermal holding times followed by an immediate quench, which exhibited a fully recrystallised prior-austenite grain structure in the Nb steel. The prior-austenite grains coarsened with increasing the isothermal holding times, as shown in Fig. 5.2 (b-f).

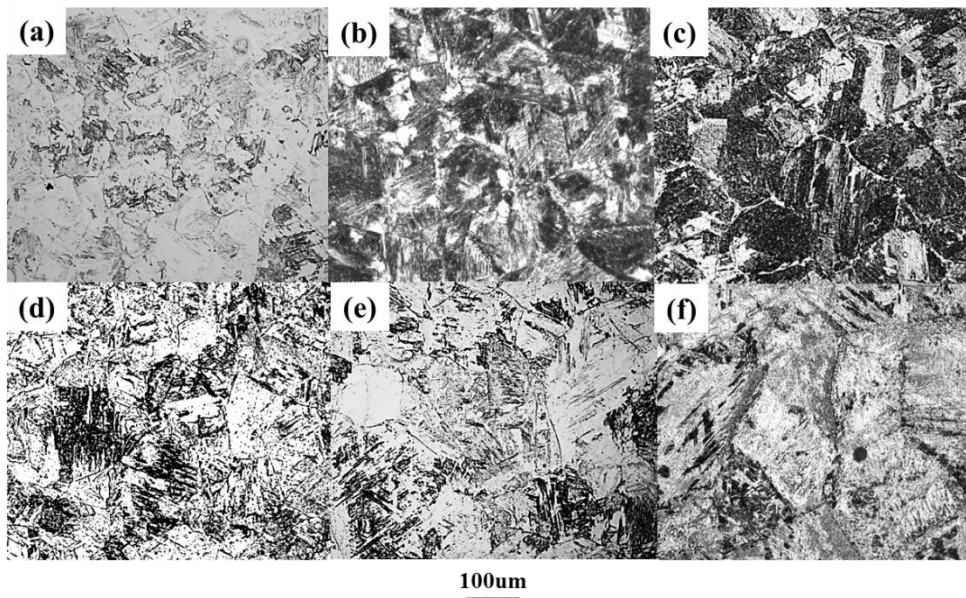


Fig. 5.2 Light micrographs illustrating prior-austenite structures with reheating at 1200 °C and holding for different times in Nb steel, (a) 0s, (b) 10s, (c) 20s, (d) 40s, (e) 100s, (f) 1000s. (Etched by picric acid)

### 5.2.2.2 Nb-Ti steel

The morphologies of prior-austenite grains for Nb-Ti steel are presented in Fig. 5.3, which was heat treated in the same way as the Nb steel. Full recrystallisation had occurred giving equiaxed prior-austenite grains during reheating to 1200 °C for various times followed by water quenching immediately. The prior-austenite grains coarsened with increasing isothermal holding times. The prior-austenite grain size in the Nb-Ti steel was smaller than that of the Nb steel, especially for the longer holding times at 1200 °C.

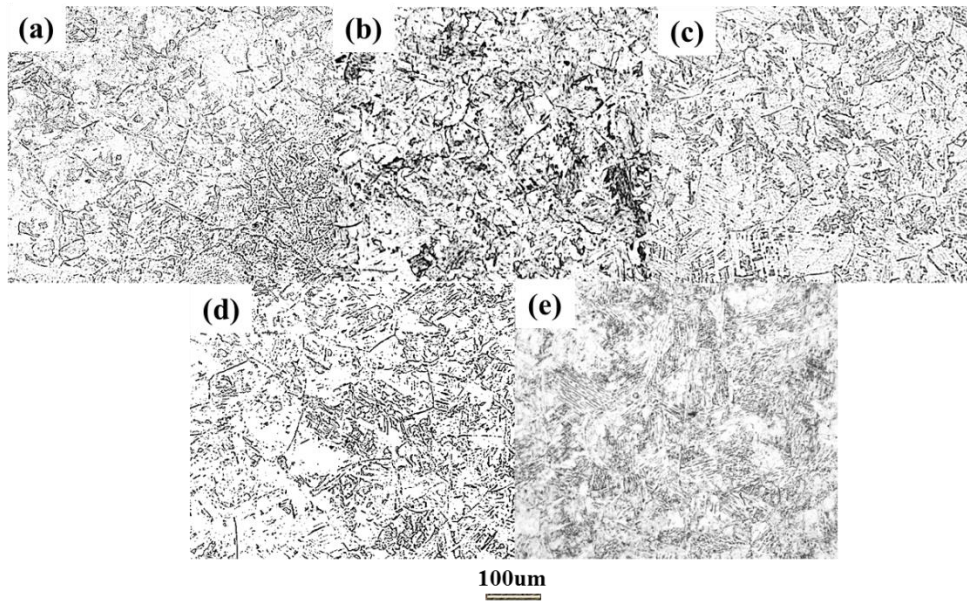


Fig. 5.3 Light micrographs illustrating prior-austenite structures with reheating at 1200 °C and holding for different times in Nb-Ti steel, (a) 0 s, (b) 10 s, (c) 40 s, (d) 100 s, (e) 1000 s. (Etched by picric acid)

### 5.3 Grain size measurements

The prior-austenite grain size was measured from optical micrograph using 8 images for each specimen and is shown in Table 5.1. The prior-austenite grain growth as a function of isothermal holding times was clear for both Nb and Nb-Ti steels. Figs. 5.2 (a) and 5.3 (a) show the samples reheated to 1200 °C followed by an immediate quench, with an average size of  $73.1 \pm 3.9 \mu\text{m}$  in the Nb steel and  $47.8 \pm 3.6 \mu\text{m}$  in the Nb-Ti steel. When the steels were held for 10 s at 1200 °C, the recrystallised structure coarsened slightly (Figs. 5.2 (b) and 5.3 (b)) with  $86.4 \pm 3.5 \mu\text{m}$  in the Nb steel and  $50 \pm 5.5 \mu\text{m}$  in the Nb-Ti steel. The prior-austenite grain size increased to  $109.7 \pm 2.9 \mu\text{m}$  at 20 s and  $120.5 \pm 3.9 \mu\text{m}$  at 40 s in the Nb steel, and  $64.5 \pm 2.5 \mu\text{m}$  at 40 s in the Nb-Ti steel. More grain growth occurred with an increase in holding time from 100 s to 1000 s, while the measurement of the average prior-austenite grain rapidly increased from  $141.3 \pm 5.3 \mu\text{m}$  to  $260.7 \pm 9.8 \mu\text{m}$  in the Nb steel, and from  $91.2 \pm 4.7 \mu\text{m}$  to  $112.4 \pm 5.4 \mu\text{m}$  in the Nb-Ti steel. Clearly the prior-austenite grain size of the Nb steel grew more rapidly during the reheating process compared to the Nb-Ti steel.

Table 5.1

The average prior-austenite grain size as a function of isothermal holding time in the Nb and Nb-Ti steels

Materials	Reheated Process	Average Grain Size ( $\mu\text{m}$ )
Nb Steel	1200 °C/0 s	73.1±3.9
	1200 °C/10 s	86.4±3.5
	1200 °C/20 s	109.7±2.9
	1200 °C/40 s	120.5±3.9
	1200 °C/100 s	141.3±5.3
	1200 °C/1000 s	260.7±9.8
Nb-Ti Steel	1200 °C/0 s	47.8±3.6
	1200 °C/10 s	50±5.5
	1200 °C/40 s	64.5±2.5
	1200 °C/100 s	91.2±4.7
	1200 °C/1000 s	112±5.4

## 5.4 TEM carbon extraction replicas

### 5.4.1. Rough rolling SIP

The morphologies of SIP have been observed by TEM with roughing at the temperature of 850 °C for Nb and Nb-Ti steels and are shown in Fig. 5.4. With a strain of 0.3 at a constant strain rate of  $10 \text{ s}^{-1}$ , nanoscale precipitates were observed in carbon replica samples.

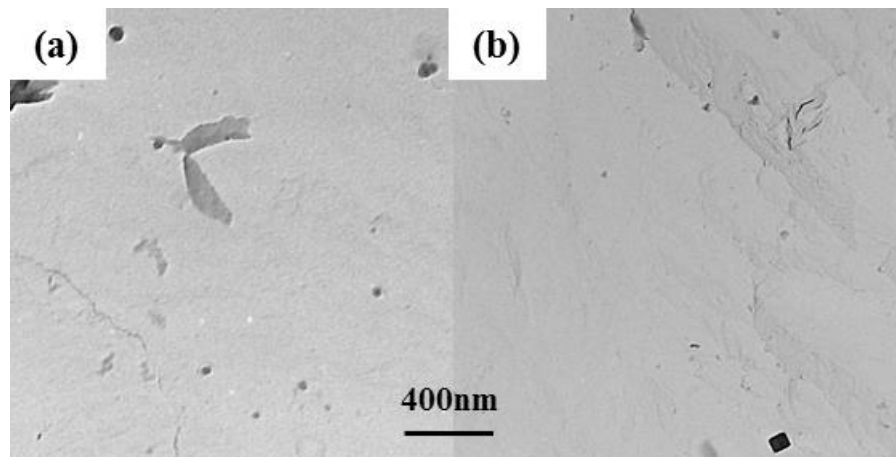


Fig. 5.4 TEM images of SIP after rough rolling at 850 °C followed by water quenching immediately, (a) Nb Steel, (b) Nb-Ti Steel.

## 5.4.2. Reheating SIP

After deformation at 850 °C followed by an immediate reheat to 1200 °C for different durations, the precipitate particle diameter, morphology and number density of precipitates were observed as a function of isothermal holding by TEM, shown in Figs 5.5-5.14 for both steels.

### 5.4.2.1 Nb steel

For the Nb steel, the results of the morphology and precipitate diameter distribution for different holding times are summarised in Figs. 5.5-5.9. The morphology of precipitates is shown in Figs. 5.5 (a)-5.9 (a). In Figs. 5.5 (b)-5.9 (b), the distribution of precipitates over the entire range was bimodal and the number density of precipitates reduced with increasing holding time, which was calculated from 10 bright field images for each sample. The precipitates continually dissolved into the austenite matrix during the whole reheating process. The average diameter of the precipitates initially increased from  $20 \pm 0.4$  nm to  $22 \pm 1.1$  nm at 10 s, followed by a continuous reduction from  $20.4 \pm 1.2$  nm at 20 s to  $16.4 \pm 1.8$  nm at a 100 s holding.

The fit curve for assumption of log-normal distribution was calculated from Eq. (5.1) [202], [203]:

$$y = \frac{1}{\sigma_g \sqrt{2\pi}} \exp \left[ -\frac{1}{2} \left( \frac{\ln D - \ln D_m}{\ln \sigma_g} \right)^2 \right] \quad (5.1)$$

where D is the set of the particles diameters,  $D_m$  is the mode and  $\sigma_g$  is the geometric standard deviation. The simulated size distribution of precipitates fits well with the results obtained from measurement performed on TEM images.

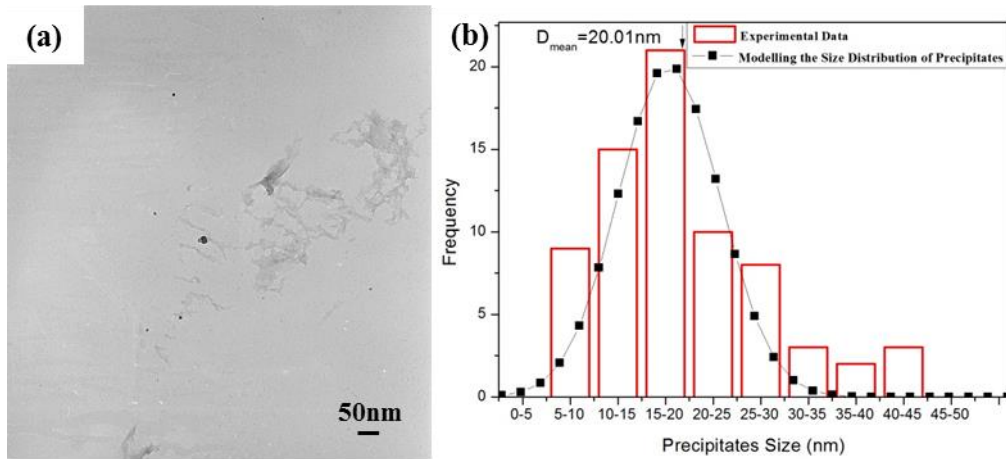


Fig. 5.5 Precipitates and the corresponding size distribution in specimen of Nb steel with rough rolling at 850 °C and reheated to 1200 °C followed by water quenching immediately, (a) TEM image showing spherical precipitates; (b) size distribution of precipitates from the same sample of (a).

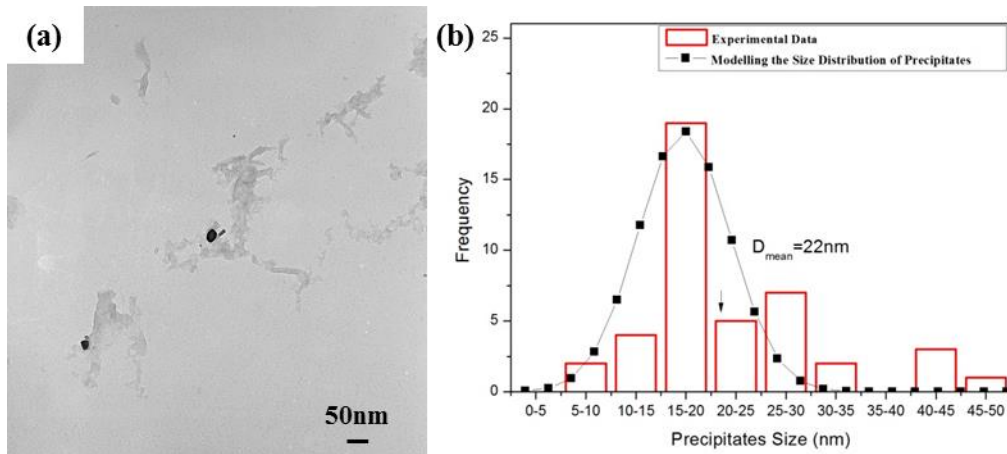


Fig. 5.6 Precipitates and the corresponding size distribution in specimen of Nb steel with rough rolling at 850 °C and reheated to 1200 °C for 10 s followed by water quenching, (a) TEM image showing spherical precipitates; (b) size distribution of precipitates from the same sample of (a).

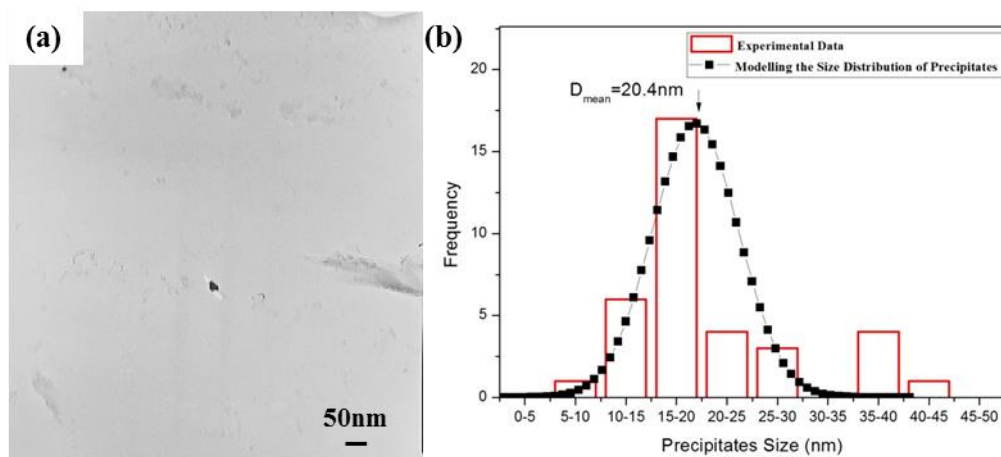


Fig. 5.7 Precipitates and the corresponding size distribution in specimen of Nb steel with rough rolling at 850 °C and reheated to 1200 °C for 20 s followed by water quenching, (a) TEM image showing spherical precipitates; (b) size distribution of precipitates from the same sample of (a).

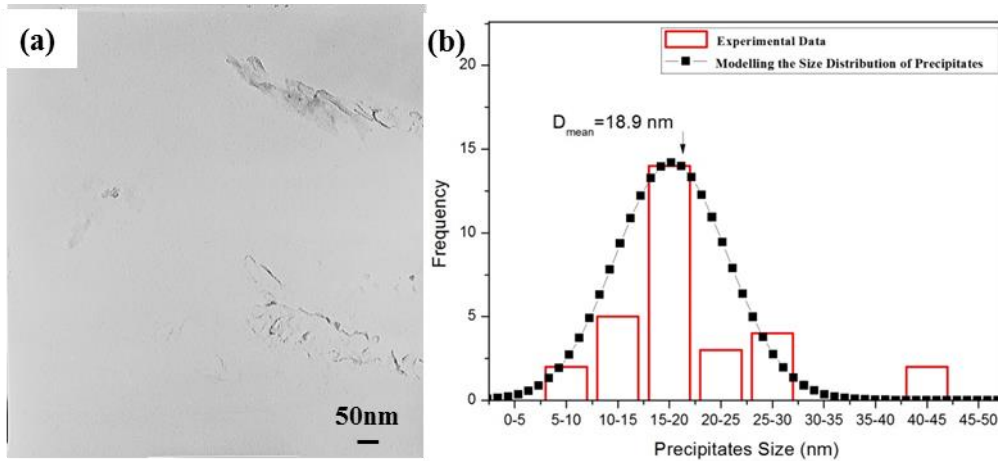


Fig. 5.8 Precipitates and the corresponding size distribution in specimen of Nb steel with rough rolling at 850 °C and reheated to 1200 °C for 40 s followed by water quenching, (a) TEM image showing spherical precipitates; (b) size distribution of precipitates from the same sample of (a).

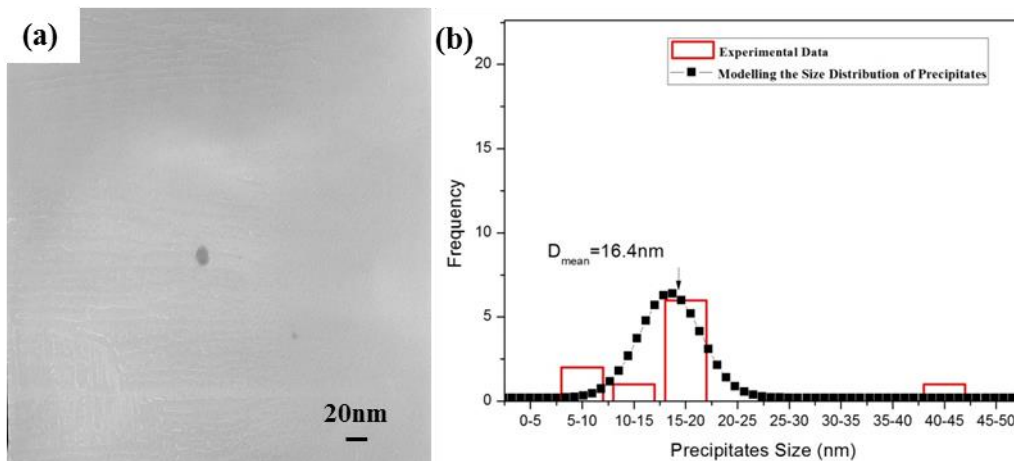


Fig. 5.9 Precipitates and the corresponding size distribution in specimen of Nb steel with rough rolling at 850 °C and reheated to 1200 °C for 100 s followed by water quenching, (a) TEM image showing spherical precipitates; (b) size distribution of precipitates from the same sample of (a).

#### 5.4.2.2 Nb-Ti steel

For the Nb-Ti steel, the effect of the reheating process on the morphology and the size distribution of precipitates was analysed from TEM images shown in Figs. 5.10-5.14. The precipitates changed to a cubic morphology, believed to be due to the Ti content of these particles (Figs. 5.10 (a)-5.14 (a)). The average diameter of the particles increased over the entire period. The average size of precipitates was  $31.0 \pm 2.5$  nm at the beginning, and then increased to  $32.4 \pm 2.4$  nm after holding for 10 s at 1200 °C. With continually increasing the isothermal holding time, the mean size of precipitates coarsened to  $34.2 \pm 3.1$  nm at 40 s and  $38.9 \pm 6.2$  nm at 100 s. Finally, the average size of precipitates was  $46.8 \pm 3.9$  nm for a hold of 1000 s at 1200 °C.

The precipitate diameter distribution for different holding times are summarised in Figs. 5.10(b)-5.14 (b) for the Nb-Ti steels. In the Nb-Ti steel, the precipitates were divided into two groups, i.e. precipitates with diameters less than about 30 nm and those with a diameter greater than about 30 nm. It can be seen that the distribution of particles with the diameter less than ~30 nm is unimodal with the number of precipitates decreasing with increasing holding time. For precipitate diameters greater than ~30 nm, the peak value of the distribution moves from 30 nm after 0 s and 10 s to 50 nm after 40 s, up until 100 nm after holding to 100 s and 1000 s.

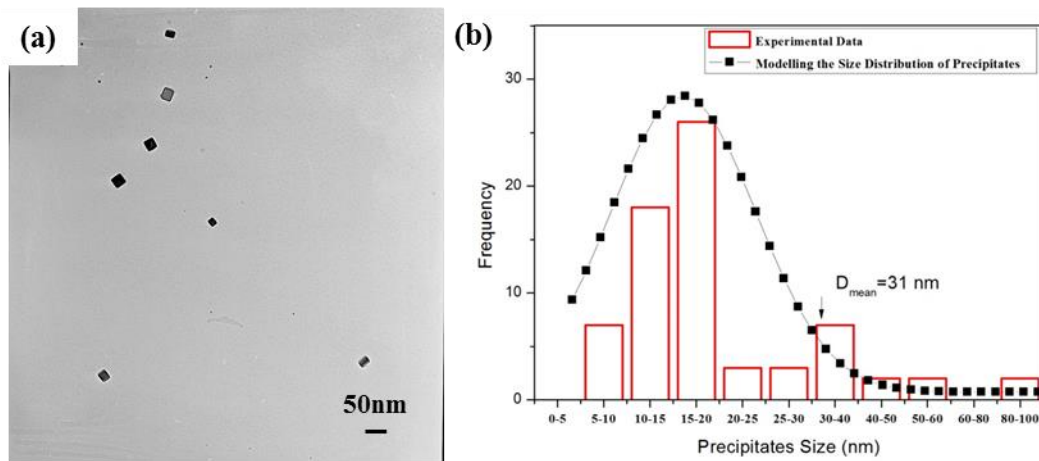


Fig. 5.10 Precipitates and the corresponding size distribution in specimen of Nb-Ti steel with rough rolling at 850 °C and reheated to 1200 °C followed by water quenching immediately, (a) TEM image showing cubic-shaped precipitates; (b) size distribution of precipitates from the same sample of (a)

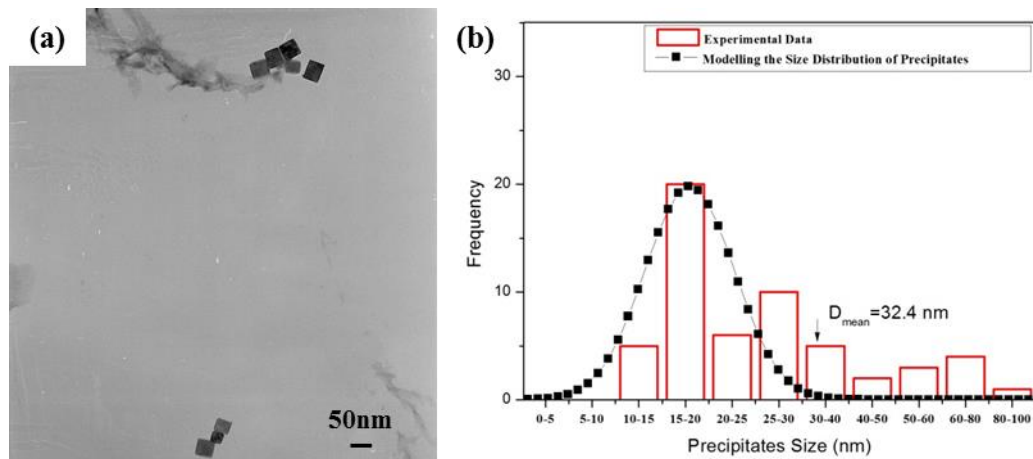


Fig. 5.11 Precipitates and the corresponding size distribution in specimen of Nb-Ti steel with rough rolling at 850 °C and reheated to 1200 °C for 10 s, (a) TEM image showing cubic-shaped precipitates; (b) size distribution of precipitates from the same sample of (a).

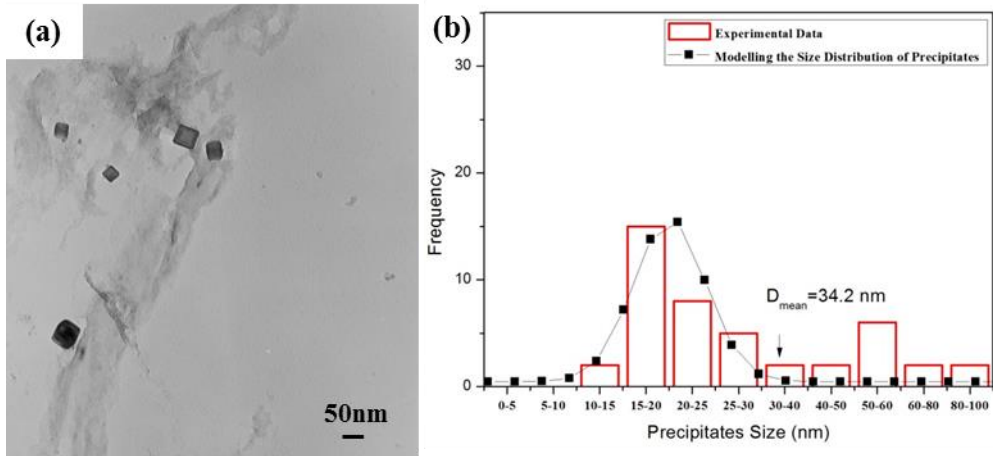


Fig. 5.12 Precipitates and the corresponding size distribution in specimen of Nb-Ti steel with rough rolling at 850 °C and reheated to 1200 °C for 40 s, (a) TEM image showing cubic-shaped precipitates; (b) size distribution of precipitates from the same sample of (a).

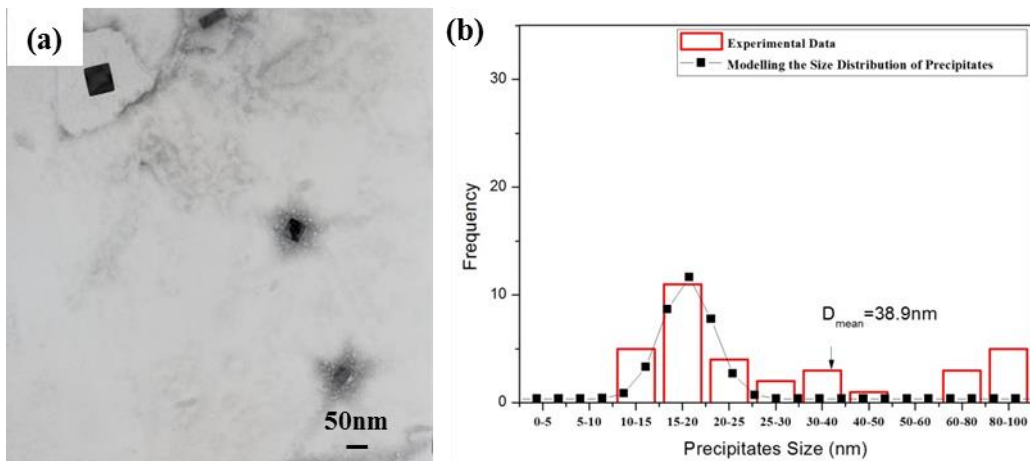


Fig. 5.13 Precipitates and the corresponding size distribution in specimen of Nb-Ti steel with rough rolling at 850 °C and reheated to 1200 °C for 100 s, (a) TEM image showing cubic-shaped precipitates; (b) size distribution of precipitates from the same sample of (a).

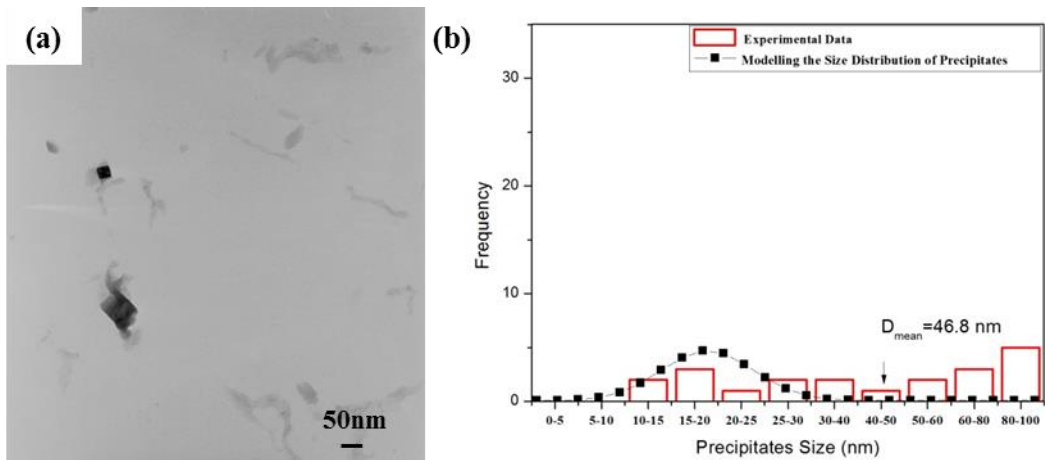


Fig. 5.14 Precipitates and the corresponding size distribution in specimen of Nb-Ti steel with rough rolling at 850 °C and reheated to 1200 °C for 1000 s, (a) TEM image showing cubic-shaped precipitates; (b) size distribution of precipitates from the same sample of (a).

To summarise, there appeared to be a difference in behaviour of the two steels. In the Nb-Ti steel, coarsening of the precipitates was dominant. In contrast, in the Nb steel, after initial coarsening, dissolution of the precipitates occurred during isothermal heat treatment at 1200 °C.

## 5.5 Precipitate morphology and chemistry

The composition of precipitates was identified by TEM, EDX and EELS spectra and is presented in Figs. 5.15-5.27 for Nb and Nb-Ti steels. The EDX was good at identifying higher atomic number elements, such as Nb, while EELS was used to observe the light elements, such as N and C. To analyse the effect of reheating process on the composition of precipitates, the particles were separated into two groups. The first group includes the size of precipitates less than 10 nm and the second group has the size of precipitates larger than 10 nm for both Nb and Nb-Ti steels.

### 5.5.1. Nb steel

After deformation at 850 °C followed by a rapid reheat to 1200 °C for different times followed by an immediate water quench, the morphology of the precipitates was examined by TEM (HRTEM), and the composition of these precipitates was investigated by EDX and EELS, Figs. 5.15-5.19. The round-shaped precipitates with the size less than 10 nm shown in Figs. 5.15 and 5.17 were confirmed by TEM, EDX and EELS analysis to be NbC with the measured spacing equal to 0.253 nm from the fast Fourier transformed diffractogram and presented the Nb K and L lines from EDX spectrum.

Figs. 5.16 and 5.18 show the precipitates with the size larger than 10 nm, which were shown to be Nb(CN) by the the C K-, Nb M- and N K-edges in EELS spectra shown in Fig. 5.16 (d) and 5.18 (d) after subtraction of the background preceding the C K-edge. The EDX spectrum taken from those particles is shown in Figs. 5.16 (c) and 5.18 (c) with the Nb L and K lines. Even after holding for 100 s at 1200 °C, there were still NbC present (Fig. 5.19 (a) and (b)). There were particles with a size larger than 10 nm at 100 s, Fig 5.19 (b), which did not contain nitrogen due to the long-time holding at 1200 °C.

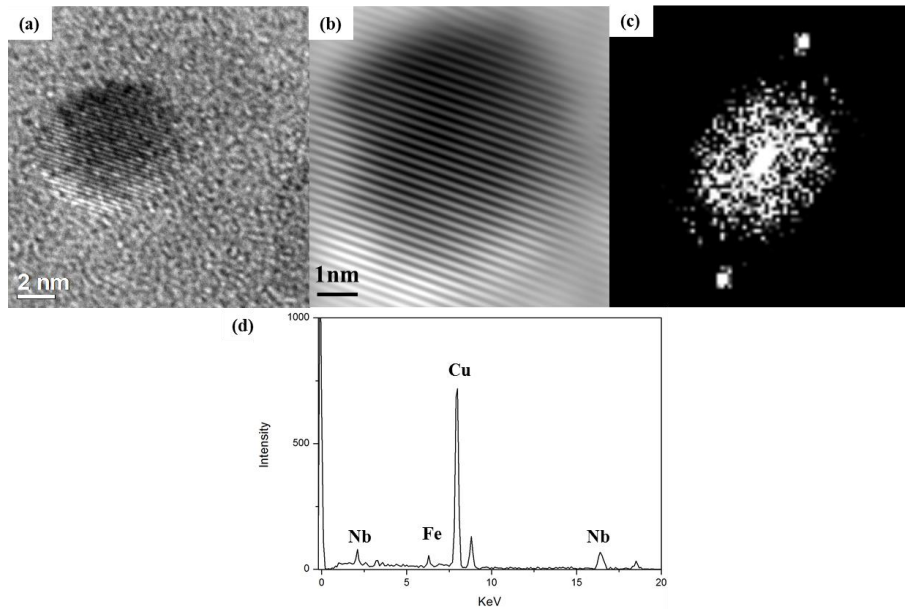


Fig. 5.15 NbC in the Nb steel isothermally held at 1200 °C followed by water quenching immediately, (a) HRTEM image of NbC; (b) IFFT image of the precipitate shown in (a); (c) the corresponding fast Fourier transformed diffractogram of (a); (d) EDX spectra indicated in (a).

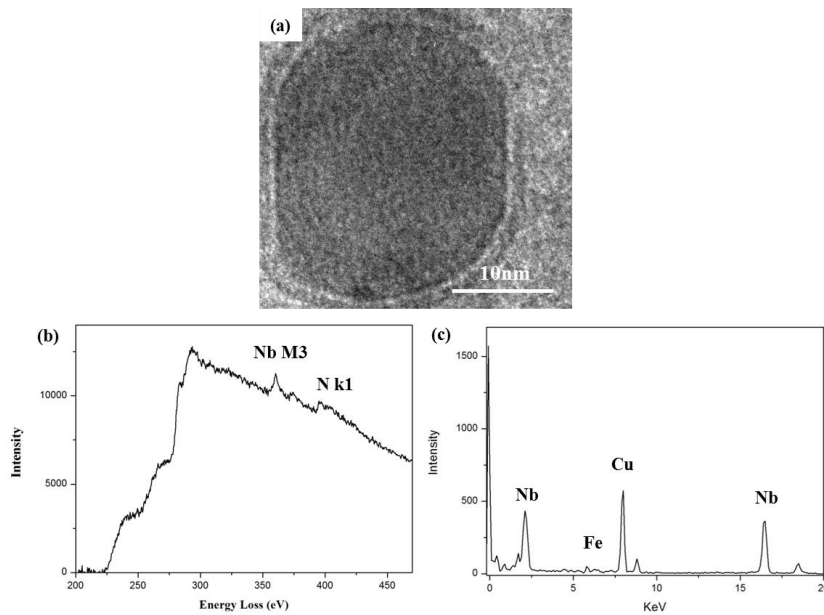


Fig. 5.16 Nb(CN) with the size larger than 20 nm in the Nb steel isothermally held at 1200 °C followed by water quenching immediately, (a) TEM image of Nb(CN); (b) EELS spectrum indicated in (a); (c) EDX spectra indicated in (a).

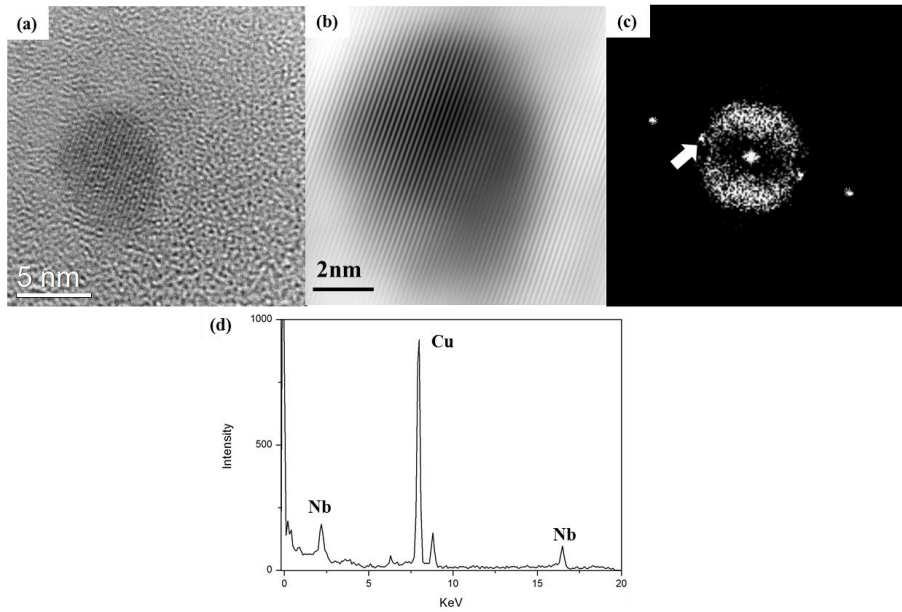


Fig. 5.17 NbC in the Nb steel isothermally held at 1200 °C for 10 s followed by water quenching, (a) HRTEM image of NbC; (b) IFFT image of the precipitate shown in (a); (c) the corresponding fast Fourier transformed diffractogram of (a); (d) EDX spectra indicated in (a).

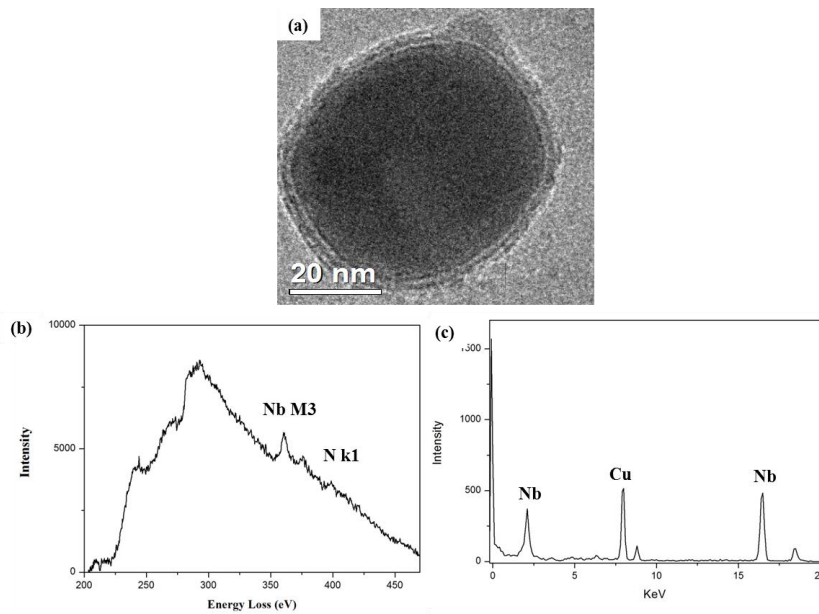


Fig. 5.18 Nb(CN) with the size larger than 20 nm in the Nb steel isothermally held at 1200 °C for 10 s followed by water quenching, (a) TEM image of Nb(CN); (b) EELS spectrum indicated in (a); (c) EDX spectra indicated in (a).

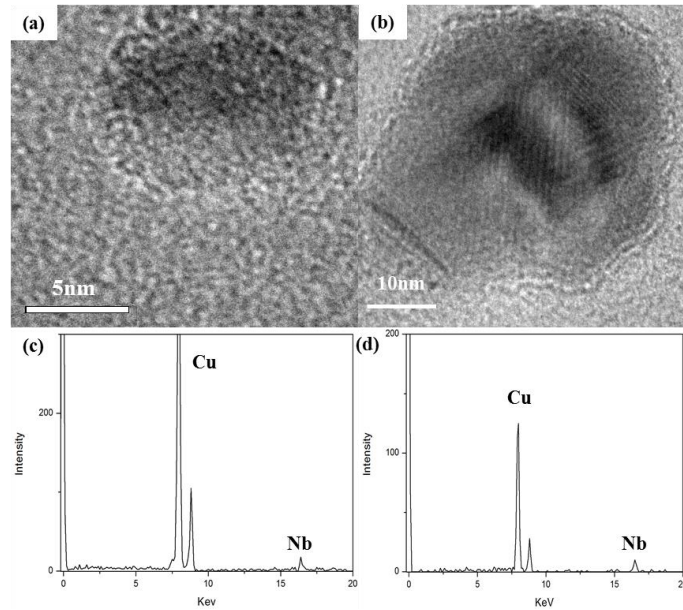


Fig. 5.19 NbC in the Nb steel isothermally held at 1200 °C for 100 s followed by water quenching, (a) TEM image of NbC with the size less than 10 nm; (b) TEM image of NbC with the size larger than 10 nm; (c) EDX spectra indicated in (a); (d) EDX spectra indicated in (b).

### 5.5.2. Nb-Ti steel

For Nb-Ti steel, after deformation at 850 °C followed by a rapid reheat to 1200 °C for different times, and then an immediate water quench, the morphologies of precipitates were investigated by TEM (HRTEM), EDX and EELS, Figs. 5.20-5.24. Fig. 5.20 gives a particle typical of those <10 nm, which was shown to be (Ti,Nb)C, with no N K-edge present in the EELS spectrum. The second type of precipitates with the size larger than 10 nm shown in Figs. 5.21-5.24 are detected to be (Ti,Nb)(C,N) by EELS and EDX spectrums. The background in the EELS spectrum has been subtracted showing the presence of the Ti L- and N K-edge (Figs. 5.21 (b), 5.22 (b), 5.23 (b) and 5.24 (b)) and the Nb and Ti lines are present in Figs. 5.21 (c), 5.22 (c), 5.23 (c) and 5.24 (c) in EDX spectra.

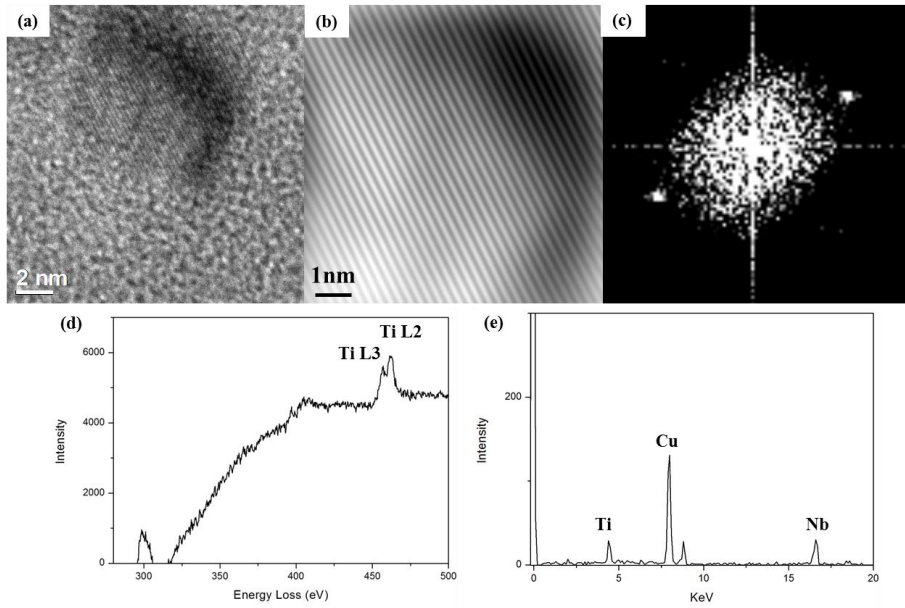


Fig. 5.20 (Nb, Ti)C with the size less than 10 nm in the Nb-Ti steel isothermally held at 1200 °C followed by water quenching immediately, (a) HRTEM image of (Nb, Ti)C; (b) IFFT image of the precipitate shown in (a); (c) the corresponding fast Fourier transformed diffractogram of (a); (d) EELS spectrum indicated in (a); (e) EDX spectra indicated in (a).

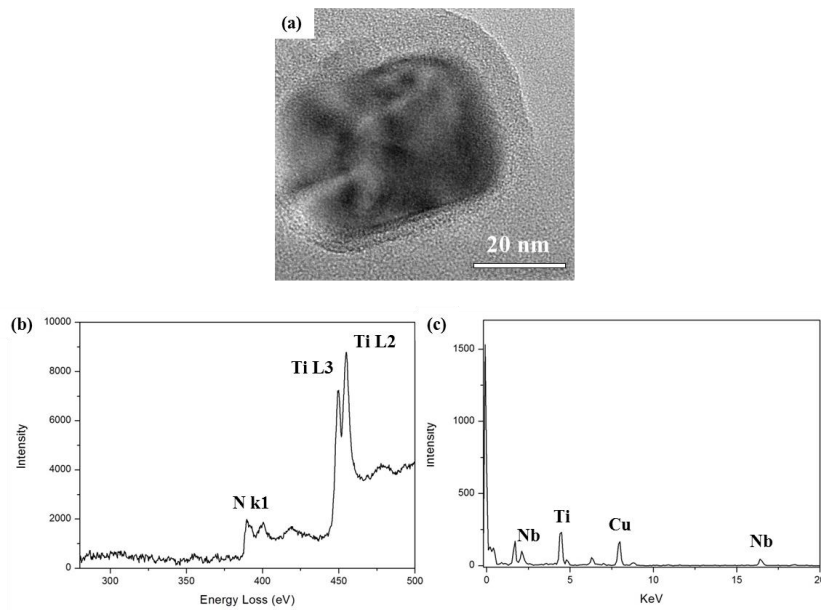


Fig. 5.21 (Nb,Ti)(C,N) with the size larger than 10 nm in the Nb-Ti steel isothermally held at 1200 °C followed by water quenching immediately, (a) TEM image of (Nb,Ti)(C,N); (b) EELS spectrum indicated in (a); (c) EDX spectra indicated in (a).

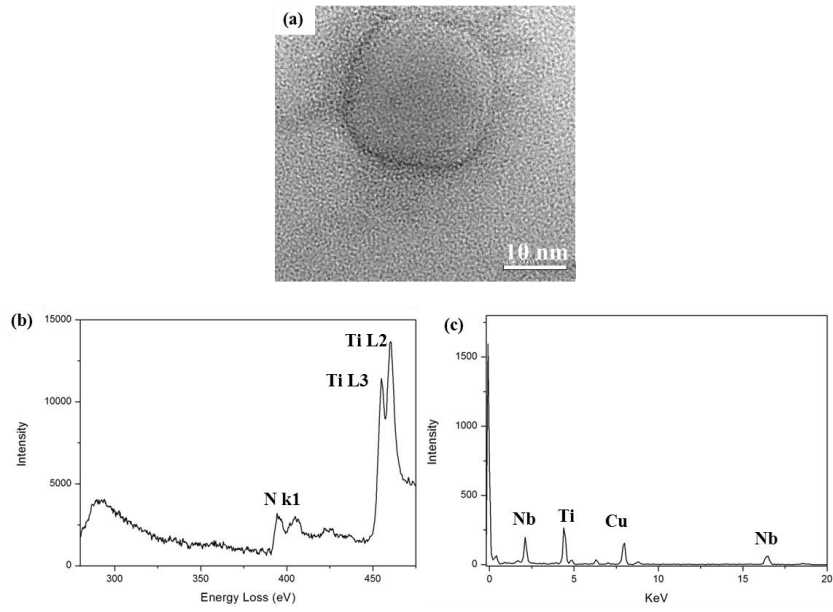


Fig. 5.22 (Nb,Ti)(C,N) in the Nb-Ti steel isothermally held at 1200 °C for 10 s followed by water quenching, (a) TEM image of (Nb,Ti)(C,N); (b) EELS spectrum indicated in (a); (c) EDX spectra indicated in (a).

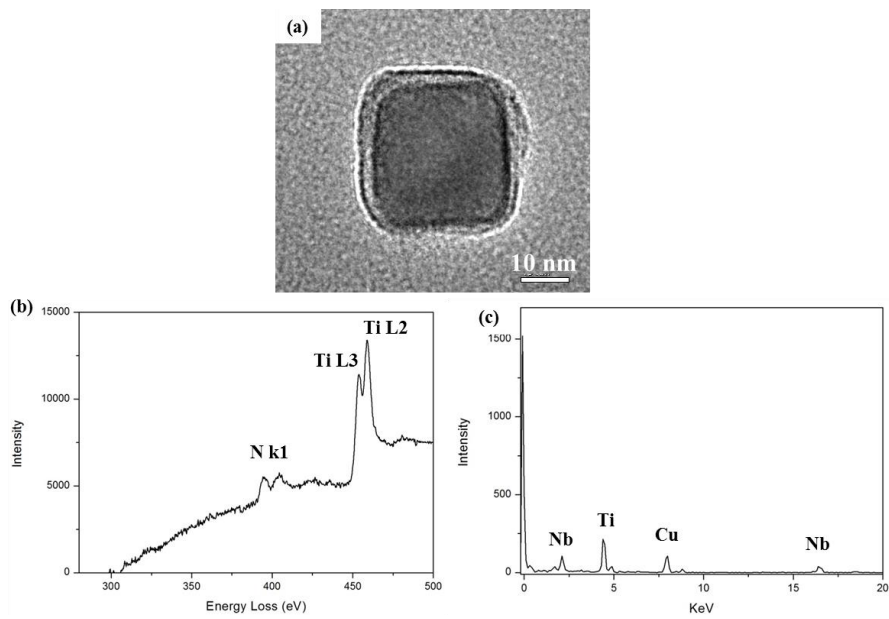


Fig. 5.23 (Nb,Ti)(C,N) in the Nb-Ti steel isothermally held at 1200 °C for 100 s followed by water quenching, (a) TEM image of (Nb,Ti)(C,N); (b) EELS spectrum indicated in (a); (c) EDX spectra indicated in (a).

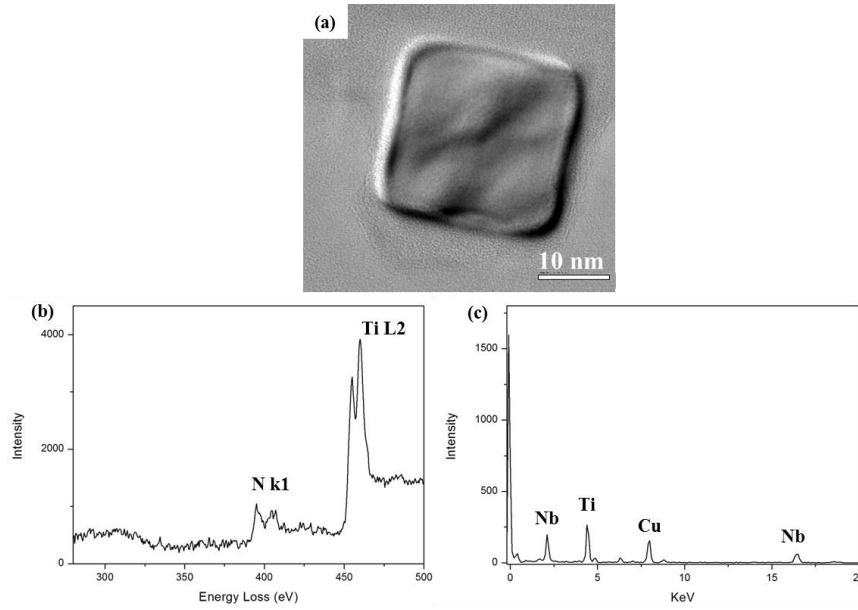


Fig. 5.24 (Nb,Ti)(C,N) in the Nb-Ti steel isothermally held at 1200 °C for 1000 s followed by water quenching, (a) TEM image of (Nb,Ti)(C,N); (b) EELS spectrum indicated in (a); (c) EDX spectra indicated in (a).

## 5.5 The solid solution of microalloyed elements during isothermal holding

### 5.5.1 The content of Nb in solid solution

The volume fraction of precipitates determined by TEM replica results are shown in Table 5.2. It is clear that the volume fraction of precipitates decreases with increasing isothermal holding times at 1200 °C. The amount of Nb in solution can be expressed by incorporating the experimentally measured volume fraction of precipitates using Eq. (5.2) [20,194,195,204].

$$f(t) = \left[ \frac{\rho_r}{\rho_{precipitate}} \times \left( \frac{Z+1}{Z} \right) \right] \times (W_m - [Nb]) \quad (5.2)$$

$$Z = \{Nb\} / \{C\} \quad (5.3)$$

where  $f(t)$  is volume fraction of precipitates coordinated with holding times;  $\rho_r$  and  $\rho_{precipitate}$  are the densities of the austenite and that of the precipitates, respectively;  $W_m$  is the total atomic weight of microalloyed elements in each steel;  $[Nb]$  is Nb in solution;  $\{Nb\}$  and  $\{C\}$  are the Nb and C in precipitates as NbC at equilibrium. The data for Nb in solution is shown in Table 5.2.

Table 5.2

Data from carbon extraction replicas results for Nb and Nb-Ti steels showing the volume fraction of precipitates and the amount of [Nb] (Nb in solution) under different holding times at 1200 °C

Materials	Reheating Temperature (°C)	Time (s)	Diameter (nm)	Volume Fraction of Precipitates ( $10^{-5} \mu\text{m}^{-3}$ )	[Nb] (wt%)
Nb Steel	1200	0	20.0±0.4	13.5±1.6	0.018±0.001
		10	21.8±1.1	9.8±1.4	0.021±0.001
		20	20.4±1.2	7.2±0.7	0.024±0.0006
		40	19±0.4	4.8±0.5	0.026±0.0004
		100	16.4±1.8	1.0±0.6	0.029±0.0006
Nb-Ti Steel	1200	0	31±0.8	60.4±2.9	0.007±0.001
		10	32.4±1.2	53.6±1.7	0.012±0.0012
		40	34.2±1.8	47.7±3.1	0.015±0.0028
		100	39±1.2	46.7±4.3	0.0165±0.003
		1000	46.8±1.6	34.6±3.2	0.025±0.0023

For the Nb steel, most of the Nb (0.029 wt%) was dissolved into the matrix after holding for 100 s. However, the amount of Nb in solution was only 0.0165 wt% at the same holding time for the Nb-Ti steel. From the data shown in Table 5.2, it can be inferred that the presence of Ti increases the thermodynamic stability of the Nb(CN) at this temperature, thus suppressing the dissolution kinetics.

#### 5.5.2 Ti/(Ti+Nb) ratio from precipitation in the Nb-Ti steel

For the Nb-Ti steel, the effect of Ti on the dissolution behaviour of Nb based complex carbonitrides during the reheating process at 1200 °C with different holding times was investigated using EDX to identify the Ti/(Ti+Nb) ratio with the mean Ti/(Ti+Nb) value obtained from over 30 precipitates for each specimen. The results are listed in Table 5.3 and Fig. 5.25, as a function of holding times. It is clear that the ratio of Ti/(Ti+Nb) in the Nb-Ti steel increased with the increasing holding times at 1200 °C. After rough rolling at 850 °C and reheating to 1200 °C followed by immediate water quenching, the atomic ratio of

Ti/(Ti+Nb) was only 0.42 at%, which means that most of the precipitates are Nb-rich carbonitrides. Then after a hold for 10 s at 1200 °C, the ratio of Ti/(Ti+Nb) rapidly increased to 0.77 at% and the precipitates therefore became Ti-rich carbonitrides. Increasing the holding time to 100 s, the ratio of Ti/(Ti+Nb) increased to 0.82 at%. Then, the ratio of Ti/(Ti+Nb) became constant and only slightly increased to 0.88 at% at 1000 s during the isothermal holding. Furthermore, the atomic ratio of Ti/(Ti+Nb) was also calculated from the volume fraction of precipitates using the Eq. (5.2) and is shown in Table 5.3 and Fig. 5.25 as well. The calculated ratio also increased with increasing isothermal holding times, with 0.63 at% at 0 s, 0.68 at% at 10 s and 0.74 at% at 100 s, as well as 0.89 at% at 1000 s. The atomic ratio of Ti/(Ti+Nb) from calculation using Eq. (5.2) fits well with that of the EDX data.

**Table 5.3**  
The ratio of Ti to (Ti+Nb) in the precipitates in the Nb-Ti steel

Methods	Reheating Temperature (°C)	Time (s)	Ti/(Ti+Nb) ratio (atom %)
EDX	1200	0	0.42
		10	0.77
		100	0.82
		1000	0.88
Calculated Data	1200	0	0.63
		10	0.68
		100	0.74
		1000	0.89

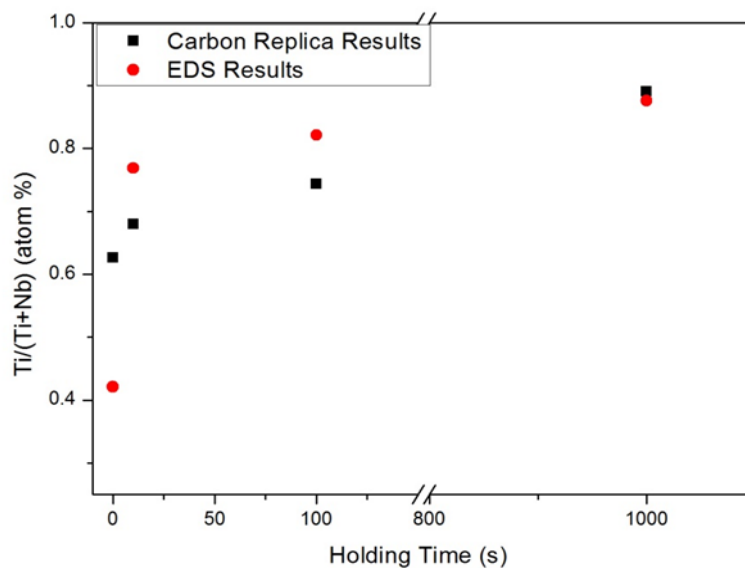


Fig. 5.25 The ratio of Ti to (Ti+Nb) in the precipitates in Nb-Ti steel obtaining from EDX and carbon replica data.

## 5.6 Vickers micro-hardness

The Vickers micro-hardness values of rough rolled and reheated steels were measured and listed in Fig. 5.26. The micro-hardness increased with increasing holding times in both Nb and Nb-Ti steels. At 0 s, the micro-hardness was  $209.5 \pm 4.6$  Hv in the Nb steel and  $196.9 \pm 3.3$  Hv in the Nb-Ti steel, which were similar to the rough rolling micro-hardness with  $205.7 \pm 2.6$  Hv in the Nb steel and  $198.2 \pm 3.6$  Hv in the Nb-Ti steel. The micro-hardness increased rapidly to  $239.9 \pm 3.9$  Hv at 10 s in the Nb steel. However, the micro-hardness in the Nb-Ti steel increased only slightly to  $210.6 \pm 3.3$  Hv at the same holding time with Nb steel. After an initial rapid increase, the rate of increase slowed down for holding time of 100 s for both steels. For the Nb steel, the micro-hardness slightly increased to  $246.5 \pm 8.3$  Hv, and for Nb-Ti steel it was  $218.9 \pm 9.0$  Hv. Finally, after holding for 1000 s at 1200 °C, the micro-hardness increased to  $251.8 \pm 6.9$  Hv in the Nb steel and  $233 \pm 4.3$  Hv in the Nb-Ti steel.

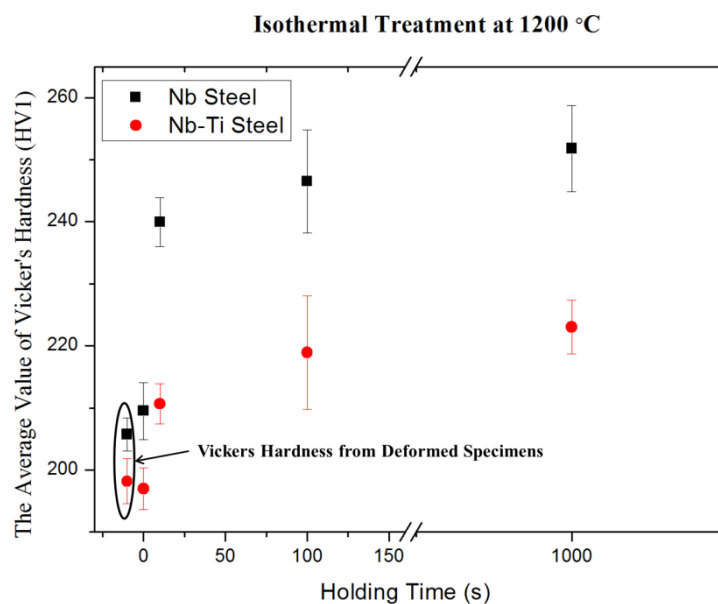


Fig. 5.26 The average value of Vickers micro-hardness in the Nb and Nb-Ti steels.

## 5.7 Summary

Following rolling at 850 °C and subsequent isothermal heating at 1200 °C for various times, the prior-austenite grains, for both Nb and Nb-Ti steels, became equiaxed after the temperature was rapidly increased to 1200 °C, because full recrystallisation occurred. Then, grain growth occurred, an inevitable effect of the reduced pinning force of precipitates on the grain boundaries. The rate of grain growth was less for the Nb-Ti steel than the Nb steel

because of the higher temperature stability of the (Ti, Nb)C or (Ti, Nb)(C, N) than the NbC or Nb(C, N).

The average diameter of the Nb precipitates in the Nb steel initially coarsen up to 10 s hold, but then decreased as they dissolved into the matrix. However, the (Ti, Nb)C and (Ti, Nb)(C, N) particles in the Nb-Ti steel exhibited continuous coarsening over the duration of the holding period. The dissolution rate of Nb in the Nb steel was much quicker than that in the Nb-Ti steel. The Nb continually dissolved into the austenite during reheating in both the Nb and Nb-Ti steels.

For the Nb-Ti steel, the ratio of Ti/(Ti+Nb) increased during the entire holding period (Fig. 5.25), with the precipitates changing from Nb-rich to Ti-rich. The reheating temperature of 1200 °C is higher than the equilibrium temperature of NbC and Nb(C,N), but there was still Nb present in the Nb steel after holding for 100 s at 1200 °C and in the Ti carbonitride, even after holding for 1000 s at 1200 °C.

The Vickers micro-hardness increased with increasing isothermal holding times in both the Nb and Nb-Ti steels. The effect of solid solution from the microalloyed elements on micro-hardness was significantly higher than the negative effect of increasing grain size and dissolution of precipitates.

## CHAPTER 6: FINISH ROLLING IN STEELS MICROALLOYED WITH NIOBIUM

### 6.1 Introduction

A new type of thermomechanical control process (TMCP), which consists of rough rolling at 850 °C, reheating at 1200 °C for different durations, and then finish rolling at 850 °C, was analysed in this study to obtain an ultra-fine microstructure through deformation-induced ferrite transformation (DIFT). This should yield an excellent combination of strength and impact toughness properties for microalloyed steels. Moreover, with adding a high temperature heat treatment between rough and finish rolling, it provides a wide range of the finish rolling temperatures. The higher the finish rolling temperature is, the lower the load requirement on the rolling equipment. Therefore, the new type of rolling process conquered the limitations of thermomechanical control rolling, such as high load requirement and low productivity. In this chapter, the microstructures and the SIP behaviour have been analysed after processing by the new TMCP. Then, the effect of the non-equilibrium temperature heat treatment and finish rolling parameters on the DIFT microstructure has been analysed through the nucleation and phase transformation kinetics.

### 6.2 Characterisation of the microstructures by OM and SEM

#### 6.2.1. Morphology of the prior-austenite grains and the DIFT

Optical micrographs revealed the typical prior-austenite grain morphologies when etched by picric acid after finish rolling at 850 °C for the Nb and Nb-Ti steels. Then, the 2% nitric acid was used for etching the ferrite second phase. However, OM has its limitation to analyse the complexity of the multiphase microstructure. Therefore, to capture more details of the features, SEM was used in this study as well. All the microstructures of the austenite grains and DIFT are shown in Figs. 6.1-6.16.

##### 6.2.1.1 Nb steel

1) The finish rolling schedules A-10, B-10, C-10 and D-10 corresponding to a heat treatment at 1200 °C for 10 s

In this section, the specimens from the Nb steel were heat treatment at 1200 °C hold for 10 s. The finish rolling schedules consisted of A-10, B-10, C-10 and D-10 as shown in Fig. 3.5. The microstructure of prior-austenite grains and the second phase of DIFT are shown in Figs.

6.1-6.4. For the Nb steel, the average grain size was refined with increasing strain, and the isothermal 10 s holding after deformation at 850 °C. DIFT was located mainly on the prior austenite grain boundaries. The morphology of the DIFT and martensite after finish rolling for schedule A-10 was similar to the other schedules of B-10, C-10 and D-10.

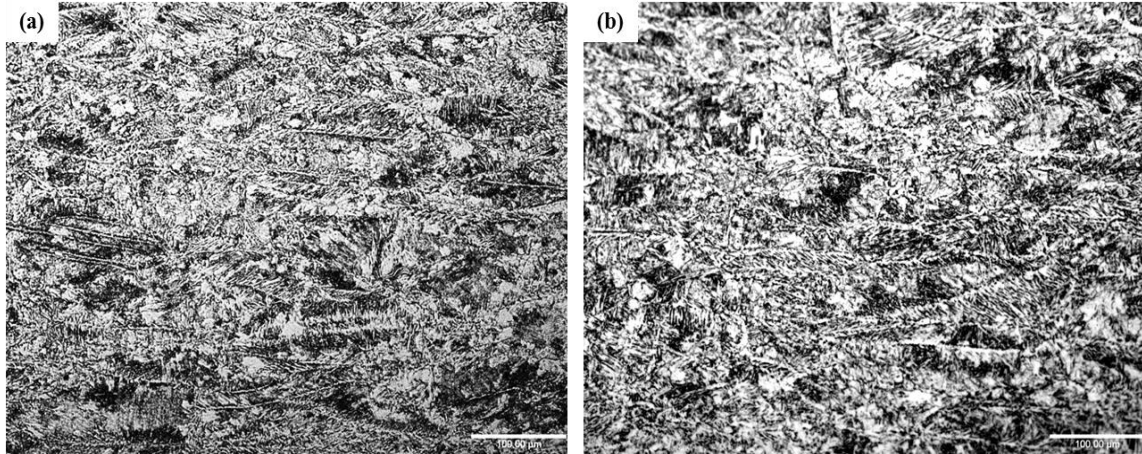


Fig. 6.1 OM of prior austenite grains in the Nb steel after reheating to 1200 °C for 10 s and finish rolling at 850 °C with 0.3 strain, (a) WQ immediately (A-10); (b) hold for 10 s+WQ (B-10) (Etched by picric acid).

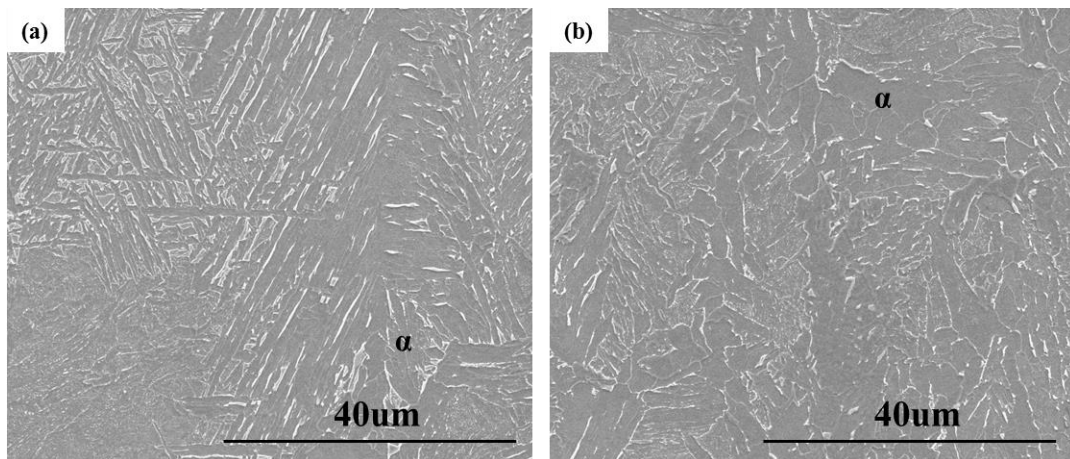


Fig. 6.2 SEM observation of DIFT for Nb steel after finish rolling with the rolling schedule A-10 and B-10, (a) WQ immediately (A-10); (b) hold for 10 s+WQ (B-10) (Etched by 2% 2 % nitric acid).

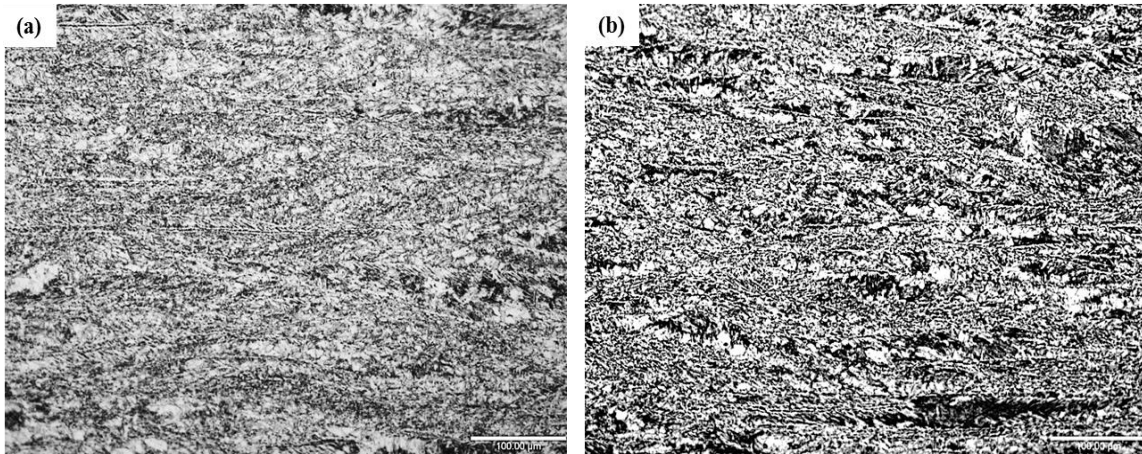


Fig. 6.3 OM of prior austenite grains in the Nb steel after reheating to 1200 °C for 10 s and finish rolling at 850 °C with 0.6 strain, (a) WQ immediately (C-10); (b) hold for 10 s+WQ (D-10) (Etched by picric acid).

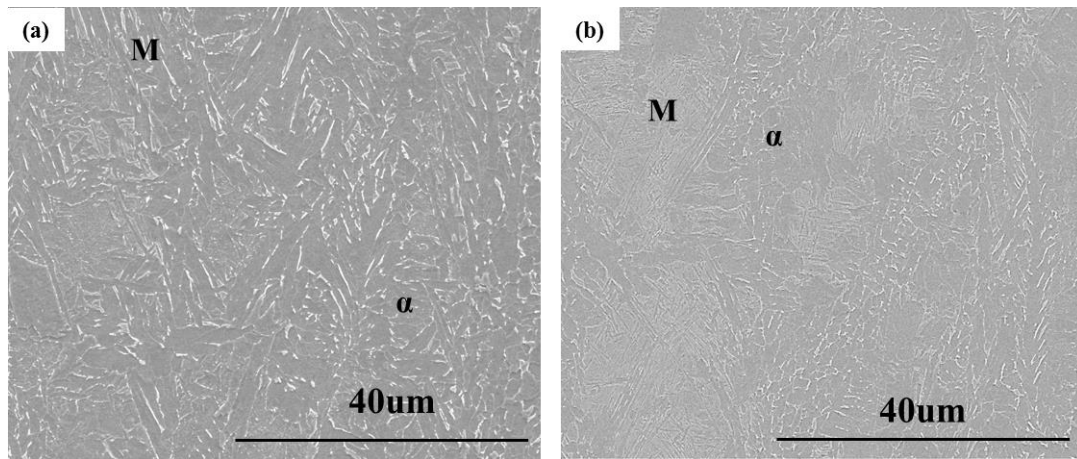


Fig. 6.4 SEM observation of DIFT for Nb steel after finish rolling with the rolling schedule C-10 and D-10, (a) WQ immediately (C-10); (b) hold for 10 s+WQ (D-10) (Etched by 2% 2 % nitric acid).

2) Finish rolling schedules A-100, B-100, C-100 and D-100 corresponding to heat treatment at 1200 °C for 100 s

The specimens from the Nb steel were heat treated at 1200 °C for 100 s. The finish rolling schedules A-100, B-100, C-100 and D-100 were shown in Fig. 3.5. The microstructures of the prior-austenite grains and the second phase of DIFT are shown in Figs. 6.5-6.8. The average grain size was refined with increasing strain, and the isothermal 10 s holding after deformation at 850°C. DIFT was located mainly on the prior austenite grain boundaries. The morphology of DIFT and martensite after finish rolling with other schedules of B-100, C-100 and D-100 are similar to that at A-100.

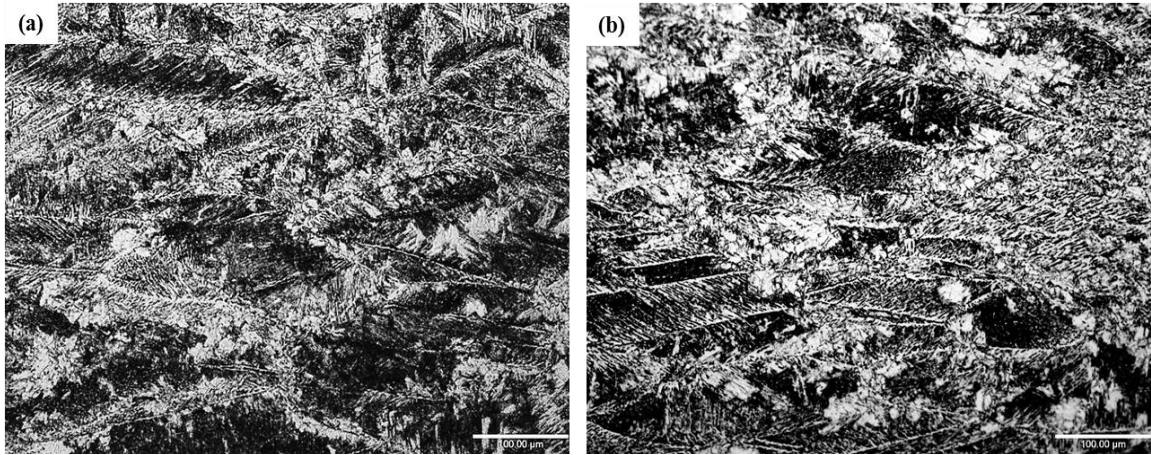


Fig. 6.5 OM of prior austenite grains in the Nb steel after reheating to 1200 °C for 100 s and finish rolling at 850 °C with 0.3 strain, (a) WQ immediately (A-100); (b) hold for 10 s +WQ (B-100) (Etched by picric acid).

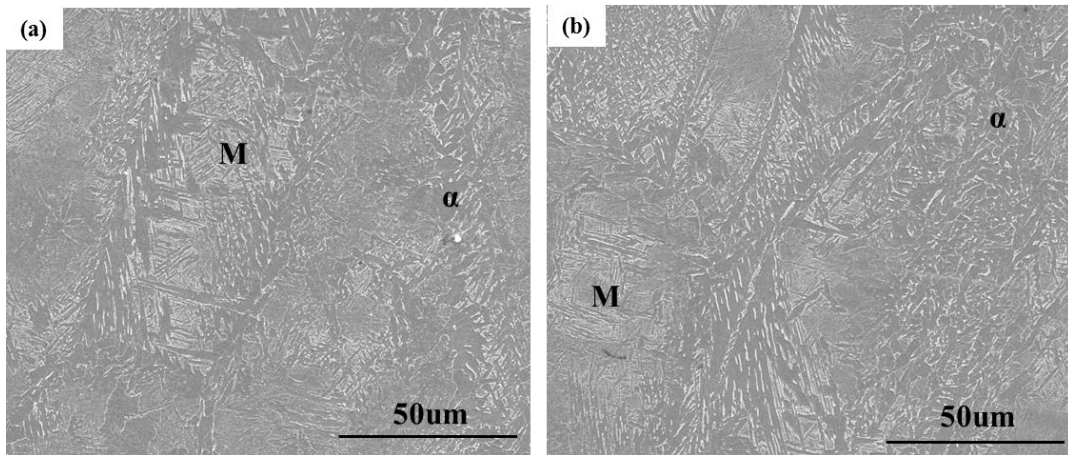


Fig. 6.6 SEM observation of DIFT for Nb steel after finish rolling with the rolling schedule A-100 and B-100, (a) WQ immediately (A-100); (b) hold for 10 s + WQ (B-100) (Etched by 2% 2 % nitric acid).

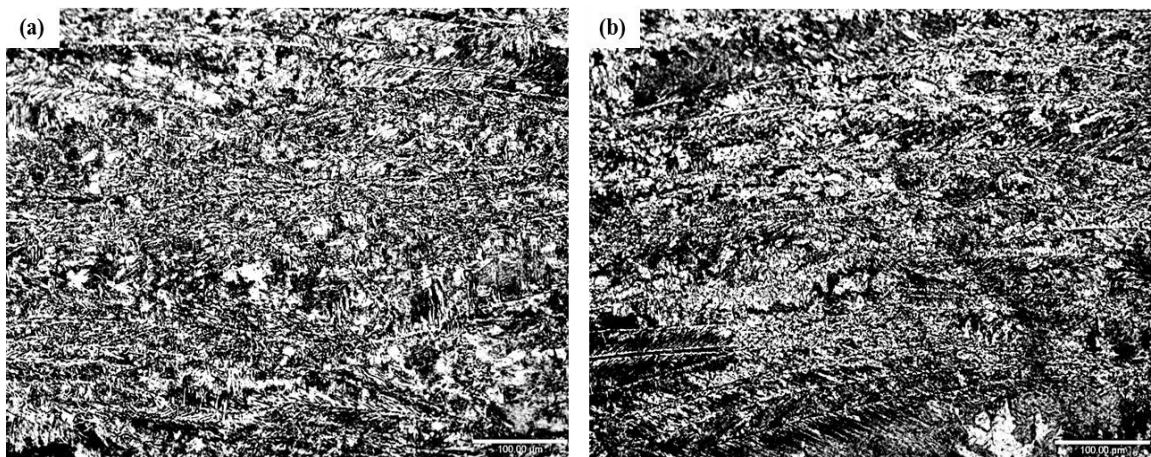


Fig. 6.7 OM of prior austenite grains in the Nb steel after reheating to 1200 °C for 100 s and finish rolling at 850 °C with 0.6 strain, (a) WQ immediately (C-100); (b) hold for 10 s+WQ (D-100) (Etched by picric acid).

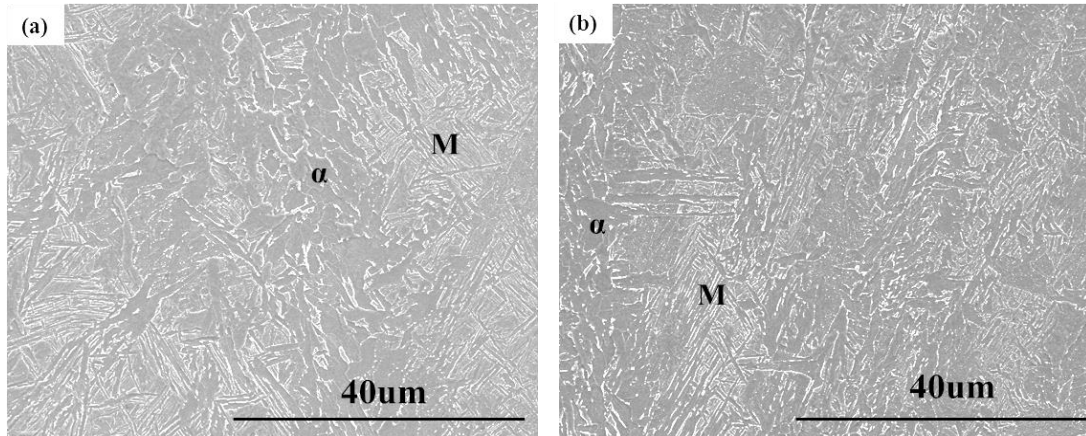


Fig. 6.8 SEM observation of DIFT for Nb steel after finish rolling with the rolling schedule C-100 and D-100, (a) WQ immediately (C-100); (b) hold for 10 s+WQ (D-100) (Etched by 2% 2 % nitric acid).

### 6.2.1.2 Nb-Ti steel

1) Finish rolling schedules A-10, B-10, C-10 and D-10 corresponding to heat treatment at 1200 °C for 10 s

The finish rolling schedules consisted of A-10, B-10, C-10 and D-10, which are shown in Fig. 3.5. After finish rolling with those schedules, the microstructures of prior-austenite grains and the second phase of DIFT are shown in Figs. 6.9-6.12 for the Nb-Ti steel. The average prior austenite grain size decreased with increasing strain, and the isothermal 10 s holding after deformation at 850 °C. From SEM observation, there was an amount of DIFT which was located mainly on the prior austenite grain boundaries. The morphology of the DIFT after finish rolling with other schedules of B-10, C-10 and D-10 was similar to that seen in A-10.

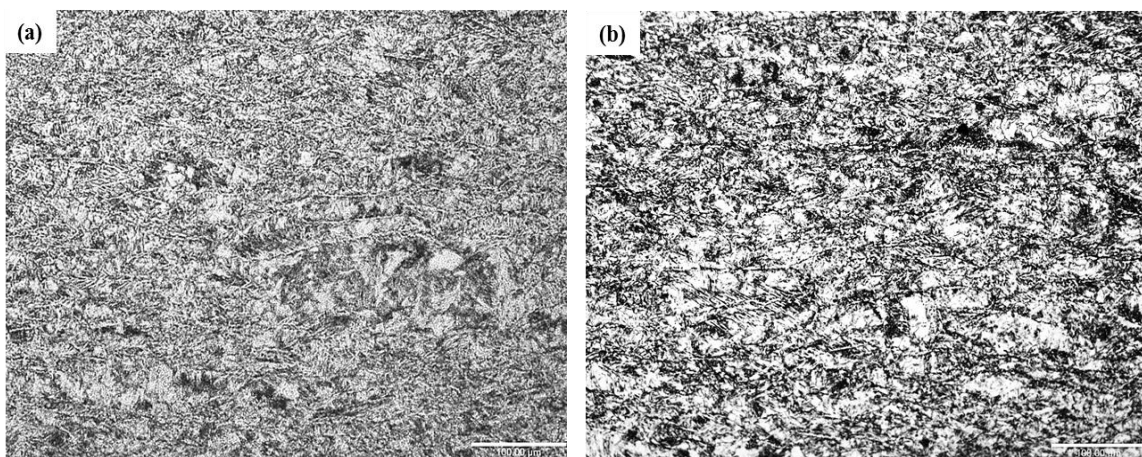


Fig. 6.9 OM of prior austenite grains in the Nb-Ti steel after reheating to 1200 °C for 10 s and finish rolling at 850 °C with 0.3 strain, (a) WQ immediately (A-10); (b) hold for 10 s+WQ (B-10) (Etched by picric acid).

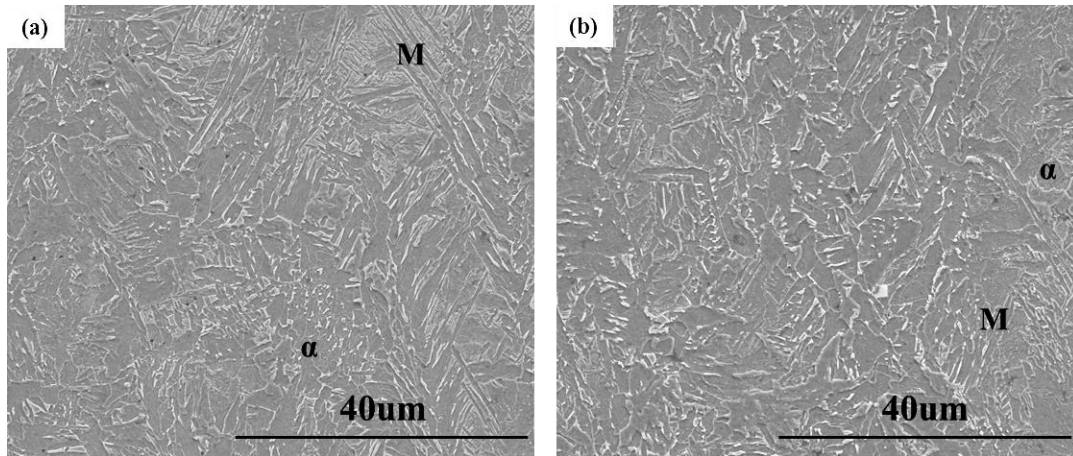


Fig. 6.10 SEM observation of DIFT for Nb-Ti steel after finish rolling with the rolling schedule A-10 and B-10, (a) WQ immediately (A-10); (b) hold for 10 s+WQ (B-10) (Etched by 2% 2 % nitric acid).

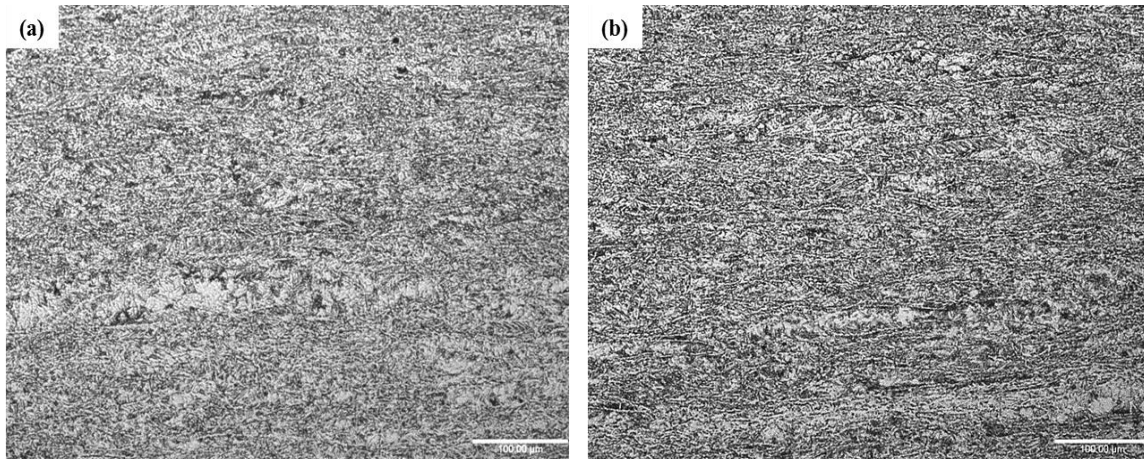


Fig. 6.11 OM of prior austenite grains in the Nb-Ti steel after reheating to 1200 °C for 100 s and finish rolling at 850 °C with 0.6 strain, (a) WQ immediately (C-10); (b) hold for 10 s+WQ (D-10) (Etched by picric acid).

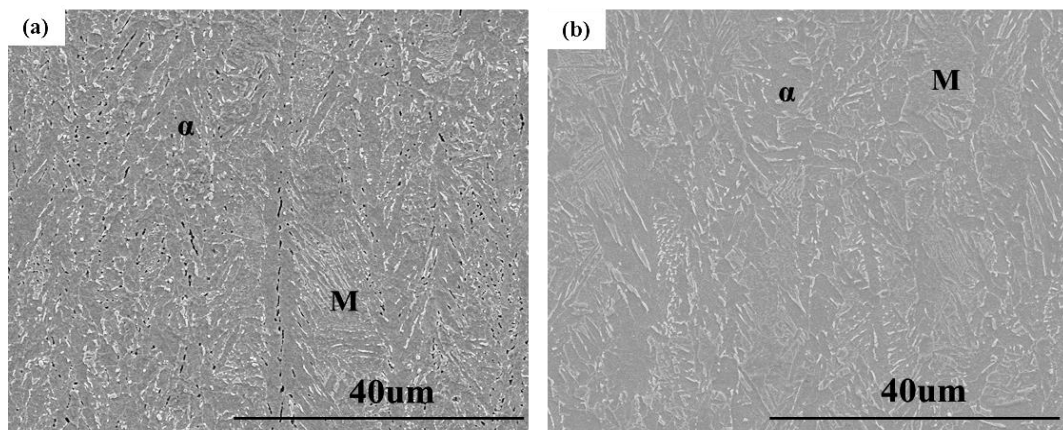


Fig. 6.12 SEM observation of DIFT for Nb-Ti steel after finish rolling with the rolling schedule C-10 and D-10, (a) WQ immediately (C-10); (b) hold for 10 s+WQ (D-10) (Etched by 2% 2 % nitric acid).

2) Finish rolling schedules A-100, B-100, C-100 and D-100 corresponding to heat treatment at 1200 °C for 100 s

After increasing the holding time to 100 s at 1200 °C, the microstructures were observed using OM and SEM, and presented in Figs. 6.13-6.16. The elongated prior austenite grains in all four specimens after finish rolling decreased with the increasing strain, and isothermal holding for 10 s after deformation. SEM images of the DIFT located on the grain boundaries are shown in Figs. 6.14 and 6.16.

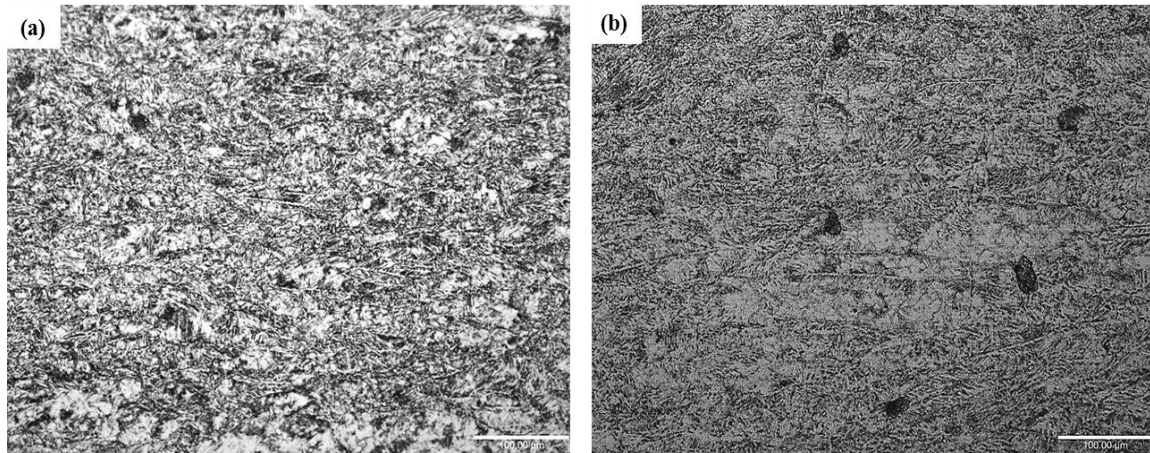


Fig. 6.13 OM of prior austenite grains in the Nb-Ti steel after reheating to 1200 °C for 100 s and finish rolling at 850 °C with 0.3 strain, (a) WQ immediately (A-100); (b) hold for 10 s+WQ (B-100) (Etched by picric acid).

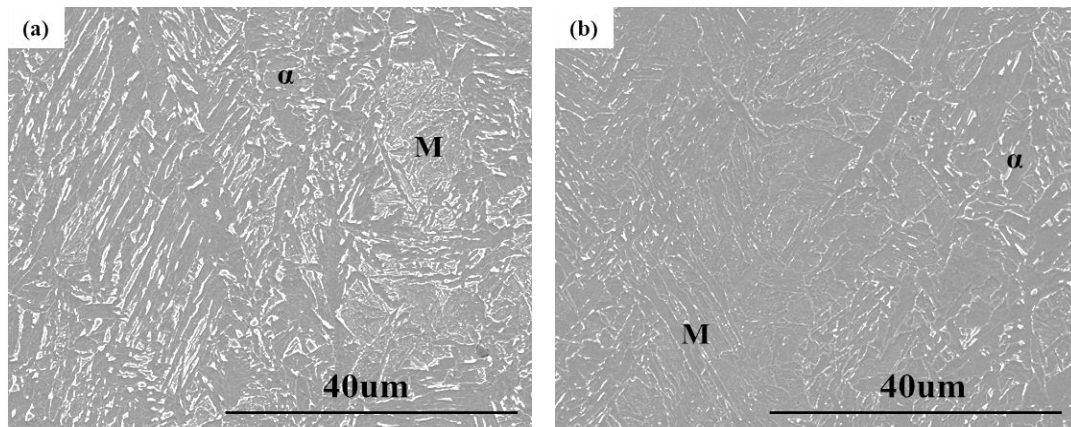


Fig. 6.14 SEM observation of DIFT for Nb-Ti steel after finish rolling with the rolling schedule A-100 and B-100, (a) WQ immediately (A-100); (b) hold for 10 s+WQ (B-100) (Etched by 2% 2 % nitric acid).

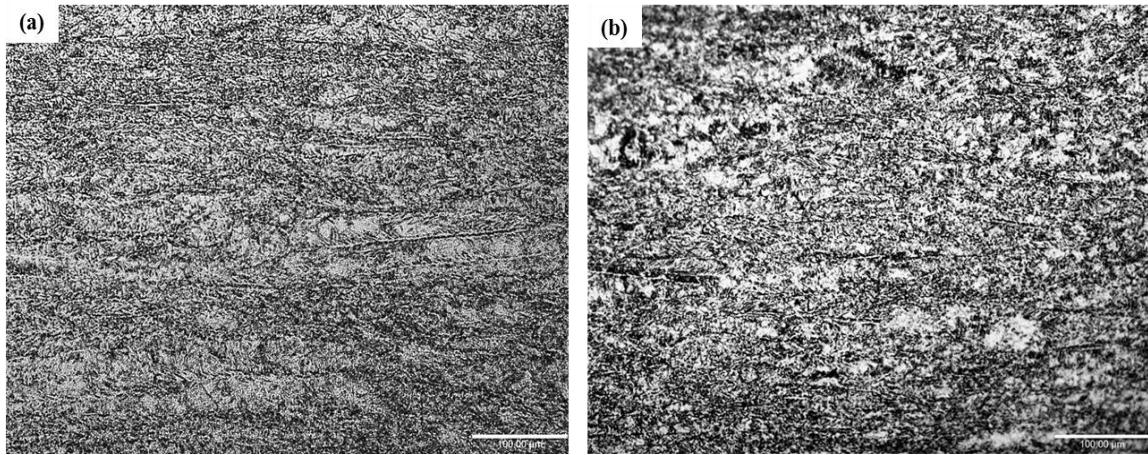


Fig. 6.15 OM of prior austenite grains in the Nb-Ti steel after reheating to 1200 °C for 100 s and finish rolling at 850 °C with 0.6 strain, (a) WQ immediately (C-100); (b) hold for 10 s+WQ (D-100) (Etched by picric acid).

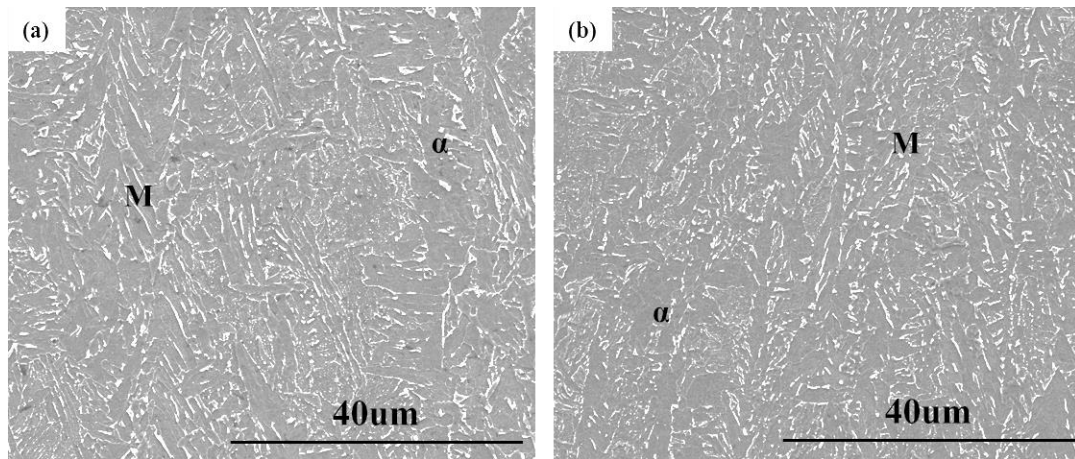


Fig. 6.16 SEM observation of DIFT for Nb-Ti steel after finish rolling with the rolling schedule of C-100 and C-100, (a) WQ immediately (C-100); (b) hold for 10 s+WQ (D-100) (Etched by 2% 2 % nitric acid)

In summary, the microstructure for Nb and Nb-Ti steels exhibited dual phase structures: martensite and ferrite. The DIFT observed in the micrographs had formed by the deformation and was mainly located on the elongated prior austenite grain boundaries and deformed bands, as well as within the grains. The mean prior austenite grain size decreased with increasing strain or isothermal holding for 10 s for both Nb and Nb-Ti steels.

### 6.2.2. Prior-austenite grain size and volume fraction of second phase ferrite measurements

The mean prior-austenite grain size and volume fraction of DIFT were calculated from OM and SEM images as shown in Figs. 6.1-6.16, and are presented in Figs. 6.17, 6.18 and Table 6.1. Fig. 6.17 gives the average prior austenite grain size measured as a function of processing condition and steel composition. The average prior-austenite grain size in the Nb

steel was larger than that in the Nb-Ti steel for the same rolling schedules. When considering the effect of the heat treatment on the mean deformed grain size, with longer holding at 1200 °C for 100 s, the deformed grain size is larger than that at 1200 °C for 10 s with the same rolling parameters.

The volume fraction of DIFT as a function of rolling parameters was calculated from SEM images and is shown in Fig. 6.18. It can be seen that the volume fraction of DIFT in the Nb-Ti steel was larger than that in the Nb steel for each process condition. The volume fraction of DIFT increased with increasing strain for both Nb and Nb-Ti steels. It also increased with the 10 s isothermal hold after deformation for a given strain. After one pass deformation and holding for 10 s at 850 °C, there was a much higher volume fraction of DIFT than after the finish rolling without subsequent hold. The volume fraction of DIFT continually increased with increasing strain to 0.6, but with a decreasing rate as the strain increased. When considering the effect of the holding time at 1200 °C on the volume fraction of DIFT, a 100 s hold at 1200 °C produced slightly more DIFT during finish rolling than a 10 s hold at 1200 °C under the same rolling conditions with the strain at 0.3.

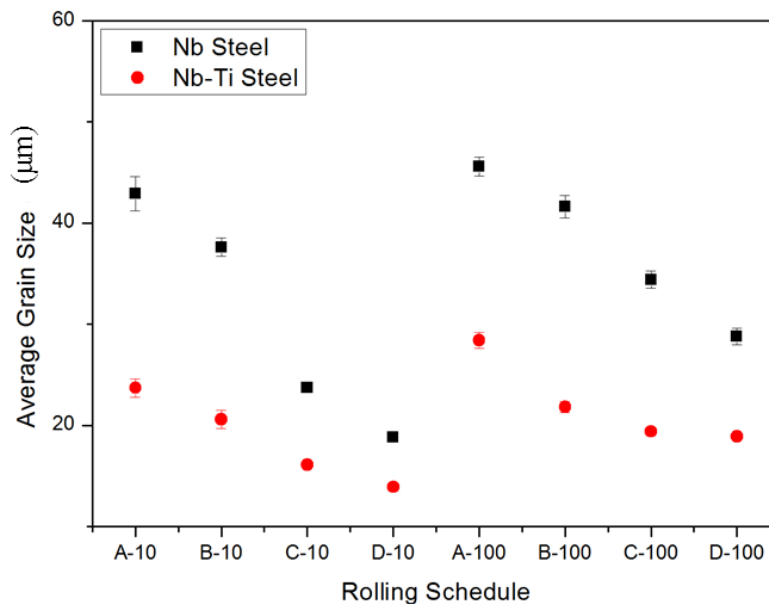


Fig. 6.17 The average prior austenite grain size as a function of finish rolling schedules, which shown in Fig. 3.5, A-10, B-10, C-10 and D-10 are heat treatments at 1200 °C for 10 s; A-100, B-100, C-100 and D-100 are heat treatments at 1200 °C for 100 s.

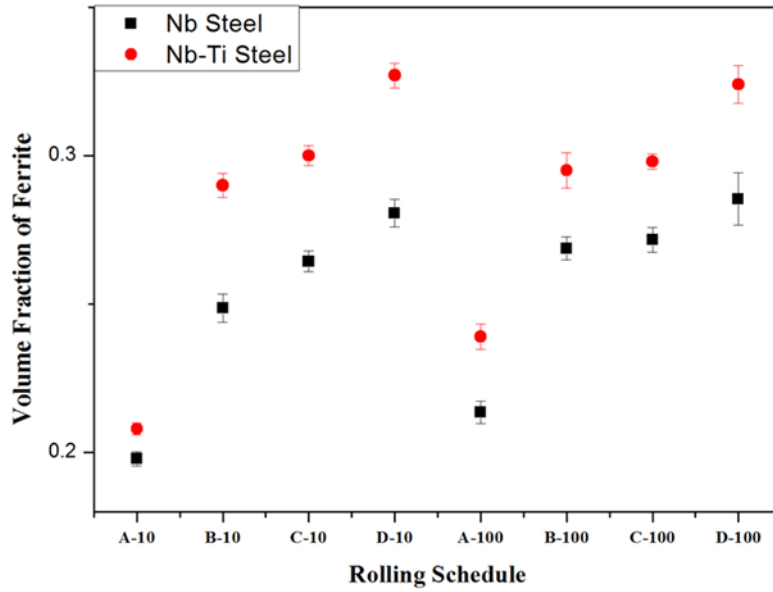


Fig. 6.18 The volume fraction of DIFT as a function of rolling parameters in the Nb and Nb-Ti steels, which shown in Fig. 3.5, A-10, B-10, C-10 and D-10 are heat treatments at 1200 °C for 10 s; A-100, B-100, C-100 and D-100 are heat treatments at 1200 °C for 100 s.

Table 6.1

Summary of the prior-austenite grain sizes and volume fraction of ferrite, as a function of different heat treatment and finish rolling parameters, as shown in Fig. 3.5.

Materials	Rolling Schedules	Average Grain Size ( $\mu\text{m}$ )	Volume Fraction of Ferrite
Nb Steel	A-10	42.9±6.4	0.20±0.02
	B-10	37.6±4.1	0.25±0.05
	C-10	23.7±3.6	0.27±0.04
	D-10	18.8±2.5	0.29±0.04
	A-100	45.6±6.2	0.21±0.03
	B-100	41.6±4.9	0.27±0.05
	C-100	34.4±6.3	0.28±0.04
	D-100	28.8±6.1	0.30±0.09
Nb-Ti Steel	A-10	23.7±3.3	0.21±0.01
	B-10	20.6±3.1	0.28±0.04
	C-10	16.1±1.5	0.29±0.04
	D-10	13.9±1.5	0.31±0.06
	A-100	28.4±5.2	0.24±0.03
	B-100	21.8±3.8	0.29±0.04
	C-100	19.4±2.9	0.30±0.03
	D-100	18.9±1.9	0.33±0.05

### 6.3 TEM carbon extraction replicas

In order to analyse the effect of finish rolling on the SIP behaviour for Nb and Nb-Ti steels, TEM, EDX and HRTEM were used to observe the morphology, composition, size distribution and the volume fraction of precipitates. The size distribution and the volume fraction of precipitates were calculated from carbon extraction replica samples using bright field TEM images. Moreover, the size distribution of the precipitates was also calculated using Eq. 5.1 and compared with the individual measurement data. The amount of Nb or Nb and Ti in precipitates was calculated using Eq. 4.7 from the volume fraction of precipitation. EDX and EELS were used to analyse the composition of SIP as well.

#### 6.3.1 The size distribution of the SIP

Following cooling from the finish deformation at 850 °C, the size distribution and the average diameter of SIP in the Nb and Nb-Ti steels was determined from TEM carbon replicas, Figs. 6.19-6.26.

##### 6.3.1.1 Nb steel

1) Finish rolling schedules A-10, B-10, C-10 and D-10 corresponding to heat treatment at 1200 °C for 10 s

Figs. 6.19 and 6.20 show SIP produced by rolling schedules A-10, B-10, C-10 and D-10 (Fig. 3.5). Most of the precipitates had a spherical shape with a size less than 20 nm. The average size of precipitates decreased with the increasing strain, and isothermal holding for 10 s. The average precipitate size was  $9 \pm 0.2$  nm at the beginning (A-10) and then decreased to  $8.8 \pm 0.23$  nm with isothermal hold for 10 s at a deformation temperature of 850 °C (B-10). Increasing the strain to 0.6, the mean size of precipitates decreased to  $8.4 \pm 0.32$  nm (C-10) and then reduced to  $7.4 \pm 0.15$  nm with isothermal hold for 10 s (D-10).

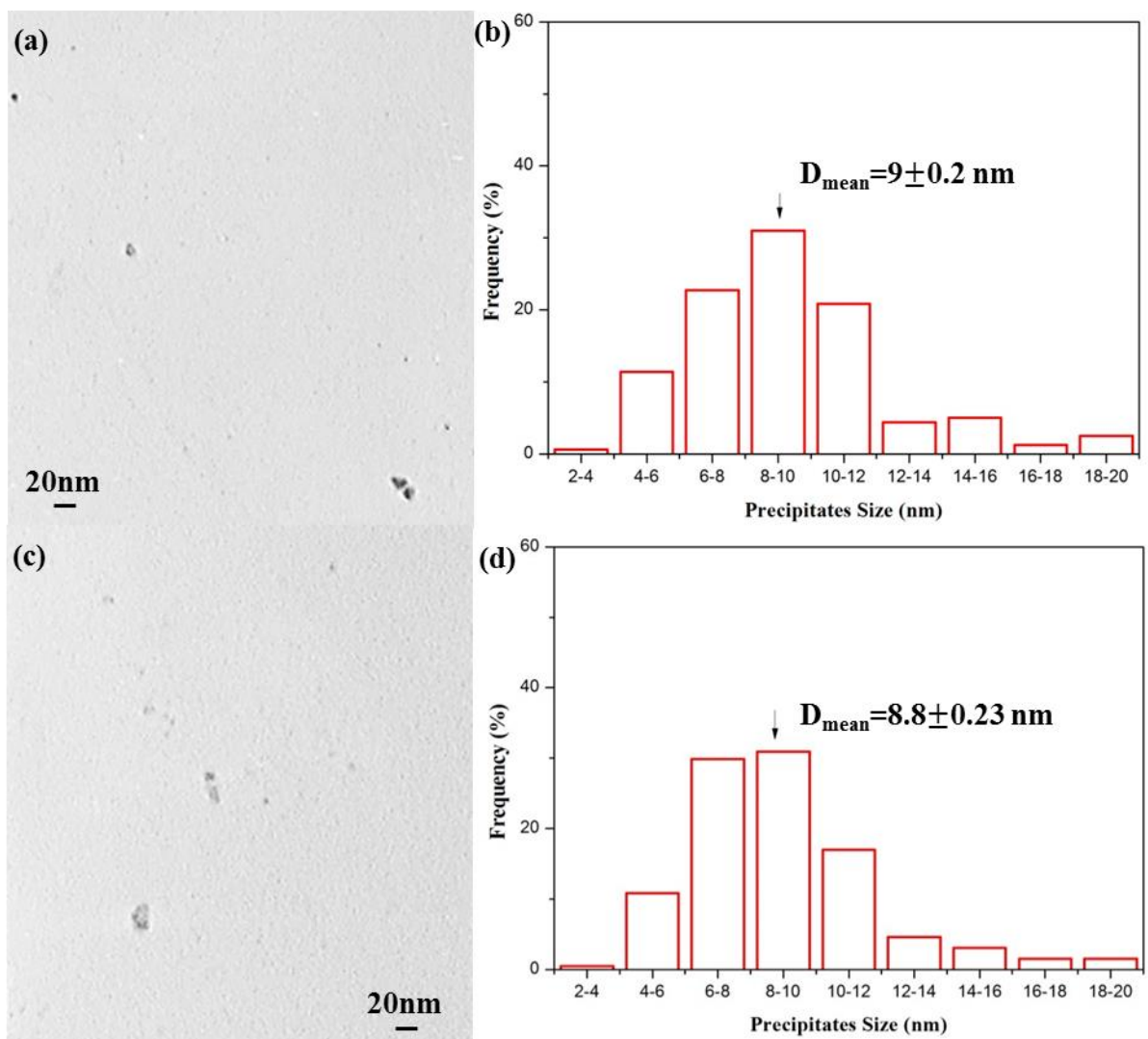


Fig. 6.19 Precipitates and the corresponding size distribution in the Nb steel with heat treatment at 1200 °C for 10 s followed by deformation at 850 °C with strain of 0.3, (a) TEM image showing spherical SIP with rolling schedule A-10; (b) size distribution of SIP calculated from TEM images like image (a); (c) TEM image showing spherical SIP with rolling schedule of B-10; (d) size distribution of SIP calculated from TEM images like image (c).

The precipitate diameter distribution for different finish rolling schedules was unimodal over the entire range, and the number density of precipitates increased with increasing strain or isothermal holding for 10 s. The peak value of the distribution was between 8 and 10 nm, and then changed to 6-8 nm with a strain increase to 0.6. The simulated size distribution of precipitation in Figs. 6.19 (b), (d) and 6.20 (d), (d) fits well with the results from carbon replica data.

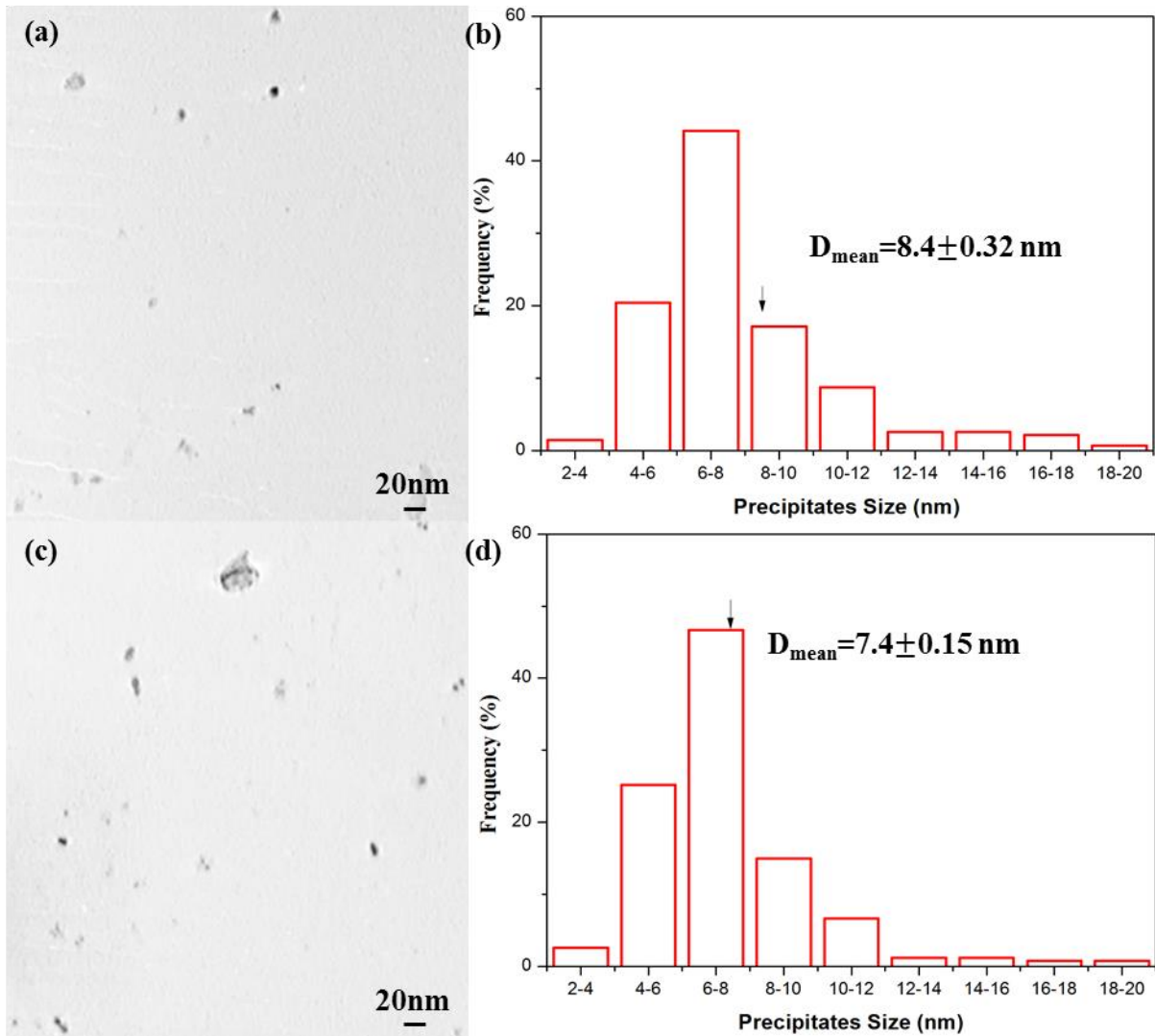


Fig.6. 20 Precipitates and the corresponding size distribution in the Nb steel with heat treatment at 1200 °C for 10 s followed by deformation at 850 °C with strain of 0.6, (a) TEM image showing spherical SIP with rolling schedule C-10; (b) size distribution of SIP calculated from TEM images like image (a); (c) TEM image showing spherical SIP with rolling schedule of D-10; (d) size distribution of SIP calculated from TEM images like image (c).

2) Finish rolling schedules A-100, B-100, C-100 and D-100 corresponding to heat treatment at 1200 °C for 100 s

Figs. 6.21 and 6.22 show SIP with rolling schedules A-100, B-100, C-100 and D-100 (Fig. 3.5). The average precipitate size decreased with the increasing strain, and isothermal holding for 10 s. The average precipitate size was  $9.2 \pm 0.36$  nm at the beginning (A-100) and then decreased to  $9.0 \pm 0.51$  nm with isothermal hold for 10 s at a deformation temperature of 850 °C (B-100). With increased strain to 0.6, the mean size of precipitates decreased to  $8.1 \pm 0.24$  nm (C-100) and then reduced to  $7.6 \pm 0.15$  nm with isothermal hold for 10 s (D-100). The precipitate diameter distribution was calculated as a function of the rolling parameters. The distribution of precipitates over the entire range was unimodal, and the

number density of precipitates increased with increasing strain or isothermal holding for 10 s. The peak value of the distribution was between 8 and 10 nm at A-100, and then changed to 6-8 nm with the finish rolling at B-100, C-100 and D-100. The simulated size distribution of precipitation in Figs. 6.21 (b), (d) and 6.22 (d), (d) fits well with the calculated results from carbon replica data.

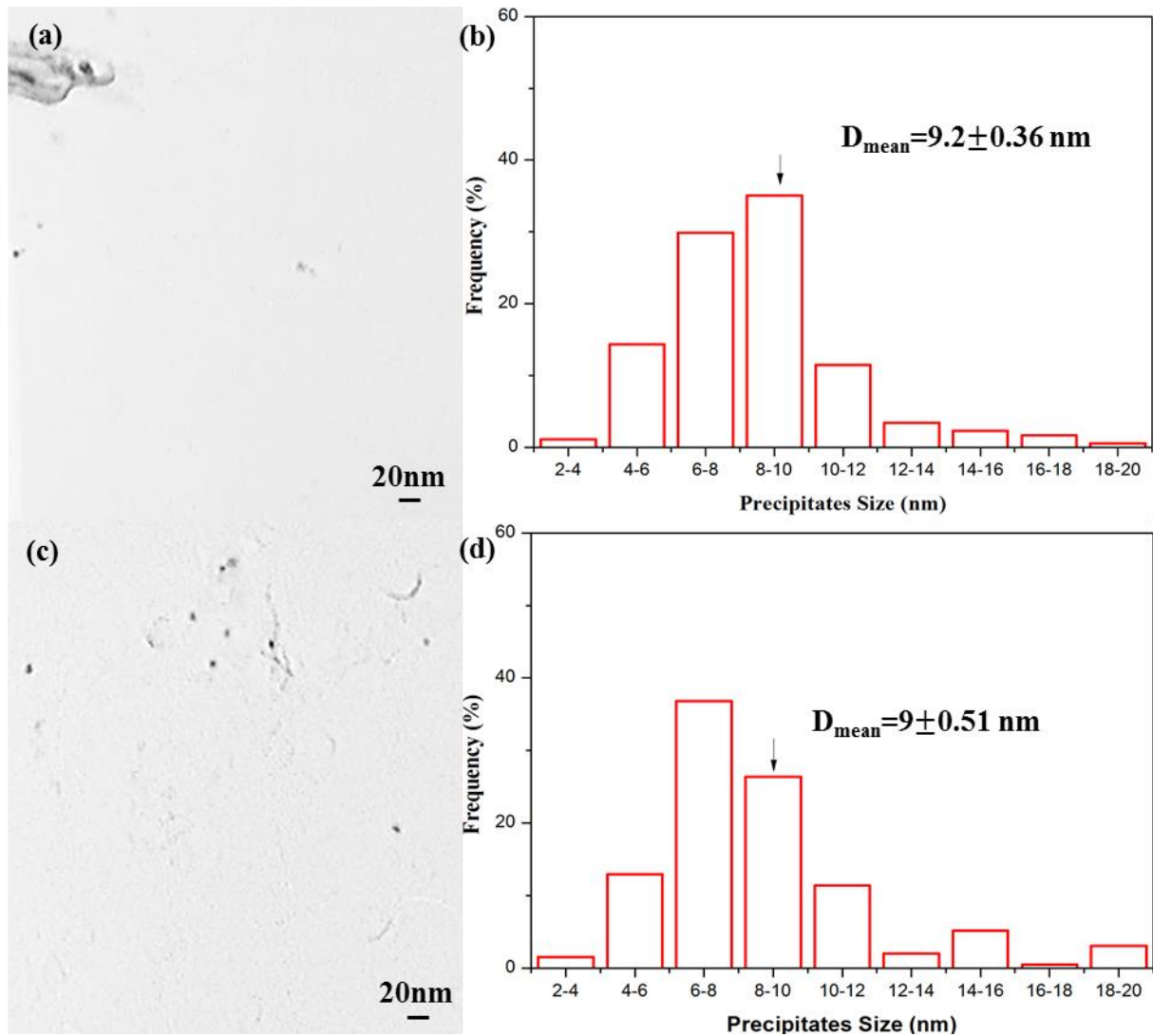


Fig. 6.21 Precipitates and the corresponding size distribution in the Nb steel with heat treatment at 1200 °C for 100 s followed by deformation at 850 °C with strain of 0.3, (a) TEM image showing spherical SIP with rolling schedule A-100; (b) size distribution of SIP calculated from TEM images like image (a); (c) TEM image showing spherical SIP with rolling schedule B-100; (d) size distribution of SIP calculated from TEM images like image (c).

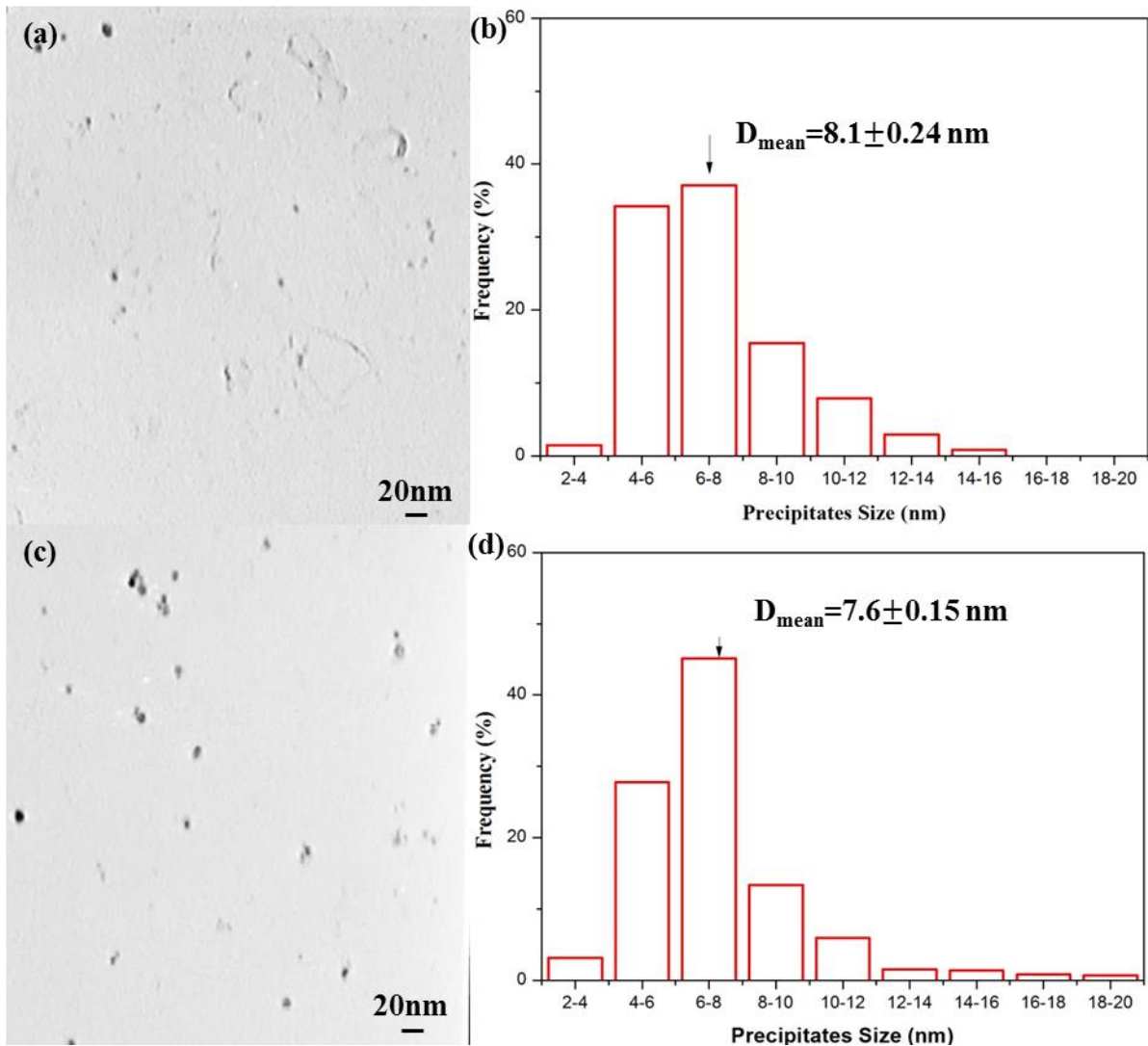


Fig. 6.22 Precipitates and the corresponding size distribution in the Nb steel with heat treatment at 1200 °C for 100 s followed by deformation at 850 °C with strain of 0.6: (a) TEM image showing spherical SIP with rolling schedule C-100; (b) size distribution of SIP calculated from TEM images like image (a); (c) TEM image showing spherical SIP with rolling schedule D-100; (d) size distribution of SIP calculated from TEM images like image (c).

To summarise, with holding for 100 s at 1200 °C, the number density of particles are higher than that for 10 s holding at 1200 °C under the same rolling process. The isothermal holding times after deformation at 850 °C influenced the number density of precipitates. From Figs. 6.21 and 6.22, it is obvious that there are more precipitates with a size between 6 and 8 nm for a hold of 10 s (B-100 and D-100), compared to water quenched samples (A-100 and C-100) under the same rolling parameters. There are many more precipitates at the higher strain of 0.6 compared to a strain of 0.3. The mean size of precipitates decreased with the increasing strain or isothermal hold for 10 s.

### 6.3.1.2 Nb-Ti steel

1) Finish rolling schedules A-10, B-10, C-10 and D-10 corresponding to heat treatment at 1200 °C for 10 s

The SIP produced by the rolling schedules A-10, B-10, C-10 and D-10 (Fig. 3.5) are shown in Figs. 6.23 and 6.24. There are two types of precipitates: one has an irregular shape with a size less than 20 nm; another is cuboid with a size larger than 20 nm. In this study, only the SIP with the size less than 20 nm was measured. The average size of precipitation decreased with the increasing strain, and isothermal holding for 10 s at the deformation temperature. The average precipitate size was  $10.1 \pm 0.24$  nm at the beginning (A-10) and then decreased to  $9.2 \pm 0.22$  nm with isothermal hold for 10 s at the deformation temperature of 850 °C (B-10). Increasing the strain to 0.6 resulted in a reduction in the mean precipitate size to  $9.02 \pm 0.45$  nm (C-10), and then this further reduced to  $8.03 \pm 0.28$  nm with isothermal hold for 10 s (D-10). The precipitate diameter distribution for different finish rolling schedules was studied. The number density of precipitates increased with increasing strain or isothermal holding for 10 s. The peak value of the distribution was between 8 and 10 nm at the beginning, and then changed to 6-8 nm as the strain increased to 0.6. The simulated size distributions of precipitates in Figs. 6.23 (b), (d) and 6.24 (b), (d) have been calculated through Eq. 5.1 and fits well with the results from carbon replica samples.

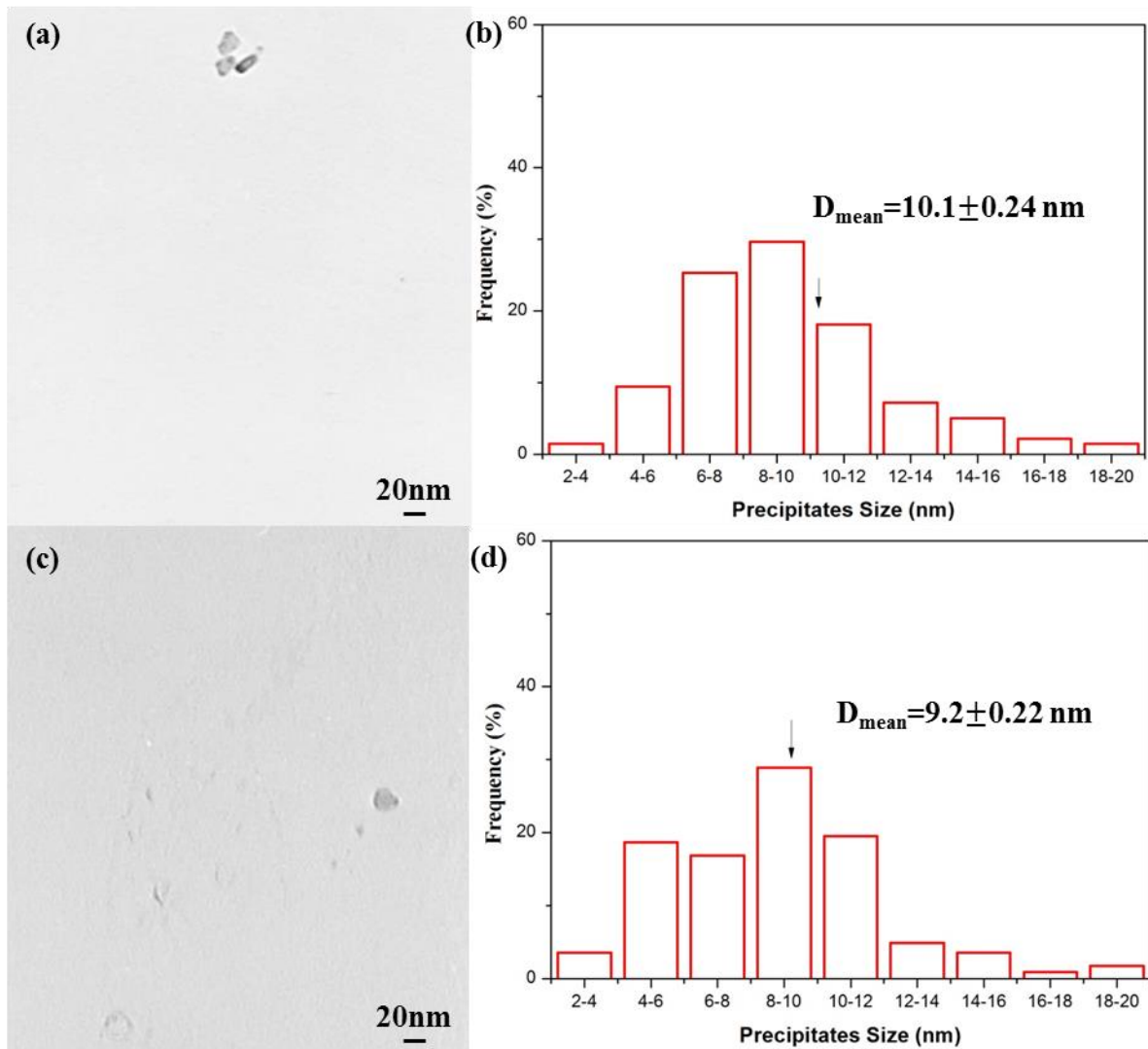


Fig. 6.23 Precipitates and the corresponding size distribution in the Nb-Ti steel with heat treatment at 1200 °C for 10 s followed by deformed at 850 °C with strain of 0.3: (a) TEM image showing irregularly shaped precipitates with rolling schedule A-10; (b) size distribution of SIP calculated from TEM images like image (a); (c) TEM image showing irregularly shaped precipitates with rolling schedule B-10; (d) size distribution of size distribution of SIP calculated from TEM images like image (c).

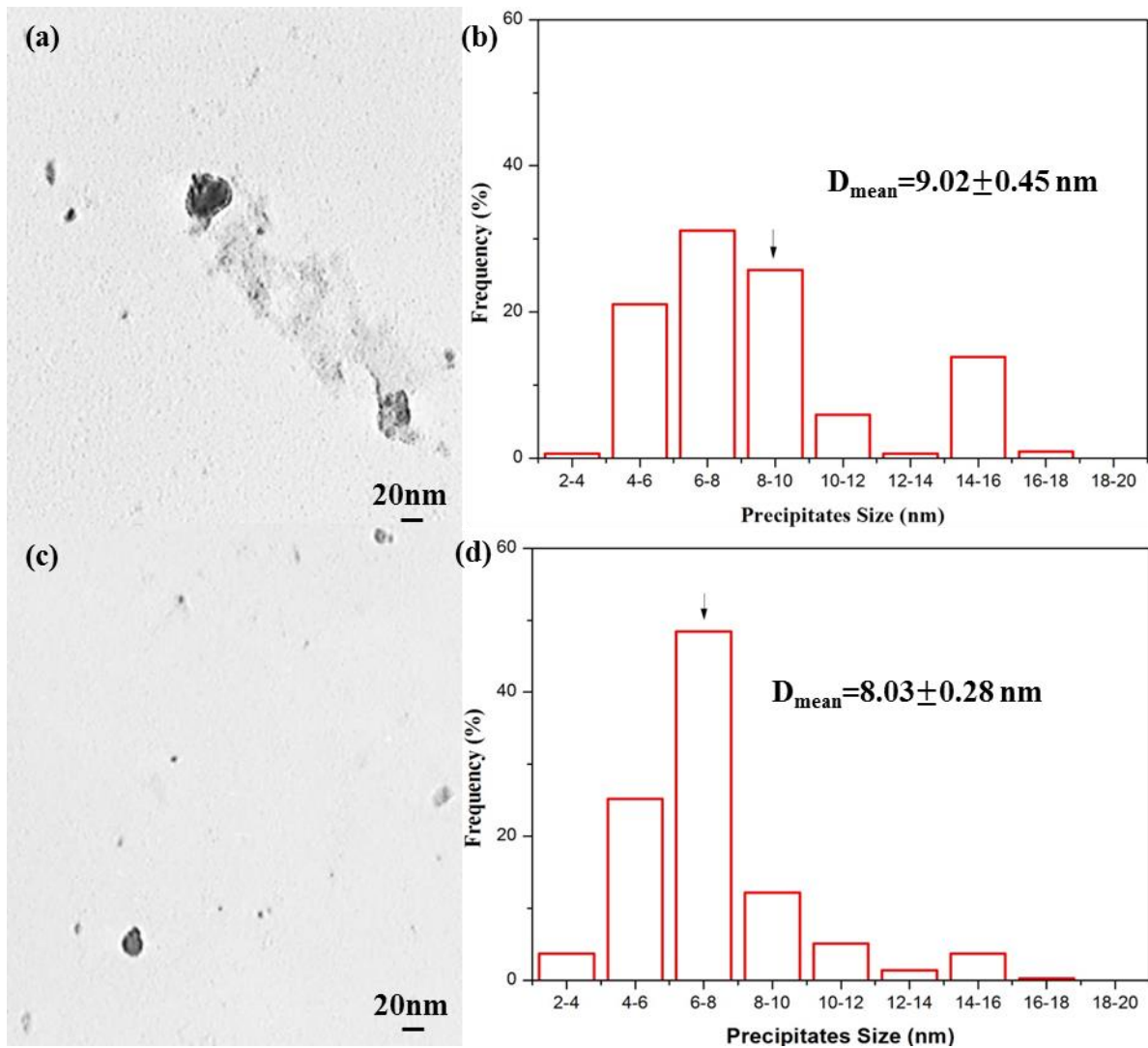


Fig. 6.24 Precipitates and the corresponding corresponding size distribution in the Nb-Ti steel with heat treatment at 1200 °C for 10 s followed by deformed at 850 °C with strain of 0.6: (a) TEM image showing irregularly shaped precipitates with rolling schedule C-10; (b) size distribution of SIP calculated from TEM images like image (a); (c) TEM image showing irregularly shaped precipitates with rolling schedule D-10; (d) size distribution of size distribution of SIP calculated from TEM images like image (c).

2) The finish rolling schedules of the A-100, B-100, C-100 and D-100 corresponding to heat treatment at 1200 °C for 100 s

The SIP produced from rolling schedules A-100, B-100, C-100 and D-100 (Fig. 3.5) are shown in Figs. 6.25 and 6.26. The average size of precipitates decreased with increasing strain, and isothermal holding for 10 s. The average precipitate size was  $9.4 \pm 0.44$  nm at the beginning (A-100) and then decreased to  $9.05 \pm 0.47$  nm with isothermal hold for 10 s at the deformation temperature of 850 °C (B-100). With increasing strain, the mean precipitate size decreased to  $9 \pm 0.45$  nm for a strain of 0.6 (C-100), and then  $8.4 \pm 0.48$  nm for a strain of 0.6 followed by an isothermal hold for 10 s (D-100). The precipitate diameter distribution for different finish rolling schedules was calculated from TEM images. The number density of

precipitates increased with increasing strain or isothermal holding for 10 s. The peak value of the size distribution was in the range of 8 to 10 nm at the beginning, and then moved to 6-8 nm with the finish rolling of B-100, C-100 and D-100. The simulated size distribution curve fit well with the results from carbon replica samples shown in Fig. 6.25 (b), (d) and 6.26 (b), (d).

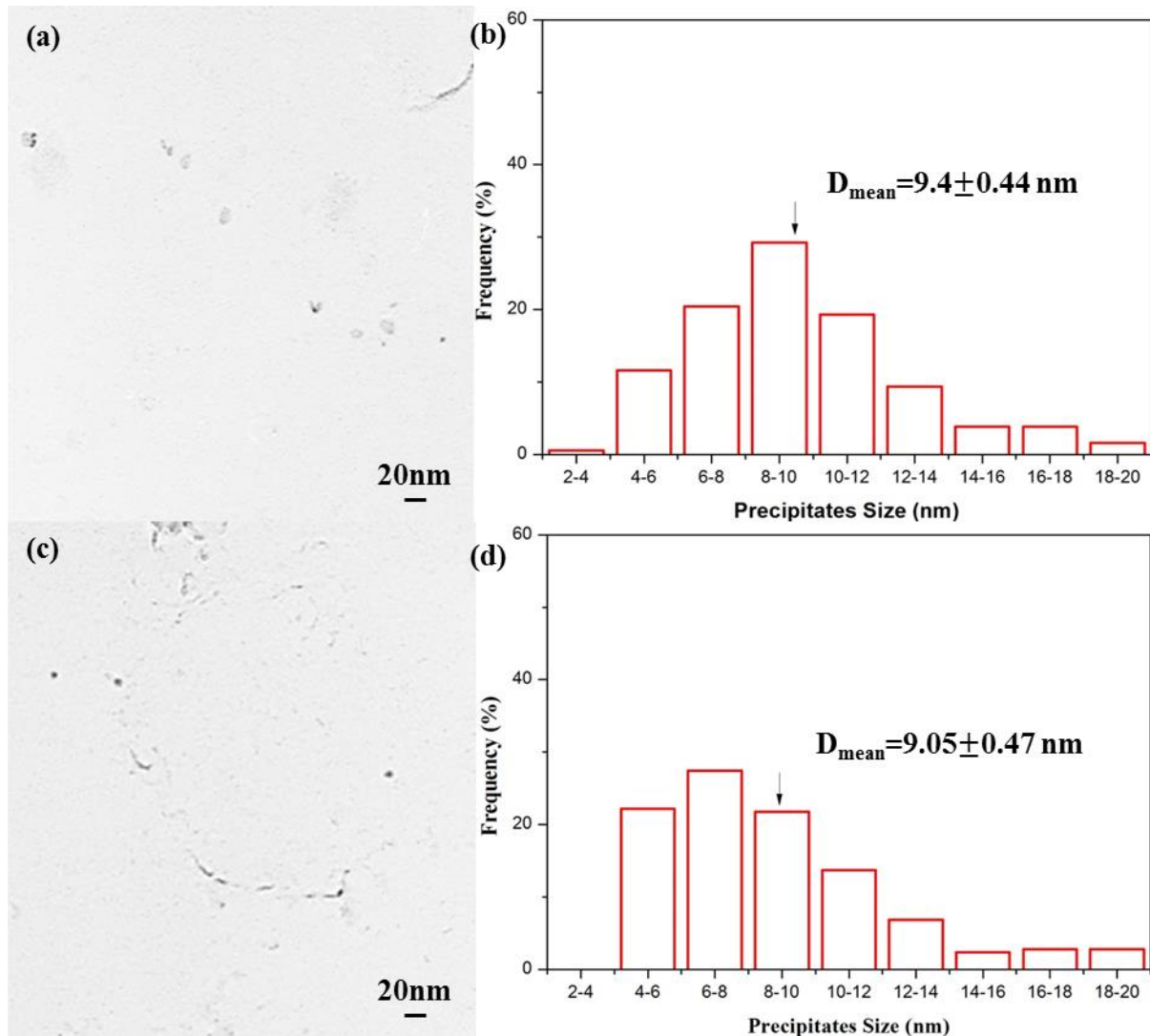


Fig. 6.25 Precipitates and the corresponding size distribution in the Nb-Ti steel with heat treatment at 1200 °C for 100 s followed by deformed at 850 °C with strain of 0.3: (a) TEM image showing irregularly shaped precipitates with rolling schedule A-100; (b) size distribution of SIP calculated from TEM images like image (a); (c) TEM image showing irregularly shaped precipitates with rolling schedule B-100; (d) size distribution of size distribution of SIP calculated from TEM images like image (c).

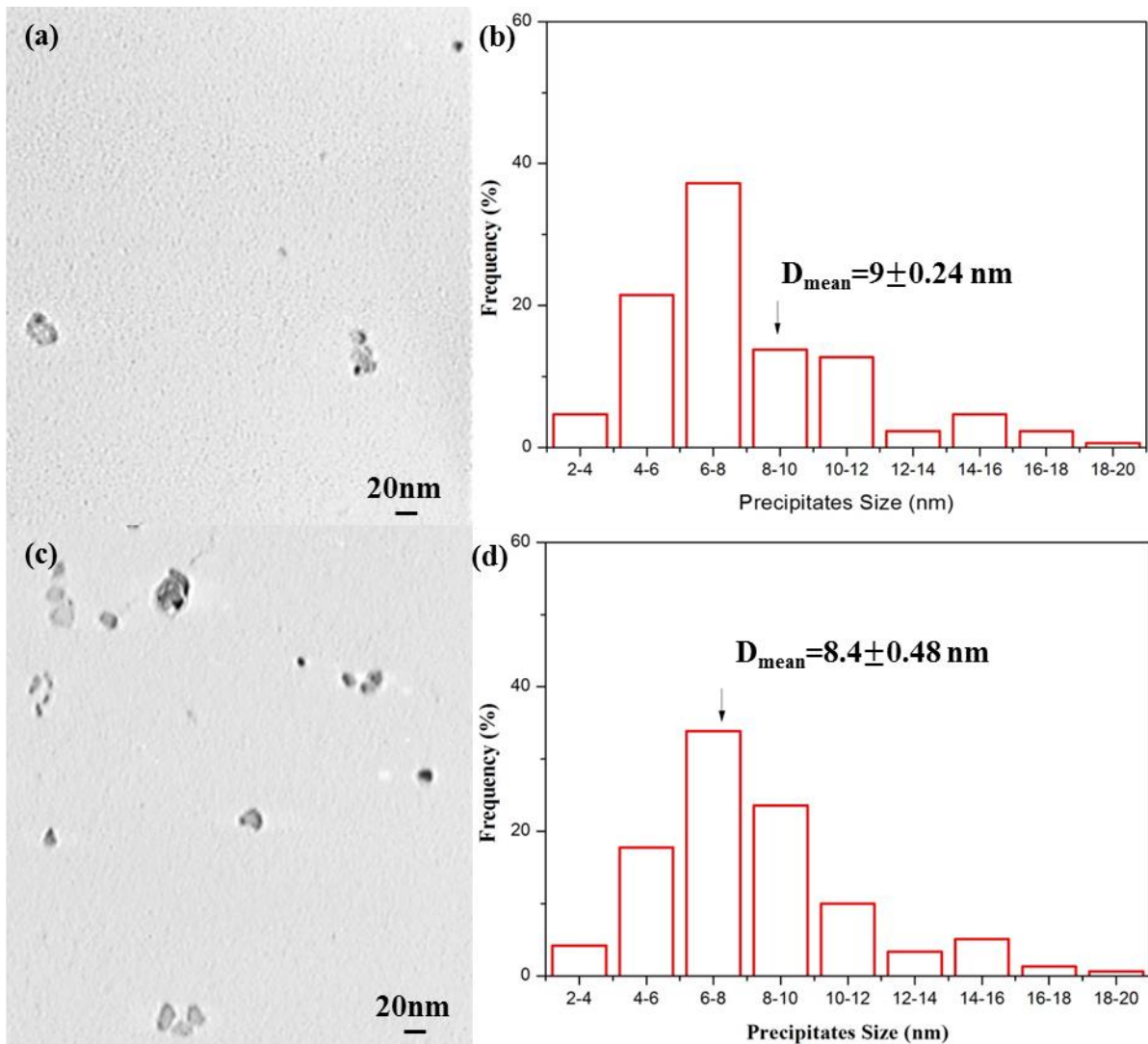


Fig. 6.26 Precipitates and the corresponding size distribution in the Nb-Ti steel with heat treatment at 1200 °C for 100 s followed by deformed at 850 °C with strain of 0.6: (a) TEM image showing irregularly shaped precipitates with rolling schedule C-100; (b) size distribution of SIP calculated from TEM images like image (a); (c) TEM image showing irregularly shaped precipitates with rolling schedule D-100; (d) size distribution of size distribution of SIP calculated from TEM images like image (c).

To summarise, with holding for 100 s at 1200 °C, there were more particles than for 10 s holding at 1200 °C under the same rolling process. Then, with 10 s holding after deformation (B-10 and D-10), the number density of SIP was more than in the immediately water quenched specimens (A-10 and C-10), while the mean size of precipitates was less than the water quenched specimens. The increasing strain also influenced the number density. With the increasing strain to 0.6, the precipitate number density continually increased, but the mean size of precipitates decreased.

### 6.3.2 The volume fraction of the SIP and the content of Nb in these precipitates

The volume fraction of precipitation per each rolling schedule was determined from 10 TEM images and listed in Table 6.2. It is clear that the volume fraction of SIP increased with increasing strain for both Nb and Nb-Ti steels. It also increases with the 10 s isothermal hold after deformation at 850 °C when compared with water quenched samples at the same strain for both steels. The mean size of precipitates decrease with the increasing strain or isothermal holding for 10 s under the same heat treatment holding time at 1200 °C.

Moreover, with longer holding time at 1200 °C, there are more precipitates after deformation at 850 °C with different finish rolling parameters. However, the average precipitate size was similar between 10 s and 100 s holding at 1200 °C under the same rolling parameters. For the Nb steel, the average size and the volume fraction of precipitates were both smaller than that for Nb-Ti steel, when compared at the same rolling parameters.

Table 6.2

Data from carbon extraction replica results in the Nb and Nb-Ti steels showing radius, volume fraction of precipitation, as well as the amount of [Nb] and [Nb+Ti] in precipitates under different rolling parameters.

Materials	Schedule	Radius (nm)	Volume Fraction of Precipitation ( $10^{-5} \mu\text{m}^{-3}$ )	[Nb] (wt%) (Nb in Precipitates)
Nb Steel	A-10	9.1	5.04	0.0044
	B-10	9	5.89	0.0052
	C-10	8.4	6.89	0.0061
	D-10	7.4	8.55	0.0075
	A-100	9.2	5.21	0.0046
	B-100	9	5.98	0.0053
	C-100	8.1	7.5	0.0067
	D-100	7.6	9.24	0.0081
Materials	Schedule	Radius (nm)	Volume Fraction of Precipitation ( $10^{-5} \mu\text{m}^{-3}$ )	[Nb+Ti] (wt%) (Nb and Ti in Precipitates)
Nb-Ti Steel	A-10	10.1	5.68	0.0050
	B-10	9.2	5.99	0.0053
	C-10	9.02	6.11	0.0054
	D-10	8.03	7.23	0.0064
	A-100	9.4	6.3	0.0055
	B-100	9.05	7.12	0.0065
	C-100	9	7.79	0.0069
	D-100	8.4	10.71	0.0094

The amounts of Nb in precipitates can be expressed by incorporating the volume fraction of precipitation using Eq. 4.7 and shown in Table 6.2. The trend of the Nb in precipitates is the same with the changing of volume fraction of precipitates as a function of the different rolling parameters.

### 6.3.3 The chemical composition in SIP

High resolution lattice image and EDX were used to analyse the SIP, taken from typical specimens after processing with the rolling schedule shown in Fig. 3.5 for both Nb and Nb-Ti steels. The crystal structure was identified using the inverse fast Fourier transformation (IFFT).

#### 6.3.3.1 Nb steel

Figs. 6.27-6.30 show HRTEM images of a spherical shaped particle from the Nb steel. The corresponding inverse fast Fourier transform indicates the lattice spacing. Fig. 6.27 observed along the zone axis of  $[100]_{MC}$  with  $d$  about 0.22 nm, which is close to the  $d_{(200)}$  of NbC. Figs. 6.28, 6.29 and 6.30 were imaged along a  $[110]_{MC}$  zone axis with the measured  $d$  spacing about 0.25 nm, which is close to published values for the  $d_{(111)}$  spacing of NbC of 0.258 nm. The chemical composition of the particle was measured by EDX with the Nb L line. The structure and EDX results suggest that the nanometer-sized particle was NbC in the Nb steel.

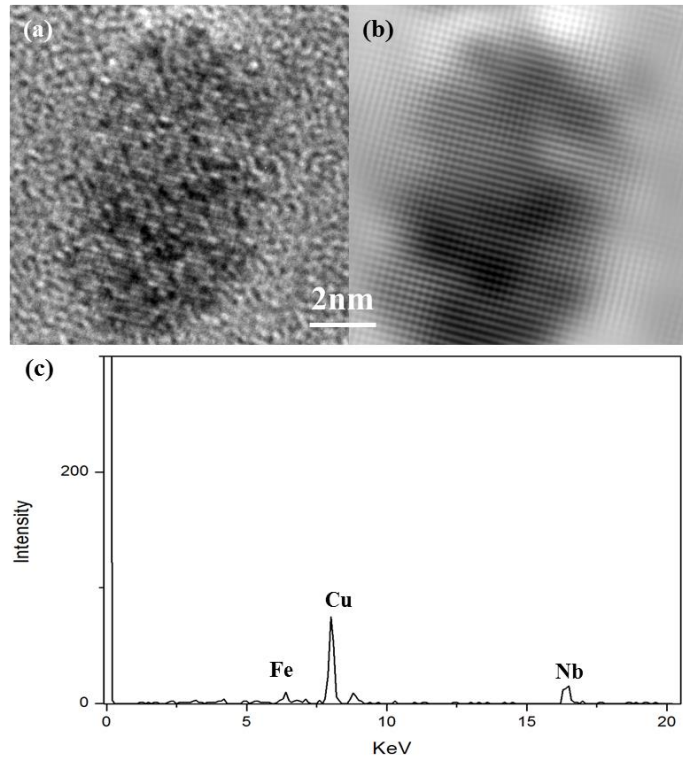


Fig. 6.27 Precipitation in carbon replica specimen for Nb steel after heat treatment at 1200 °C for 10 s followed by deformation at 850°C with rolling schedule of A-10, (a) HRTEM image showing a nanoscale precipitates; (b) IFFT on the particle shown in (a); (c) EDX analysis of the nanoscale particle shown in (a).

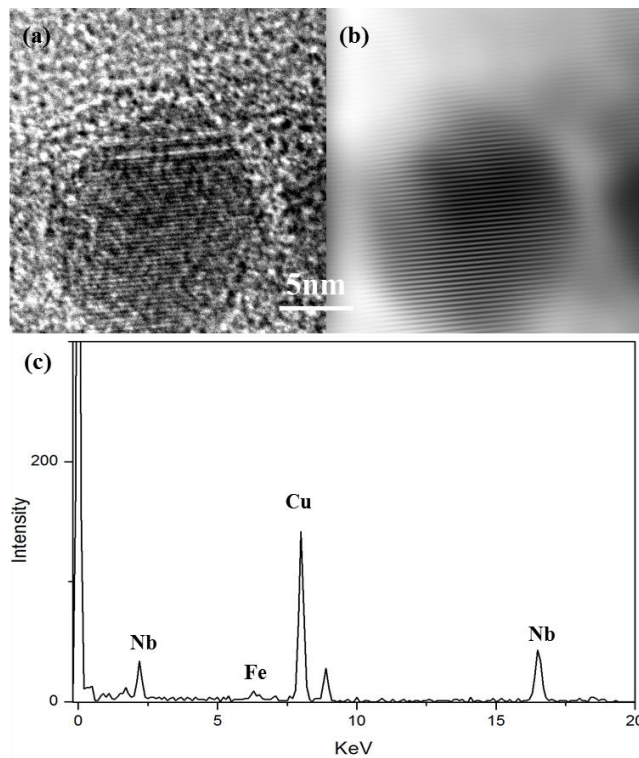


Fig. 6.28 Precipitate in carbon replica specimen for Nb steel after heat treatment at 1200 °C for 10 s followed by deformation at 850°C with rolling schedule B-10, (a) HRTEM image of a nanoscale precipitate; (b) IFFT on the particle shown in (a); (c) EDX analysis of the nanoscale particle shown in (a).

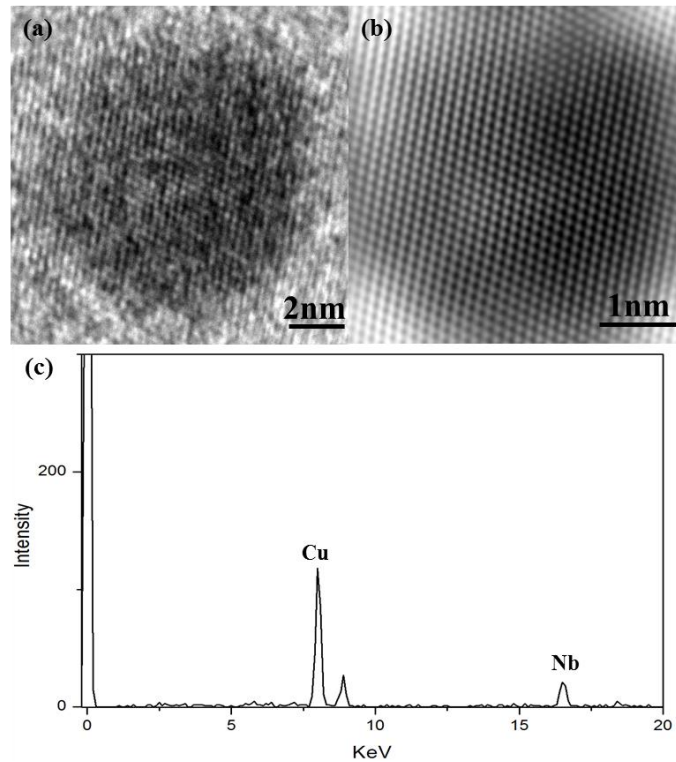


Fig. 6.29 Precipitate in carbon replica specimen for Nb steel after heat treatment at 1200 °C for 10 s followed by deformed at 850 °C with rolling schedule C-10, (a) HRTEM image of a nanoscale precipitate; (b) IFFT on the particle shown in (a); (c) EDX analysis of the nanoscale particle shown in (a).

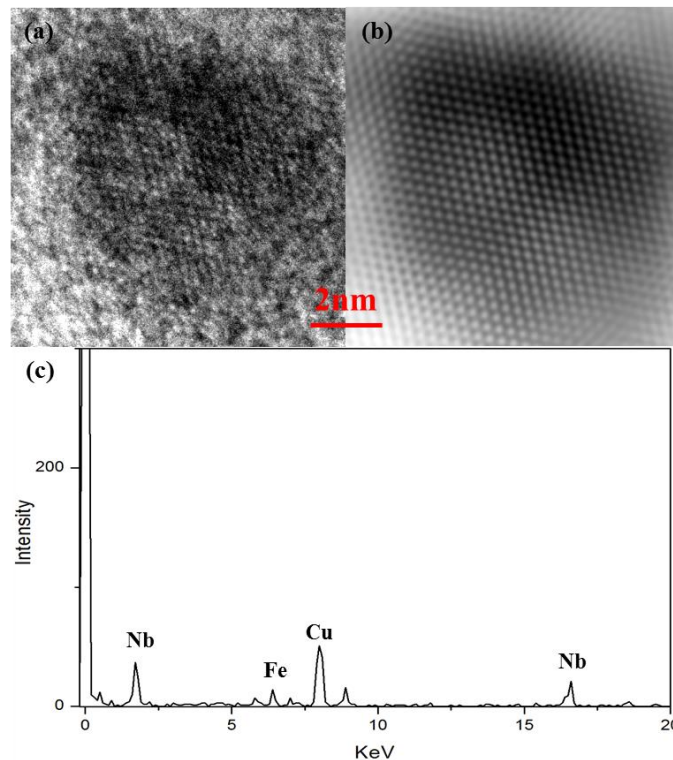


Fig. 6.30 Precipitate in carbon replica specimen for Nb steel after heat treatment at 1200 °C for 10 s followed by deformation at 850 °C with the rolling schedule D-10: (a) HRTEM image of a nanoscale precipitate; (b) IFFT on the particle shown in (a); (c) EDX analysis of the small particle shown in (a).

The chemical compositions of the SIP after heat treatment at 1200 °C for 100 s followed by finish rolling was the same as with the heat treatment for 10 s at 1200 °C. The particles after finish rolling with the schedules of A-100, B-100, C-100 and D-100 were identified as NbC, which were measured from IFFT image and EDX spectroscopy with the lattice parameter of 0.447 nm.

### 6.3.3.2 Nb-Ti steel

The HRTEM images of cuboid precipitates are presented in Figs. 6.31-6.35 from the Nb-Ti steel specimen with the same rolling schedule as for the Nb steel. The structure and the composition of the SIP were analysed by IFFT images and EDX spectra. The IFFT images of Figs. 6.32 and 6.33 suggest that those particles have a d spacing about 0.21 nm along the zone axis of  $[100]_{MC}$ . The EDX spectrum shows the Ti M and Nb L lines. The  $d_{(002)}$  spacing of (Nb, Ti)C is about 0.216 nm with the lattice parameter of 0.432 nm [205]. Therefore, the particles in Figs. 6.31-6.35 are identified as (Nb, Ti)C in the Nb-Ti steel.

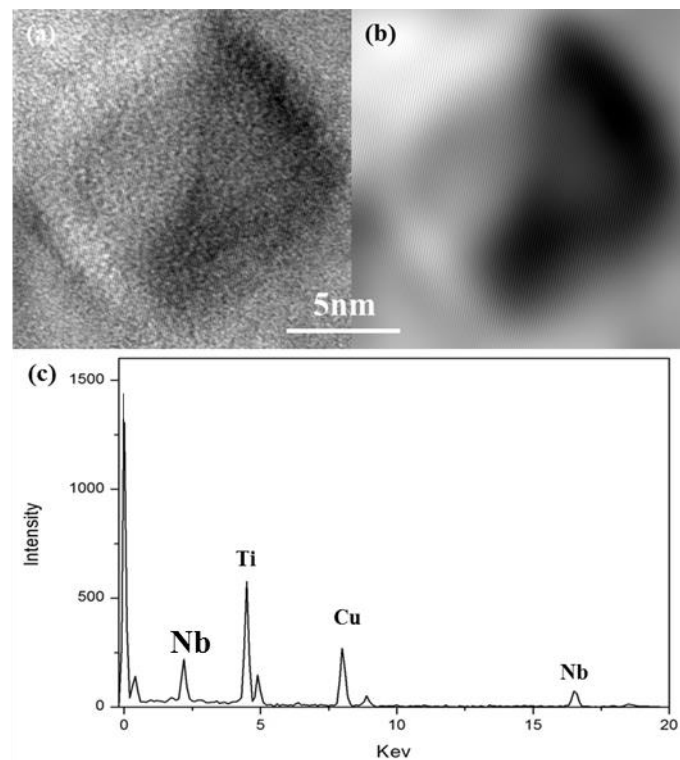


Fig. 6.31 Precipitate in carbon replica specimen for Nb-Ti steel after heat treatment at 1200 °C for 10 s followed by deformation at 850 °C with rolling schedule A-10, (a) HRTEM image of a small precipitate; (b) IFFT on the particle shown in (a); (c) EDX analysis of the small particle shown in (a).

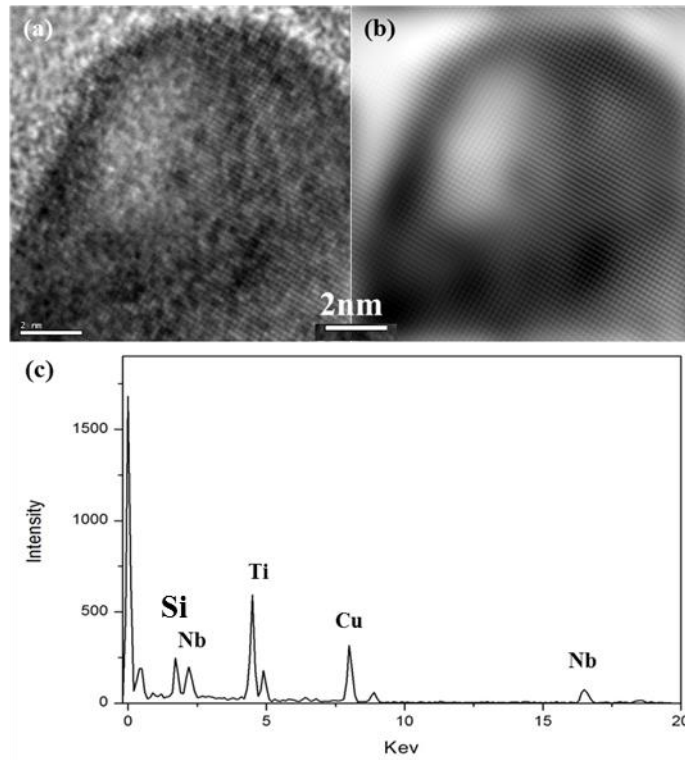


Fig. 6.32 Precipitate in carbon replica specimen for Nb-Ti steel after heat treatment at 1200 °C for 10 s followed by deformation at 850 °C with rolling schedule B-10, (a) HRTEM image of a small precipitate; (b) IFFT on the particle shown in (a); (c) EDX analysis of the small particle shown in (a).

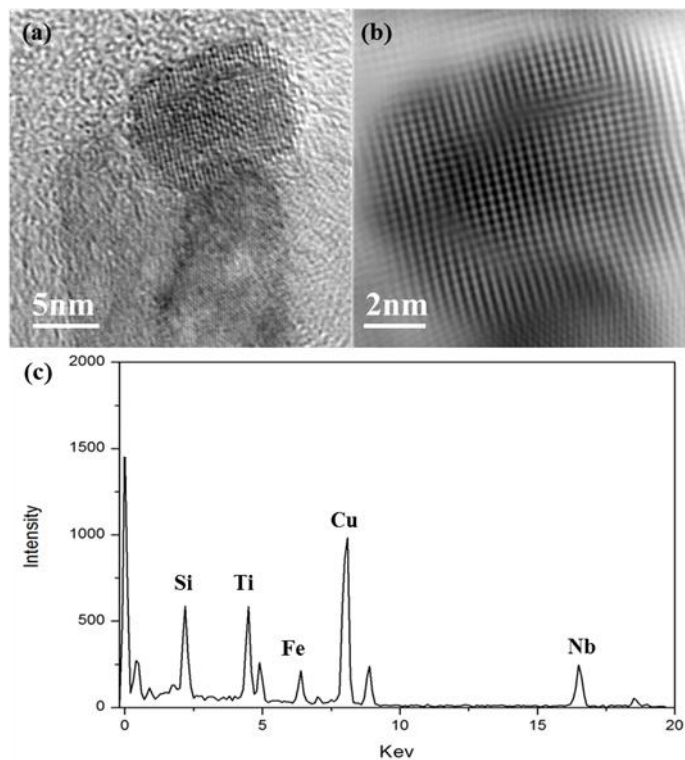


Fig. 6.33 Precipitate in carbon replica specimen for Nb-Ti steel after heat treatment at 1200 °C for 10 s followed by deformation at 850 °C with rolling schedule C-10, (a) HRTEM image of a small precipitate; (b) IFFT on the particle shown in (a); (c) EDX analysis of the left smallest particle indicated in (a); (d) EDX analysis of the right side particle indicated in (a).

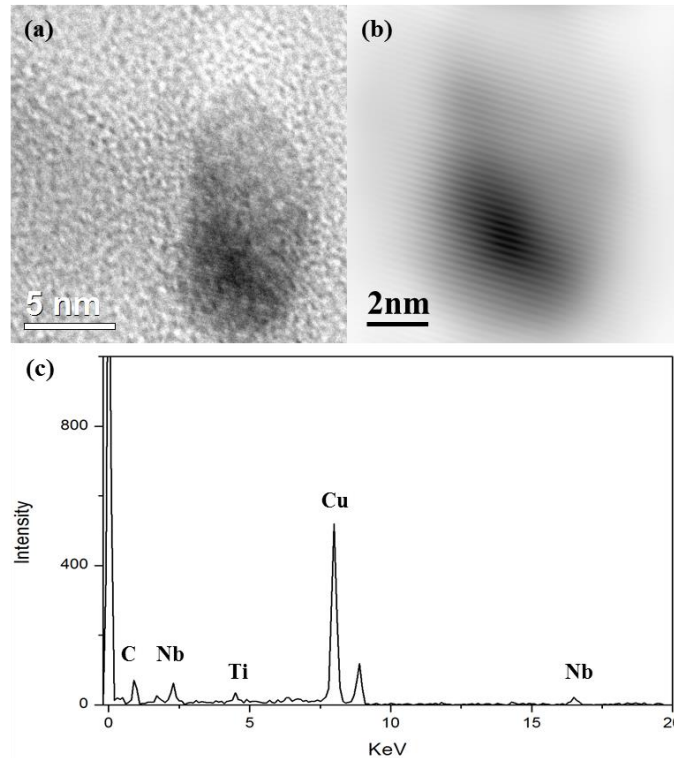


Fig. 6.34 Precipitate in carbon replica specimen for Nb-Ti steel after heat treatment at 1200 °C for 10 s followed by deformation at 850 °C with rolling schedule D-10, (a) HRTEM image of a small precipitate; (b) IFFT on the particle shown in (a); (c) EDX analysis of the small particle shown in (a).

After heat treatment at 1200 °C for 100 s followed by finish rolling with the schedules of A-100, B-100, C-100 and D-100, the microstructure and the composition of SIP were also analysed by HRTEM, EELS and EDX. The SIP content was the same as with the isothermal holding for 10 s at 1200 °C, with the Ti and Nb line presented in the EDX spectrum. Therefore, the precipitation after deformation by the schedules A-100, B-100, C-100 and D-100 was confirmed as (Ti, Nb) C.

#### 6.4 Nano-scale cementite in the deform-induced ferrite

Nanoscale cementite was observed in the deform-induced ferrite. Typical morphologies of cementite after finish rolling using the D-10 schedule are shown in Fig. 6.35. Bright field images, Fig. 6.35 (a) and (b), show nanoscale cementite particles in the ferrite matrix (red arrow) for both Nb and Nb-Ti steels with few of them sited on sub-grain boundaries. The diffraction pattern in Fig. 6.35 (c), which corresponds to the image of Fig. 6.35 (b), shows the orientation relationship of the body-centred cubic ferrite matrix and the orthorhombic cementite. Fig. 6.35 (d) shows a lattice image of a nanometer-sized cementite particle taken from the same sample as shown in Fig. 6.35 (a). The two-dimensional inverse fast Fourier transform (IFFT) (Fig. 6.35 (e)) with corresponding diffractogram (Fig. 6.35 (f)) was used to

analyse the lattice spacing and orientation shown in Fig. 6.35 (d). Using the diffraction spots from the corresponding fast Fourier transformation of the image, the TEM observation is along the zone axis of  $[2\bar{4}5]_{Fe_3C}$  with the intersection of  $(\bar{2}10)$  and  $(132)$  as  $120^\circ$ . The ferrite d spacing was identified as  $d_{(01\bar{1})}$ ,  $\sim 0.202\text{nm}$ . In Fig. 6.36 (f), the diffraction spot marked by the red arrow was a result of Moiré fringing with the spacing of parallel Moiré fringes about 0.53 nm. The Moiré fringes were produced due to the two interaction vectors from the cementite ( $d_{(132)}$ ) and ferrite ( $d_{(01\bar{1})}$ ) with the intersection angle  $\beta$  of  $8.5^\circ$ . Then the spacing of Moiré fringes can be calculated using the Eq. (6.1) [206]:

$$L = \frac{d_{ferrite} \times d_{Fe_3C}}{((d_{ferrite} - d_{Fe_3C})^2 + d_{ferrite} \times d_{Fe_3C} \times \beta^2)^{1/2}} \quad (6.1)$$

where L is the spacing of Moiré fringe with the distance of 0.53 nm, and  $d_{ferrite(01\bar{1})}$  is the spacing of  $(01\bar{1})$  about 0.202 nm. Thus, the d spacing of cementite can be calculated using Eq. (6.1) to be 0.159 nm, which is close to the  $d_{(132)}$  spacing of  $Fe_3C$  as 0.153 nm. This therefore confirms that the particle was  $Fe_3C$  imaged along the zone axis of  $[2\bar{4}5]$ .

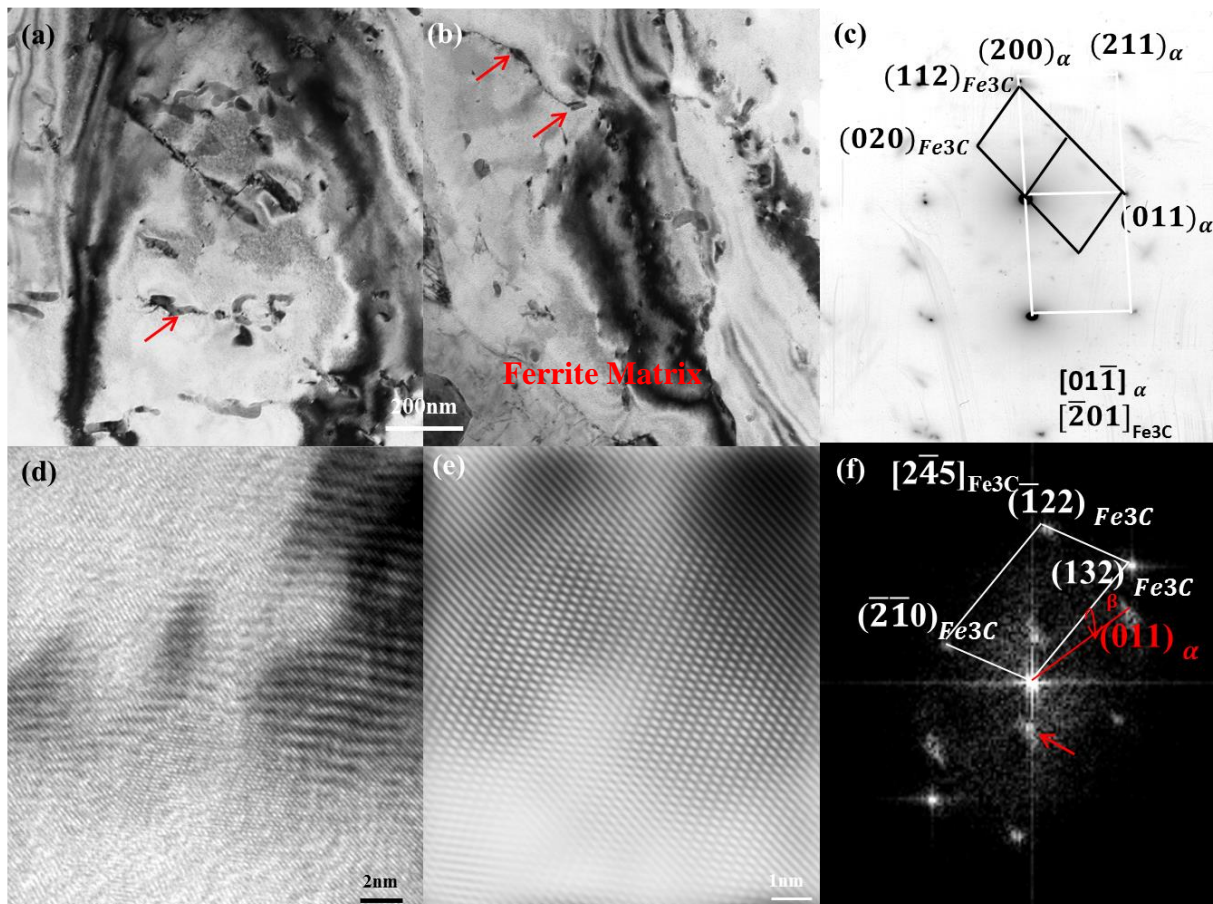


Fig. 6.35 The nanometer-sized  $Fe_3C$  with the rolling schedule of D-10: (a) Bright-field TEM micrograph of nanoscale cementite in the Nb steel and (b) Bright-field TEM micrograph of nanoscale cementite in the Nb-Ti

steel; (c) corresponding electron diffraction pattern from (b); (d) HRTEM image of one nanoscale cementite; (e) IFFT lattice image from (d); (f) the corresponding fast Fourier transformed diffractogram.

## 6.5 Vickers hardness

The microhardness was measured immediately following: (1) rough rolling and (2) after subsequent rapid reheating followed by water quenching. For the Nb steel, the microhardness after condition (1) was  $205.7 \pm 2.6$  Hv and after condition (2) was  $239.9 \pm 3.9$  Hv. The microhardness for the Nb-Ti steel following condition (1) was  $198.2 \pm 3.6$  Hv and after condition (2) was  $210.6 \pm 3.3$  Hv.

The Vickers microhardness was measured after finish rolling for the Nb and Nb-Ti steels, Figs. 6.36 and 6.37, respectively. The microhardness after finish rolling with a strain of 0.3 followed by immediate water quenching (A-10 and A-100) was higher than the hardness after heat treatment for both Nb and Nb-Ti steels, as shown in Fig. 6.36 and 6.37. The microhardness for both steel compositions rapidly decreased when the steels were held for 10s after deformation at 850 °C (B-10 and B-100). Beyond this, the hardness slightly increased with increasing the strain to 0.6 (C-10 and C-100), and increased with isothermal hold for 10s (D-10 and D-100). However, the microhardness at D-10 and D-100 was still lower than that at A-10 and A-100 for both Nb and Nb-Ti steels. The variety of microhardness for Nb and Nb-Ti steels were due to the balance between the significantly reduced grain size in the normal direction, and the formation of the DIFT. The values of microhardness were higher for the Nb steel compared to the Nb-Ti steel for each processing condition.

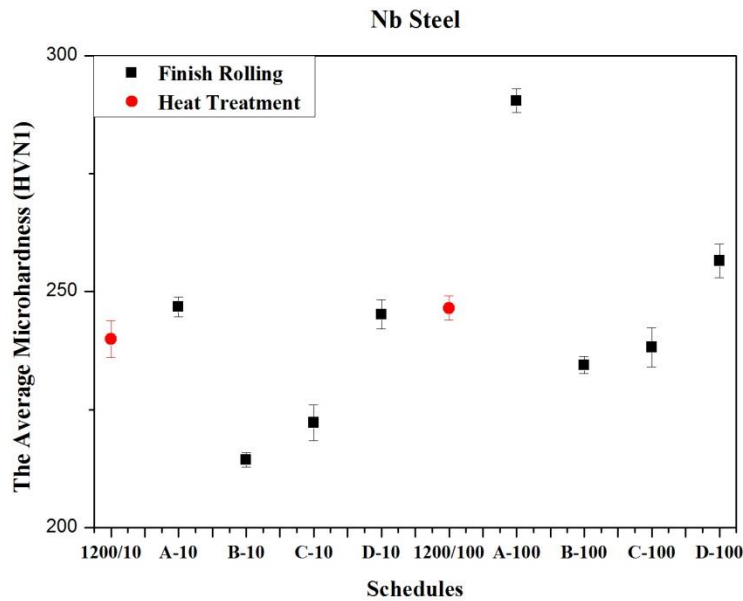


Fig. 6.36 Vickers micro-hardness values for Nb steel as a function of different rolling schedules (Fig. 3.5).

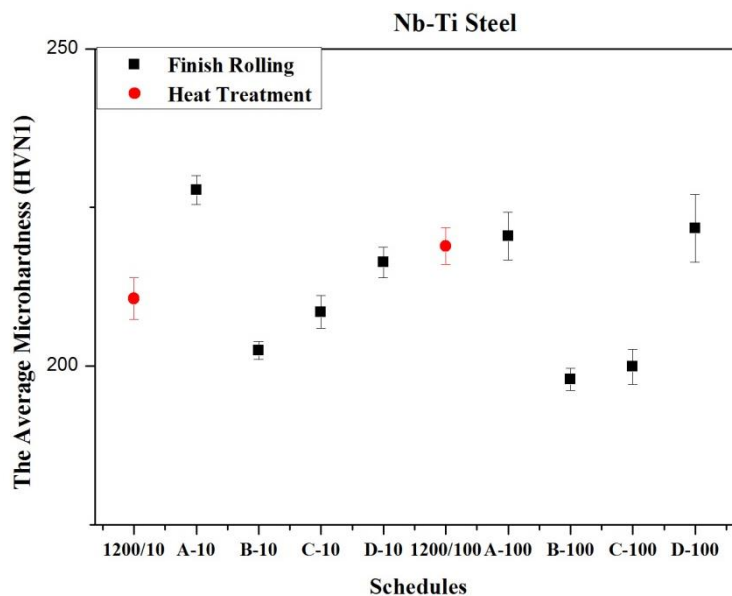


Fig. 6.37 Vickers micro-hardness values for Nb-Ti steel as a function of different rolling schedules (Fig. 3.5).

## 6.6 The ultrafine grains after a new TMCP rolling schedule

The difference between the new thermomechanical process and the conventional methods for producing DIFT [31,78,207] was the introduction of an additional heat treatment process between deformations. To further test the effect of this new TMCP on DIFT and therefore on the refinement of the final grain size, an additional test program schedule was undertaken, as shown in Fig. 6.38. The Nb-Ti steel specimen was first rough rolled at 850 °C, and then the temperature was rapidly increased to 1200 °C and held for 10 s. Following this, the

temperature was reduced to 850 °C and deformed with three passes, and then, finally, rapidly air cooled to 500 °C with a cooling rate of 20 °C/s, then at 2 °C/s to room temperature. The cooling schedule was used to simulate the coiling process. The final average ferrite grain size from the Nb-Ti steel using this new TMCP route was measured at about  $1.40 \pm 0.05 \mu\text{m}$  by EBSD shown in Fig. 6.39 (a). Fig. 6.39 (b) shows a typical misorientation profile across a few ferrite grains along the line shown in Fig. 6.39 (c). As expected, a high misorientation angle was observed across adjacent grain boundaries. Therefore, this new TMCP route produced an ultra-fine ferrite grain size with high angle grain boundaries attributed to DIFT of austenite to ferrite.

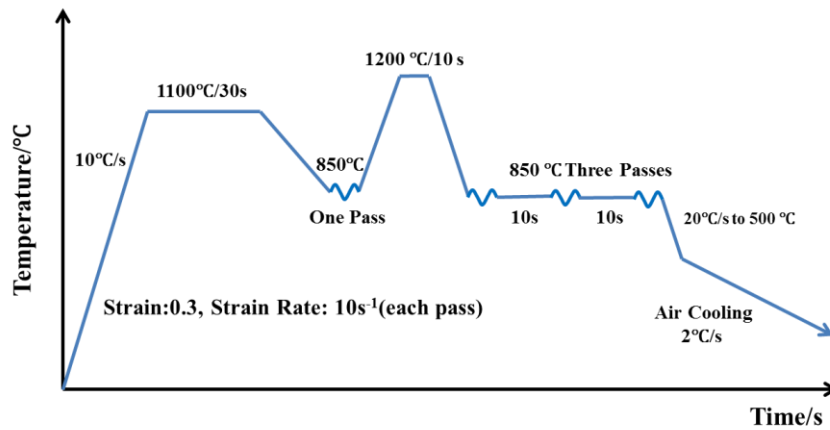


Fig. 6.38 Laboratory rolling schedule for the production of ultrafine grains on the Nb-Ti steel.

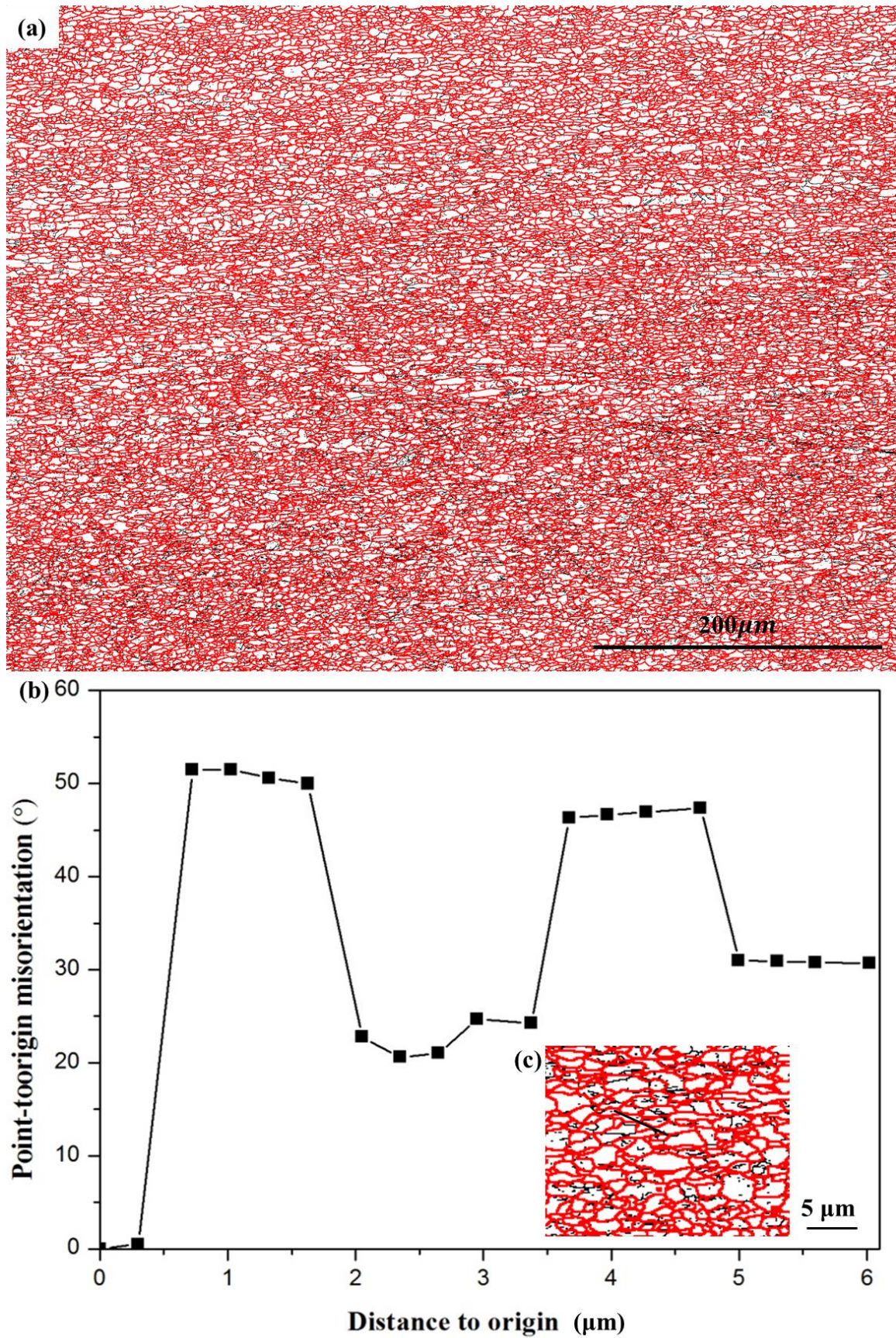


Fig. 6.39 (a) Ultra-fine grain boundary with IPF maps obtained by EBSD from Nb-Ti steel after deformation by the process shown in Fig. 10; (b) Point-to-origin misorientation profiles from (a); (c) grain boundaries with higher magnification from (a) (labelled).

## 6.7 Summary

In this chapter, the effect of different finish rolling schedules shown in Fig. 3.5 on the microstructures and the SIP for Nb and Nb-Ti steels have been analysed using OM, TEM, HRTEM, EELS and EDX, as well as Vickers microhardness. The microstructure changed from single phase after rough rolling to dual-phase of martensite and DIFT after finish rolling at 850 °C, Figs. 4.1, 4.2 and Figs. 6.1-6.16. The average prior-austenite size and the volume fraction of DIFT were calculated as a function of different rolling schedules shown in Figs. 6.17 and 6.18. With heat treatment at 1200 °C for 100 s followed by finish rolling, the prior-austenite grain size was slightly larger than that for 10 s holding at 1200 °C, compared with the same finish rolling schedule. As expected, the prior austenite grain size decreased in the normal direction with increased strain for Nb and Nb-Ti steels. When compared with the water quenched specimens, the grain size also decreased after isothermal holding for 10 s at the deformation temperature under the same deformation strain, due to the increasing volume fraction of DIFT.

DIFT occurred on and within the elongated prior-austenite grains during finish rolling as a result of the introduction of the reheat at 1200 °C. The volume fraction of DIFT increased with the increasing applied strain and isothermal hold of 10 s after deformation.

The size distribution, volume fraction and the composition of the SIP was analysed by TEM, EDX and EELS using the carbon replica specimens. The peak of the size distribution of precipitation is shifted from the range of 8-10 nm to the range of 6-8 nm, when increasing the deformation strains from 0.3 to 0.6. The average size of precipitates decreased with increasing the strain or adding 10 s holding after deformation. The compositions were detected from typical precipitates using EDX. For the Nb steel, the SIP was NbC. For Nb-Ti steel, they were (Ti, Nb)C. SIP as a function of the finish rolling parameters in the Nb-Ti steel followed a similar trend to that in the Nb steel. The volume fraction of precipitates in the Nb steel was slightly less than that in the Nb-Ti steel at the beginning, but after increasing the strain to 0.6, it became higher than that in the Nb-Ti steel.

The Vickers microhardness was measured as a function of rolling parameters shown in Figs. 6.36 and 6.37 for Nb and Nb-Ti steels, respectively. The microhardness for the Nb steel was higher than that for Nb-Ti steel. The trend of micro-hardness with different rolling schedules for Nb and Nb-Ti steels was mainly influenced by the average grain size and the DIFT

formation [187]. Therefore, after holding for 10 s at 850 °C, the microhardness for both Nb and Nb-Ti steels rapidly decreased, because of the increased volume fraction of DIFT, and then slightly increased with increasing the strain, because of the refinement of grain size.

The new TMCP combined with designed cooling rate (shown in Fig. 6.38) finally refined the ferrite grain size to 1.4  $\mu\text{m}$  with HAGBs, which attributed to the DIFT contribution.

## CHAPTER 7: DISCUSSION

### 7.1 Microstructures

For Nb and Nb-Ti steels, the specimens have been rough rolled, reheated to 1200 °C for different times and finish rolled using the schedules shown in Figs. 3.3-3.5. For rough rolling, the purpose was to maximise the number density of SIP without recrystallization. To choose the rough rolling temperature, the simulated PTT (precipitation-time-temperature) curve, the 5% recrystallization curve and the 95% recrystallization curve obtained by different models were used to calculate the theoretical values of the fully recrystallization temperature ( $T_1$ ) and recrystallization stop temperature ( $T_s$ ) and the nose temperature of precipitation. The microstructures after rough rolling at different temperatures were also observed by OM, which deduced that the actual  $T_1$  and  $T_s$  are similar to the calculated recrystallization temperatures. The volume fraction of the precipitation for both Nb and Nb-Ti steels was also calculated by TEM after deformation at different temperatures. As a result of this, the final rough rolling temperature was determined to obtain the non-recrystallization structures and maximum number density of SIP.

Using the determined rough rolling temperature followed by heat treatment at 1200 °C for different times, the prior-austenite grain coarsening kinetics could be established as a function of holding times. Then, the microalloyed Nb in solution during heat treatment and its effect on grain growth could also be analysed.

Following this, after heat treatment at 1200 °C for 10 s and 100 s, the finish rolling was investigated with different schedules. The deformation microstructures of DIFT and martensite have been observed by OM and SEM.

#### 7.1.1 Prior-austenite grain analysis

##### 7.1.1.1 Rough rolling process

The microstructures after rough rolling with different temperatures have been observed using OM and shown in Figs. 4.1 and 4.2. There were fully equiaxed prior-austenite grains for the rolling temperatures between 1100 °C and 1000 °C for Nb and Nb-Ti steels, which indicated that the full recrystallization had occurred (Figs. 4.1 (a-c) and 4.2 (a-c)). The partial recrystallization structure was obtained with the deformation temperature at 950 °C. With rough rolling temperatures at 900 °C and 850 °C, the prior-austenite grains were fully

elongated. The observed microstructures at different rough rolling temperatures fit well with the simulated full recrystallization and non-recrystallization regions for Nb and Nb-Ti steels shown in Fig. 4.1.

The average prior-austenite grain size after rough rolling at different temperatures was measured and is shown in Table 4.1 and Fig. 4.4. The average grain size remained constant after deformation in the full recrystallization region, and then increased in the rolling direction (RD) when the rolling temperatures were reduced from 950 °C to 850 °C, shown in Fig. 4.4. The average prior-austenite grain size in the RD for the Nb steel was larger than that for Nb-Ti steel at the beginning, and then it gradually became similar as the rolling temperature decreased to 850 °C.

Normally, the final step of thermomechanical processing (TMP) occurs in the fully austenite non-recrystallisation region to avoid the partial recrystallization structures and refine the final grain size. In this study, the rough rolling temperature at 850 °C for both Nb and Nb-Ti steels resulted in non-recrystallized prior austenite microstructures. Moreover, depending on the simulated PTT curve (Fig. 4.1), specimens deformed at 850 °C exhibited more rapid precipitation kinetics than at other rolling temperatures. Therefore, the rough rolling temperature for Nb and Nb-Ti steels was designed at 850 °C.

#### 7.1.1.2 Heat treatment process

After rough rolling at 850 °C, the specimens for Nb and Nb-Ti steels were reheated to 1200 °C for different times (Fig. 3.4). OM microstructures are shown in Figs. 5.2 and 5.3. The average prior-austenite grain size was measured and presented in Table 5.1. The prior-austenite grains continually grew with increasing holding times at 1200 °C for the Nb and Nb-Ti steels. The grain growth rate in the Nb steel was much quicker than that in the Nb-Ti steel, which can be explained by the following analysis. The reheating temperature of 1200 °C for this investigation was higher than the equilibrium dissolution temperature of niobium and carbon in the Nb steel, calculated using the modified solubility product which Palmiere et al. [208] gave as:

$$\log [Nb][C]=2.06-6700/T \quad (7.1)$$

However, for the Nb-Ti steel, the reheating temperature was lower than the dissolution temperature of titanium, carbon and nitrogen precipitates using previously published solubility products for these precipitates [209–211]. With the presence of the more stable TiNb carbonitrides in the Nb-Ti steel, there was a much higher pinning force suppressing

grain coarsening, compared to the Nb steel, resulting in a slower growth rate in the Nb-Ti steel during the entire reheating period.

To further analyse the grain growth mechanism combined with Zener pinning and solute drag effects, there are several models to explain that in different systems. The grain growth behaviour [42,212] of austenite during the isothermal holding period can be understood using the theory developed by Burke [213], Smith [214] and Beck [215]. Following their theories, Feltham [181] developed a more rigorous theory by using the grain diameters and grain boundary curvatures. He further indicated that the variable grain diameter to the time of isothermal growth can be calculated by Eq. (7.2)

$$(D^*)^2 - (D_0^*)^2 = (\lambda Va\sigma/h)t \exp(-H/TK) = K \times t \quad (7.2)$$

where  $D_0^*$  is the grain size at  $t=0$ s;  $D^*$  is the grain diameter at a certain time;  $\lambda$  is the number constant of order unity;  $V$  is the volume per atom;  $a$  is lattice spacing;  $\sigma$  is the specific grain-boundary energy;  $H$  is the activation energy for grain boundary self-diffusion;  $h$  is Planck's constant. Under isothermal conditions, Eq. (7.2) is equal to  $K \times t$  and  $K$  is a constant. Using Eq. (7.2) and the grain diameter data at the holding time of 0s and 10 s, the constant of  $K$  is 174.9 in the Nb steel and 23.4 in the Nb-Ti steel. The simulation of austenite grain diameters with the different values of  $K$  for the Nb and Nb-Ti steels by Eq. (7.2) was shown in Fig. 7.1. Using this relationship, the predicted austenite grain diameter in the Nb steel was 94.7  $\mu\text{m}$  at 20 s, 111.7  $\mu\text{m}$  at 40 s and 151.5  $\mu\text{m}$  at 100 s, as well as 423  $\mu\text{m}$  at 1000 s (Fig. 7.1 (a)). In the Nb-Ti steel, they are 56.7  $\mu\text{m}$  at 40 s, 95.5  $\mu\text{m}$  at 100 s and 160.3  $\mu\text{m}$  at 1000 s (Fig. 7.1 (b)). As shown in Fig. 7.1, the grain sizes predicted for the Nb and Nb-Ti steels by the Feltham theory gave a very satisfactory description of the experimental data, with the exception of the simulation data at 1000 s for the Nb steel, where the prediction of grain size was about 5x larger than the experimentally measured value.

Considering the interaction between second phase particles and a migrating grain boundary, Zener and Smith [214] proposed an analytical model for the pinning effect of particles on grain growth. Based on this theory, grain growth can be stopped when the free energy to pull the boundary away from the particles equals the free energy from retarding boundary motion through the particles. Therefore, it is predicted that the ratio  $D/r$  should be proportional to  $1/f_v$ , where  $D$  is the average grain diameter,  $r$  is the radius of the second phase and  $f_v$  is the volume fraction of the second phase. However, Zener's theory failed to account for the pinning forces produced by the relative positions of particles with respect to the boundary. He

also only accounted for the particle-boundary interactions during normal coarsening, thus omitting the interaction dynamics during abnormal grain growth. Therefore, the original model of Zener for the pinning effect of second-phase particles on grain boundaries was subsequently modified by Hellman and Hillert [216], illustrating that the mean grain size with volume fraction and diameter of particles can be expressed by:

$$D_{max}/D_p = 4((D_{max}/\bar{D}) - 1) / 3f_v \quad (7.3)$$

where  $D_{max}$  is the largest limiting grain diameter;  $D_p$  is the mean second phase particle diameter; the  $\bar{D}$  is the mean grain diameter;  $f_v$  is the particle volume fraction. Hellman and Hillert also indicated that the ratio of  $D_{max}/\bar{D}$  should be in the range of 1-2, when the limiting grain growth occurred. If  $D_{max} > 2\bar{D}$ , the grains would grow without being limited, called abnormal grain growth. Depending on the experimental data from the present investigation, the abnormal grain growth was not observed in either the Nb or the Nb-Ti steels during the isothermal holding at 1200 °C until 1000 s. Considering the experimental data for a holding time of 0 s in these steels, the ratio of  $D_{max}/\bar{D}$  is 1.5 for the Nb steel and 1.8 for the Nb-Ti steel. Then, accounting for the given data of precipitates volume fraction ( $f_v$ ) and the average diameter ( $D_p$ ) in Table 5.2, the limiting prior austenite grain size would be calculated by Eq. (7.3), shown in Fig. 7.1. For the Nb steel, the predicted grain sizes are 65.8  $\mu\text{m}$  at 0 s, 95.9  $\mu\text{m}$  at 10 s, 126.5  $\mu\text{m}$  at 20 s, and 176.8  $\mu\text{m}$  at 40 s, as well as 770  $\mu\text{m}$  at 100 s. The predicted grain sizes using Eq. 7.3 corroborate well with the experimental data, except at 100 s. The reason for this behaviour will be explained later by taking into account solute drag. For the Nb-Ti steel, the average prior-austenite grain sizes are 32.4  $\mu\text{m}$  at 0 s, 38.2  $\mu\text{m}$  at 10 s, 45.3  $\mu\text{m}$  at 40 s, 52.6  $\mu\text{m}$  at 100 s and 85.4  $\mu\text{m}$  at 1000 s. The predicted data of prior-austenite grain size are lower than the experimental data over the entire holding period, due to the data predicted using Eq. (7.3) over-estimating the pinning effect exerted on the boundaries by second phase particles. The reason for this is that the volume fraction of precipitates in the Nb-Ti steel includes a number of particles larger than 30 nm, and the larger the precipitates, the less the Zener pinning effect on grain boundaries.

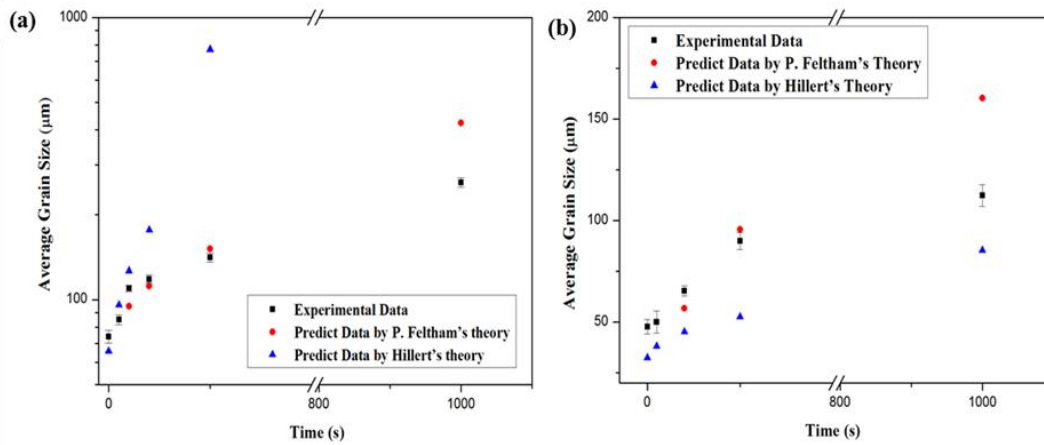


Fig. 7.1 Simulated the average prior-austenite grain size in Nb and Nb-Ti steels as a function of isothermal holding times using Eqs. 7.2 and 7.3, compared with experimental data, (a) Nb steel; (b) Nb-Ti steel.

Furthermore, as Hellman and Hillert's theory only considers the effect of the Zener pinning effect on boundaries, the predicted data of the austenite grain diameter is larger than the experimental data when holding for 100 s for the Nb steel. This is because for a longer isothermal holding time, most of the niobium, carbon and nitrogen rapidly dissolved into the matrix in the Nb steel, shown in Table 5.2. The Zener pinning effect by precipitates on a grain boundary becomes weak after holding for 100 s at 1200 °C. However, the grain diameter does not grow as large as would be predicted. The result indicates that solute drag represents another force acting to retard the motion of grain boundaries. To study the effect of solute drag on the migration of a grain boundary, Fan et al. [217] developed the grain power growth law followed as:

$$R_t^m - R_0^m = kt \quad (7.4)$$

Where  $R_0$  is the initial average grain size,  $R_t$  is the average grain size at time  $t$ , and  $k$  is the kinetic coefficient,  $m$  is the growth exponent. According to Fan's theory, if the lattice diffusion is much slower than grain boundary migration,  $m$  is close to 3, with the motion of the grain boundary controlled by lattice diffusion, regarded as an Ostwald ripening process. For solute drag,  $m$  is between 2 and 3, which depends on the ratio of lattice diffusion and grain boundary mobility. In the current work,  $m$  is assumed to be 2.5 and the constant  $K$  is calculated by the average grain size at 0 s and 10 s and is equal to 1950.5. The predicted grain size by Eq. (7.4) is much better than Eq. (7.2), when compared with the experimental data.

Cahn and other researchers [158,218–220] also studied the effect of solute drag on migration of a grain boundary from a different aspect. Cahn suggested that the grain boundary

migration is affected by the interaction of impurity atmosphere and predicted that, according to the migration velocity and driving force, the average grain size at time  $t$  is equal to  $V \times t$ , where  $V$  is velocity of a mobile grain boundary. The velocity of a grain boundary can be expressed by

$$V = M_{eff} * F_{met} \quad (7.5)$$

where the  $M_{eff}$  is the grain boundary mobility and  $F_{met}$  the driving force for grain boundary migration. It is now necessary to evaluate the  $M_{eff}$  and  $F_{met}$ . Considering the effect of solute drag,  $M_{eff}$  is calculated by

$$1/M_{eff} = 1/M_0 + \lambda C_S (1/(1 + \omega^2 v^2)) \quad (7.6)$$

where  $\lambda$  is the constant,  $M_0$  is solute-free mobility and is expressed by

$$M_0 = \alpha D_{Fe}^I V_m \delta / (b^2 RT) \quad (7.7)$$

where  $\alpha$  is mobility factor which varies between 0.1 and 0.7 for steel,  $\delta$  is the grain boundary thickness,  $b$  is the Burgers vector, and  $D_{Fe}^I$  is the diffusion coefficient of Fe,  $V_m$  is the molar volume,  $C_S$  is solute atomic concentration and is given by

$$C_S = C_0 - f_p C_p \quad (7.8)$$

where  $C_0$  is the content of Nb in steels, and  $C_p$  is the content of Nb in precipitates. The  $M_{eff}$  can be simplified by assuming that the driving force of grain boundary migration is low:

$$M_{eff} = M_0 (1 + M_0 \lambda C_S)^{-1} \quad (7.9)$$

The driving force for grain boundary migration depends on the interaction between recrystallization and the Zener pinning

$$F_{met} = F_\gamma - P_z \quad (7.10)$$

where  $F_\gamma$  is the recrystallisation driving force and is given by

$$F_\gamma = 0.5 \mu \rho b^2 \quad (7.11)$$

where  $\mu$  is Shear modulus,  $\rho$  is dislocation density,  $b$  is Burgers vector.  $P_z$  is the Zener pinning force and can be shown to be

$$P_z = \phi f_p r_p^{-1} \quad (7.12)$$

where  $f_p$  is the volume fraction of precipitates,  $r_p$  is the radius of precipitates and  $\phi$  is constant and is given by

$$\phi = (1.5-3) \times (1.3115 - 0.0005T) \quad (7.13)$$

With all the equations from (7.5) to (7.13), the predicted average grain size is shown in Fig.7.2.

From Fig. 7.2, the calculated average grain size taking into account both particle pinning and solute drag effect provides a better fit to the experimental data than from that of Feltham and Hellman and Hillert's theories alone. From Fan's theory, the average grain size is slightly smaller than the experimental data from 20 s to 100 s. At 1000 s, the simulated average grain size is 331.2  $\mu\text{m}$ , which is a better fit to the experimental data than from that predicted by Feltham's theory. In Cahn's theory, the predicted average grain size is lower at the short holding times, and then it gradually approaches the experimental data with the increasing holding times. The comparison of solute drag and Zener pinning can be made by comparing the predictions from Hellman and Hillert's and Cahn's theories. Using Hellman and Hillert's theory, without considering the solute drag effect, the simulated grain size for a 100 s hold was substantially overestimated at 770  $\mu\text{m}$  compared to the measured value of 141  $\mu\text{m}$  in the Nb steel. When considering the Zener pinning and solute drag effects at 100 s, the predicted grain size using Cahn's theory was much lower at 273  $\mu\text{m}$ . This shows that the effect of solute drag on grain growth could not be neglected for Nb steel at 100 s.

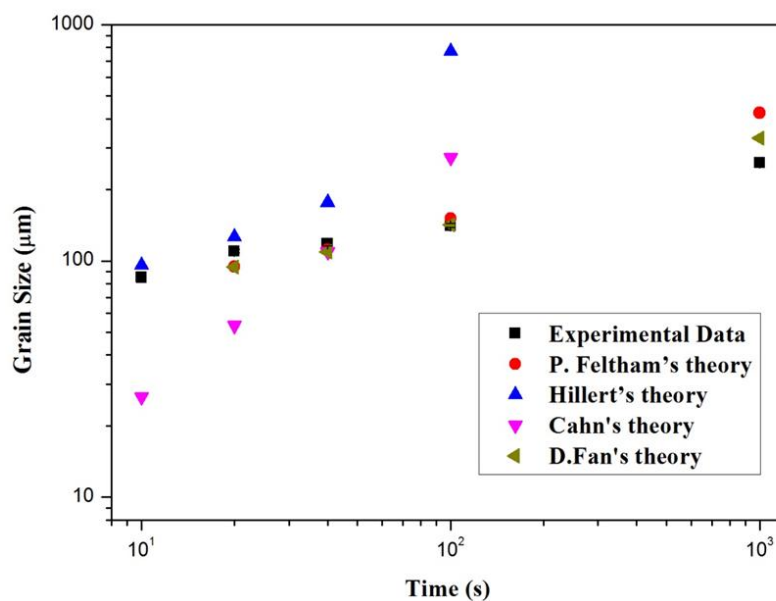


Fig. 7.2 Simulated the average grain size in Nb steel considering the solute drag theory, compared with experimental data.

In summary, for the Nb steel, the migration of grain boundaries was suppressed by both solute drag and Zener pinning for times up to 100 s, but for longer times solute drag was the main contribution, since the volume fraction of precipitates available at the grain boundaries to promote Zener pinning was small. The solute drag effect was more significant for the Nb

steel than it was for the Nb-Ti steel after holding for a longer time, which is a result of most of the niobium and carbon being dissolved into the austenite in the Nb steel after holding for 100 s at 1200 °C (Table 5.2).

#### 7.1.1.3 Finish rolling process

Figs. 6.1-6.16 show the observations of elongated prior austenite grain structures after finish rolling at 850 °C with different rolling schedules (Fig. 3.5). The prior-austenite grain size in the ND was measured and is listed in Table 6.1 and Fig. 6.17. From Fig. 6.17, the mean grain size gradually reduced with the increasing strain or adding isothermal holding time after deformation. The reason that the prior-austenite grain size in the ND was refined by isothermal holding for 10 s at the deformation temperature is due to the rapidly increasing amount of DIFT on grain boundaries.

The refinement of prior-austenite grains in ND as a function of strain can be simulated by Sellars' theory [221] followed by:

$$d(t)=0.9 \times d_0^{0.67} \times \varepsilon^{-0.67} \quad (7.14)$$

Where  $d_0$  is the reheated grain size and  $\varepsilon$  is the true strain of the final rolling deformation. The predicted data of the grain diameter in the Nb steel are 39.5  $\mu\text{m}$  (A-10), 24.9  $\mu\text{m}$  (C-10) and 55.5  $\mu\text{m}$  (A-100) as well as 34.9  $\mu\text{m}$  (C-100) as shown in Fig. 7.3. In the Nb-Ti steel, they are 27.7  $\mu\text{m}$  at A-10, 17.4  $\mu\text{m}$  at C-10 and 38.9  $\mu\text{m}$  at A-100 as well as 24.5  $\mu\text{m}$  at C-100 (Fig. 7.3). The predicted prior-austenite grain sizes decreased with the increasing strain and fit well with their corresponding experimental data for Nb and Nb-Ti steel, except at A-100 for Nb-Ti steel (Fig. 7.3). The predicted data is higher than the experimental data, which can be explained by the higher volume fraction of DIFT on grain boundaries for A-100 than A-10 for Nb-Ti steel (Table 6.1).

The kinetics of prior-austenite grain growth during deformation is also related to the SIP. The Hellman and Hillert [216] model was used to simulate the mean prior-austenite grain size with volume fraction and diameter of second phase particles. Considering the experimental data of the maximum and mean grain size at the rolling schedule of A-10, the ratio of  $\frac{D_{max}}{\bar{D}}$  is assumed to be 1.3 in Nb steel and 1.2 in Nb-Ti steel. Then, using the data of volume fraction ( $f_v$ ) and the average diameter ( $D_p$ ) of precipitates in Table 6.2, the simulated mean prior-austenite grain size was calculated by Eq. (7.3) and presented in Fig. 7.3 (a) for the Nb steel

and Fig. 7.3 (b) for Nb-Ti steel. The predicted grain sizes for Nb and Nb-Ti steels fit well with the experimental data after holding for 10 s at 1200 °C followed by different finish rolling schedules. When a holding time of 1200 °C for 100 s was used, the predicted grain sizes are higher than the experimental data, especially for the Nb-Ti steel. This is because the DIFT occurred on prior-austenite grain boundaries which reduced the measured grain size. Since a higher volume fraction of DIFT was measured after holding for 100 s than 10 s at 1200 °C (Table 6.2), the measured prior-austenite grains size was smaller than the calculated values. Therefore, the predicted data from Hellman and Hillert model is larger at 100 s than 10 s at 1200 °C.

In summary, the prior austenite grain size decreased with the increasing strain or adding 10s holding after deformation. For the Nb steel, the average grain size in the ND was larger than that in the Nb-Ti steel, because of the much larger initial prior austenite grain size arising from heating at 1200 °C for various times before deformation. The longer the holding time at 1200 °C, the larger the average grain size after finish rolling due to the initial larger grains before deformation. Moreover, most of the predicted average grain sizes from Sellars' and Hillert's theory are higher than the equivalent experimental data. This is because the predicted data by Sellars' and Hillert's theory does not consider the formation of DIFT on the prior austenite boundaries, which reduced the grain size for both Nb and Nb-Ti steels.

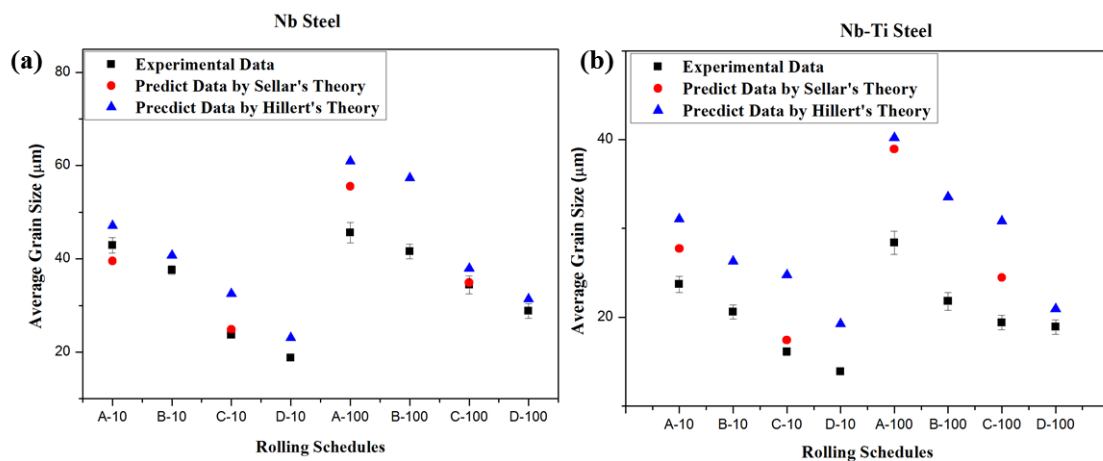


Fig. 7.3 Simulated average grain size with different rolling parameters shown in Fig. 3.5, compared with experimental data by Eqs. (7.3) and (7.14): (a) in the Nb steel; (b) in the Nb-Ti steel.

## 7.1.2 DIFT Analysis

### 7.1.2.1 Transformation mechanism of DIFT

The empirical formula is an efficient method to determine  $A_{r3}$ . In the present study, the experimental materials for Nb steel contains 0.065 wt% carbon and for Nb-Ti steel contains 0.067 wt% carbon. Therefore, the Tamura equation [93] is used in this study to estimate the  $A_{r3}$  for controlled rolled steels with a carbon content between 0.03-0.16 wt% and is expressed as:

$$A_{r3} = 910 - 310(\%C) - 80(\%Mn) - 20(\%Cu) - 15(\%Cr) - 55(\%Ni) - 80(\%Mo) \quad (7.15)$$

where the content of elements in Eq. 7.15 are listed in Table 3.1. The  $A_{r3}$  temperature is calculated as 827 °C in the Nb steel and 826 °C in the Nb-Ti steel, which are lower than the rough rolling temperature of 850 °C. Therefore, after rough rolling at 850°C followed by water quenching, the microstructure should be single phase martensite without the second phase of ferrite. The experimental results shown in Figs. 4.2 (f) and 4.3 (f) further showed that the microstructures of Nb and Nb-Ti steels after rough rolling consisted of single phase austenite without any ferrite structures.

Then, after heat treatment at 1200 °C for 10 s and 100 s followed by finish rolling at 850 °C with different schedules shown in Fig. 3.5, an amount of ferrite was observed formed on the grain boundaries (Figs. 6.1-6.17). With the same rough rolling and finish rolling parameters, the heat treatment at 1200 °C was the only difference and is therefore responsible for the observation of DIFT on the prior austenite grain boundaries. The microstructural observations therefore demonstrated that the phase transformation temperature ( $A_{r3}$ ) had increased to higher than the deformation temperature of 850 °C. The increased phase transformation temperature due to the heat treatment at 1200 °C could be explained from the free energy and kinetics of phase transformation.

First of all, it is known that as the austenite is rapidly cooled to the deformation temperature and deformed, part of the deformation energy will be stored in the austenite in the absence of any restoration phenomena with large undercooling [222]. Then, the free energy change of the  $\alpha/\gamma$  transformation can be increased by the deformation and undercooling compared with the equilibrium phase transformation free energy without deformation, which is expressed by:

$$\Delta G_v = V(\Delta G_{chem} + \Delta G_D + \Delta G_{\Delta T} - \Delta G_S) - A\sigma_{\alpha\gamma} \quad (7.16)$$

where  $\Delta G_{chem}$  is the chemical driving force;  $\Delta G_D$  is the deformation stored energy;  $\Delta G_{\Delta T}$  is undercooling driving force;  $\Delta G_S$  is the volume strain energy; and  $\sigma_{\alpha\gamma}$  is the boundary energy. From Eq. (7.16), this accumulated energy due to deformation and undercooling can raise the  $\gamma \rightarrow \alpha$  transformation temperature [30], regarded as the upper limit transformation temperature for DIFT,  $A_{rd3}$ . The reheat at 1200 °C increased the undercooling at the deformation temperature of finish rolling [223], which consequently increased the phase transformation temperature as a consequence of the accumulated energy, when compared with the rough rolling. This is consistent with the experimental results shown in Figs. 6.1-6.17 with the ferrite structures located on the grain boundaries and within grains.

Moreover, reheating at 1200 °C would also shorten the incubation time for ferrite phase transformation during finish rolling. Lange et al. [224] provided an equation to calculate the nucleation rate,  $\tau$  of new ferrite on a traditional disk-shaped pillbox nucleus, expressed as:

$$\tau = 12k_B T a^4 \sigma_{\alpha\gamma} / D_C^{\gamma} \bar{x} v_{\alpha} 2\Delta G_v^2 \quad (7.17)$$

where  $k_B$  is Boltzmann constant;  $D_C^{\gamma}$  is the diffusivity of carbon in austenite;  $v_{\alpha}$  is the volume of an atom of iron in ferrite;  $a$  is the average of the lattice parameters of both phases, ferrite and austenite;  $\bar{x}$  is the average carbon content in austenite in mole fraction;  $\Delta G_v$  is the volume free energy change associated with the formation of the nucleus;  $\sigma_{\alpha\gamma}$  is the interfacial energy; and  $T$  is the isothermal temperature. Eq (7.17), shows that reheating at 1200 °C for 10 s can increase the carbon content in austenite and also increase the free energy for phase transformation. Therefore, the incubation time of ferrite transformation was shortened during finish rolling making nucleation of DIFT more favourable than for rough rolling.

Finally, the prior-austenite grains during heat treatment at 1200 °C coarsened with a mean grain size of 86.4  $\mu\text{m}$  in the Nb steel, and 50  $\mu\text{m}$  in the Nb-Ti steel. However, the initial grain size before rough rolling was 40  $\mu\text{m}$  for the Nb steel and 30  $\mu\text{m}$  for the Nb-Ti steel. It is well known that the prior austenite grain size can influence the growth kinetics of idiomorphic ferrite through decomposition of austenite [225,226]. The volume fraction of the idiomorphic ferrite is directly proportional to the prior austenite grain size, which is expressed as:

$$\varepsilon_{\alpha} = \varepsilon_{\alpha}^{EQ} \left[ 1 - \exp\left(-\frac{8\pi}{15} \frac{12d_r}{a_3(d_1+d_2)} IV_v \alpha_3^3 t^{5/2}\right) \right] \quad (7.18)$$

where  $\varepsilon_{\alpha}^{EQ}$  is the equilibrium volume fraction of idiomorphic ferrite;  $d_r$  is the prior austenite grain size;  $d_1$ ,  $d_2$  and  $d_3$  are the inclusion diameters in a transversal and longitudinal section;  $V_v$  is the volume fraction of inclusions in the steels;  $\alpha_3$  is the three-dimensional parabolic thickening constant;  $t$  is the deformation time, which relate to the strain rate. Thus, as the prior austenite grain size increases, idiomorphic ferrite formation is promoted. Beynon et al. [227] also reported that a coarse austenite grain size appeared to be more favourable for DIFT under the condition of single pass rolling, because the formation of pro-eutectoid ferrite was prevented and produces large undercooling due to the extreme coarse austenite grain size.

To summarise, the DIFT from the austenite that occurred during finish rolling is due to the undercooling in austenite which increase the phase transformation free energy, the shortened the incubation time for ferrite transformation and the large austenite grains which are beneficial for the formation of idiomorphic ferrite within grains.

#### 7.1.2.2 The nanoscale cementite in DIFT

Fig. 6.44 shows nanoscale cementite in the DIFT, because the fast strain rate and the large undercooling limited the carbon diffusion during the phase transformation, which prevented the formation of pro-eutectoid ferrite. Then, according to the Kaufman-Radcliffe-Cohen (KRC) thermodynamic model [228], the austenite ( $\gamma$ ) to ferrite ( $\alpha$ ) and cementite ( $\text{Fe}_3\text{C}$ ) model can take place. Because the finish rolling was followed by water quenching with a fast cooling rate, the lamellar pearlite structures were avoided and displaced by an amount of nanoscale cementite. There are several researchers, such as Enomoto et al. [229] and Hurley et al. [230] who also detected that the carbon was enriched during transformation in DIFT, which would accelerate the nucleation of cementite. Moreover, Sun [207] also indicated that the existing transition zone in front of the  $\gamma/\alpha$  boundary or the depleted zone around sub-grain boundaries and dislocations in the  $\alpha$  region lead to the enrichment of cementite on them. The Fig. 6.35 (a) and (b) shows the high carbon phase of cementite that takes place on the grain boundaries and dislocations, which further supports Sun's theory.

#### 7.1.2.3 The effect of prior austenite grain size, deformation strain and SIP on the DIFT

The prior austenite grain size and the strain are the main factors that influence the volume fraction of DIFT. The volume fraction of DIFT in the Nb-Ti steel is higher than that in the Nb steel as shown in Fig. 6.18 and Table 6.1. This is because the ferrite mainly nucleates at deformed prior austenite grain boundaries at lower strains [101] and therefore the smaller

prior austenite grain size in the Nb-Ti steel (Fig. 6.17) will have promoted more nucleation sites than that in the Nb steel [231]. In addition, the volume fraction of DIFT continually increased with the increasing strain as well. This is because the grain size reduced with increasing strain [101], providing more nucleation site for DIFT at austenite grain boundaries.

The volume fraction of ferrite will also be affected by the isothermal hold at 10 s after deformation. From Fig. 6.18, the ferrite fraction rapidly increased after holding for 10 s at 850 °C compared with the water quenched samples, especially for the first pass deformation of B-10 and B-100. It is believed that the increase of ferrite fraction with the holding time is related to the SIP (Table 6.2), for the DIFT did not only form on the prior austenite grain boundaries, but also within grains. It can be explained that the precipitation decreases the content of the dissolved elements, which can provide a depleted zone formed around these particles. The Nb and carbon depleted zone can improve the driving force for DIFT nucleation within austenite grains [14,222]. Moreover, those precipitates can also become the sites for heterogeneous nucleation of ferrite [232]. Therefore, the isothermal holding for 10s after deformation is indirectly beneficial to increasing the volume fraction of DIFT.

## 7.2 SIP and the state of Nb in solution or in precipitates

### 7.2.1. The state of Nb in precipitates after rough rolling

There was no SIP (less than 20 nm) after rough rolling at 1100 °C in the Nb steel, but some precipitation was observed in the Nb-Ti steel (Table 4.2). At 1000 °C, the percentage of SIP was 4.8 % in the Nb steel and 2.4 % in the Nb-Ti steel, which was too little to result in a sufficient Zener pinning force to halt the recrystallization. Down to 950°C, more than 50 % of the precipitates were smaller than 20 nm in the Nb steel and 48 % of them in the Nb-Ti steel. The mixed microstructures observed at 950 °C in both steels (Figs. 4.1 (d) and 4.2 (d)) indicated that the recrystallization happened at the beginning and then was halted by the rapid increase of small precipitates. As the volume fraction of SIP continually increased with reducing the rolling temperatures to 850 °C, the recrystallization was fully restricted (Figs. 4.1 (e, f) and 4.2 (e, f)). The highest volume fraction of SIP was at 850 °C for both steels, which fits well to the calculation of the nose precipitated temperature at 840 °C by Eq. (4.1) (Fig. 4.1). For the large precipitates ( $\geq 20\text{nm}$ ), the percentage volume fraction continuously decreased (Table 4.2), because the volume fraction of SIP increased with the decreasing rough rolling temperatures for Nb and Nb-Ti steels.

When considering the effect of the rolling temperature on the state of titanium and niobium in the SIP, the ratio of Ti/(Ti+Nb) for Nb-Ti steel was calculated as a function of rolling temperatures and shown in Fig. 4.7. For large precipitates ( $\geq 20$  nm), the ratio of Ti/(Ti+Nb) was approximately constant for all rolling temperatures (Fig. 4.7), which showed that the rolling temperature does not influence the state of Nb and Ti in large precipitates. This is because most of the large precipitates are undissolved particles, and the equilibrium dissolution temperature of TiNb carbides is much higher than the rough rolling temperatures between 1100 °C and 850 °C. Therefore, the large precipitates containing Ti are much more stable at different rolling temperatures. For SIP with the size less than 20 nm, the ratio of Ti/(Ti+Nb) slightly increased at the beginning, and then decreased as a function of rolling temperatures (Fig. 4.7). The results showed that the deformation temperatures lower than 950 °C leads to a higher proportion of niobium in the precipitates, as the ratio of Ti/(Ti+Nb) increased. From the PTT curve shown in Fig. 4.1, it is obvious that the Nb precipitates need a shorter time to form than the titanium precipitates, especially at lower deformation temperatures. So, at the beginning, the Ti content was slightly higher than Nb in the precipitates, but with the deformation temperature reduced to 950 °C, the Nb in the precipitates became higher than the Ti.

7.2.2. The state of microalloyed elements in solution after reheating at 1200°C with different holding times

7.2.2.1 The dissolution behaviour of Ti and Nb during high temperature reheating process

The reheating temperature of 1200 °C for this investigation was higher than the equilibrium dissolution temperature of niobium and carbon in the Nb steel, calculated using the modified solubility product which the Irvine's equation [11] gave as:

$$\log [\text{Nb}][\text{C} + 12\text{N}/14] = 2.26 - 6770/T \quad (7.19)$$

Then, the equilibrium solution temperature of Nb(CN) in the Nb steel can be estimated at 1100 °C. The equilibrium solution temperature of Nb(CN) in the Nb steel was lower than the heat treatment temperature of 1200 °C. However, there is about 40 % of Nb remaining as undissolved precipitates after reheating at 1200 °C after rough rolling at 850 °C (Table 5.2). Moreover, the NbC and Nb(CN) were also observed even after holding for 100 s at 1200 °C (Fig. 5.19) with a size larger than 10 nm. The small amount of Nb in precipitates is indicated using the EDX analysis (Figs. 5.19 (c) and (d)) at 100 s compared with the EDX analysis

(Figs. 5.16 (c) and 5.18 (c)) at 0 s and 10 s, respectively, and this can be attributed to the rapid diffusion of Nb within the austenite at 1200 °C.

In order to predict the Ti and Nb dissolution kinetics [233], the volume fraction of precipitates in the Nb and Nb-Ti steels was calculated first using TEM images shown in Figs. 5.5-5.14. Then, with the experimental measurements for precipitate volume fraction, the amount of Nb in solution during isothermal heat treatment can be calculated by Eqs. (5.2) and (5.3) and the data presented in Table 5.2. These results indicate that, in the case of continuous isothermal holding at 1200 °C, precipitates in the Nb steel rapidly dissolved into the matrix with 96.8 % of the total Nb in solution after 100 s. However, in the Nb-Ti steel, there was only 55 % of the total Nb in solution after holding for 100 s at 1200 °C, showing that the addition of Ti significantly retards the dissolution kinetics of Nb as a result of increasing the thermodynamic stability of the complex  $\text{TiNb(CN)}$  [13]. The measurement of average diameter of precipitates in both the Nb and Nb-Ti steels with different holding time is also given in Table 5.2. According to the results in Table 5.2, the average dimension of niobium carbonitrides coarsened slightly when held for 10 s, and then reduced after that point in the Nb steel. However, the average diameter of  $(\text{Ti,Nb})(\text{CN})$  in the Nb-Ti steel continually coarsened during the entire reheating process. This is because for the Nb-Ti steel, the reheating temperature was lower than the dissolution temperature of titanium, carbon and nitrogen precipitates using previously published solubility products for these precipitates [209–211]. Therefore, the average diameter of  $(\text{Ti,Nb})(\text{CN})$  in the Nb-Ti steel can coarsen during the whole period.

As the Ti effectively restricts the diffusion of Nb during high temperature isothermal reheating, there is still observed Nb in EDX analysis for holding times as long as 1000 s at 1200 °C (Figs. 5.24). The ratio of  $\text{Ti}/\text{Ti+Nb}$  was calculated using EDX spectra for Nb-Ti steel after heat treatment for different times and listed in Table 5.3 and Fig. 5.25. The ratio of  $\text{Ti}/\text{Ti+Nb}$  increased with the increasing holding times in EDX analysis, which further indicated that the niobium continually dissolved into the matrix (Table 5.2). The ratio of  $\text{Ti}/\text{Ti+Nb}$  as a function of the isothermal holding times was also calculated from the volume fraction of precipitates using the Eq. (5.2) and shown in Table 5.3 and Fig. 5.25 as well. From these two methods of EDX and calculated data, the ratio of  $\text{Ti}/\text{Ti+Nb}$  from Nb-Ti steel have been compared (Fig. 5.25), and these two data fit well with each other. Therefore, the results indicate that the amount of niobium in solution for Nb-Ti steel which is calculated using Eq. (5.2), are acceptable during heat treatment at 1200 °C for different times.

The TEM observations of the precipitation behaviour and subsequently inferred dissolution behaviour of precipitates in the Nb steel and the Nb-Ti steel during isothermal reheating at 1200 °C can suggest two key results: first, it was observed that the dissolution kinetics of Nb was much more rapid in the Nb steel than in the Nb-Ti steel. It is believed that the presence of Ti in precipitates of Nb-Ti steel restricts the dissolution behaviour of Nb; secondly, the Ti-rich precipitates are more stable during heat treatment at 1200 °C, even when held for 1000 s. These Ti-rich precipitates provided Zener pinning of the grain boundaries, leading to a lower coarsening rate in the Nb-Ti steel than in the Nb steel (Figs. 5.2 and 5.3).

#### 7.2.2.2 Modelling the Nb in solution in austenite during the reheating process in the Nb and Nb-Ti steels

Modelling the amount of Nb in solution during reheating in both Nb and Nb-Ti steels can be simulated by using a modified JMAK equation to estimate the volume fraction of precipitate that formed as a function of time [5,187,234]. The form of the JMAK equation is given by

$$f(t) = 1 - \exp(-kt^n) \quad (7.20)$$

where  $f(t)$  is the volume fraction of precipitates;  $t$  is the isothermal time;  $k$  is a factor related to the nucleation rate and growth rate; and  $n$  is factor of nucleation rate. From classical nucleation theory, the volume fraction of precipitates at the start time is zero. However, in the present study, at the start, there were a small amount of undissolved precipitates in the Nb and Nb-Ti steels. Thus, the measurement of this initial volume fraction of precipitates at the start was added, and the modified JMAK equation is given by

$$f(t) = 1 + f_0 - \exp(-kt^n) \quad (7.21)$$

where  $f_0$  is the volume fraction of precipitates at the beginning of the isothermal heat treatment. In the present case, the amount of Nb contained in the matrix can be analysed by Eq. (5.2) using the volume fraction of precipitates. Therefore, the modelling of Nb in solution as a function of holding time was simulated using the Eqs. (5.2) and (7.21). The values of  $k$  and  $n$  in Eq. (7.21) were determined by the experimental data of 10 s and 100 s.

The measurement of Nb in solution in both the Nb and Nb-Ti steels with different holding time is given in Fig. 7.4 and compared with the calculations using Eqs. (5.2) and (7.21). Additional experimental data was included, namely a 20 s and 40 s hold at 1200 °C for the Nb steel and one at 40 s in the Nb-Ti steel. It can be seen that the Nb solution model as a

function of holding time provides a reasonable prediction of the amount of Nb in the precipitates.

The simulation indicates that the Nb was fully dissolved into the matrix after 115 s in the Nb steel. However, at the same time, there was only 0.017 wt% of Nb dissolved into the matrix in the Nb-Ti steel. This is consistent with the observed dimensions of the precipitates.

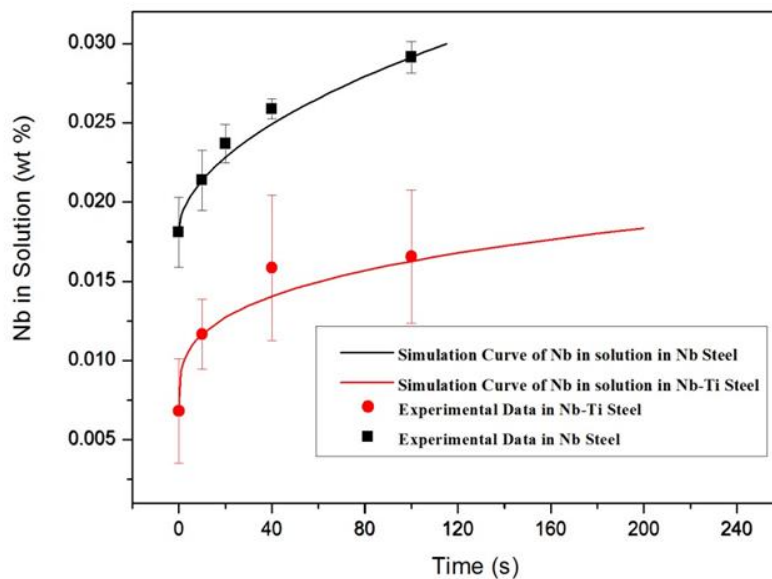


Fig.7.4. Simulation of the diversification of equilibrium solubility product of [Nb] in solution in Nb and Nb-Ti steels with holding times using Eqs. (5.2) and (7.21).

### 7.2.3 The state of Nb in precipitates after finish rolling

The SIP in the Nb and Nb-Ti steels after finish rolling with different rolling schedules, observed from carbon replica samples, are presented in bright-field TEM images shown in Figs. 6.19-6.26. The size distribution of precipitates was calculated using the carbon replica data (Figs. 6.19-6.26) and well represented by simulated distribution with the Eq. (5.1) and shown in Figs. 6.19-6.26. The volume fraction of SIP shown in Table 6.2 increased with the increasing strain or the extended 10 s holding time at a deformation temperature of 850 °C. The average size of SIP (less than 20 nm) decreased with increasing strain or extended 10s holding time (Table 6.2). In this section, the SIP behaviour during finish rolling was discussed from the supersaturation of the matrix before deformation, the deformation strains and the isothermal holding for 10 s at the deformation temperature.

At the beginning, the rapid reheating to 1200 °C for 10 s and 100 s after rough rolling at 850 °C would have gradually dissolved the SIP that formed during rough rolling, and the Nb dissolution rate was faster in the Nb steel than in the Nb-Ti steel [235]. The volume fraction and average diameter of SIP after finish rolling was analysed by TEM (HRTEM). The average diameter of the SIP was much smaller and the volume fraction of the SIP higher after finish rolling than that after rough rolling under the same rolling parameters for both Nb and Nb-Ti steels. As expected, the increased supersaturation led to a higher driving force for the nucleation of precipitation for both Nb and Nb-Ti steels [23,236]. It is also because the increased undercooling between heat treatment and deformation led to higher nucleation rates during finish rolling than that in rough rolling [223,237]. The volume fraction of SIP with 10 s holding at 1200 °C followed by finish rolling is less than that with 100 s holding at 1200 °C, compared with the same rolling parameters, especially for the Nb steel. The volume fraction of SIP was 10 % higher at 1200 °C for 100s followed by finish rolling A-100 than 10 s by A-10. This is because the longer the holding time at 1200 °C, the more elements such as Nb and C dissolve into the austenite matrix (Table 5.2). Thus, with higher supersaturation of the elements for 100 s holding at 1200 °C before deformation, the driving force for nucleation was increased [23,236].

For the samples that were subject to a 10 s hold at 850 °C after either the first or second pass of finish deformation, the volume fraction of SIP was also higher than in those samples that were immediately water quenched. This is in agreement with many publications for precipitation kinetics [8,233,238], which shows that the 10 s hold at 850 °C can provide sufficient incubated time for precipitation. When the strain was increased to 0.6 during finish rolling, the effect of the 10 s holding at 850 °C on the volume fraction of SIP was higher than that at the lower strain at 0.3, especially for the Nb steel. In addition, the average diameter of the SIP was also refined. Therefore, the 10 s hold time combined with the deformation strains during finish rolling were the main factors to refine the size and increase the volume fraction of precipitation.

When consider the effect of deformation strain during finish rolling on the SIP for both Nb and Nb-Ti steels, with increasing the strain from 0.3 to 0.6, the volume fraction of SIP increased and its average size reduced due to the increased driving force of precipitates from deformation store energy.

The composition and the microstructures of SIP have been identified by HRTEM, EDX and EELS and shown in Figs. 6.27-6.34. There are two different kinds of SIP: the first type is the spherical shaped precipitates in the Nb steel and they were identified as NbC (Figs. 6.27-6.30); the second one had a cuboidal shaped regarded as (Ti, Nb)C in the Nb-Ti steel (Fig. 6.31-6.34).

### 7.3 Vickers micro-hardness

#### 7.3.1 The effect of rough rolling process on the Vickers micro-hardness

After rough rolling at different temperatures (Fig. 3.3), the Vickers micro-hardness was measured and is shown in Fig. 4.12. Vickers micro-hardness slightly decreased at the beginning, and then increased with the deformation temperature decreasing for both Nb and Nb-Ti steels. There are several factors that can influence the micro-hardness, such as precipitation strengthening, grain size strengthening and the solid solution strengthening. In this study, before rough rolling, the specimens were reheated to 1100 °C and held for 30 s to obtain higher solid solution strengthening at the beginning. Then, at the high deformation temperatures of 1100 °C and 1000 °C, the volume fraction of SIP was much lower than that at the deformation temperatures between 950 °C and 850 °C (Table. 4.2). The average grain size at the deformation temperature between 1100 °C and 1000 °C was constant as well (Fig. 4.4). Therefore, the micro-hardness was mainly determined by the solid solution of microalloyed elements, because of the lower precipitation strengthening and the constant grain size strengthening. As the solid solution of elements decreased with the decreasing rough rolling temperatures, the micro-hardness for Nb and Nb-Ti steels decreased with the rough rolling temperature between 1100 °C and 1000 °C. Because of the higher solid solution in the Nb steel, the micro-hardness was also higher than in the Nb-Ti steel.

Then, with the rough rolling temperatures continually decreasing from 950 °C to 850 °C, the micro-hardness gradually increased for both Nb and Nb-Ti steels. This can be explained by the rapid increase in volume fraction of SIP (Table 4.2) and refining of the prior-austenite grain size (Fig. 4.4). The precipitate strengthening and grain size strengthening became the main factors affecting the micro-hardness when compared with the solid solution strengthening. Moreover, the variation of micro-hardness between Nb and Nb-Ti steels gradually became smaller for the deformation temperatures between 950 °C and 850 °C compared to the temperatures between 1100 °C and 1000 °C. This is because the volume fraction of SIP and the average grain size in both Nb and Nb-Ti steels become similar after

the deformation at 950 °C and 850 °C (Tables 4.1 and 4.2). The trend of micro-hardness changing with different rough rolling temperatures fits well with the experimental data of the volume fraction of precipitation, prior-austenite grain size and the solid solution of microalloyed elements for Nb and Nb-Ti steels.

### 7.3.2 The effect of reheating on the Vickers micro-hardness

The Vickers micro-hardness was measured for specimens after rough rolling at 850 °C and reheating to 1200 °C with different holding times and is shown in Fig. 5.26. In general, the microalloyed elements in solution result in an increase in the microhardness [188]. However, the grain growth and the reducing volume fraction of precipitates results in a decrease in the micro-hardness, as expected [78,239]. In this study, the Vickers hardness (Fig. 5.26) continually increased with the increasing holding times at 1200 °C, showing that the solid solution strengthening from microalloyed elements in both steels (Table 5.2) provided a much greater effect on hardness than the negative effect of grain size coarsening (Figs. 5.2 and 5.3) and precipitation resolution (Table 5.2). The simulation of Nb in solution in both Nb and Nb-Ti steels is shown in Fig. 7.4 is a better fit with the micro-hardness curves (Fig. 5.26), which further demonstrated that the Nb elements gradually dissolved into the matrix, increasing the hardness of the matrix. In summary, with the negative effect of the precipitate dissolution and grain size growth on micro-hardness, the micro-hardness continually increased with increasing isothermal holding times due to the significant effect of solid solution of microalloyed elements and carbon in the Nb and Nb-Ti steels.

### 7.3.3 The effect of finish rolling on the Vickers micro-hardness

The Vickers micro-hardness was measured as a function of rolling parameters and is shown in Figs. 6.36 and 6.37. The refined prior austenite grain size and the increased SIP result in an increase in the micro-hardness [41]. In contrast, the DIFT leads to work softening after deformation [78,240]. Therefore, the micro-hardness at each finish rolling parameter would be influenced by the combination of these three factors. With the precipitation strengthening and fine grain strengthening, the micro-hardness increased after one pass deformation at 850 °C (A-10 and A-100), when compared with hardness from the heat treated samples at 1200 °C for Nb and Nb-Ti steels. The micro-hardness at A-100 was higher than that at A-10, especially for Nb steel. This is because of the refined grain strengthening at A-100 on the hardness value are much higher than that at A-10. However, the micro-hardness rapidly decreased after deformation followed by 10 s holding at 850 °C using the rolling parameters

of B-10 and B-100. The value of hardness at B-100 in the Nb-Ti steel was even lower than the hardness after heat treatment at 1200°C. This is because the prior austenite grain size (Fig. 6.17) and the volume fraction of SIP (Table 6.2) was only slightly changed after holding for 10 s at the deformation temperature (B-10 and B-100), when compared with the increased rate of DIFT at the same stage (Fig. 6.18 and Table 6.1). Then, after finish rolling with the schedules of C-10 and C-100, the micro-hardness slightly increased with the increasing strain (Figs. 6.36 and 6.37). This is because the effect of the volume fraction of precipitates and the refined grain size on the micro-hardness becomes higher than the opposing effect of DIFT (Fig. 6.18), due to the low increasing rate of volume fraction of DIFT. Therefore, the total microhardness increased with the increasing strain (C-10 and C-100). In the end, after finish rolling with schedules of D-10 and D-100, the micro-hardness continually increased with 10 s holding at the deformation temperature, because the volume fraction of precipitates increased, which increase the precipitate strengthening on microhardness. Furthermore, the micro-hardness in the Nb steel was higher than that in the Nb-Ti steel, because of the higher volume fraction of DIFT in the Nb-Ti steel reduced hardness. Also, the refinement of austenite grain size for Nb steel is much more significant than that for Nb-Ti steel, so the effect of fine grain size strengthening is higher in the Nb steel than in the Nb-Ti steel (Tables 5.1 and 6.1). To compare with the experimental data, the trend of the total microhardness fits well with the trend of grain size, volume fraction of precipitates and DIFT as a function of rolling parameters.

In this study, the precipitation strengthening, grain size strengthening and the second phase of DIFT strengthening are the main strengthening mechanisms on the mechanical properties in the Nb and Nb-Ti steels, which can be expressed as:

$$\sigma_y = \Delta\sigma_0 + \Delta\sigma_{ss} + \Delta\sigma_{GB} + \Delta\sigma_{trans} + \Delta\sigma_{ppt} + \Delta\sigma_{Dis} \quad (7.22)$$

Where  $\sigma_y$  is the friction of yield stress,  $\Delta\sigma_{ss}$  is the increased yield stress due to solid solute strengthening,  $\Delta\sigma_{GB}$  is the increased yield stress due to grain size strengthening,  $\Delta\sigma_{trans}$  is from the second phase of ferrite strengthening and  $\Delta\sigma_{ppt}$  is from precipitate strengthening.  $\Delta\sigma_{Dis}$  is from the dislocation density.

The base yield strength for both Nb and Nb-Ti steels is determined by the grain size and microalloyed elements in steels. It can be calculated by Eq. (7.23) for plain low-carbon steel [43]:

$$\sigma_{base} = \Delta\sigma_0 + \Delta\sigma_{ss} + \Delta\sigma_{GB} = 15.4 \left[ 3.5 + 2.1(Mnwt\%) + 5.4(Siwt\%) + 23.4(Cwt\%) + 23(Nfwt\%) + 1.13D^{-1/2} \right] \quad (7.23)$$

where Mn, Si and C are the weight percent of microalloyed elements in the Nb and Nb-Ti steels, and Nf is the free nitrogen content. D is the prior-austenite grain size in ND.

The  $\Delta\sigma_{ppt}$  can be calculated from the Ashby–Orowan equation, which was modified by Gladman [241] for microalloyed steels and expressed as:

$$\Delta\sigma_{ppt} = \frac{Kf^{1/2}}{d} \ln \frac{d}{b} \quad (7.24)$$

Where K is a constant equal to 0.1836 Gb, G is the shear modulus (MPa), b is the Burgers vector in the slip direction (m), f is the volume fraction of precipitates and r is the average radius of the precipitates (m).

The increased yield stress which resulted from increasing dislocation density can be expressed by:

$$\Delta\sigma_{Dis} = \alpha M G b \sqrt{\rho} \quad (7.25)$$

where  $\alpha$  is a constant; M is the Taylor factor and  $\rho$  is the dislocation density. With water quenched samples, the dislocation contribution would be approximately 120 MPa [41]. The dislocation density of martensite is assumed to be  $10^{14} \text{ m}^{-2}$  in the present estimation.

Second phases of ferrite and martensite produced a strengthening effect in Nb and Nb-Ti steels which can be represented follows by the ferrite structures varying from 0 to 100 %:

$$\Delta\sigma_{trans} = X_f^{1/3}(\sigma)_f + (1-X_f^{1/3})(\sigma)_M \quad (7.26)$$

Where  $X_f$  is the volume fraction of ferrite,  $(\sigma)_M$  is the yield stress of martensite and  $(\sigma)_f$  is the yield stress of ferrite. According to experimental data [242], the Eq. (7.27) can be further expressed as:

$$\Delta\sigma_{trans} = X_f^{1/3}(35+58Mn+17.4d^{-1/2}) + (1-X_f^{1/3})(178+3.8s^{-1/2}) \quad (7.27)$$

Where d is the ferrite grain size (mm) and s is the average interlamellar spacing of martensite (mm). Thus, the combined effect of these parameters on the yield stress was calculated by Eqs. (7.22-7.27) and listed in Table 7.3. The second phase strengthening for Nb steel was

281.1 MPa and 275.4MPa for Nb-Ti steel after rolling with schedule A-10, which correspond to the Vickers micro-hardness of 246.8 Hv and 220.7 Hv respectively (Figs. 6.36 and 6.37). Then, after deformation at 850 °C followed by isothermal holding for 10 s (B-10), the second phase strengthening decreased to 265.9 MPa and 263.7 MPa in the Nb and Nb-Ti steels, respectively, with a corresponding micro-hardness of 214.5 Hv for Nb steel and 202.5 Hv for Nb-Ti steel. After that, the second phase strengthening slightly increased with increasing strain to 0.6 for both Nb and Nb-Ti steels due to the refined grain size. The trend of the yield stress produced by the second phase after deformation by A-100, B-100, C-100 and D-100 is the same with that by A-10, B-10, C-10 and D-10.

Table 7.3

The components of the yield stress after reheating and rolling with the schedules shown in Fig. 3.5 for Nb and Nb-Ti steels.

Martials	Rolling	A-10	B-10	C-10	D-10	A-100	B-100	C-100	D-100
	Schedule								
Nb Steel	$\sigma_{base}$ (MPa)	191.8	192	192.8	193.2	191.7	191.9	192.2	192.5
	$\Delta\sigma_{ppt}$ (MPa)	27.9	30.4	35.1	42.7	30.1	31.2	37.8	43.6
	$\Delta\sigma_{Dis}$ (MPa)	120	120	120	120	120	120	120	120
	$\Delta\sigma_{trans}$ (MPa)	281.1	265.9	282.5	288.5	274.6	257.6	279.1	281.2
	$\sigma_y$ (MPa)	620.8	608.3	630.4	644.4	616.4	600.7	629.1	637.3
Nb-Ti Steel	$\sigma_{base}$ (MPa)	192.8	193	193.5	193.9	192.5	192.9	193.2	193.2
	$\Delta\sigma_{ppt}$ (MPa)	28	31.1	32	37.2	30.1	32.1	34.4	38.1
	$\Delta\sigma_{Dis}$ (MPa)	125	125	125	125	125	125	125	125
	$\Delta\sigma_{trans}$ (MPa)	275.4	263.7	281.2	287.1	269.8	255.9	274.9	279.9
	$\sigma_y$ (MPa)	621.2	612.8	631.7	643.2	617.4	605.9	627.5	636.2

Therefore, the trend of the second phase yield strength as a function of finish rolling schedules shown in Fig. 3.5 is consistent with the measurements of Vickers micro-hardness. The results indicated that the second phase of ferrite and martensite produced strengthening contributions to the main factors for the total yield stress. Moreover, the yield stress was also tested after finish rolling, with 610 MPa for D-10 and 600 MPa for D-100 from Nb steel. This is consistent with the simulated results from Eqs. (7.22-7.27) at the same rolling parameters, which indicated that the predicted data of the yield stress for Nb and Nb-Ti steel is reasonable for this study.

## CHAPTER 8: CONCLUSIONS

The work shown in this thesis can be broken down into three main sections. In the first part, the effect of rough rolling temperatures on microstructures and SIP has been discussed, and, based on this work, a final rough rolling temperature has been selected at 850°C (chapter 4). Then, in the second section, the reheating process, with different isothermal holding times after rough rolling, has been analysed in terms of the microstructure, volume fraction of precipitates and microalloyed elements solution, as well as the Vickers micro-hardness. Then, the precipitate dissolution kinetics, together with the austenite grain coarsening kinetics, was established. Finally, after rough rolling and reheating, the specimens were finish rolled with different parameters. The prior austenite grain size in this study was measured in the normal direction in this new thermo-mechanical process route for Nb and Nb-Ti steels. The presence of DIFT was identified in microstructures obtained from OM and SEM by quenching after deformation, which provided a martensite matrix (which was austenite at the rolling temperature) and ferrite, which resulted from the DIFT on grain boundaries and within grains in the Nb and Nb-Ti steels. The volume fraction of SIP has been analysed by TEM. The Vickers micro-hardness was measured to explain the effect of precipitation strengthening, grain size strengthening and the second phase strengthening on total mechanical properties.

### 8.1. Rough rolling

- 1) Recrystallization occurred during rough rolling with the temperatures in the range from 1100 °C to 1000 °C; At 950 °C, partial recrystallisation occurred. At 900 °C and 850 °C, recrystallisation of the austenite was prevented.
- 2) The precipitation start temperature, the recrystallization start and finish temperatures for Nb and Nb-Ti steels were computed using the PTT diagrams obtained by the Dutta et al. and Johnson et al. models. From the simulated PPT curves, the precipitation start time for Nb-Ti steel was delayed compared to the Nb steel. The delay of SIP resulted from the reduced solution of microalloyed elements in the Nb-Ti steel. The Nb solubility in austenite was reduced by the stable (Ti,Nb)(CN) precipitates during a heat treatment at 1100 °C for 30 s.
- 3) When considering the effect of SIP on the microstructures, the Zener pinning force from SIP was too low to halt the recrystallization in the range of 1100 °C-1000 °C, with full recrystallization resulting. However, after the rolling temperature was reduced under 950 °C,

the Zener pinning force was large enough to retard the recrystallizing driving force. This is consistent with the changing of the volume fraction of precipitates.

4) The micro-hardness for both Nb and Nb-Ti steels decreased with decreasing the deformation temperatures until 950 °C, because of the decreased solid solution strengthening. Then, the opposite trend occurred, with hardness increasing with a decrease in the temperature until 850 °C due to the precipitate strengthening and grain refinement strengthening.

5) The SIP in the Nb and Nb-Ti steels have been examined via TEM, including image analysis, electron diffraction patterns, HRTEM and EDX. The results strongly suggest that these carbides have a NaCl-type crystal structure and lattice parameters of 0.447 nm for NbC and 0.437 nm for (Ti, Nb)C.

6) The orientation relationship (OR) between the precipitates and matrix was calculated from electron diffraction patterns. Depending on the Davenport et al. theory and the coordinated matrix of precipitates and ferrite, the OR between precipitates and austenite transforming to ferrite was established, which further indicated that those particles formed in the austenite region related to the ferrite matrix.

## 8.2. Reheating

1) After rough rolling with a final temperature of 850 °C, the prior-austenite grains coarsened during isothermal heating at 1200 °C with various times, because of the reduced pinning force of precipitates on the grain boundaries. The high temperature stability of (Ti, Nb)C or (Ti, Nb)(C, N) retards the grain growth rate in the Nb-Ti steel.

2) The Nb continually dissolved into the austenite during reheating in both the Nb and Nb-Ti steels. Furthermore, the dissolution rate of Nb in the Nb steel was quicker than in the Nb-Ti steel.

3) The average diameter of the Nb precipitates in the Nb steel initially coarsened up to a 10 s hold, but then the size of most precipitates reduced or they totally dissolved at longer times. However, the (Ti, Nb)C or (Ti, Nb)(C, N) particles in the Nb-Ti steel continually coarsened over the entire duration of the holding period.

4) The austenite grain coarsening kinetics has been constructed by Feltham and Fan's theory considering the carbon diffusion. Then, with Hillert and Cahn's theory, the

combination of average grain size with volume fraction and diameter of precipitates has been produced. Considering the solute drag effect in the Nb steel, the models by Fan and Cahn's theory fitted well with the experimental data.

5) The kinetics of Nb in solution can be characterized using a modified JMAK Equation by  $f(t) = 1 + f_0 - \exp(-kt^n)$ . This model provides a quick and accurate method to predict the amount of Nb in solution with the function of holding time.

6) The effect of solid solution of microalloyed elements on micro-hardness is significantly higher than the negative effect of coarse grain size and solution of precipitates. The micro-hardness for Nb steel is higher than that for Nb-Ti steel. The micro-hardness curves as a function of isothermal holding times fit well with the Nb in solution curves for Nb and Nb-Ti steels.

### 8.3. Finish Rolling

A new thermomechanical controlled process route has been developed to obtain DIFT, which was determined to be one of the most effective methods to refine the final grain size combined with reducing the rolling force and improvement of the productivity. The study of prior-austenite grain size, the precipitation behaviour, and their effects on the DIFT has been discussed after deformation through the new TMCP, with the following conclusions:

1) As expected, the prior austenite grain size decreased with the increased strain for Nb and Nb-Ti steels. When compared with the water quenched specimens, the grain size also decreased after isothermal holding for 10s at the deformation temperature under the same deformation strain, due to the increasing volume fraction of DIFT.

2) The spherically shaped SIP in the Nb steel were identified as NbC, while the cuboid shaped precipitates in the Nb-Ti steel were (Nb,Ti)C. The volume fraction of SIP increased with the increasing strain. The isothermal hold of 10s after deformation at 850 °C produced more precipitation due to the increased time available for precipitation. In addition, the reheat to 1200 °C increased the supersaturation of microalloyed elements in the matrix leading to a slightly higher volume fraction and smaller diameter of SIP after finish rolling compared to rough rolling with the same rolling parameters.

3) The prior austenite grain size was modelled by Sellars' theory considering the strains, which fit well with the experimental data. Hellman and Hillert's modified Zener pinning

model also provided a good prediction of the experimental data for volume fraction and diameter of SIP for the Nb steel. However, the match was less good for the Nb-Ti steel because of the error introduced by the formation of DIFT at the rolling temperature in this steel.

4) DIFT occurred during finish rolling as a result of the introduction of the reheat at 1200 °C. The volume fraction of DIFT increased with the increasing applied strain and isothermal hold of 10 s after deformation. The DIFT nucleated on and within the elongated prior-austenite grains.

5) The increased volume fraction of DIFT during isothermal holding of 10 s after the one pass deformation leads to the dynamic softening of microhardness. With increasing strains to 0.6, the effect of the grain size refinement strengthening on hardness became larger than the opposing effect of DIFT, due to the low increasing rate of volume fraction of DIFT. With this new TMCP, the final grain size could be refined to 1.4  $\mu\text{m}$ .

## CHAPTER 9: FUTURE WORK

In this chapter, considering the outcomes from the whole project, the proposed further work consists of three parts, these being the deformation textures after finish rolling, the controlled cooling and the application in various steels.

### 9.1 The deformation textures

The present work is only focused on the recrystallization texture and how it rotated during grain coarsening, but this has not been presented in the thesis. However, the effects of the different finish rolling parameters on the textures have been neglected during this study. Indeed, the analysis of the deformation textures in finish rolling section is important due to the understanding of the recrystallization texture effect on the deformation textures. It is also because the textures after deformation with the strain of 0.3 are different from the typical deformation textures after rough rolling. It is not clear that the recrystallization textures delay or change the orientation of the deformation textures.

### 9.2 Controlled cooling process

To analyse the microstructures and precipitation behaviour, the majority of the specimens were water quenched immediately to room temperature after deformation or heat treatment, to preserve the microstructures and have minimum effect of phase transformation on them. Moreover, the water quenching is also the favoured option for the rolling parameters to obtain the refined deformation grain size and maximum volume fraction of precipitates. However, without controlled cooling combined with TMCP, the mechanical properties, like elongation and toughness, could not satisfy the requirement of the application in industry. Therefore, in the next step after optimized TMCP, controlled cooling will be analysed to obtain a good combination of strength, toughness and weldability of microalloyed steels.

### 9.3 Chemical composition

In this study, we only focused on microalloyed steels, like Nb and Nb-Ti steels, to optimize the microstructures after TMCP. After obtaining the satisfactory controlled cooling with excellent mechanical properties, in the future, the new TMCP+control cooling could apply for different steels, like twinning induced plasticity steels and ultra-high strength steels.

## CHAPTER 10: PUBLICATION AND CONFERENCE PRESENTATION

### 10.1 Publications

P. Gong, E.J. Palmiere and W.M. Rainforth, “Dissolution and precipitation behaviour in steels microalloyed with niobium during thermomechanical processing”, *Acta Materialia* 97 (2015) pp 392-403.

P. Gong, E.J. Palmiere and W.M. Rainforth, “Understanding the Precipitation behaviour and the deformation-induced ferrite transformation in steels microalloyed with niobium during a new type thermomechanical processing”, In preparation for submission to *Acta Materialia*, 2015.

### 10.2 Conference presentation

Peng GONG, Eric Palmiere, Mark Rainforth. MS&T14 International conference in Pittsburgh (USA) Oct 2014.

## References

- [1] Meuser H, Grimpe F, Meimeth S, Heckmann CJ. in International Conference on Microalloying for New Steel Processes and Applications Int. Symposium. 2005. San Sebastian, Spain.
- [2] Rodrigues PCM, Pereloma EV, Santos DB. Mater Sci Eng A 2000;283:136.
- [3] Ghosh A, Sahoo S, Ghosh M, Ghosh RN, Chakrabarti D. Mater Sci Eng A 2014;613:37.
- [4] Hong SG, Jun HJ, Kang KB, Park CG. Scr Mater 2003;48:1201.
- [5] Timokhina IB, Hodgson PD, Ringer SP, Zheng RK, Pereloma EV. Scr Mater 2007;56:601.
- [6] Yen HW, Huang CY, Yang JR. Scr Mater 2009;61:616.
- [7] Patel JK, Wilshire B. J Mater Process Technol 2002;120:316.
- [8] Hong SG, Kang KB, Park CG. Scr Mater 2002;46:163.
- [9] Show BK, Veerababu R, Balamuralikrishnan R, Malakondaiah G. Mater Sci Eng A 2010;527:1595.
- [10] Elwazri A, Yue S, Wanjara P. Metall Mater Trans A 2005;36:2297.
- [11] Dutta B, Sellars CM. Mater Sci Technol 1987;3:197.
- [12] Yuan S, Liang G, Zhang X. J Iron Steel Res Int 2010;17:60.
- [13] Qin YL, Luo HW, Kooi B, Hosson J De. in: Proceedings of the 4<sup>th</sup> International Conference on Physical and Numerical Simulation of Materials Processing. Shanghai. 2004.
- [14] Sakuma T, Honeycombe RWK. Met Sci 1984;18.
- [15] Ghosh A, Das S, Chatterjee S, Mishra B, Ramachandra Rao P. Mater Sci Eng A 2003;348:299.
- [16] Zhao MC, Yang K, Shan Y. Mater Sci Eng A 2002;335:14.
- [17] Ghosh A, Mishra B, Das S, Chatterjee S. Mater Sci Eng A 2004;374:43.
- [18] Gomez M, Valles P, Medina SF. Mater Sci Eng A 2011;528:4761.
- [19] Phaniraj MP, Behera BB, Lahiri AK. J Mater Process Technol 2005;170:323.
- [20] Egorov NT. Metal 2015 2005;24-26:1.

- [21] Dhua SK, Sen SK. *Mater Sci Eng A* 2011;528:6356.
- [22] Dhua SK, Ray A, Sarma DS. *Mater Sci Eng A* 2001;318:197.
- [23] Palmiere EJ, Garcia CI, DeARDO AJ. *Metall Mater Trans A* 1994;25:277.
- [24] Eghbali B, Abdollah-zadeh A. *J Mater Process Technol* 2006;180:44.
- [25] Guo WM, Wang ZC, Liu S, Wang XB. *J Iron Steel Res Int* 2011;18:42.
- [26] Jahazi M, Egbali B. *J Mater Process Technol* 2000;103:276.
- [27] Equihua F, Salinas A, Nava E. *Rev Metal* 2010;46:78.
- [28] Chen J, Li F, Liu Z, Tang S, Wang G. *ISIJ Int* 2013;53:1070.
- [29] Imandoust A, Zarei-Hanzaki A, Abedi HR. *Scr Mater* 2012;67:995.
- [30] Eghbali B, Abdollah-zadeh A. *Scr Mater* 2006;54:1205.
- [31] Ohmori A, Torizuka S, Nagai K, Koseki N, Kogo Y. *Mater Trans* 2004;45:2224.
- [32] Song R, Ponge D, Raabe D, Speer JG, Matlock DK. *Mater Sci Eng A* 2006;441:1.
- [33] Hodgson PD, Hickson MR, Gibbs RK. *Scr Mater* 1999;40:1179.
- [34] Morrison WB, Woodhead JH. *J Iron Steel Inst* 1963;201:43.
- [35] Hu W. Iowa State University 2008.
- [36] Pickering FB. Wiley-VCH Verlag GmbH&Co. KGaA, Sheffield, UK 2006.
- [37] Adamczyk J. *J Achiev Mater* 2006;14:9.
- [38] Chen Y, Zhang D, Liu Y, Li H, Xu D. *Mater Charact* 2013;84:232.
- [39] Zhang YQ, Zhang HQ, Liu WM, Hou H. *Mater Sci Eng A* 2009;499:182.
- [40] Bedolla-Jacuinde A, Zuno-Silva J. [www. iim.umich.mx](http://www.iim.umich.mx).
- [41] Charleux M, Poole WJ, Militzer M, Deschamps A. *Mater Trans A* 2001;32A:1635.
- [42] Zhou TH, Zurob HS. *Can Metall Q* 2011;50:389.
- [43] Morrison W, Woodhead J. *J Iron Steel Inst* 1963;201:43.
- [44] Farag M, Sellars C, Tegart W. *Iron Steel Inst London, UK* 1968:60.
- [45] Irvine KJ, Burton D, Jones JD, Rothwell AB. *ISI Special Report* 1967;104:110.

- [46] Irani JJ, Burton D, Jones JD, Rothwell AB. *J Iron Steel Inst* 1967;104:135.
- [47] Facco GG. University of Pittsburgh 2009.
- [48] Misra RDK, Weatherly GC, Hartmann JE, Boucek AJ. *Mater Sci Technol* 2001;17:1119.
- [49] Ouchi C. *ISIJ Int* 2001;41:542.
- [50] Ikeshima T. *Trans Iron Steel Inst* 1980;20:561.
- [51] Kozasu I. *Iron Steel Inst Japan*, 1988:420.
- [52] Ohtomo A, Takatuka K, Takahashi I. *J Iron Steel Inst Jpn* 1988;74:99.
- [53] Hanzaki A, Hodgson PD, Yue S. *Metall Mater Trans A* 1997;28A:2405.
- [54] Fujiwara K, Okaguchi S, Ohtani H. *ISIJ Int* 1995;35:1006.
- [55] El-fawakhry KA, Monhamed FM, Michael LM, Mamdouh ME. *ISIJ Int* 1991;31:1020.
- [56] Mekkawy MF, Ei-fawakhry KA, Mishreky ML, Eissa MM. *Mater Sci Technol* 1991;7:28.
- [57] Pereloma E, Boyd J. *Mater Sci Technol* 1996;12:808.
- [58] Ouchi C, Okita T, Yamamoto S. *Trans Iron Steel Inst* 1982;22:608.
- [59] Eghbali B, Abdollah-zadeh A. *Scr Mater* 2005;53:41.
- [60] Stuart H. *JOM* 1991:35.
- [61] Dean SW, Gorni AA, Dolabela da Silveira JH. *J ASTM Int* 2008;5:101777.
- [62] Dhua SK, Mukerjee D, Sarma DS. *Metal Mater Trans A* 2003;34A:241.
- [63] Zhao M, Yang K, Shan Y. *Mater Sci Eng A* 2002;335:14.
- [64] Hwang GC, Lee S, Yoo JY, Choo WY. *Mater Sci Eng A* 1998;252:256.
- [65] Duan Z, Li Y, Zhang M, Shi M, Zhu F, Zhang S. *J Wuhan Univ Technol Sci Ed* 2012;27:1024.
- [66] Watanabe Y, Yoshida Y, Nishioka K, Funato K, Works HTK, City K, Okamura JY. *Vessel Pip Conf New Orleans, Louisiana*, 1992; 239.
- [67] Mabuchi H, Uemori R, Fujioka M. *ISIJ Int* 1996;36:1406.
- [68] Tomita Y, Saito N, Tsuzuki T, Tokunaga Y, Okamoto K. *ISIJ Int* 1994;34:829.

- [69] Elmer JW, Palmer TA, Zhang W, Wood B, DebRoy T. *Acta Mater* 2003;51:3333.
- [70] Homma H, Ohkita S, Matsuda S, Yamamoto K. *Weld J* 1987;66:301.
- [71] Tabuchi M, Watanabe T, Kubo K, Matsui M, Kinugawa J, Abe F. *Inter J Pres Ves Pip* 2001;78:779.
- [72] Denys R. *International Conference on Evaluation of Materials Performance in Severe Environments* 1989;2.
- [73] Bang KS Kim WY. *Weld J* 2002;81:174.
- [74] Gianetto JA, Braid JEM, Bowker JT, Tyson WR. *J Offshore Mech Arct Eng* 1997;119:134.
- [75] Kawabata F, Matsui K, Obinata T, Komori T, Takemure M, Kubo T. *JFE Tech Rep* 2004;2:85.
- [76] Nakata H, Kami C, Matsuo N. *JFE Tech Rep* 2008;12:27.
- [77] Hayashi K, Nagao A, Matsuda Y. *JFE Tech Rep* 2008;11:19.
- [78] Calcagnotto M, Adachi Y, Ponge D, Raabe D. *Acta Mater* 2011;59:658.
- [79] Hickson M, Hurley P, Gibbs R. *Mater Trans A* 2002;33:1019.
- [80] Ghosh A, Mishra B, Das S, Chatterjee S. *Metall Mater* 2005;36:703.
- [81] Ghosh A, Mishra B, Das S, Chatterjee S. *Mater Sci Eng A* 2005;396:320.
- [82] Bandyopadhyay PS, Kundu S, Ghosh SK, Chatterjee S. *Metall Mater Trans A* 2010;42:1051.
- [83] Ewing JA, Walter Rosenhain W. *Philosophical Transactions of the Royal Society of London, Series A* 1900;193:353.
- [84] Taylor G. *Philosophical Transactions of the Royal Society of London, Series A* 1932;230:323.
- [85] Rice JR. *J Appl Mech* 1970;37:728
- [86] Borsi R, Cecotti M, Rotti M, Zorzi R. *Stainl Steel'99: Sci Mark* 1999:287.
- [87] Scholtz E, Craig IK, Pistorius PC. *ISI Int* 2000;40:1003.
- [88] Chao HC. *ASM Trans Quart* 1967;60:37.
- [89] Wright RN. *Metall Trans* 1972;3:83.
- [90] Li X, Huang M. *Polym Int* 1999;391:387.

- [91] Hall E. Proc Phys Soc Sect B 1951;747.
- [92] Weng YQ, Wang GD, Zhu J. Beijing Metallurgical Industry Press 2003;140:118.
- [93] Tamura I, Sekine H, Tanaka T, Ouchi C. Butterworth-Heinemann 2013.
- [94] Hodgson PD, Hickson MR, Gibbs RK. Scr Mater 1999;40:1179.
- [95] Quang P, Jeong YG, Yoon SC, Hong SH, Kim HS. J Mater Process Technol 2007;187-188:318.
- [96] Sarwar M, Priestner R. J Mater Sci 1996;31:2091.
- [97] Tsuji N, Maki T. Scr Mater 2009;60:1044.
- [98] De AK, Murdock DC, Mataya MC, Speer JG, Matlock DK. Scr Mater 2004;50:1445.
- [99] Han D. The Chinese Society for Metals, Beijing 2001;41.
- [100] Yang Z, Wang R. ISIJ Int 2003;43:761.
- [101] Dong H, Sun X. Curr Opin Solid State Mater Sci 2005;9:269.
- [102] Ueji R, Tsuji N, Minamino Y, Koizumi Y. Acta Mater 2002;50:4177.
- [103] Saito Y, Utsunomiya H, Tsuji N, Sakai T. Acta Mater 1999;47:579.
- [104] Balluffi RW, Ruoff a. L. J Appl Phys 1963;34:1634.
- [105] Ruoff a. L, Balluffi RW. J Appl Phys 1963;34:2862.
- [106] Prokoshkin SD, Khmelevskaya IY, Dobatkin SV, Trubitsyna IB, Tatyandin EV, Stolyarov VV, Prokofiev E a. Acta Mater 2005;53:2703.
- [107] Belyakov a, Sakai T, Miura H, Kaibyshev R, Tsuzaki K. Acta Mater 2002;50:1547.
- [108] Belyakov a., Kimura Y, Tsuzaki K. Mater Sci Eng A 2005;403:249.
- [109] Zhang Y, Gey N, He C, Zhao X, Zuo L, Esling C. Acta Mater 2004;52:3467.
- [110] Stewart GR, Jonas JJ, Montheillet F. ISIJ Int 2004;44:1581.
- [111] Fiaabe D. Steel Res 1995;5:66.
- [112] Maji BC, Krishnan M. Scr Mater 2003;48:71.
- [113] Zaefferer S, Ohlert J, Bleck W. Acta Mater 2004;52:2765.
- [114] Sakai T, Ohashi M, Chiba K, Jonas J. Acta Metall 1988;36.

- [115] Martínez-de-Guerenu a, Arizti F, Díaz-Fuentes M, Gutiérrez I. *Acta Mater* 2004;52:3657.
- [116] Komura S, Horita Z, Nemoto M, Langdon TG. *J Mater Res* 2011;14:4044.
- [117] Ryan ND, McQueen HJ, Evangelista E. *Mater Sci Eng* 1986;81:259.
- [118] Doong SH, Socie DF, Robertson MI. *J Eng Mater Technol* 1990;112:456.
- [119] Hsun H. *Acta Metall* 1962;10:1112.
- [120] Yoshie A, Morikawa H, Onoe Y, Itoh K. *Trans Iron Steel Inst* 1987;27 425.
- [121] Bon A Le, Rofes-Vernis J, Rossard C. *Met Sci* 1975:36.
- [122] Harase J. *Can Metall Q* 1995;34:185.
- [123] Cotterill P, Mould PR. Krieger Pub Co 1976.
- [124] Hayakawa Y, Muraki M, Szpunar J. *Acta Mater* 1998;46:1063.
- [125] Dickson MJ, Green D. *Mater Sci Eng* 1969;4:304.
- [126] Ralph B. *Mater Sci Technol* 1990;6:1139.
- [127] Rossi P, Sellars CM. *Acta Mater* 1997;45:137.
- [128] Drury M, Urai J. *Tectonophysics* 1990;112:235.
- [129] Vervynckt S, Verbeken K, Lopez B, Jonas JJ. *Int Mater Rev* 2012;57:187.
- [130] Rios P, Jr FS, Sandim H. *Mater Res* 2005;8:225.
- [131] Johnson WA, Mehl RF. *Trans Aime* 1939;135:396.
- [132] Burgers WG. *Principles of Recrystallization, In Art and Science of Growing Crystals* Wiley New York 1963.
- [133] Koch E. Academic Press London; 1977.
- [134] Tsukatani I. *ISIJ Int* 1998;38:625.
- [135] Ye W, Le Gall R, Saindrenan G. *Mater Sci Eng A* 2002;332:41.
- [136] Yoda R, Tsukatani I, Inoue T, Saito T. *ISIJ Int* 1994;34:70.
- [137] Ueki M, Horie S, Nakamura T. *Mater Sci Technol* 1987;3:329.
- [138] Sellars CM. *Mater Sci Technol* 1990;6:1072.

- [139] Hansen SS, Vander Sande JB, Cohen M. Metall Trans A 1980;11:387.
- [140] DeArdo AJ, Ratz GA, Wray PJ. Proceedings of the International Conference on the Thermomechanical Processing of Microalloyed Austenite. Metallurgical Society of AIME 1982.
- [141] Sellars CM, Whiteman J. Met Sci 1979;13:187.
- [142] Malow T, Koch C. Acta Mater 1997;45:2177.
- [143] Burke J, Turnbull D. Prog Met Phys 1952;3:220.
- [144] Anderson M, Srolovitz D, Grest G, Sahni P. Acta Metall 1984;32:783.
- [145] Srolovitz D, Grest G, Anderson M. Acta Metall 1985;33:2233.
- [146] Holm E a., Miodownik M a., Rollett a. D. Acta Mater 2003;51:2701.
- [147] Doucet A, De Freitas N, Gordon N. Springer New York 2001.
- [148] Doherty RD. Phys Metall 1996;2:1456.
- [149] Porter DA, Easterling KE, Sherif M. CRC Press; 2011.
- [150] Robson J, Bhadeshia H. Mater Sci Technol 1997;13:631.
- [151] Perez M. Scr Mater 2005;52:709.
- [152] Nabarro FRN. Elsevier Science, Amsterdam:North Holland 1967.
- [153] Verhoeven JD. Wiley New York; 1975.
- [154] Reed-Hill RE, Abbaschian R. New York, Van Nostrand 2<sup>nd</sup> ed 1973.
- [155] Turnbull D. J Chem Phys 1950;18:198.
- [156] Fievet F, Lagier J, Blin B, Beaudoin B, Figlarz M. Solid State Ionics 1989;33:198.
- [157] Goetz R, Seetharaman V. Metall Mater Trans A 1998;29:2307.
- [158] Cahn J. Acta Metall 1962;10:789.
- [159] Bradley JR, Rigsbee JM, Aaronson HI. Metall Trans A 1977;8:323.
- [160] Russell K. Adv Colloid Interface Sci 1980;13:205.
- [161] Dutta B, Valdes E, Sellars CM. Acta Metall 1992;40:653.
- [162] Liu WJ, Jonas JJ. Metall Trans A 1988;19:1403.

- [163] Siradj ES, Sellars CM, Whiteman JA. *Mater. Sci. Forum* 1998;284:143.
- [164] Dutta B, Palmiere EJ, Sellars CM. *Acta Mater* 2001;49:785.
- [165] Okaguchi S, Hashimoto T. *ISIJ Int* 1992;32.
- [166] Rainforth WM, Black MP, Higginson RL, Palmiere EJ, Sellars CM, Prabst I, Warbichler P, Hofer F. *Acta Mater* 2002;50:735.
- [167] Aaronson HI, Jr WTR, Purdy G. *Metall Mater* 2006;37:1731.
- [168] Enloe CM. Department of Metallurgical and Materials Engineering, The Colorado School of Mines, PhD Thesis 2013.
- [169] Fernández J, Illescas S, Guilemany JM. *Mater Lett* 2007;61:2389.
- [170] Craven A, He K, Garvie L, Baker T. *Acta Mater* 2000;48:3857.
- [171] Schoen FJ, Owen WS. *Metall Trans* 1971;2:2431.
- [172] Suehiro M, Liu Z, Ågren J. *Metall Mater Trans A* 1998;29:1029.
- [173] Mendeleev MI, Srolovitz DJ, E W. *Philos Mag A* 2001;81:2243.
- [174] Ghosh SK, Mondal S. *Mater Charact* 2008;59:1776.
- [175] Takaki S, Kawasaki K, Kimura Y. *J Mater Process* 2001;117:6.
- [176] Eckert J, Holzer JC, Johnson WL. *J Appl Phys* 1993;73:131.
- [177] Detert K. *Recrystallization of metallic materials* 1978:97.
- [178] Gleiter H. *Acta Metall* 1970;18:117.
- [179] Markham R, Smith JD. *Biochem J* 1952;52:552.
- [180] Hillert M. *Acta Metall* 1965.
- [181] Feltham P. *Acta Metall* 1957;5:97.
- [182] Loveday M, Mahon G. *Mater high T* 2006;23:85.
- [183] Williams DB, Carter CB. Springer New York 1996.
- [184] Joy DC, Egerton RF, Maher DM. *Scanning Electron Microsc Vol IIAMF O'Hare, Chicago* 1979:817.
- [185] Leapman R. *J Microsc* 2003;210:5.
- [186] Palmiere EJ. *Diss Abstr Int* 1992;52:217.

- [187] Yen HW, Chen PY, Huang CY, Yang JR. *Acta Mater* 2011;59:6264.
- [188] Zurob HS, Hutchinson CR, Brechet Y, Purdy G. *Acta Mater* 2002;50:3077.
- [189] Batzer S, Haan D, Rao P. *Process Technol* 1998.
- [190] Johnson W, Mehl R. *Trans Aime* 1939;135:396.
- [191] Tarafder M, Sinha P, Kundu A, Strangwood M, Davis C. *Mater Charact* 2013;85:92.
- [192] Homsher CN. *Materials Science*, Colorado School of Mines, MS Thesis 2013.
- [193] Vervynckt S, Verbeken K, Thibaux P, Houbaert Y. *Mater Sci Eng A* 2011;528:5519.
- [194] Lupis CH., Elliott J. *Acta Metall* 1966;14:529.
- [195] Palmiere EJ. *The School of Engineering*, University of Pittsburgh 1992.
- [196] Park SH. *Department of Mining and Metallurgical Engineering*, McGill University, PhD Thesis 1991.
- [197] Davenport AT, Brossardlc LC, Miner RM. *J Met* 1975;27:21.
- [198] Kurdjumov GV, Sachs G. *Z Phys* 1930;64:325.
- [199] Baker RG, Nutting J. *Iron and Steel Institute* 1959.
- [200] Ghosh P, Ray RK, Ghosh C, Bhattacharjee D. *Scr Mater* 2008;58:939.
- [201] Soto R, Saikaly W, Bano X, Issartel C, Rigaut G, Charai A. *Acta Mater* 1999;47:3475.
- [202] Korcakova L, Hald J, Somers MA. *Mater Charact* 2001;47:111.
- [203] Underwood E. *Metals Handbook* 1973:35.
- [204] Dieter G. *Mechanical Metallurgy*. 1986.
- [205] Ono K, Moriyama J. *J Less Common Met* 1981;79:255.
- [206] Williams DB, Carter CB. *Transmission Electron Microscopy: A Textbook for Materials Science*. Springer US; 2009.
- [207] Sun ZQ, Yang WY, Qi JJ, Hu AM. *Mater Sci Eng A* 2002;334:201.
- [208] Palmiere EJ, Garcia C, Ardo AD. *Metall Mater Trans A* 1994;25:277.
- [209] Olson G, Ling H, Montgomery J. *MRS Proc* 1981;8:355.
- [210] Wang K. *University of Canterbury*, Phd Thesis 2003.

- [211] Yuan SQ, Liang GL. *Mater Lett* 2009;63:2324.
- [212] Illescas S, Fernández J, Guilemany JM. *Mater Lett* 2008;62:3478.
- [213] Burke J, Shiau Y. *Aime Trans* 1948;175:141.
- [214] Smith C S. *Trans AIME* 1948;175:15.
- [215] Beck PA. *Adv Phys* 1954;3:245.
- [216] Hellman P, Hillert M. *Scand J Metall* 1975;4:211.
- [217] Fan D, Chen SP, Chen LQ. *J Mater Res* 2011;14:1113.
- [218] Mallick A. *Comput Mater Sci* 2013;67:27.
- [219] Michels A, Krill CE, Ehrhardt H, Birringer R, Wu DT. *Acta Mater* 1999;47:2143.
- [220] Le Gall R, Jonas J. *Acta Mater* 1999;47:4365.
- [221] Sellars CM. *Czechoslov J Phys* 1985;35:239.
- [222] Beladi H, Kelly GL, Hodgson PD. *Mater Trans* 2004;45:2214.
- [223] Quested TE, Greer a. L. *Acta Mater* 2005;53:2683.
- [224] Lange W, Enomoto M, Aaronson H. *Metall Mater* 1988;19:427.
- [225] Jones SJ, Bhadeshia HKDH. *Acta Mater* 1997;45:2911.
- [226] Capdevila CF, Capdevila C, Farcia De Andres G. *ISIJ* 2001;41:1093.
- [227] Harase J, Shimizu R. *Mater Sci Forum* 1992;94:339.
- [228] Aaronson H, Zackay V. *Interscience Pub* 1962.
- [229] Enomoto M, Sonoyama T, Yada H. *Mater Trans JIM* 1998;39:189.
- [230] Hurley PJ, Hodgson PD, Muddle BC. *Scr Mater* 1999;40:433.
- [231] Capdevila C, Caballero FG, Andrés C. *Mater Sci Technol* 2003;19:581.
- [232] Hurley PJ, Muddle BC, Hodgson PD. *Metall Mater Trans A* 2001;32:1507.
- [233] Dutta B, Palmiere EJ, Sellars CM. *Acta Mater* 2001;49:785.
- [234] Pereloma E, Crawford B, Hodgson P. *Mater Sci Eng A* 2001;299:27.
- [235] Gong P, Palmiere EJ, Rainforth WM. *Acta Mater* 2015;97:392.

- [236] Dijk NHV, Offerman SE, Bouwman MT. *Mater Trans A* 2002;33A:1883.
- [237] Cahn JW. *Acta Metall* 1956;4:572.
- [238] Medina S. *Scr Metall Mater* 1995;32:43.
- [239] Björklund S, Donaghey L, Hillert M. *Acta Metall* 1972;20:867.
- [240] Luo H, Sietsma J, Zwaag SVD. *Metall Mater* 2004;35:2789.
- [241] Gladman T. *Maney Pub* 1997;615.
- [242] Licka S, Wozniak J, Kosar M, Prnka T. *Thermomechanical Processing of Microalloyed Austenite* 1981:521.